UAB LIBRARIES
The University of Alabama at Birmingham

University of Alabama at Birmingham
UAB Digital Commons

All ETDs from UAB

UAB Theses & Dissertations

2020

A Mesoscale-Based Computational Mechanics Framework For Constitutive Characterization And Homogenization Of Particulate Media

Gerald Pekmezi
University of Alabama at Birmingham

Follow this and additional works at: https://digitalcommons.library.uab.edu/etd-collection

Recommended Citation

Pekmezi, Gerald, "A Mesoscale-Based Computational Mechanics Framework For Constitutive Characterization And Homogenization Of Particulate Media" (2020). *All ETDs from UAB*. 2695.
https://digitalcommons.library.uab.edu/etd-collection/2695

This content has been accepted for inclusion by an authorized administrator of the UAB Digital Commons, and is provided as a free open access item. All inquiries regarding this item or the UAB Digital Commons should be directed to the UAB Libraries Office of Scholarly Communication.

A MESOSCALE-BASED COMPUTATIONAL MECHANICS FRAMEWORK FOR CONSTITUTIVE CHARACTERIZATION AND HOMOGENIZATION OF PARTICULATE MEDIA

by

GERALD PEKMEZI

DAVID L. LITTLEFIELD, CHAIR
STEPHEN A. AKERS
KENT DANIELSON
BRADLEY MARTIN
DEAN L. SICKING
NASIM UDDIN

A DISSERTATION

Submitted to the graduate faculty of The University of Alabama at Birmingham,
in partial fulfillment of the requirements for the degree of
Doctor of Philosophy

BIRMINGHAM, ALABAMA

2020

A MESOSCALE-BASED COMPUTATIONAL MECHANICS FRAMEWORK FOR CONSTITUTIVE CHARACTERIZATION AND HOMOGENIZATION OF PARTICULATE MEDIA

GERALD PEKMEZI

INTERDISCIPLINARY ENGINEERING

ABSTRACT

A complete meso-to-macro computational homogenization approach for particulate materials has been devised and implemented in this study. Starting with experimental distributions of the micromechanical characteristics of constitutive grains, this framework uses computational modeling of mesoscale statistical ensembles to characterize effective mechanical behavior at incrementally larger mesoscopic scales. This approach is found to be useful in several ways: 1) the effective Representative Volume Element (RVE) size of particulate media can be identified using the most rigorous homogenization criterion, the Hill-Mandel macrohomogeneity condition, 2) a statistical description is possible of the effective mechanical properties of particulate media at scales below the RVE, where these properties are spurious and non-deterministic, 3) ensemble modeling results can be used to optimize and calibrate continuum models of particulate materials with Finite Element Analysis, 4) ensemble averages of finite strain simulations can be used to study internal state variable evolution, and 5) uncertainty quantification (UQ) of the mechanical response of particulate media is possible using propagation of uncertainty from the mesoscale ensemble results.

This approach hinges on a newly developed real-time interface tracking algorithm for particle-based simulation methods that can be used to study the bounds of discrete particle aggregates such as sand. The interface tracking algorithm uses an advanced surface

extraction technique based on the alpha shape paradigm of computational geometry. When used concurrently with particle-based methods, this algorithm can track the evolution of the simulation boundaries and applying accurate micro-boundary conditions on them. The micro-boundary conditions may be of Dirichlet type, Neumann type, or mixed-orthogonal type and may be tensorial.

This framework enables the heretofore limited use of particle-based simulations in upscaling studies by providing a path for homogenization and uncertainty quantification (UQ) of granular media. Thus, this framework provides an additional path for constitutive characterization of particle aggregates, particularly in hydrocode modeling of high confinement, finite deformation phenomena.

ACKNOWLEDGEMENTS

I would like to express my sincere gratitude to Dr. David Littlefield, my doctoral adviser and research mentor, for his guidance, patience and constructive feedback. This research topic was his brainchild; to his great credit he gave me the freedom and opportunity to adopt it and mold it after my own ideas.

I would also like to recognize and thank Dr. Stephen Akers, Dr. Kent Danielson, Dr. Bradley Martin, Dr. Dean Sicking, and Dr. Nasim Uddin, for serving on my dissertation committee and giving me feedback on improving and finalizing this manuscript. I am also appreciative of the faculty and staff of the Mechanical Engineering Department at the University of Alabama at Birmingham. They have contributed to a healthy and productive research environment.

My gratitude also goes to the developers of the Yade open source Discrete Element code, particularly Prof. Bruno Chareyre of the University of Grenoble, whose expertise and creativity with computational geometry helped my research progress beyond the conceptual phase.

Lastly, I would like to thank my family for their love, support and encouragement during this process. My wife, Dr. Dori Pekmezi, has had boundless patience and love on this journey, encouraging me along the way and shouldering the bulk of the parenting duties as this manuscript gathered momentum. My three little boys, Ian, Aleks, and Julian, have provided the ultimate motivation. I want to thank my mother Beti and my father Maks, my late grandfather Pineu, my grandmother Pina, my uncle Toni as well as all my family

still in my original homeland of Albania. The world I was born into changed while I was growing up, it was the intellectual thirst they instilled that allowed me to find a place in it.

TABLE OF CONTENTS

Page

ABSTRACT ii

ACKNOWLEDGEMENTS iv

LIST OF FIGURES ix

LIST OF TABLES xxii

CHAPTER

1 INTRODUCTION 1

Motivation 2
Scope and Objectives 4
Mesoscale Modeling 4
Statistical Geomechanics 5
Homogenization 6
Uncertainty Quantification 7
Calibration of Continuum Models 8
Dissertation Organization 9

2 THEORY AND BACKGROUND 12

A Brief History of Soil Mechanics 12
Important Concepts of Sand Mechanics 14
Physics of Sand 15
Classification and Testing 19
Some Common Sand Models 23
A Bridge from the Grain to the Continuum 31
Homogenization – Analytical and Computational 32
Separation of Scales 35
Volume Elements – Representative and Stochastic 36
The Hill Condition for Particle Aggregates 37
Mesoscale Bounds of Particle Aggregates 38
Computational Mechanics through Statistics, Probability, and Optimization 41
Statistical Mechanics of Random Heterogeneous Materials 42
Propagation of Uncertainty at the Mesoscale 46
Model Calibration through Mathematical Optimization 47

3 FORMULATION OF COMPUTATIONAL AND MATHEMATICAL MODELS.... 50

Discrete Element Modeling of Sand.... 50
Explicit Numerical Scheme.... 51
Contact Model.... 53
Global Damping Mechanism.... 55
Weibull Survival Probabilities of Sand Grains.... 56
Brazilian Criterion of Grain Fracture.... 60
Hybrid-Elastic-Plastic Models.... 61
Volumetric Behavior in the HEP Model.... 62
Deviatoric Behavior in the HEP Model.... 67
Statistical Ensemble Generation and Analysis.... 69
Generation of Ab-Initio Realizations for Homogenization.... 69
Iterative Domain Partitioning for Propagation of Uncertainty.... 76
Anomaly Detection with Grubbs Test for Outliers.... 78
Weibull Distribution Fitting of Results.... 80
Wasserstein Metric of Statistical Distance.... 81
Mathematical Optimization Algorithms.... 82
Single Objective Genetic Algorithm.... 83
Multi-Objective Genetic Algorithm.... 85

4 MICRO-MECHANICAL BOUNDING OF PARTICLE AGGREGATES 86

A Line in the Sand – Boundaries of Particle Aggregates.... 86
A Novel Approach to Particle Aggregate Boundaries.... 89
Voronoi Diagrams and Delaunay Triangulations.... 89
Surface Reconstruction with Alpha-Shapes.... 92
LaGuerre-Voronoi Diagrams on Particle Aggregate Boundaries.... 96
Ancillary Surface Mapping with Regular Grids.... 98
Numerical Implementation of Boundary Conditions.... 102
Kinematic Uniform Boundaries.... 102
Static Uniform Boundaries.... 104
Periodic Boundaries.... 105
Particle Kinematics and the Deformation Gradient Tensor.... 107
Love-Weber Average of the Cauchy Stress Tensor.... 109
Work-Conjugate Measures of Stress and Strain.... 111

5 EGLIN SAND MESOSCALE ENSEMBLE SIMULATIONS AND RESULTS 114

Micromechanical Parameters.... 115
Computational Homogenization without Fragmentation.... 116
Comminution due to Grain Fragmentation.... 120
Mesoscopic Physical Characteristics of the Ensembles.... 125
Computational Homogenization with Comminution.... 132
Ensemble Averaged Finite Strain Response.... 137
Ensemble Thermomechanical Statistics of Eglin Sand.... 147
Summary and Discussion of Mesoscale Results.... 154

6 MESOSCALE-BASED MODELING AND UQ WITH THE HEP MODEL 160

Confined Triaxial Simulations with Library HEP Model.... 161

Calibration of the HEP Model from Discrete Modeling 166

7 CONCLUSIONS …..... 176

Future Work 177

REFERENCES 179

APPENDIX

A HISTOGRAMS OF MESOSCALE ELASTIC MODULI OF EGLIN SAND WITHOUT COMMINUTION 195

B HISTOGRAMS OF MESOSCALE ELASTIC MODULI OF EGLIN SAND AFTER COMMINUTION 220

LIST OF FIGURES

Figure *Page*

1.1: Disordered Heterogeneous Packing of Sand Grains 7

2.1: Pressure-compression behavior in the HEP model 16

2.2: Modes of grain crushing in sand 17

2.3: Sand specimen in SHPB testing 22

2.4: SHPB schematic 22

2.5: Mohr-Coulomb Failure Surface 24

2.6: Drucker-Prager Failure Surface 25

2.7: Modified Cam-Clay Yield Surface and Critical State Line 27

2.8: Yield surface in the Cap Model 28

2.9: Yield surface of the three-phase modified Cam-Clay Model 30

2.10: Heterogeneous Packing of Sand Grains 35

2.11: Hierarchy of scale-dependent bounds 40

3.1: Grain probability distribution of normalized strengths for normalized diameters 58

3.2: Apollonian Sphere Packings at increasing levels of refinement 59

3.3: Apollonian packing blowout under 1D compression 60

3.4: Pressure-compression behavior in the HEP model 64

3.5: Simple HEP deviatoric behavior 68

3.6: Four typical $1x10^4$ particle ab-initio realizations confined to average isotropic stress of 5 MPa in a “bounding box” 73

3.7: Four typical $1x10^4$ particle ab-initio realizations gradually confined to a uniform isotropic micro-stress of 5MPa 75

3.8: RVE-sized $5x10^6$ particle Discrete Element model decomposed into a grid of 8x8x8 subdomains 77

3.9: RVE-sized $5x10^6$ particle Discrete Element model decomposed into a grid of 17x17x17 subdomains 78

4.1: A set of 20 points and their Voronoi polygons 91

4.2: Alpha-shape reconstruction of a 2D point set boundary 93

4.3: Alpha-shape reconstruction of a 2D point set boundary 94

4.4: 2-dimensional Power Diagram of 4 Circles 98

4.5: The two types of boundary surfaces considered 99

4.6: First stage of ancillary surface grid interpolation stage 101

4.7: Second stage of ancillary surface grid interpolation stage 101

5.1: Eglin Sand PSD from the sieve data as well as the Weibull fit 116

5.2: Ratios of elastic moduli Voigt to Reuss bounds at 1 MPa confinement 117

5.3: Ratios of elastic moduli Sachs to Taylor bounds at 1 MPa confinement 117

5.4: Ratios of elastic moduli Voigt to Reuss bounds at 5 MPa confinement 118

5.5: Ratios of elastic moduli Sachs to Taylor bounds at 5 MPa confinement 118

5.6: Ratios of elastic moduli Voigt to Reuss bounds at 20 MPa confinement 119

5.7: Ratios of elastic moduli Sachs to Taylor bounds at 20 MPa confinement 119

5.8: Eglin Sand PSD evolution during crush-up for compression up to 200 MPa 120

5.9: Comminuted PSDs of the Statistical Ensembles at 20 MPa Confinement 121

5.10: Comminuted PSDs of the Statistical Ensembles at 50 MPa Confinement 122

5.11: Comminuted PSDs of the Statistical Ensembles at 100 MPa Confinement 122

5.12: Comminuted PSDs of the Statistical Ensembles at 200 MPa Confinement 123

5.13: Comminuted PSDs of the Statistical Ensembles at 400 MPa Confinement 123

5.14: Average realization window size of ensembles with virgin PSD 126

5.15: Average realization porosity of ensembles with virgin PSD 126

5.16: Average window size of ensembles with comminuted PSD at 20 MPa 127

5.17: Average porosity of ensembles with comminuted PSD at 20 MPa 127

5.18: Average window size of ensembles with comminuted PSD at 50 MPa 128

5.19: Average porosity of ensembles with comminuted PSD at 50 MPa 128

5.20: Average window size of ensembles with comminuted PSD at 100 MPa 129

5.21: Average porosity of ensembles with comminuted PSD at 100 MPa 129

5.22: Average window size of ensembles with comminuted PSD at 200 MPa 130

5.23: Average porosity of ensembles with comminuted PSD at 200 MPa 130

5.24: Average window size of ensembles with comminuted PSD at 400 MPa 131

5.25: Average porosity of ensembles with comminuted PSD at 400 MPa 131

5.26: Ratios of elastic moduli Voigt to Reuss bounds at 20 MPa confinement..... 132

5.27: Ratios of elastic moduli Sachs to Taylor bounds at 20 MPa confinement 133

5.28: Ratios of elastic moduli Voigt to Reuss bounds at 50 MPa confinement..... 133

5.29: Ratios of elastic moduli Sachs to Taylor bounds at 50 MPa confinement 134

5.30: Ratios of elastic moduli Voigt to Reuss bounds at 100 MPa confinement..... 134

5.31: Ratios of elastic moduli Sachs to Taylor bounds at 100 MPa confinement 135

5.32: Ratios of elastic moduli Voigt to Reuss bounds at 200 MPa confinement..... 135

5.33: Ratios of elastic moduli Sachs to Taylor bounds at 200 MPa confinement 136

5.34: Ratios of elastic moduli Voigt to Reuss bounds at 400 MPa confinement..... 136

5.35: Ratios of elastic moduli Sachs to Taylor bound at 400 MPa confinement..... 137

5.36: Isotropic compression of Eglin sand using SUBC and KUBC..... 138

5.37: Eglin Sand volumetric compression response at mean stress up to 400 MPa 139

5.38: Volumetric response with interpolated double porosity..... 140

5.39: Deviatoric response of CTC axial loading at 20 MPa confinement 141

5.40: Volumetric response of CTC axial loading at 5 MPa confinement..... 141

5.41: Deviatoric response of CTC axial loading at 20 MPa confinement 142

5.42: Volumetric response of CTC axial loading at 20 MPa confinement..... 142

5.43: Deviatoric response of CTC axial loading at 50 MPa confinement 143

5.44: Volumetric response of CTC axial loading at 50 MPa confinement..... 143

5.45: Deviatoric response of CTC axial loading at 100 MPa confinement 144

5.46: Volumetric response of CTC axial loading at 100 MPa confinement..... 144

5.47: Deviatoric response of CTC axial loading at 200 MPa confinement 145

5.48: Volumetric response of CTC axial loading at 200 MPa confinement..... 145

5.49: Deviatoric response of CTC axial loading at 400 MPa confinement 146

5.50: Volumetric response of CTC axial loading at 400 MPa confinement..... 146

5.51: Work and energy dissipation during volumetric loading..... 148

5.52: Work and dissipation during CTC axial loading at 5 MPa confinement..... 149

5.53: Work and dissipation during CTC axial loading at 20 MPa with crush-up..... 149

5.54: Work and dissipation during CTC axial loading at 20 MPa without crush-up..... 150

5.55: Work and dissipation during CTC axial loading at 50 MPa with crush-up..... 150

5.56: Work and dissipation during CTC axial loading at 50 MPa without crush-up..... 151

5.57: Work and dissipation during CTC axial loading at 100 MPa with crush-up..... 151

5.58: Work, dissipation during CTC axial loading at 100 MPa without crush-up 152

5.59: Work and dissipation during CTC axial loading at 200 MPa with crush-up..... 152

5.60: Work, dissipation during CTC axial loading at 200 MPa without crush-up 153

5.61: Work and dissipation during CTC axial loading at 400 MPa with crush-up..... 153

5.62: Work, dissipation during CTC axial loading at 400 MPa without crush-up 154

5.63: RVE size for Eglin sand based on mesoscale simulations..... 157

5.64: Effective bulk moduli for $1x10^5$ particle ensembles..... 158

5.65: Effective Young's moduli for $1x10^5$ particle ensemble..... 158

5.66: Effective shear moduli for $1x10^5$ particle ensemble..... 159

6.1: Hexahedral single element in Epic 162

6.2: Isotropic response of library sand material..... 162

6.3: Axial loading response of library sand material at 5 MPa confinement..... 163

6.4: Axial loading response of library sand material at 20 MPa confinement..... 163

6.5: Axial loading response of library sand material at 50 MPa confinement..... 164

6.6: Axial loading response of library sand material at 100 MPa confinement..... 164

6.7: Axial loading response of library sand material at 200 MPa confinement..... 165

6.8: Axial loading response of library sand material at 400 MPa confinement..... 165

6.9: Objective function contours for parametric optimization of PSUB1 vs. PSUB2.... 167

6.10: Objective contours for parametric optimization of PSUB2 vs. PSUBC..... 168

6.11: Objective contours for parametric optimization of USUB2 vs. USUBC 168

6.12: Objective contours for parametric optimization of ASUB0 vs. ASUB1..... 169

6.13: Objective contours for parametric optimization of ASUB0 vs. ASUB1..... 169

6.14: Histogram of PSUB1 optimized to each realization..... 171

6.15: Histogram of PSUB2 optimized to each realization..... 171

6.16: Histogram of PSUBC optimized to each realization 172

6.17: Histogram of USUB2 optimized to each realization 172

6.18: Histogram of USUBC optimized to each realization..... 173

6.19: Histogram of ASUB0 optimized to each realization 173

6.20: Histogram of ASUB1 optimized to each realization 174

6.21: Histogram and fit of ASUB2 optimized to each realization..... 174

6.22: Histogram of ASUBC optimized to each realization..... 175

A.1: Secant Young's Modulus for $1x10^3$ Particle Ensemble at 1MPa 196

A.2: Secant Shear Modulus for $1x10^3$ Particle Ensemble at 1MPa 196

A.3: Secant Bulk Modulus for $1x10^3$ Particle Ensemble at 1MPa 196

A.4: Tangent Young's Modulus for $1x10^3$ Particle Ensemble at 1MPa 197

A.5: Tangent Shear Modulus for $1x10^3$ Particle Ensemble at 1MPa..... 197

A.6: Tangent Bulk Modulus for $1x10^3$ Particle Ensemble at 1MPa 197

A.7: Secant Young's Modulus for $1x10^3$ Particle Ensemble at 5MPa 198

A.8: Secant Shear Modulus for $1x10^3$ Particle Ensemble at 5MPa 198

A.9: Secant Bulk Modulus for $1x10^3$ Particle Ensemble at 5MPa 198

A.10: Tangent Young's Modulus for $1x10^3$ Particle Ensemble at 5MPa 199

A.11: Tangent Shear Modulus for $1x10^3$ Particle Ensemble at 5MPa..... 199

A.12: Tangent Bulk Modulus for $1x10^3$ Particle Ensemble at 5MPa 199

A.13: Secant Young's Modulus for $1x10^3$ Particle Ensemble at 20MPa 200

A.14: Secant Shear Modulus for $1x10^3$ Particle Ensemble at 20MPa 200

A.15: Secant Bulk Modulus for $1x10^3$ Particle Ensemble at 20MPa 200

A.16: Tangent Young's Modulus for $1x10^3$ Particle Ensemble at 20MPa 201

A.17: Tangent Shear Modulus for $1x10^3$ Particle Ensemble at 20MPa 201

A.18: Tangent Bulk Modulus for $1x10^3$ Particle Ensemble at 20MPa 201

A.19: Secant Young's Modulus for $1x10^4$ Particle Ensemble at 1MPa 202

A.20: Secant Shear Modulus for $1x10^4$ Particle Ensemble at 1MPa 202

A.21: Secant Bulk Modulus for $1x10^4$ Particle Ensemble at 1MPa 202

A.22: Tangent Young's Modulus for $1x10^4$ Particle Ensemble at 1MPa 203

A.23: Tangent Shear Modulus for $1x10^4$ Particle Ensemble at 1MPa 203

A.24: Tangent Bulk Modulus for $1x10^4$ Particle Ensemble at 1MPa 203

A.25: Secant Young's Modulus for $1x10^4$ Particle Ensemble at 5MPa 204

A.26: Secant Shear Modulus for $1x10^4$ Particle Ensemble at 5MPa 204

A.27: Secant Bulk Modulus for $1x10^4$ Particle Ensemble at 5MPa 204

A.28: Tangent Young's Modulus for $1x10^4$ Particle Ensemble at 5MPa 205

A.29: Tangent Shear Modulus for $1x10^4$ Particle Ensemble at 5MPa 205

A.30: Tangent Bulk Modulus for $1x10^4$ Particle Ensemble at 5MPa 205

A.31: Secant Young's Modulus for $1x10^4$ Particle Ensemble at 20MPa 206

A.32: Secant Shear Modulus for $1x10^4$ Particle Ensemble at 20MPa 206

A.33: Secant Bulk Modulus for $1x10^4$ Particle Ensemble at 20MPa 206

A.34: Tangent Young's Modulus for $1x10^4$ Particle Ensemble at 20MPa 207

A.35: Tangent Shear Modulus for $1x10^4$ Particle Ensemble at 20MPa 207

A.36: Tangent Bulk Modulus for $1x10^4$ Particle Ensemble at 20MPa 207

A.37: Secant Young's Modulus for $1x10^5$ Particle Ensemble at 1MPa 208

A.38: Secant Shear Modulus for $1x10^5$ Particle Ensemble at 1MPa 208

A.39: Secant Bulk Modulus for $1x10^5$ Particle Ensemble at 1MPa 208

A.40: Tangent Young's Modulus for $1x10^5$ Particle Ensemble at 1MPa 209

A.41: Tangent Shear Modulus for $1x10^5$ Particle Ensemble at 1MPa..... 209

A.42: Tangent Bulk Modulus for $1x10^5$ Particle Ensemble at 1MPa 209

A.43: Secant Young's Modulus for $1x10^5$ Particle Ensemble at 5MPa 210

A.44: Secant Shear Modulus for $1x10^5$ Particle Ensemble at 5MPa 210

A.45: Secant Bulk Modulus for $1x10^5$ Particle Ensemble at 5MPa 210

A.46: Tangent Young's Modulus for $1x10^5$ Particle Ensemble at 5MPa 211

A.47: Tangent Shear Modulus for $1x10^5$ Particle Ensemble at 5MPa..... 211

A.48: Tangent Bulk Modulus for $1x10^5$ Particle Ensemble at 5MPa 211

A.49: Secant Young's Modulus for $1x10^5$ Particle Ensemble at 20MPa 212

A.50: Secant Shear Modulus for $1x10^5$ Particle Ensemble at 20MPa 212

A.51: Secant Bulk Modulus for $1x10^5$ Particle Ensemble at 20MPa 212

A.52: Tangent Young's Modulus for $1x10^5$ Particle Ensemble at 20MPa 213

A.53: Tangent Shear Modulus for $1x10^5$ Particle Ensemble at 20MPa..... 213

A.54: Tangent Bulk Modulus for $1x10^5$ Particle Ensemble at 20MPa 213

A.55: Secant Young's Modulus for $1x10^6$ Particle Ensemble at 1MPa 214

A.56: Secant Shear Modulus for $1x10^6$ Particle Ensemble at 1MPa 214

A.57: Secant Bulk Modulus for $1x10^6$ Particle Ensemble at 1MPa 214

A.58: Tangent Young's Modulus for $1x10^3$ Particle Ensemble at 1MPa 215

A.59: Tangent Shear Modulus for $1x10^6$ Particle Ensemble at 1MPa..... 215

A.60: Tangent Bulk Modulus for $1x10^6$ Particle Ensemble at 1MPa 215

A.61: Secant Young's Modulus for $1x10^6$ Particle Ensemble at 5MPa 216

A.62: Secant Shear Modulus for $1x10^6$ Particle Ensemble at 5MPa 216

A.63: Secant Bulk Modulus for $1x10^6$ Particle Ensemble at 5MPa 216

A.64: Tangent Young's Modulus for $1x10^6$ Particle Ensemble at 5MPa 217

A.65: Tangent Shear Modulus for $1x10^6$ Particle Ensemble at 5MPa..... 217

A.66: Tangent Bulk Modulus for $1x10^6$ Particle Ensemble at 5MPa 217

A.67: Secant Young's Modulus for $1x10^6$ Particle Ensemble at 20MPa 218

A.68: Secant Shear Modulus for $1x10^6$ Particle Ensemble at 20MPa 218

A.69: Secant Bulk Modulus for $1x10^6$ Particle Ensemble at 20MPa 218

A.70: Tangent Young's Modulus for $1x10^6$ Particle Ensemble at 20MPa 219

A.71: Tangent Shear Modulus for $1x10^6$ Particle Ensemble at 20MPa..... 219

A.72: Tangent Bulk Modulus for $1x10^6$ Particle Ensemble at 20MPa 219

B.1: Secant Young's Mod. for $1x10^3$ Comminuted Particle Ensemble at 20 MPa 221

B.2: Secant Shear Modulus for $1x10^3$ Comminuted Particle Ensemble at 20 MPa 221

B.3: Secant Bulk Modulus for $1x10^3$ Comminuted Particle Ensemble at 20 MPa..... 221

B.4: Tangent Young's Mod. for $1x10^3$ Comminuted Particle Ensemble at 20 MPa 222

B.5: Tangent Shear Mod. for $1x10^3$ Comminuted Particle Ensemble at 20 MPa..... 222

B.6: Tangent Bulk Mod. for $1x10^3$ Comminuted Particle Ensemble at 20 MPa 222

B.7: Secant Young's Mod. for $1x10^3$ Comminuted Particle Ensemble at 50 MPa 223

B.8: Secant Shear Modulus for $1x10^3$ Comminuted Particle Ensemble at 50 MPa 223

B.9: Secant Bulk Modulus for $1x10^3$ Comminuted Particle Ensemble at 50 MPa..... 223

B.10: Tangent Young's Mod. for $1x10^3$ Comminuted Particle Ensemble at 50 MPa 224

B.11: Tangent Shear Mod. for $1x10^3$ Comminuted Particle Ensemble at 50 MPa..... 224

B.12: Tangent Bulk Mod. for $1x10^3$ Comminuted Particle Ensemble at 50 MPa 224

B.13: Secant Young's Mod. for $1x10^3$ Comminuted Particle Ensemble at 100 MPa 225

B.14: Secant Shear Mod. for $1x10^3$ Comminuted Particle Ensemble at 100 MPa 225

B.15: Secant Bulk Modulus for $1x10^3$ Comminuted Particle Ensemble at 100 MPa..... 225

B.16: Tangent Young's Mod. for $1x10^3$ Comminuted Particle Ensemble at 100 MPa.. 226

B.17: Tangent Shear Mod. for $1x10^3$ Comminuted Particle Ensemble at 100 MPa..... 226

B.18: Tangent Bulk Mod. for $1x10^3$ Comminuted Particle Ensemble at 100 MPa 226

B.19: Secant Young's Mod. for $1x10^3$ Comminuted Particle Ensemble at 200 MPa 227

B.20: Secant Shear Mod. for $1x10^3$ Comminuted Particle Ensemble at 200 MPa 227

B.21: Secant Bulk Mod. for $1x10^3$ Comminuted Particle Ensemble at 200 MPa 227

B.22: Tangent Young's Mod. for $1x10^3$ Comminuted Particle Ensemble at 200 MPa.. 228

B.23: Tangent Shear Mod. for $1x10^3$ Comminuted Particle Ensemble at 200 MPa..... 228

B.24: Tangent Bulk Mod. for $1x10^3$ Comminuted Particle Ensemble at 200 MPa 228

B.25: Secant Young's Mod. for $1x10^3$ Comminuted Particle Ensemble at 400 MPa 229

B.26: Secant Shear Mod. for $1x10^3$ Comminuted Particle Ensemble at 400 MPa 229

B.27: Secant Bulk Mod. for $1x10^3$ Comminuted Particle Ensemble at 400 MPa 229

B.28: Tangent Young's Mod. for $1x10^3$ Comminuted Particle Ensemble at 400 MPa.. 230

B.29: Tangent Shear Mod. for $1x10^3$ Comminuted Particle Ensemble at 400 MPa..... 230

B.30: Tangent Bulk Mod. for $1x10^3$ Comminuted Particle Ensemble at 400 MPa 230

B.31: Secant Young's Mod. for $1x10^4$ Comminuted Particle Ensemble at 20 MPa 231

B.32: Secant Shear Modulus for $1x10^4$ Comminuted Particle Ensemble at 20 MPa 231

B.33: Secant Bulk Modulus for $1x10^4$ Comminuted Particle Ensemble at 20 MPa..... 231

B.34: Tangent Young's Mod. for $1x10^4$ Comminuted Particle Ensemble at 20 MPa.... 232

B.35: Tangent Shear Mod. for $1x10^4$ Comminuted Particle Ensemble at 20 MPa..... 232

B.36: Tangent Bulk Mod. for $1x10^4$ Comminuted Particle Ensemble at 20 MPa 232

B.37: Secant Young's Mod. for 1x10^4 Comminuted Particle Ensemble at 50 MPa 233

B.38: Secant Shear Mod. for 1x10^4 Comminuted Particle Ensemble at 50 MPa 233

B.39: Secant Bulk Modulus for 1x10^4 Comminuted Particle Ensemble at 50 MPa..... 233

B.40: Tangent Young's Mod. for 1x10^4 Comminuted Particle Ensemble at 50 MPa 234

B.41: Tangent Shear Mod. for 1x10^4 Comminuted Particle Ensemble at 50 MPa..... 234

B.42: Tangent Bulk Mod. for 1x10^4 Comminuted Particle Ensemble at 50 MPa 234

B.43: Secant Young's Mod. for 1x10^4 Comminuted Particle Ensemble at 100 MPa 235

B.44: Secant Shear Mod. for 1x10^4 Comminuted Particle Ensemble at 100 MPa 235

B.45: Secant Bulk Mod. for 1x10^4 Comminuted Particle Ensemble at 100 MPa 235

B.46: Tangent Young's Mod. for 1x10^4 Comminuted Particle Ensemble at 100 MPa .. 236

B.47: Tangent Shear Mod. for 1x10^4 Comminuted Particle Ensemble at 100 MPa..... 236

B.48: Tangent Bulk Mod. for 1x10^4 Comminuted Particle Ensemble at 100 MPa 236

B.49: Secant Young's Mod. for 1x10^4 Comminuted Particle Ensemble at 200 MPa 237

B.50: Secant Shear Mod. for 1x10^4 Comminuted Particle Ensemble at 200 MPa 237

B.51: Secant Bulk Mod. for 1x10^4 Comminuted Particle Ensemble at 200 MPa 237

B.52: Tangent Young's Mod. for 1x10^4 Comminuted Particle Ensemble at 200 MPa .. 238

B.53: Tangent Shear Mod. for 1x10^4 Comminuted Particle Ensemble at 200 MPa..... 238

B.54: Tangent Bulk Mod. for 1x10^4 Comminuted Particle Ensemble at 200 MPa 238

B.55: Secant Young's Mod. for 1x10^4 Comminuted Particle Ensemble at 400 MPa 239

B.56: Secant Shear Mod. for 1x10^4 Comminuted Particle Ensemble at 400 MPa 239

B.57: Secant Bulk Mod. for 1x10^4 Comminuted Particle Ensemble at 400 MPa 239

B.58: Tangent Young's Mod. for 1x10^4 Comminuted Particle Ensemble at 400 MPa .. 240

B.59: Tangent Shear Mod. for 1x10^4 Comminuted Particle Ensemble at 400 MPa..... 240

B.60: Tangent Bulk Mod. for $1x10^4$ Comminuted Particle Ensemble at 400 MPa 240

B.61: Secant Young's Mod. for $1x10^5$ Comminuted Particle Ensemble at 20 MPa 241

B.62: Secant Shear Modulus for $1x10^5$ Comminuted Particle Ensemble at 20 MPa 241

B.63: Secant Bulk Modulus for $1x10^5$ Comminuted Particle Ensemble at 20 MPa..... 241

B.64: Tangent Young's Mod. for $1x10^5$ Comminuted Particle Ensemble at 20 MPa 242

B.65: Tangent Shear Mod. for $1x10^5$ Comminuted Particle Ensemble at 20 MPa..... 242

B.66: Tangent Bulk Mod. for $1x10^5$ Comminuted Particle Ensemble at 20 MPa 242

B.67: Secant Young's Mod. for $1x10^5$ Comminuted Particle Ensemble at 50 MPa 243

B.68: Secant Shear Mod. for $1x10^5$ Comminuted Particle Ensemble at 50 MPa 243

B.69: Secant Bulk Modulus for $1x10^5$ Comminuted Particle Ensemble at 50 MPa..... 243

B.70: Tangent Young's Mod. for $1x10^5$ Comminuted Particle Ensemble at 50 MPa 244

B.71: Tangent Shear Mod. for $1x10^5$ Comminuted Particle Ensemble at 50 MPa..... 244

B.72: Tangent Bulk Modulus for $1x10^5$ Comminuted Particle Ensemble at 50 MPa 244

B.73: Secant Young's Mod. for $1x10^5$ Comminuted Particle Ensemble at 100 MPa 245

B.74: Secant Shear Mod. for $1x10^5$ Comminuted Particle Ensemble at 100 MPa 245

B.75: Secant Bulk Mod. for $1x10^5$ Comminuted Particle Ensemble at 100 MPa 245

B.76: Tangent Young's Mod. for $1x10^5$ Comminuted Particle Ensemble at 100 MPa .. 246

B.77: Tangent Shear Mod. for $1x10^5$ Comminuted Particle Ensemble at 100 MPa..... 246

B.78: Tangent Bulk Mod. for $1x10^5$ Comminuted Particle Ensemble at 100 MPa 246

B.79: Secant Young's Mod. for $1x10^5$ Comminuted Particle Ensemble at 200 MPa 247

B.80: Secant Shear Mod. for $1x10^5$ Comminuted Particle Ensemble at 200 MPa 247

B.81: Secant Bulk Mod. for $1x10^5$ Comminuted Particle Ensemble at 200 MPa 247

B.82: Tangent Young's Mod. for $1x10^5$ Comminuted Particle Ensemble at 200 MPa .. 248

B.83: Tangent Shear Mod. for $1x10^5$ Comminuted Particle Ensemble at 200 MPa..... 248

B.84: Tangent Bulk Mod. for $1x10^5$ Comminuted Particle Ensemble at 200 MPa..... 248

B.85: Secant Young's Mod. for $1x10^5$ Comminuted Particle Ensemble at 400 MPa 249

B.86: Secant Shear Mod. for $1x10^5$ Comminuted Particle Ensemble at 400 MPa..... 249

B.87: Secant Bulk Mod. for $1x10^5$ Comminuted Particle Ensemble at 400 MPa 249

B.88: Tangent Young's Mod. for $1x10^5$ Comminuted Particle Ensemble at 400 MPa.. 250

B.89: Tangent Shear Mod. for $1x10^5$ Comminuted Particle Ensemble at 400 MPa..... 250

B.90: Tangent Bulk Mod. for $1x10^5$ Comminuted Particle Ensemble at 400 MPa..... 250

LIST OF TABLES

Table *Page*

5.1: Eglin sand parameters used in mesoscale modeling 115

5.2: Wasserstein distance between comminuted PSDs of ensembles of different sizes . 124

6.1: Simple HEP model variables relevant to optimization study 166

6.2: Optimized simple HEP model bulk response variables 170

6.3: Optimized simple HEP model deviatoric response variables 175

CHAPTER 1

INTRODUCTION

While engineering soil analysis has as long a history as any other material, constitutive modeling of soils under transient loading is a relatively recent endeavor. With the development of hydrocodes such as CTH, Epic, Pronto3D, LS-Dyna etc., research into the transient modeling of soil behavior accelerated, since soils are prominent constituents of the commercial and defense applications these hydrocodes are built to model. Soil is a particularly challenging material to model as a continuum since it is a large assemblage of individual particles, which have all possible three-dimensional degrees of freedom. Consequently, modeling of soil behavior, particularly for highly-transient response, is still largely based on empirical formulae customized from field tests.

Of the models developed for soil modeling, the Mohr-Coulomb model is still the best known due to its agreement with experiments for modeling stress at failure. Its "inconvenience" for computational modeling due to its corners and singularities, has led to adoption of the Drucker-Prager model, which may be considered a smooth generalization of the Mohr-Coulomb model. However, both models suffer from similar problems: they predict excessive dilatancy, cannot predict hysteresis, do not account for compaction and crushing, cannot predict strain softening, and do not account for strain rate. The development of pressure cap plasticity, first proposed by Drucker [1], was a very important evolution in soil modeling. The modified Cam-clay model [2] was based on critical state theory and contains an elliptical yield surface rather than a cap, and has been very popular

especially in modeling clays. Finally, effective stress models are three-phase soil models that explicitly account for the two fluid phases in the soil

Motivation

The Hybrid Elastic Plastic (HEP) series of geomaterial model fits have been used extensively in several military/defense hydrocodes (CTH, Epic, Pronto) due to their versatility and ease of customization. The fits were produced from the computational code "SABER-PC", which implemented a geomechanical constitutive model that used an Effective Stress formulation in the sense of Terzaghi [3] and Bishop [4]. The SABER-PC Effective Stress Model (ESM) is a phenomenological framework with a number of options for soil constitutive behavior and equations of state. That is to say the ESM is a rather loose agglomeration of the constitutive modeling efforts resulting from several experimental characterizations of various soil samples. When porting the framework from SABER-PC to the various hydrocodes, the HEP fits were extracted for the soils the ESM was based on, however the ESM itself was not ported.

Currently, using the HEP to model soil in hydrocodes typically involves a three-stage calibration process. In the first stage, a relevant library fit is identified from the particle size distribution obtained using a sieve and hydrometer analysis. Next, in the second stage, the model parameters are adjusted to match the laboratory test results (triaxial, uniaxial, constant volume). Finally, in the third step, further adjustment of the many model parameters is typically required when dynamic testing results become available. Such results typically come from flyer plate experiments or Impulse Measurement Devices. The main reason for the multi-stage approach to model calibration, is that the underlying physics of soil behavior, particularly during highly-transient phenomena, is not very well

understood. While the HEP models can model a wide range of soil behaviors, there is not a linear process of selecting its parameters from readily available laboratory analyses and tests.

The current work will explore the underlying mechanics of the ESM using mesoscale simulations of the physics involved. It will do so by first creating “avatars” of all the soils that have had HEP fits using the ESM. These avatars will essentially be computational representations of the soils using spheres as idealized soil grains. The avatars will be created using a sequence of two-types of particle-based modeling efforts. The initial type of model will use a particle-packing algorithm followed by an isotropic triaxial compression simulation to achieve the necessary physical characteristics. The second type of model, will model the shear behavior of the avatar. Depending on the mesoscale and macroscale characteristics of the soil being investigated, many particle models will be synthesized at different scales to model the behavior of the soil at different confining pressures. The process may be repeated until the model is ultimately homogenized into a continuum representative of the relevant soil at the macroscale.

This work also aims to establish an alternative means of calibrating continuum material behavior. Rather than fitting the mathematical material model directly to the experimental data from triaxial testing, the material model is fit to the granular mesoscale avatar. Once the computational avatar is calibrated to adequately match the soil behavior in the available test data, the avatar can be used to explore the underlying statistics and add to the data available from the physical tests with data from virtual ones. Whereas some characteristics of a soil’s evolution with deformation are typically inferred indirectly from the triaxial test data, herein these characteristics will be tested for and quantified from virtual

testing of the soil avatar. Characteristics such as third-invariant dependence, the shape and evolution of the shear-limiting failure surface, pressure-cap evolution, onset of yielding, etc. can be evaluated directly from the computational avatar, if the avatar is adequately matched to the physical sample.

The data compiled from the various models can further be used to identify a unifying constitutive framework that can bring the different fits under a single mathematical umbrella. The documentation for SABER-PC along with the data from Ehrgott [5], will provide a fair amount of experimental data among a range of soils. Once modeled, calibrated, and quantified in the context of the current work, there will be enough information to form such a framework from the combination of physical data and mesoscale models.

Scope and Objectives

This work has two main objectives: homogenization and uncertainty quantification of a geomaterial. The geomaterial is sand for this particular study, however the framework is expected to be widely applicable to other types of granular media. The stated goals are accomplished using tools adapted for this specific study: simulation at the mesoscale, geomechanics derived from the statistical parameters of mesoscale ensembles, and calibration of the mesoscale ensembles using mathematical optimization.

Mesoscale Modeling

With the significant increase in available computational power and resources over the last decade, geomaterial modeling has seen both evolutionary and revolutionary changes. One such “revolution” has been the dramatic rise in popularity of particle methods such as the Discrete Element Method (DEM). DEM is very closely related to molecular dynamics (MD), in fact one of the more popular DEM applications (LIGGGHTS) [6] is a

fork of the most widely used MD code, LAMMPS [7]. The inclusions of rotational degrees of freedom and nonlinear contact with friction are the main attributes that separate DEM from MD. DEM can be useful in modeling soils in dynamic applications considering the large deformations involved. As with any other simulation paradigm, there is a potential for misuse with DEM. The approach, methodology, and output expectations need to be weighed carefully, otherwise the Discrete Element Method becomes nothing more than a relatively inexpensive, visually appealing, but mechanistically meaningless gimmick.

Statistical Geomechanics

Among the characteristics that make the constitutive behavior of geomaterials different from many other materials, is the degree of variability and uncertainty exhibited in most applications. This uncertainty has two primary sources: the heterogeneity and complexity of the soil structure as well as the inherent difficulty in measuring material properties. These uncertainty sources coincide with the two categories of uncertainties commonly used in the scientific discipline of Uncertainty Quantification (UQ): aleatory uncertainty and epistemic uncertainty [8]. Aleatory uncertainty is also sometimes called irreducible or stochastic uncertainty, and consists of the sources of uncertainty that are inherent to a material and are impossible to avoid. Epistemic uncertainty on the other hand, is uncertainty due to the lack of, or imprecision in, the available data. In recent years there have been some efforts to address uncertainties in geomaterial modeling. These efforts are primarily focused towards dealing mathematically with aleatory uncertainty by introducing probabilistic models to the physics, e.g. Monte Carlo simulations and Stochastic Finite Elements (SFE) [9] [10]. The current work will quantify aleatory uncertainty at the mesoscale, but will do so in the context of identifying a trend and a threshold for homogenization to a

deterministic model. Furthermore, this work aims to introduce a possible means of reducing epistemic uncertainty by offering the possibility of conducting virtual experiments on soil avatars, experiments that would be very difficult, if not impossible, to conduct on physical samples.

Homogenization

The primary assumption of any effort to quantify the behavior of a material at the macroscale, is the existence of a Representative Volume Element (RVE). Herein, the RVE is understood in the sense of Hill [11]. The existence of the RVE is readily ascertained via a unit cell in the case of periodic microstructures, such as those constituting many matrix/fiber composites. However, the identification and determination of the RVE is rather more difficult when dealing with random heterogeneous media such as soils. Mathematically, an infinite number of grains would be required to attain the RVE scale, due to the complete randomness and heterogeneity of the grains.

Consider the random sand grain distribution of Figure 0.1. The figure shows two cross-sections of the same cubic sand grain packing, and illustrates the concept of Separation of Scales. The separation suggested here and based on [8], involves three scales

1. The microscale d, which represents the size of the typical grain, or an inclusion.
2. The mesoscale L, the RVE size
3. The macroscale L_{macro}, macroscopic sample size

$$\left.\begin{matrix} d < \\ d << \end{matrix}\right\} L << L_{macro} \tag{1.1}$$

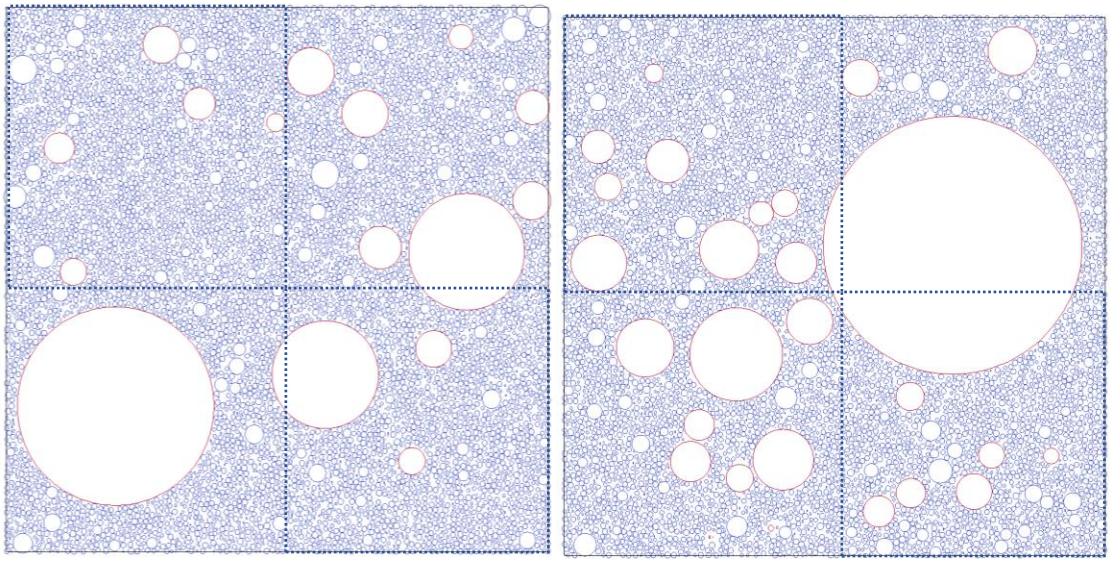

Figure 0.1: Disordered Heterogeneous Packing of Sand Grains

The inequality of Equation (1.1) contains two options as the mismatch in geometry and properties may be small or great. In the current work the mismatch is always great, requiring the use of the second form of the left-hand side of the inequality.

In addition to the concept of the RVE, it is also beneficial at this point to introduce the related concept of the Statistical Volume Element (SVE), which is sometime also called the Stochastic Volume Element, for obvious reasons. The SVE represents any and all realizations of the microscale greater than the typical grain, but smaller than the RVE. Where the RVE material properties are the same as those of the macroscale, the SVE properties are represented by statistical quantities like the Probability Density Function (PDF) and Statistical Bounds.

Uncertainty Quantification

Among the characteristics that make the constitutive behavior of geomaterials different from many other materials, is the degree of variability and uncertainty exhibited in most applications. This uncertainty has two primary sources: the heterogeneity and complexity of the soil structure as well as the inherent difficulty in measuring material

properties. These uncertainty sources coincide with the two categories of uncertainties commonly used in the scientific discipline of Uncertainty Quantification (UQ): aleatory uncertainty and epistemic uncertainty [8]. Aleatory uncertainty is also sometimes called irreducible or stochastic uncertainty, and consists of the sources of uncertainty that are inherent to a material and are impossible to avoid. Epistemic uncertainty on the other hand, is uncertainty due to the lack of, or imprecision in, the available data. In recent years there have been some efforts to address uncertainties in geomaterial modeling. These efforts are primarily focused towards dealing mathematically with aleatory uncertainty by introducing probabilistic models to the physics, e.g. Monte Carlo simulations and Stochastic Finite Elements (SFE) [9] [10]. The current work will quantify aleatory uncertainty at the mesoscale, but will do so in the context of identifying a trend and a threshold for homogenization to a deterministic model. Furthermore, this work aims to introduce a possible means of reducing epistemic uncertainty by offering the possibility of conducting virtual experiments on soil avatars, experiments that would be very difficult, if not impossible, to conduct on physical samples.

Calibration of Continuum Models

It is common practice when modeling a particular soil in many simulation packages to go through a multi-stage calibration process. In the first stage, a relevant library fit is identified from the particle size distribution obtained using a sieve and hydrometer analysis. Next, the model parameters are adjusted to match the laboratory test results (triaxial, uniaxial, constant volume). Finally, further adjustment of the many model parameters is typically required when additional experimental results, such as from dynamic testing, become available. Such results typically come from flyer plate experiments or Impulse

Measurement Devices. The main reason for the multi-stage approach to model calibration, is that the underlying physics of soil behavior, particularly during highly-transient phenomena, is not very well understood.

The current work will explore the physical evolution of sand fabric using mesoscale simulations of the physics involved. It will do so by first creating "avatars" of the sand using the Discrete Element Method (DEM). Each avatar will essentially be a particle-based computational representation of the sand. The avatars will be created by using a particle-packing algorithm followed by isotropic triaxial compression to attain the highest hydrostatic stress seen in physical testing. Subsequently, the DEM avatar will be calibrated to match as closely as possible the response seen during isotropic unloading in the physical tests. Only the unloading portion of the isotropic compression tests is used for calibration herein. During the loading part of the test, the sand's response depends not only on the contact stiffness, but also on the friction angle, the shape of the grains, initial porosity, moisture content etc. Once the sand is highly compressed however, only the grain contact stiffness is important and unloading may be used to extract the Hertzian contact parameters.

Dissertation Organization

This dissertation is organized as follows:

In Chapter 1, the motivation for this work as well as the objectives of the research have been described along with a brief introduction to the topics covered in this manuscript.

In Chapter 2, a brief review is presented of the relevant topics from the different disciplines that form the theoretical background to this study. First, a quick audit of the history and basics of soil mechanics is introduced. Next, there is a review of the state-of-research as pertains to computational homogenization and upscaling. Finally, there is an

introduction to the wider mathematics disciplines that are integrated in this work with the more familiar computational mechanics methods.

In Chapter 3, a deeper dive is taken into the mathematical foundations and the respective computational implementations. First, the underpinnings of the mesoscale simulation method used here, the Discrete Element Method (DEM), are laid out along with specific adaptations necessitated by the scope of this framework. Next, there is a review the basics of the continuum model used for the Finite Element Analysis (FEA) part of this study, the Hybrid Elastic Plastic (HEP) model. Following the first two sections on the computational modeling paradigms used here, the next two sections focus on the broader mathematical lattice of the framework. beginning with the statistics and probability theory tools required to construct and analyze the mesoscale ensembles used in this work. The second of these sections, and the last one in the chapter, describes the mathematical optimization algorithms used for the upscaling part of this multiscale simulation.

In Chapter 4, arguably the most important single development introduced with this framework is presented. Heretofore, use of the Discrete Element Method in micromechanics has been hampered by the inability to impose boundary values of stress and strain in the sense of Neumann and Dirichlet. To build a complete meso-to-macro framework, this needed to be remedied. First, a review of boundary implementations in particle methods is given. Next, the real-time surface tracking algorithm that allows this novel approach to micromechanical boundaries is described. Following that introduction, the specific implementation of the boundaries using the surface diagrams is defined. Finally, volume-averaging methods required to enable characterization of deformation and stress from particle aggregates in the continuum sense are derived.

In Chapter 5, the results of the many mesoscale ensemble simulations of Eglin sand are presented. In the first section, the Particle Size Distribution and the distributions of the micromechanical experimental characteristics of Eglin sand are summarized. Next, the equivalent physical characteristics of the mesoscale ensembles are computed. The following section presents the homogenization results for Eglin sand at relatively low confinements, neglecting any consideration of grain fracture. Results of ensemble simulations of grain fracture and the ensuing comminution are given in the next section. Homogenization results at higher confinements accounting for grain comminution follow. Next, bounds and distributions of the mesoscale moduli are extracted from the RVE-level simulations. In the two sections that follow, finite strain volumetric and deviatoric ensemble simulation responses are presented. The last section of this chapter presents ensemble statistics of strain energy and dissipation evolution during the finite strain simulations.

In Chapter 6, Finite Element Analysis results are presented for simulations with the Hybrid Elastic Plastic model. In the first section of this chapter, “off-the-shelf” library fits of constitutive properties are used to demonstrate the model’s response to the triaxial testing data for Eglin sand. Next, results from optimization of the HEP variables to mesoscale responses are presented. The final section shows the results of triaxial simulations and associated uncertainty, using the optimized properties.

Chapter 7 concludes this dissertation with a discussion of the results attained, an evaluation of the degree of success in achieving the stated objectives, and near-sighted as well as “blue sky” perspectives on the future directions of this line of research.

CHAPTER 2

THEORY AND BACKGROUND

The aim of this chapter is to provide a qualitative background on the concepts and theory underlying this work. That may indeed be a tall order, considering the various disciplines that this study seeks to marry.

A Brief History of Soil Mechanics

It has been said that soil is the oldest engineering material. This goes along with the notion that soil is also the most primitive engineering material. It has also been said that soil is the most complex engineering material. The evidence for those statements lies both in the remains of ancient dwellings and in the latest endeavors of engineering mechanics research studies such as this one. Ancient humans certainly did not conceive of soil mechanics with quite the rigor of today, however they had clearly developed some practice with using it as an engineering material for burial sites, flood protection, and shelter against the (other) elements.

The code of Hammurabi (2500 B.C.) is the oldest surviving text that attempts to codify building. Meanwhile the writings of Vitruvius, who served as engineer during the reign of Emperor Augustus in the first century B.C., paid great attention to soil types and to the design and construction of foundations thereof. In the Middle Ages the tendency of soil to consolidate under triaxial pressure, had become obvious to European engineers involved in the construction of great cathedrals. The uncertainty inherent in soil

characterization was a hard lesson that was learned, though perhaps not exactly in those terms, when the tower at Pisa stood less than perfectly vertical.

Soil mechanics in the sense understood today, has its genesis with Charles-Augustin de Coulomb who was, among many other things, a member of the French Royal Engineers. It was Coulomb in 1776, who introduced the concepts of frictional and cohesive resistance for solid bodies [12]. He also made the intellectual leap of assuming that these resistances applied to the grains of soils, and in so doing was possibly the first to understand the importance of micro-mechanics to the behavior of heterogeneous materials. It is no surprise that the shear strength theory bearing his name is also intrinsic to the computational model used herein.

Another important year in the history of soil mechanics is the year 1856. That is the year of publication for Darcy's law of soil permeability [13] and for Stokes' law of solid particle velocity in liquid media [14]. The subsequent year, 1857, marks the year of publication of Scottish engineer William John Macquorn Rankine's theory on earthen pressure and equilibrium of earth masses [15]. In 1871 German engineer Christian Otto Mohr developed his rupture theory and established the concept of stress circles, a concept still taught today extensively in soil mechanics classes under the name Mohr's circle. The 19th century history of the development of soil mechanics also includes French mathematician Joseph Valentin Boussinesq's theory of stress distribution in a semi-infinite, homogeneous, isotropic medium under a surface point load [16].

The 20th century saw an explosion in the collective understanding of soil mechanics. Swedish agriculturist Albert Atterberg was the first to define consistency limits for cohesive soils in 1911 [17]. These are still widely used in geotechnical engineering today.

Another important development came out of Sweden not long after Atterberg's report, in the form of a report by the Swedish Geotechnical Commission of the State Railways of Sweden headed by Wolmar Fellenius [18]. This commission was established to investigate geotechnical failures after several landslides on railways, canals, and harbor structures. This report contained many new concepts and testing methods, including the concept of clay sensitivity and overconsolidation.

This is arguably where the pre-history of soil mechanics ends, and soil mechanics as it is understood today begins. This threshold is marked by the publication of the first soil mechanics textbook, authored by Austrian engineer Karl von Terzaghi [19]. There is perhaps no argument needed for this, considering "soil mechanics" is the English translation of his book "Erdbaumechanik". Enumeration of Terzaghi's contributions to the field would require a separate dedicated chapter, however if one were required to pick but a single concept, it would have to be the concept of effective stress. Other, prominent early contributions to the field were made by Ralph Proctor [20], Arthur Casagrande [21], Donald Taylor [22], Ralph B. Peck [23], Alec Skempton [24], Laurits Bjerrum [25], and Harry Bolton Seed [26], among others.

Important Concepts of Sand Mechanics

This work relies on certain accepted concepts and measures in the mechanics of sand. This section lays out those concepts, starting with the relevant physics of sand at all scales, the methods by which sand is usually qualified and quantified, and finally some mathematical/computational frameworks commonly used to model sand.

Physics of Sand

A constitutive model of a material is merely a mathematical abstraction of the assumed underlying physics. No matter how good or complex the math is, if the assumed physics is inaccurate the output produced will not be useful. This is especially true for the current work, as the physics is explicitly modeled at the mesoscale, whereas on the balance constitutive modeling efforts are aimed at phenomenological agreement. A brief review of the physics relevant to the current work follows.

The first relevant aspect of soil behavior that is encountered empirically, is the **plasticity of soil**. Plasticity, in general terms refers to non-reversible changes to the shape of a material in response to applied forces. The reversible deformation is termed elastic deformation, while the irrecoverable deformation is plastic deformation. For many engineering materials, plasticity is only assumed under deviatoric loading, however for soils the concept of "soil compaction" is also used to refer to plasticity under mean stress loading. A further look into sand plasticity is included in the following section on commonly-used constitutive models.

Bulk response refers to the response of the material under hydrostatic loading conditions and is also called "volumetric response" in reference to the volumetric straining of the material. The bulk response is described by the so-called pressure-compression curve. The pressure-compression curve used in the HEP material model is shown in Figure 0.1, and is illustrative of the typical bulk response of sand. The response can be divided into three major regions. In the first region, the response may be assumed to be elastic. In this region, the sand response comes mostly from the contact forces between sand grains, without significant frictional sliding or changes in the distribution of particle sizes.

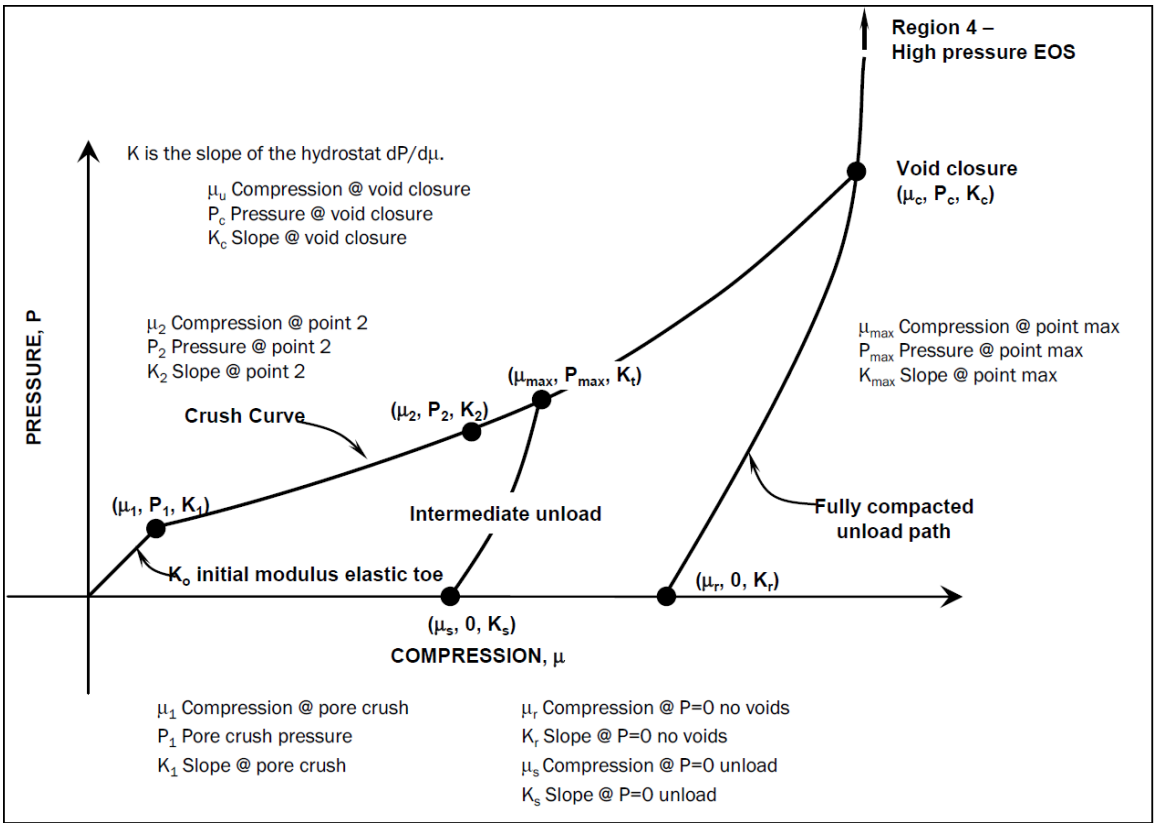

Figure 0.1: Pressure-compression behavior in the HEP model

The response in the second region is neither elastic or linear, and typically involves a hysteretic unloading-reloading loop. The response in this region comes from dissipative effects in the sand fabric, nominally frictional sliding and grain crush-up. Grain crushing comes in the three distinct “flavors” shown on : abrasion, attrition, and fracture [27]. The dominant form of crushing in sand is fracture [28]. Finally, in the third region virtually all air pores have been closed and virtually all grains that can be crushed, have been. The response here comes once again mostly from contact forces, though there may be enough plastic deformation at the contact points to make the response nonlinear.

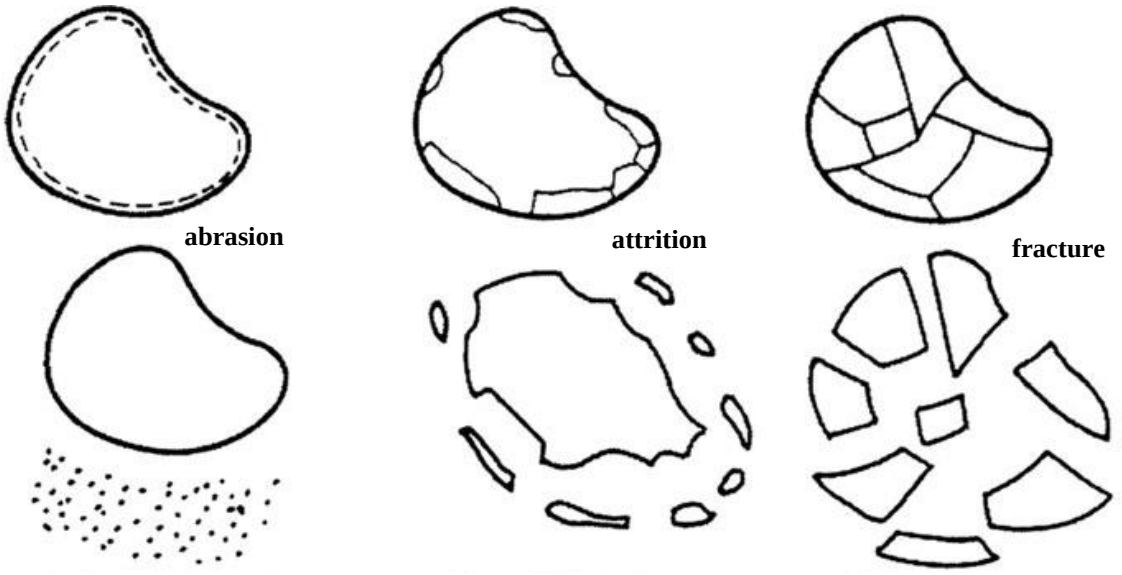

Figure 0.2: Modes of grain crushing in sand [27]

The next important characteristic of soil behavior is its **shear response**, which includes deformation and strength under shear forces. Most soils have only a small elastic region, and deform inelastically almost from the onset of the loading, however are frequently modeled as having a discrete yield surface as a convenience for separating linear from nonlinear shear stress-strain response.

Soil response to external loads is predicated on intergranular behavior, the grains need to slide, be elevated, and/or rotated over each other to respond to these external forces. Therefore, the emergent behavior depends strongly on bulk (volumetric) response. This is what is termed as the **"dilatancy" of sand**. It should be noted that the ESM implemented in SABER does not include rigorous volumetric/distortional coupling, and is therefore incapable of predicting shear-induced dilation. It was assumed that strongly empirically-based bulk pressure response was more important than shear-bulk coupling. This will be reevaluated in the course of the current work.

Also of importance, is the **strain hardening and softening** behavior of the soil. Hardening refers to the elastoplastic response of a material once the yield surface has been reached but prior to failure. Softening refers to a well-compacted soil's tendency to flow under shear loading. Again, neither hardening nor softening is predicted by the simple HEP library fits.

Sand is often thought of as a cohesionless soil. While it is certainly true that sand does not have the electrostatic forces that make clays cohesive, **cohesion** is usually present in sand due to either chemical cementation, capillary action, or pore pressure hysteresis. The **tensile strength** of a soil at the mesoscale and above, is due to any intergranular adhesion, whether from capillary forces or some sort of chemical cementation present (at the microscale there are also electrochemical forces like van der Waals and the electrical double layer).

Physical response of the soil depends on pore-scale fluid flow, or **drainage**. The highly-transient phenomena that are the focus of the current work, may be safely assumed to occur only at undrained timescales/conditions. However, in order to accurately match the mesoscale physics with the experimental data, drained conditions need to be accounted for as present during triaxial compression testing.

There are some physics that are ignored in this work. One prominent example is **viscoplasticity** (creep). Viscoplasticity is not usually relevant in hydrocode simulations with the HEP model, considering such simulations are carried out at very high strain rates where viscous effects are not important. Viscoplasticity does need to be considered in triaxial testing, as even with the slow loading rate adopted there is some creep at constant

stress. This triaxial creep is however small and the recorded stress and strain measures do follow a brief pause in monotonic loading.

Classification and Testing

When soils are described, the terms “gravels”, “sands”, “silts’ and “clays” are commonly used to refer to the texture of specific soils. Broadly speaking, gravels and sands are generally understood to be “coarse-grained” soils, while silts and clays are “fine-grained” soils. If texture is the “feel” of a soil, then coarse-grained soils feel gritty and rough, while fine-grained soils feel soft and smooth.

Since the inception of soil mechanics as an engineering science, there have been concerted efforts to adopt a classification system for soils that can succinctly describe to an engineer the nature of the particular material at hand. As typically happens in such cases, many different systems have been proposed over time to classify soils based on relevant properties, including texture, plasticity, strength etc. Some of these systems have indeed gained relatively wide acceptance and applicability, nonetheless seldom have all engineers’ requirements been met by a classification system.

The **Unified Soil Classification System** is the most widely used engineering soil classification system in North America. Its “cousin”, the European soil classification system is very similar in scope and differs mainly in its classification of plasticity in silts and clays. The USCS is geared towards identifying soils in terms of their texture and plasticity, then grouping them further by mechanical response. Terms such as “gravel”, “sand”, and “clay” have been adopted into the USCS as a means of prescribing the expected behavior rather than as descriptive of a soil’s geological history. Indeed, one is unlikely to find

naturally occurring homogeneous gravel or sand, soils are usually a mixture of varying fractions of different particle sizes.

The parameters below are fundamental to the nature of a soil's behavior, and form the basis of the USCS:

- Relative fractions of gravel, sand, silts, and clays.
- Shape of the particle-size-distribution (PSD) curve
- Compressibility and plasticity

The size distribution of particles for coarse-grained soils is obtained by screening the soil through a stack of sieves of progressively finer openings. Each of these sieves is identified by a number that matches the number of square openings in each linear inch of the sieve mesh. The particle mass retained in each sieve may be weighed and its percentage relative to the sample computed. The results may then be plotted on the familiar particle size distribution curves which are a type of cumulative distribution chart with the particle size usually plotted on a logarithmic scale.

The sieve-based screening approach cannot be used for fine-grained soils. Typically, the size distribution of fine-grained soils is obtained through hydrometer analysis. In the hydrometer test, a small amount of the soil is placed into suspension and the settlement of the various particles observed over time. The larger particles settle quickly, while the smaller ones remain in suspension longer. The hydrometer is lowered into the suspension until the buoyancy force balances its weight. The hydrometer can be calibrated to the density of the suspension at different times.

The **Split-Hopkinson pressure bar (SHPB)** is an apparatus for measuring the high strain rate response of materials. It is named after Bertram Hopkinson [29], though it is

also frequently referred to as the Kolsky bar [30] after Herbert Kolsky who refined the original Hopkinson setup by using two bars in series (split-Hopkinson bar). The SHPB is a highly useful method for determining dynamic material properties in a range of strain rates. Different configurations of the SHPB test enable testing of tensile, compressive, or shear responses in a material specimen. Additionally, the SHPB test can be used to obtain the dynamic fracture toughness of a specimen in three-point bending

Arrangements and techniques in common use for SHPB testing are numerous, however the operational principles and measurement methods are virtually identical. The material specimen lies between the inside edges of two bars, which are called the *incident bar* and the *transmitted bar* [31]. A stress wave is created in the incident bar, typically at its far end, which then propagates through the bar and into the material tested. This *incident wave* splits into two smaller waves once it meets the material specimen. These two smaller waves are labeled the *transmitted wave* and *the reflected wave*. The transmitted wave is thusly termed since it travels through the material specimen, continuing into the transmitted bar and causing plastic deformation into the latter. The reflected wave on the other hand, travels back down the incident bar after being reflected away from the material specimen [32]. Strain gauges are generally used to measure the deformation and stress response caused by the induced stress waves [33].

Mesoscale modeling carried out in this study uses experimental data from “modified long SHPB” testing on Eglin sand by Luo et al. [34] shown in Figure 0.3.

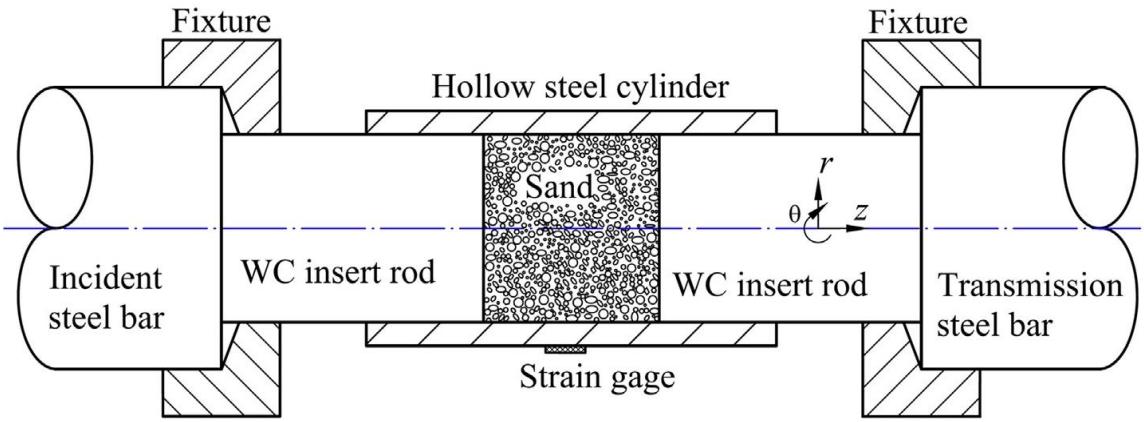

Figure 0.3: Sand specimen in SHPB testing [34]

In that investigation they made use of an 11 m long SHPB using pulse shaping with an annealed copper disk meant to stretch the dynamic compression over a relatively long duration. Their SHPB consisted of a striker bar in a gun barrel, solid stainless steel incident and transmission bars, and a strain data acquisition system. The strain data included lateral deformation through measurement of the circumferential strain on the outer surface of the specimen sleeve [35]. Figure 0.4 shows a schematic of the modified SHPB.

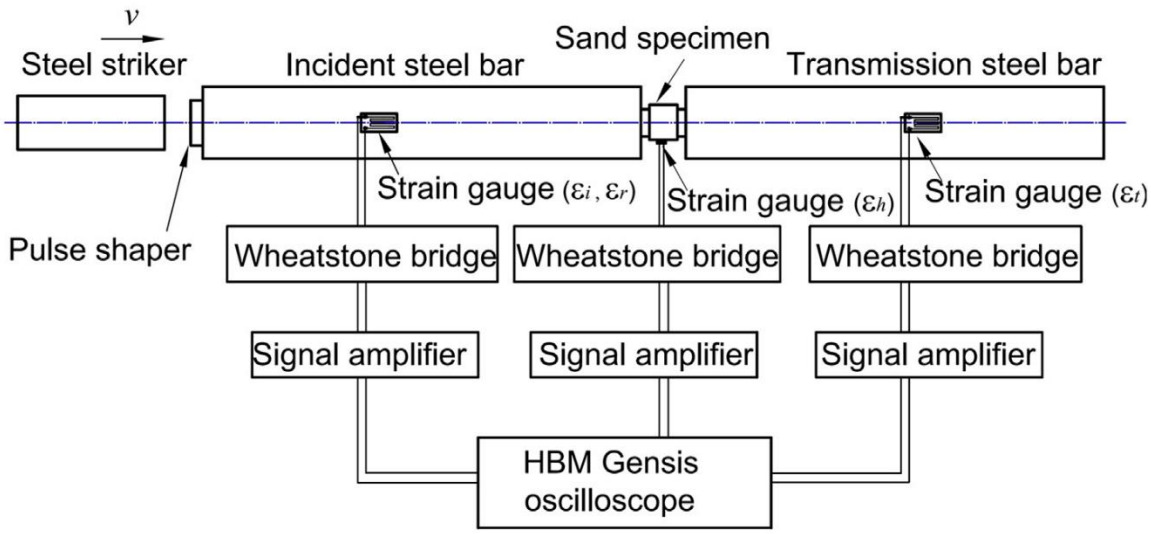

Figure 0.4: SHPB schematic [34]

Some Common Sand Models

In Soil Mechanics, a "model" of the material's mechanical behavior can be as simple as a single linear equation or as complex as an entire framework of equations. For the former, one need look no further than the equation often considered the genesis of all material models, Hooke's Law. For the latter, the HEP model used here is an example, though by no means the most complex model that can be identified in the literature. Hooke's Law is obviously too simple to describe important aspects of soil response [36], other common constitutive models are reviewed here.

The seminal **Elastic-Perfectly Plastic** model in geomechanics is the **Mohr-Coulomb** model. The number of parameters used in the Mohr-Coulomb model is five. Of these five parameters, two are elastic parameters from Hooke's Law: the Young's modulus (E) and Poisson's ratio (ν). Another two parameters come from Coulomb's failure criterion: the friction angle (φ) and cohesion (c). The final parameter is the dilatancy angle (ψ), which corresponds to the irreversible volume change from shearing for non-associated flow rules. The yield criterion of the Mohr-Coulomb model in 1D is simply:

$$f = |\tau| - (c - \sigma \tan\phi) = 0 \tag{2.1}$$

where τ represents the shear stress, while σ represents the normal stress. For a 3D state of stress, the Mohr-Coulomb yield surface is:

$$f = \frac{1}{3} I_1 \sin\phi + \sqrt{J_2}\,\sin\left(\theta + \frac{\pi}{3}\right) + \sqrt{\frac{J_2}{3}}\,\cos\left(\theta + \frac{\pi}{3}\right)\sin\phi - c\cos\phi = 0 \tag{2.2}$$

where is the first invariant of the stress tensor, J_2 is the second stress invariant of the deviatoric stress tensor, and θ is the Lode angle. The Lode angle is defined as:

$$\cos(3\theta) = \frac{3\sqrt{3}}{2}\frac{J_3}{J_2^{3/2}} \tag{2.3}$$

where $J_3 = |\mathbf{s}|$ is the third invariant of the deviatoric stress tensor. The failure surface may be visualized in principals stress space as the hexagonal pyramid shown in Figure 0.5.

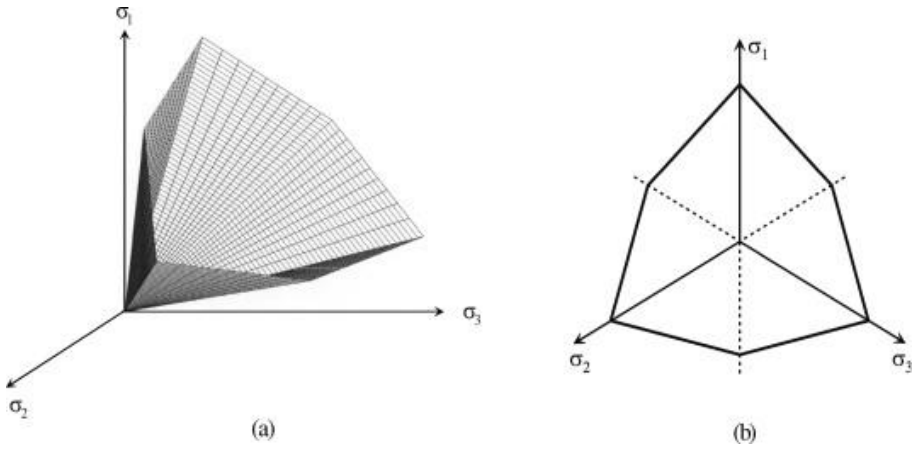

Figure 0.5: Mohr-Coulomb Failure Surface

The Mohr-Coulomb is still the best known model for soils, and experimental studies using triaxial testing generally agree with the model's predictions of stress at failure [37]. However, the model is computationally inconvenient principally due to the presence of corners and singularities. Hence, a smooth generalization of the Mohr-Coulomb model, the **Drucker-Prager model** [38], is widely used to model failure in computational implementations. The Drucker-Prager model replaces the hexagonal pyramid of the Mohr-Coulomb model with the simple cone shown in Figure 0.6.

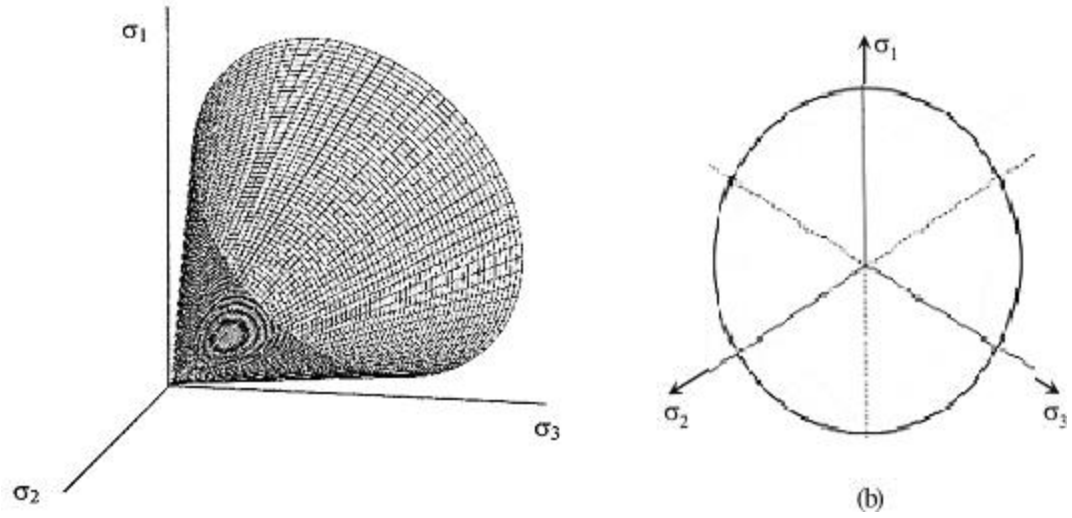

Figure 0.6: Drucker-Prager Failure Surface

For many situations the dominant load path is triaxial, whether compression or extension. Other problems may be rightly simplified as plane strain problems. For these situations, generalization of the failure surface into the Drucker-Prager formulation is not divergent from what can be obtained with the Mohr-Coulomb surface. However, for situations with multiple loading paths, the Drucker-Prager surface does not capture failure well [37]. For this reason, the Mohr-Coulomb is considered superior to the Drucker-Prager model.

Shortcomings of both the Mohr-Coulomb model and the Drucker-Prager model include:

- Both models predict more dilatancy than observed in experiments.
- Experiments exhibit hysteresis in load-unload cycles. This cannot be modeled using a single value for the bulk modulus or without a pressure cap [39].
- Neither model can model strain softening behavior.

Strain hardening and strain softening are important components of the constitutive response of soil. Drucker et al. [1] were the first to suggest using work-hardening plasticity theories developed for metals to model soil as an elastic-plastic work-hardening material. The idea espoused therein, was to use successive extended Drucker-Prager cones with a spherical cap, with both cone and cap able to expand. This concept was reworked into numerous work-hardening soil models, which may be grouped into two categories: modified Cam-clay models and generalized cap models.

The **modified Cam-clay model** is based on critical state theory, and was originally developed at Cambridge University to simulate near-normally consolidated clays undergoing triaxial testing [2]. The version of the Cam-Clay model that gained acceptance was the version proposed by Burland with a modified flow rule [40], hence most references to the model contain the "modified" moniker.

The primary assumption in the Modified Cam-Clay model is that of a logarithmic relationship between the mean effective stress p' and the void ratio e. This implies that stress is linearly-dependent on the stiffness. Another important aspect of the model is that there is a difference in response between "primary" loading beyond the pre-consolidation stress level p_c and unloading or reloading up to the pre-consolidation stress. The pre-consolidation stress increases in the model by means of hardening plasticity. Any loading past a normally-consolidated state leads to volumetric plastic straining according to a ratio of plastic volumetric strain to plastic deviatoric strain. This ratio depends on the internal friction; once the mobilized internal friction has reached a critical value there is no more volumetric strain while the deviatoric strain goes to infinity. This is the so-called Critical State associated with the failure of the material. The Critical State Line in the Modified Cam-

Clay model is analogous to the Drucker-Prager failure criterion. A typical yield surface and Critical State line are shown in Figure 0.7.

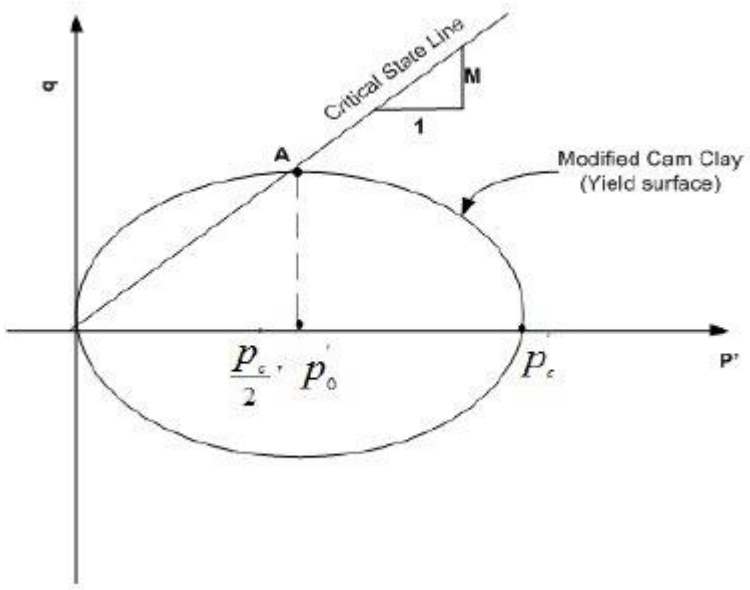

Figure 0.7: Modified Cam-Clay Yield Surface and Critical State Line (after Wood [41])

The Modified Cam-Clay model contains four model parameters and two state parameters. The model parameters are: the isotropic logarithmic compression index λ, the swelling index κ, Poisson's ratio for unloading and reloading ν, and the friction constant M. The state parameters of the model are the previously mentioned pre-consolidation stress p_c and void ratio e. Notice that the model does not contain a cohesion parameter, shear strength is specified implicitly through the effective friction constant.

Caveats with regards to using the Modified Cam-Clay model include all those previously mentioned for Drucker-Prager vis-à-vis the inaccuracy of the failure surface/critical state. An additional caveat particular to the model is a tendency towards a non-physically long elastic range for soils in an over-consolidated stress state. In fact the Modified Cam-Clay model should be considered unsuitable for highly over-consolidated soils.

The **Generalized Cap** model was first conceived by DiMaggio and Sandler [39] inspired by the work of Drucker et al. [1]. The model's yield function combines a deviatoric plastic part with an elliptical cap that advances according to the amount of plastic volumetric strain as shown in Figure 0.8. The model is therefore able to predict dilatancy by reversing strain-hardening

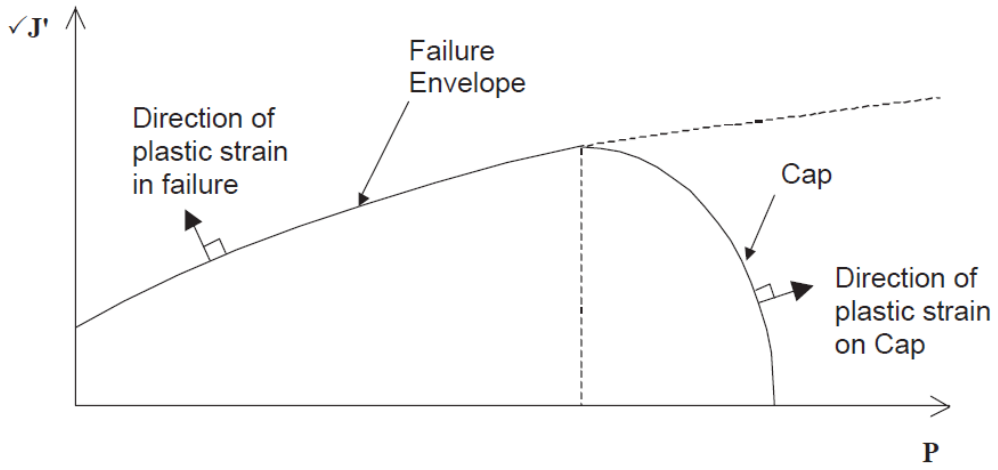

Figure 0.8: Yield surface in the Cap Model [42]

Three different types of responses are possible with the Generalized Cap Model:

1. The response is elastic if the stress point lies inside the yield surface.
2. The response is perfectly plastic/failing if the stress point is on the yield surface/failure envelope.
3. The response exhibits volumetric hardening when the stress point is on the cap.

The elastic part of the model response always results in recoverable deformations. There are, however, many extensions of the model and some of them include nonlinear elastic behavior as well as viscoelastic representations. The failure surface of the response in the model is the same as the yield surface with the assumption of perfect plasticity. This

has the effect of limiting the level of shear stress in the material. Again, as for linear elasticity, many extensions of the model exist that add hardening to the yield surface. The flow rule is associated, requiring plastic strain rate vector to be normal to the failure surface. This implies that there must be a dilatant component to plastic strain during yielding/failure.

When the stress point is on the cap, the response pushes the cap outward. This implies a plastic volumetric strain through a hardening rule. There are many versions of the cap model, however in the original the cap was assumed to be elliptical. The associated flow rule implies that there must be a shear component to the plastic strain along with a volumetric component. The latter represents the permanent compaction related to void closure observed in granular materials.

Many extensions of the original Generalized Cap Model have been developed over the years. Sandler and Baron [43] introduced viscoelastic response inside the yield surface. Isenberg et al. [44] included hardening within the failure envelope. A formulation incorporating the third invariant of the deviatoric stress tensor was introduced by Levine [45]. A damage parameter was introduced by Mould et al. [46] to represent cracking in the material and softening therein. However, the most successful and widely used extension of the Generalized Cap model is the Continuous Surface Cap model, introduced by Pelessone [47], adapted by Rubin [48], and implemented into LS-Dyna by Schwer and Murray [49].

The next development in constitutive modeling of soils came about in the 1980s with the advent of so-called **three-phase soil models**. Herein, three-phase models are used in the sense of models such as the one presented by Loret and Khalili [50]. This development married three existing concepts: Terzaghi's concept of "effective stress" or stress in

the solid skeleton of the soil, elastic-plastic modeling using existing models applied to this effective stress, and the theory of mixtures. Three-phase models are specifically meant to describe the behavior of unsaturated soils, wherein the three phases are: solid “skeleton”, fluid (water), and gas (air). Terzaghi’s description of effective stress in saturated soils is well-established in describing plastic behavior, however the same cannot be said for unsaturated soils. Bishop’s effective stress was shown experimentally by Bishop and Blight [51] through observation that the bulk and deviatoric responses are not affected if the net stress and water pressure (suction) are kept constant.

The yield surface of the three-phase model of [50] is shown in Figure 0.9 and is in the plane of effective mean stress $\bar{p}$ and shear stress q defined as:

$$\bar{p} = -\frac{1}{3} tr(\bar{\sigma}) \tag{2.4}$$

$$q = \left(\frac{3}{2} dev(\bar{\sigma}) : dev(\bar{\sigma})\right)^{1/2} \tag{2.5}$$

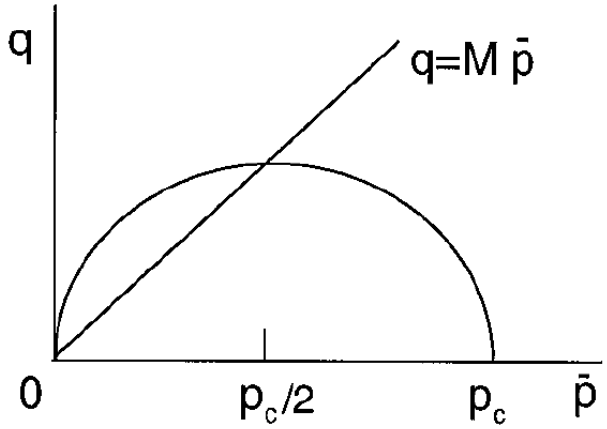

Figure 0.9: Yield surface of the three-phase modified Cam-Clay Model [50]

It is evident that the third effective stress invariant is not considered, thus the yield surface is circular cross-sections along deviatoric planes. The yield surface is then described below:

$$f = f\left(\bar{p}, q, p_c\right) = \frac{q^2}{M^2 \bar{p}} + \bar{p} - p_c \tag{2.6}$$

where M is a material parameter representing the slope of the critical state line. The pre-consolidation stress p_c describes the size of the yield surface.

The main downside of using a three-phase model is the lack of experimental results to justify its complexity, and the need to carry out many experiments to identify the many coefficients, such as the coefficients describing the soil-water characteristic curve (SWCC) that is incorporated in the model.

A Bridge from the Grain to the Continuum

Heterogeneity is a feature of virtually all engineering materials at one scale or another. This tends to make characterization of the material response a difficult task indeed. Carrying out experiments with the goal of capturing the various mechanically relevant properties is a prohibitive endeavor in terms of time and effort. Turning to computational models for clarity is not a realistic option for the foreseeable future, a numerical simulation of an entire material specimen that captures the relevant microstructure is a task that even the most high-powered, high-performance systems are not currently capable of computing.

Including heterogeneity in characterization of material response poses a problem that has in recent decades been answered using multiscale modeling methods. The multiscale modeling paradigm has been developed along two different tracks. On the first of these tracks, one can find *concurrent multiscale methods* where the scales are coupled. On the second of the two multiscale modeling tracks is the one with *homogenization methods*, where the scales are clearly separated

The main feature of concurrent methods is the transfer of microstructural properties to the macroscale directly. Some studies representative of concurrent multiscale methods

include the material failure analyses using domain decomposition of Guidault et al. [52], Eckardt and Könke [53], and Lloberas-Valls et al. [54]. Rather than domain decomposition, the variational multiscale method was used in the works of Hettich et al [55], as well as Loehnert and Belytschko [56]. An often-used approach to concurrent multiscale modeling is adaptive combination of numerical homogenization with a concurrent method such as by Ghosh et al [57], Larsson and Runesson [58], and Temizer and Wriggers [59]. Other important works on the concurrent multiscale track include Oden et al. [60], Takano et al. [61], Fish and Chen [62], Zhang et al [63], as well as Bitencourt et al [64].

Homogenization – Analytical and Computational

The second track, homogenization or separation of scales, is the one followed in the current work. Computational homogenization as a field of study is relatively young, most of the work has been carried out in the past two decades. However its parent field, **analytical homogenization**, has substantial literature behind it. In fact Voigt, after whom the upper elastic bound is named, used uniform strain in his 1889 analysis of heterogeneous materials [65]. Then of course Reuss, after whom the lower elastic bound is named, did the same using uniform stress [66]. It has long been recognized that these two bounds are quite wide and their use can only be justified for linear material properties [67]. There are however, nonlinear counterparts to the Voigt and Reuss bounds in the bounds of Taylor [68] and Sachs [69].

In the subsequent decades the analytical homogenization approach was extended by Hashin and Shtrikman using a variational formulation to derive bounds for bulk and shear moduli [70] and magnetic permeability [71] for isotropic composite materials. A generalization of the Hashin-Shtrikman bounds for anisotropic materials was derived by

Walpole [72] as well as Milton and Kohn [73]. Similarly, the variational approach was used by Zimmerman to obtain bounds for the Poisson's ratios of composites [74], by Rosen and Hashin to obtain bounds for thermal expansion coefficient in problems of thermoelasticity [75], and by Bisegna and Luciano to obtain bounds for effective moduli in piezoelectricity. The Hashin-Shtrikman bounds, like the Reuss-Voigt bounds, can be rather wide when the composite phases are very dissimilar. Nemat-Nasser et al [76] attempted to ameliorate this, with some success, by including phase geometrical information in the analysis.

A rather more complex approach based on the so-called "dilute family methods" was pioneered by Eshelby [77]. The fundamental assumption of these methods relates to the distribution of the heterogeneities in a composite; it is assumed that the included inhomogeneities are sufficiently diluted that one may effectively neglect any interactions among them. This renders the problem into a problem of a single elliptical inclusion and an infinite matrix. Zohdi and Wriggers pointed out that neglecting inclusion interactions is not physically realistic for materials with random heterogenous particulate microstructure [78]. Additional models in this vein of research are primarily based on mean-field homogenization [79], with models worth noting being the Mori-Tanaka method [80], the self-consistent scheme [81], the generalized self-consistent scheme [82], and the differential method [83]. Hori and Nemat-Nasser proposed a generalization that unified the self-consistent scheme with the Mori-Tanaka method, dubbing it the "double-inclusion model" [84].

Moving on to the problem of analytical homogenization of random and nonlinear composites, the groundwork was laid here by Rodney Hill, after whom the Hill-Mandel macrohomogeneity condition is partly named, with his treatment of finite deformation

elasticity [85]. Another pioneer was Ray Ogden, with his treatment of the homogenization of nonlinear composites [86]. Over the following decades, many improvements to these bounds were published at relatively steady pace. This includes the analytical homogenization studies of Ponte Castañeda and Willis [87], who managed to obtain improved bounds for two-phase random composites with nonlinear viscous phases, the work of Suquet with power-law composites [88], the work of Olson with perfectly-plastic composites [89], as well as the work of Talbot and Willis with nonlinear composites of a more generalized type [90]. Ponte Castañeda further advanced the field with a nonlinear variational principle that can be used to derive the effective mechanical properties of nonlinear composites with both ductile brittle phases [91-93].

In the last three decades, as computational methods have come to occupy a larger share of the engineering mechanics literature, homogenization studies have increased significantly with **computational homogenization** making up a larger portion of these studies over time. The earliest and most widely used computational homogenization approach is the unit-cell method. The unit-cell method is a homogenization approach that assumes a repetitive microstructure, modeling this microstructure explicitly to obtain macroscopic constitutive response characteristics [94-97]. In fact, micro-to-macro computational homogenization methods such as the approach employed in the current study, may be considered a generalization of the unit-cell method for irregular/random microstructures. A fundamental condition of this more generalized micro-to-macro approach, is that there must be an energy equivalence between the microscale problem and the macroscale problem. This energy equivalence requirement is the often-mentioned, underlying principle of this work, the Hill-Mandel macrohomogeneity condition [85, 98].

Separation of Scales

Consider the random sand grain distribution of Figure 0.1. The figure shows two cross-sections of the same cubic sand grain packing, and serves to illustrate the concept of Separation of Scales.

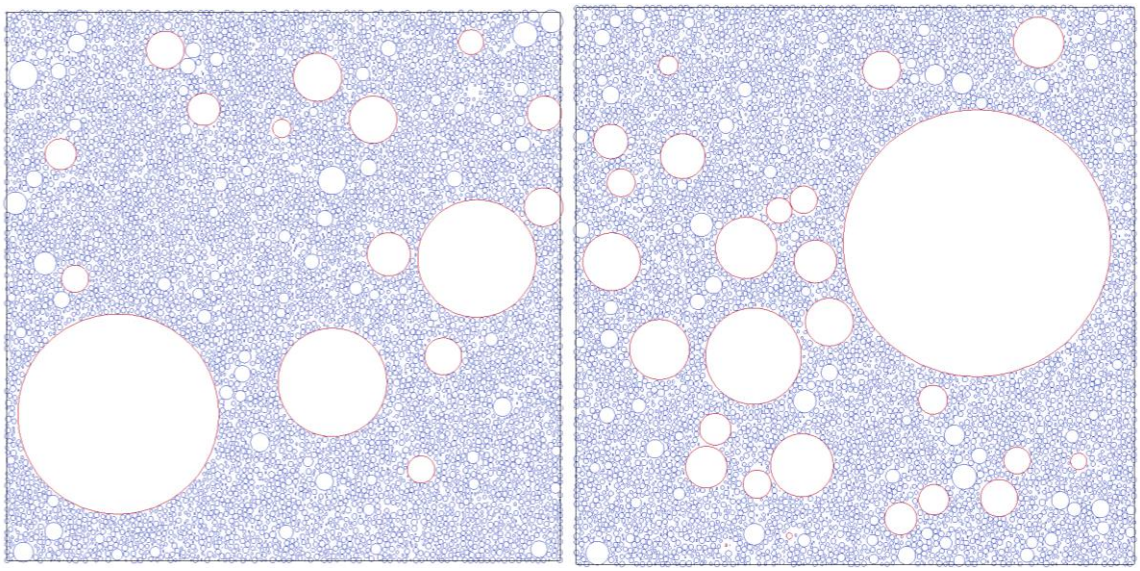

Figure 0.10: Heterogeneous Packing of Sand Grains

Separation of Scales is a principle that links the three different scales present in material mechanics:

4. The microscale *d*, which represents the size of the typical grain, or an inclusion.
5. The intermediate scale *L*, the RVE size
6. The macroscale L_{macro}, macroscopic sample size

Separation of Scales was also defined as the MMM Principle by Hashin [99], where "MMM" denoted a contraction of qualitative Equation (2.7)

$$Micro << Mini << Macro \tag{2.7}$$

Ostoja-Starzewski rewrote Equation (2.7) to define the intermediate scale as the "mesoscale" [8].

$$\left.\begin{matrix} d < \\ d << \end{matrix}\right\} L << L_{macro} \tag{2.8}$$

The inequality of Equation (2.8) contains two options as the mismatch in geometry and properties may be small or great. In the current work, the mismatch is always great, requiring the use of the second form of the left-hand side of the inequality.

Volume Elements – Representative and Stochastic

The primary assumption of any effort to quantify the behavior of a material at the macroscale, is the existence of a Representative Volume Element (RVE). Herein, the RVE is understood in the sense of the Hill-Mandel macro-homogeneity condition [11]. The existence of the RVE is readily ascertained via a unit cell in the case of periodic microstructures, such as those constituting many matrix/fiber composites. However, the identification and determination of the RVE is rather more difficult when dealing with random heterogeneous media such as soils. Mathematically, an infinite number of grains would be required to attain the RVE scale, due to the complete randomness and heterogeneity of the grains [8].

In addition to the concept of the RVE, it is also beneficial at this point to introduce the related concept of the Statistical Volume Element (SVE), which is sometime also called the Stochastic Volume Element, for obvious reasons. The SVE represents any and all realizations of the microscale greater than the typical grain, but smaller than the RVE. Where the RVE material properties are the same as those of the macroscale, the SVE properties

are represented by statistical quantities like the Probability Density Function (PDF) and Statistical Bounds.

The Hill Condition for Particle Aggregates

Consider a body $B_\delta(\omega)$ not under the action of any body forces or inertia and with stress and strain fields σ and ε due to some arbitrary boundary conditions. The stress/strain fields may be represented as a superposition of their means ($\bar{\sigma}$ and $\bar{\varepsilon}$) and trivial fluctuations (σ' and ε')

$$\begin{aligned}\sigma(\omega,\mathbf{x}) &= \bar{\sigma} + \sigma'(\omega,\mathbf{x}) \\ \varepsilon(\omega,\mathbf{x}) &= \bar{\varepsilon} + \varepsilon'(\omega,\mathbf{x})\end{aligned} \tag{2.9}$$

The volume average of the energy density over $B_\delta(\omega)$ may then be written as:

$$\begin{aligned}\bar{U} &= \frac{1}{2V}\int_{B_\delta(\omega)} \sigma(\omega,\mathbf{x}) : \varepsilon(\omega,\mathbf{x})\, dV = \frac{1}{2}\overline{\sigma:\varepsilon} \\ \bar{U} &= \frac{1}{2}\bar{\sigma}:\bar{\varepsilon} + \frac{1}{2}\overline{\sigma':\varepsilon'}\end{aligned} \tag{2.10}$$

The Hill Condition [11] means the average of a scalar product of stress and strain fields is equal to the product of their averages

$$\overline{\sigma:\varepsilon} = \bar{\sigma}:\bar{\varepsilon} \tag{2.11}$$

which requires

$$\overline{\sigma':\varepsilon'} = 0 \tag{2.12}$$

Rewriting (2.11) in indicial notation and applying the divergence theorem

$$\overline{\sigma'_{ij}\varepsilon'_{ij}} = \frac{1}{V}\int_{\partial V}\left[\left(t_i - \bar{\sigma}_{ij}n_j\right)\left(u_i - \bar{\varepsilon}_{ij}x_j\right)\right] dS \tag{2.13}$$

The triviality of the fluctuations is clearly satisfied for the macroscale L_{macro}, however for a finite mesoscale the Hill Condition is satisfied if and when Equation (2.14) holds

$$\frac{1}{V}\int_{\partial B_\delta}\left[\left(\mathbf{t}-\bar{\sigma}\cdot\mathbf{n}\right)\left(\mathbf{u}-\bar{\varepsilon}\cdot\mathbf{x}\right)\right]dS=0 \tag{2.14}$$

The condition is satisfied by three different types of uniform boundary conditions for heterogeneous media:

1. uniform displacement (Dirichlet, kinematic, KUBC) boundary condition
2. uniform traction (Neumann, static, SUBC) boundary condition
3. uniform displacement-traction (orthogonal mixed, MUBC) boundary condition

In addition to the uniform boundary conditions listed above, the Hill-Mandel condition can also be satisfied by the so-called Periodic Boundary Conditions (PBC), also sometimes more descriptively called the "periodic displacement and anti-periodic traction boundary conditions".

Mesoscale Bounds of Particle Aggregates

Consider again the particle mesoscale domain shown in Figure 0.1 and assume the state of the composite body $B_\delta(\omega)$ to be described everywhere by the local stress-strain relation $\sigma = C(\omega, x)\colon\varepsilon$. Supposing the material window is evenly divided into four subdomains $B_{\delta_s}(\omega)$, s=1, …, 4 as illustrated by the dashed lines in the figure. The uniform displacement boundary conditions for a prescribed constant strain ε^0, over the mesodomain are

$$\begin{aligned} u(x) &= \varepsilon^0\cdot x \quad \forall x\ \varepsilon\ \partial B_\delta \\ u^r(x) &= \varepsilon^0\cdot x \quad \forall x\ \varepsilon\ \partial B_{\delta_s} \quad s=1,\ldots,4 \end{aligned} \tag{2.15}$$

In Equation (2.15), the first equation represents the boundary of the entire mesodomain of Figure 0.1, while the second equation is given on the individual boundary of each sub-mesodomain. Here the superscript r indicates that the sub-mesodomain is "restricted",

i.e. is dependent of the response of the bigger mesodomain. It should be noted that, using the strain averaging theorem, the volume average strain is the same in each subdomain and also equal to that in the larger mesodomain.

$$\varepsilon^0 = \overline{\varepsilon} = \overline{\varepsilon^s} \tag{2.16}$$

Consider the minimum potential energy principle for the kinematically admissible fields $(\tilde{\sigma}, \tilde{\varepsilon})$ satisfying the local stress-strain relations $\boldsymbol{\sigma} = C(\omega, \mathbf{x}) : \varepsilon$ and the **displacement boundary** condition (2.15). The minimum potential energy principle is written as

$$\int_{\partial B_\delta^t} \mathbf{t} \cdot \tilde{\mathbf{u}} dS - \frac{1}{2} \int_{B_\delta} \tilde{\sigma} : \tilde{\varepsilon} dV \leq \int_{\partial B_\delta^t} \mathbf{t} \cdot \mathbf{u} dS - \frac{1}{2} \int_{B_\delta} \sigma : \varepsilon dV \tag{2.17}$$

From Equation (2.17), it follows that for the displacement boundary condition the inequality of Equation (2.18) holds.

$$\overline{\sigma} : \overline{\varepsilon} \leq \overline{\tilde{\sigma} : \tilde{\varepsilon}} \tag{2.18}$$

The solution $(\tilde{\sigma}^r, \tilde{\varepsilon}^r)$ to the second equation of (2.15) is a kinematically admissible solution, hence

$$\overline{\sigma} : \overline{\varepsilon} \leq \tilde{\sigma}^r : \tilde{\varepsilon}^r \tag{2.19}$$

The inequality of implies a weak inequality between mesoscale stiffness tensors under restricted and unrestricted conditions. Following this line of reasoning, an inequality is implied between smaller mesodomains and larger mesodomains, assuming homogeneity of the material. In fact, the inequality may be generalized to the hierarchy of bounds

$$\left\langle C_\infty^d \right\rangle \leq \ldots \leq \left\langle C_\delta^d \right\rangle \leq \left\langle C_{\delta'}^d \right\rangle \leq \ldots \left\langle C_1^d \right\rangle \leq C^V \qquad \forall \delta' = \delta / 2 \tag{2.20}$$

where C^V is the Voigt bound. The mesoscale stiffness hierarchy of (2.20) spans form a single grain $(\delta = 1)$ to the macroscopic response $(\delta \to \infty)$.

Similarly, under traction boundary condition

$$\left\langle S_{\infty}^{t}\right\rangle \leq \ldots \leq \left\langle S_{\delta}^{t}\right\rangle \leq \left\langle S_{\delta'}^{t}\right\rangle \leq \ldots \left\langle S_{1}^{t}\right\rangle \leq S^{R} \qquad \forall \delta' = \delta / 2 \tag{2.21}$$

where S^R is the Reuss bound.

The combined hierarchy of bounds from Equations (2.20) and (2.21) is

$$\begin{aligned} &\left\langle \mathbf{S}_{1}^{t}\right\rangle^{-1} \leq \ldots \leq \left\langle \mathbf{S}_{\delta'}^{t}\right\rangle^{-1} \leq \left\langle \mathbf{S}_{\delta}^{t}\right\rangle^{-1} \leq \ldots \leq \mathbf{C}_{\infty}^{eff} \leq \ldots \\ &\ldots \leq \left\langle \mathbf{C}_{\delta}^{d}\right\rangle \leq \left\langle \mathbf{C}_{\delta'}^{d}\right\rangle \leq \ldots \leq \left\langle \mathbf{C}_{1}^{d}\right\rangle \qquad \forall \delta' = \delta / 2 \end{aligned} \tag{2.22}$$

Figure 0.11 gives an illustration of the bounds for a disk-matrix composite with moduli ratios of 100 and 10000. As the realization window gets larger, the moduli bound obtained from the traction-controlled boundary converges with the bound obtained from the displacement-controlled bound [8].

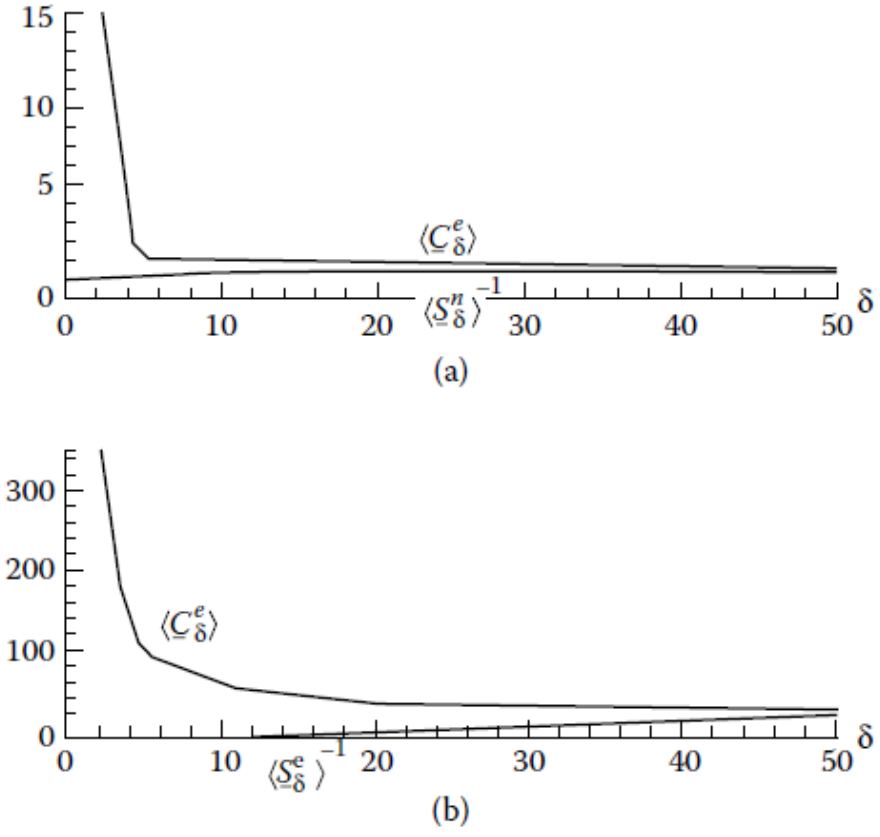

Figure 0.11: Hierarchy of scale-dependent bounds [100]

Consider a multiphase elastic-plastic-hardening material with phases $p = 1, \ldots, p_{tot}$. Each realization of is described by an associated flow rule

$$\begin{aligned} d\varepsilon'_{ij} &= \frac{d\sigma'_{ij}}{2G_p} + \lambda \frac{\partial f}{\partial \sigma_{ij}} df_p \qquad for \qquad f_p = c_p \quad and \quad df \geq 0 \\ d\varepsilon'_{ij} &= \frac{d\sigma'_{ij}}{2G_p} \qquad\qquad\qquad\quad for \qquad f_p < c_p \end{aligned} \tag{2.23}$$

and

$$d\varepsilon = \frac{1-2\nu_p}{2G_p\left(1+\nu_p\right)} d\sigma \tag{2.24}$$

where $d\varepsilon = d\varepsilon_{ii}/3$ and $d\sigma = d\sigma_{ii}/3$. Here G_p is the shear modulus, ν_p is Poisson's ratio, and c_p is the yield limit.

When loaded monotonically, elastic plastic hardening composites can be treated as elastic materials with physical nonlinearities. Again, considering the stiffness and compliance moduli as before, their tangent formulations can be defined as

$$\overline{d\boldsymbol{\sigma}} = \mathbf{C}_\delta^{Td} : \overline{d\boldsymbol{\varepsilon}} = \mathbf{C}_\delta^{Td} : d\boldsymbol{\varepsilon}^0; \qquad \overline{d\boldsymbol{\varepsilon}} = \mathbf{S}_\delta^{Tt} : \overline{d\boldsymbol{\sigma}} = \mathbf{S}_\delta^{Tt} : d\boldsymbol{\sigma}^0 \tag{2.25}$$

where the superscripts t/d denotes response under displacement or traction boundary conditions. As before, this indicates a similar hierarchy of upper and lower bounds on the effective tangent moduli

$$\begin{aligned} &\left\langle \mathbf{S}_1^{TS} \right\rangle^{-1} \equiv \left\langle \mathbf{S}_1^{Tt} \right\rangle^{-1} \leq \ldots \leq \left\langle \mathbf{S}_{\delta'}^{Tt} \right\rangle^{-1} \leq \left\langle \mathbf{S}_\delta^{Tt} \right\rangle^{-1} \leq \left\langle \mathbf{S}_\infty^{T} \right\rangle^{-1} \equiv \mathbf{C}_\infty^T \\ &\mathbf{C}_\infty^T \leq \ldots \leq \left\langle \mathbf{C}_\delta^{Td} \right\rangle \leq \left\langle \mathbf{C}_{\delta'}^{Td} \right\rangle \leq \ldots \leq \left\langle \mathbf{C}_1^{Td} \right\rangle \equiv \left\langle \mathbf{C}_1^{TT} \right\rangle \qquad \forall \delta' = \delta / 2 \end{aligned} \tag{2.26}$$

where $\left\langle \mathbf{S}_1^{TS} \right\rangle^{-1}$ and $\left\langle \mathbf{C}_1^{TT} \right\rangle$ are the Sachs and Taylor bounds.

The computational solid mechanics discipline is, by now, a mature field with a healthy and growing body of literature and a global host of researchers. As the discipline has matured, the focus of this community has turned toward integrating the accumulated knowledge of the discipline within the wider applied mathematics, physics, and general scientific research efforts. This is manifest in the expanding literature with multiscale, multi-physics, and multi-discipline objectives. However, the converse is also very much true, knowledge from other scientific disciplines has much to offer to improve computational modeling efforts in solid mechanics. Specifically, within the context of the current study, there are three mathematics disciplines that are quite useful in the micro-to-macro transition. Those disciplines are: 1) statistics and statistical mechanics, 2) probability theory and propagation of uncertainty, and 3) mathematical optimization methods.

Statistical Mechanics of Random Heterogeneous Materials

Statistical Mechanics is a branch of theoretical physics. Its objective is to evaluate the macroscale properties of systems by modeling the interactions of a system's fundamental constituents, constituents such as atoms, molecules, or, as in the present case, grains. In statistical thermodynamics, for example, statistical mechanics starts with molecular interactions and structure as determined from the laws of quantum or classical mechanics, then attempts to link these to macroscopic properties such as the temperature and pressure of a liquid. Useful insight into the constitutive behavior of random heterogeneous materials can be gained by modeling these as systems of interacting particles. This is especially true for particulate media such as soils in general and sand in particular. This section serves as a brief primer on statistical mechanics, particularly as it relates to the particle aggregates as random heterogeneous systems of particles. For a much more thorough review of statistical

mechanics, the reader is pointed towards the works of Torquato [101], Huang [102], Kardar [103], and Sethna [104].

Arguably, the most important concept of statistical mechanics drawn from in this work, is the concept of a **statistical ensemble**. In broad terms, a statistical ensemble is a compilation of conceivable "realizations" of a system resulting from non-deterministic processes. Here, a "realization" refers to a single sample of the system out of the infinite number of possible samples drawn from the random medium. In more specific terms, when dealing with physics-based modeling, a statistical ensemble is a model composed of many copies of a system in its different possible states, considered simultaneously. Another way to state this is that the Statistical Ensemble is a probability distribution for the state of the system [105]. For the concrete case of a particle model of a geomaterial such as the sand considered herein, the ensemble may be defined as a collection of particle packings of a finite size, wherein the cumulative distribution tends to that of a single packing of a near-infinite number of particles.

The idea here may be distilled down to the simple fact that a Discrete Element Model containing a near-infinite number of particles is both impractical and computationally prohibitive. However, a sufficiently large number of concurrent models of finite sizes, is quite feasible, especially so with access to High Performance Computing (HPC) resources. These models of finite size are henceforth called "realizations", wherein each is a random realization of a possible collection of particles and properties of the constituent grains.

Ensemble Averaging is the computation of the average, or possibly the statistical distribution, of a certain quantity for an ensemble of realizations. In this study, the

ensemble is a collection of Discrete Element Models, each of which represents a realization of the system of grains.

When discussing heterogeneous materials, statistical descriptors and metrics are useful in describing and quantifying the geometry of the system. The general term for these statistical geometry descriptors is *microstructural correlation functions* [101]. The first important types of correlation functions are **n-point probability functions**. These functions were introduced by Brown [106] as a means of deriving effective transport properties in random media. However, as statistical descriptors, they are also useful in determining mechanical properties of heterogeneous materials. They have, in fact, successfully been used to determine effective material elastic moduli by several authors [107-109].

Using binary variables to describe two contrasting phases in a system, an n-point probability functions expresses the probability of finding n points $x_1, x_2, \ldots, x_n$ in phase i as:

$$\mathcal{S}_n^{(i)}\left(x_1, x_2, \ldots, x_n\right) \equiv \left\langle \mathcal{I}^{(i)}\left(x_1\right)\mathcal{I}^{(i)}\left(x_2\right)\ldots\mathcal{I}^{(i)}\left(x_n\right)\right\rangle \tag{2.27}$$

where angular brackets indicate an ensemble average. Equation (2.27) gives the probability of the ensemble consisting of n points $x_1, x_2, \ldots, x_n$ being found in phase i. Following similar logic and derivation, the two-point "full-contrast" probability of finding point x_1 in phase 1, while also finding point x_2 in phase 2 is given by

$$\mathcal{S}_2^{(12)}\left(x_1, x_2\right) \equiv \left\langle \mathcal{I}^{(1)}\left(x_1\right)\left[1 - \mathcal{I}^{(1)}\left(x_2\right)\right]\right\rangle \tag{2.28}$$

This formulism can be extended to the case of polydisperse spherical microstructures. Doing this results in two edge cases, the case of overlapping or fully-penetrable

spheres, and the case of rigid or completely impenetrable spheres. For the former, the n-point probability function for phase 1 may be derived to be:

$$\mathcal{S}_n\left(x_n\right) \equiv \exp\left[-\rho\left\langle \upsilon_n\left(x_n;R\right)\right\rangle\right] \tag{2.29}$$

where υ_n is the volume of the union on n d-dimensional spheres of radius R.

Surface correlation functions contain information about a random interface av and are of basic importance in the trapping and flow problems. In this context, letting phase 1 denote the fluid or "void" phase, and phase 2 the "solid" phase. The simplest surface correlation function is the specific surface s(x) (interface area per unit volume) at point x, which is a one-point correlation function for statistically inhomogeneous media, i.e.

$$\mathcal{S}(x)=\left\langle \mathcal{M}(x)\right\rangle \tag{2.30}$$

Another interesting and useful statistical measure is called the **lineal-path function**. For statistically isotropic media, it is defined as follows:

$$\mathcal{L}^{(i)}\left(z\right) = \textit{Probability that a line segment of length z lies wholly in phase i when randomly thrown into the sample.} \tag{2.31}$$

In stochastic geometry, the quantity $\phi_i\left[1-L^{(i)}\left(z\right)\right]$ is sometimes referred to as the linear contact distribution function. The lineal-path function is a lower-order microstructural function, since it is a lower-order case of the canonical n-point correlation function.

A quantity related to the lineal-path function is **the chord-length probability density function**. Chords are all of the line segments between intersections of an infinitely long line with the two-phase interface. The density function $p^{(i)}\left(z\right)$ is defined for statistically isotropic media as follows:

$p^{(i)}(z)\mathrm{dz}$ = Probability of finding a chord of length between z and z +dz in phase i. (2.32)

Propagation of Uncertainty at the Mesoscale

Among the characteristics that make the constitutive behavior of geomaterials different from many other materials, is the degree of variability and uncertainty exhibited in the constitutive response. Certainly, much of this uncertainty is epistemic. Given just the right sample of the material, prepared in just the right way, submitted to just the right type, magnitude, and path of loading, it would be possible to predict fairly accurately how the material will respond to the environmental loading under investigation. However, tailor-made material constitutive characterization is not within the realm of possibility for virtually any real-world application. What is far more attainable, is characterization of the constitutive properties within certain bounds, meeting certain cumulative distributions if run through enough scenarios. This is where uncertainty quantification (UQ) enters the stage in this framework.

Uncertainty Quantification may be defined as the applied convergence of statistics and probability theory [110]. It is the UQ "way" to treat a problem probabilistically using mathematical models with parameters subject to some known or estimated variability. The most common type of Uncertainty Quantification problem is known as a problem of "forward uncertainty propagation", often called simply "propagation of uncertainty". Propagation of uncertainty aims to quantify the uncertainty in the outputs of a process from the uncertainty inherent in its inputs. This type of input uncertainty may also be referred to as "parametric variability". Possible objectives of a propagation of uncertainty analysis may include:

- To evaluate the moments of the output histogram, such as means, deviation etc.
- To identify a continuous or discrete statistical distribution that accurately describes the range of process outputs.
- To establish confidence limits on the expected process outcomes. This is also known as reliability analysis.

In the current framework, uncertainty quantification refers specifically to propagation of uncertainty from experimental data onto mesoscale modeling then across computational modeling paradigms. The measured micromechanical properties and the variability therein are used to model the mesoscale response using Discrete Element ensembles. The output then is uncertainty inherent to mechanical response parameters in particulate media. This is sampled from the discrete modeling paradigm of the Discrete Element Method, then propagated in turn as uncertain input to the continuum modeling paradigm of the Finite Element Method.

Model Calibration through Mathematical Optimization

In applied mathematics and computational modeling, an **optimization problem** is one where there is no unique solution and the best choice of possible solutions must be identified. There are two broad types of optimization problems, combinatorial optimization and continuous optimization. Combinatorial optimization deals with discrete values or realizations of variables. This work does not deal with combinatorial optimization. Continuous optimization, on the other hand, deals with continuous variables and can include constraints and multimodality.

The standard form of a continuous optimization problem may be written as [111]:

$$\begin{aligned} &\text{minimize}\, x && f(x) \\ &\text{subject to} && g_i(x) \le 0, \quad i = 1, \ldots, m \\ & && h_i(x) = 0, \quad i = 1, \ldots, p \end{aligned} \tag{2.33}$$

where $f(x): \mathbb{R}^n \to \mathbb{R}$ is the objective function that needs to be minimized over x, $g_i(x) \le 0$ are inequality constraints, and $h_i(x) = 0$ are equality constraints.

An **objective function** is a function that maps values of variables to a real number that represents the cost or reward associated with the variable value. When reward is used, the objective function is called a Reward or Profit Function and the goal of optimization is to maximize it. When cost is used, the Objective Function is termed a Loss Function and the goal of the optimization problem is to minimize the cost or loss number. In the context of Computational Modeling, an objective function is typically a Loss Function where the "cost" is some measure of the computational error relative to an objective measure such as experimental testing.

Optimization algorithms include Local as well as Global approaches. Local optimization approaches seek the local best solution or local minimum with no consideration to the possibility there may be a lower minimum in a distant region of the solution space. The local approach is well-suited to problems with a monotonic objective function. However, if the objective function is "bumpy", then a global approach is required to ensure the optimization has not converged to a local minimum that does not represent the optimal global result.

Additionally, optimization algorithms may be classified as either Gradient-based or Derivative-free methods. Gradient-based methods have the best accuracy and convergence rates; however, they require the computational code to provide analytic gradients, which is often not possible when dealing with Computational Fluid Dynamics and Finite Element

Method codes. This is where derivative-free methods are useful. They are inherently more expensive computationally then gradient-based methods, however they benefit greatly from parallelism and can approach the speed of gradient-based methods with sufficient asynchronous concurrency [112].

CHAPTER 3

FORMULATION OF COMPUTATIONAL AND MATHEMATICAL MODELS

This chapter presents descriptions and technical details of the computational and mathematical paradigms used in this work. There are two computational mechanics frameworks for modeling the material, another two computational learning and optimization frameworks for training the mechanics frameworks, and a statistical mechanics framework to describe the inherent heterogeneity of the material parameters and resulting response. The first computational mechanics model type is the one used for mesoscale modeling of sand, the Discrete Element Method (DEM). The second computational mechanics model, is a continuum mechanical model called the Hybrid Elastic Plastic (HEP) model, developed and used mainly for modeling granular media in hydrocode applications. To reiterate what was previously stated, the HEP model is an arbitrary choice of a macroscale/continuum model, the multiscale analysis carried out herein can be adapted to other continuum models of granular media.

Discrete Element Modeling of Sand

Discrete Element Method (DEM) is the name given to a collection of numerical methods used to model the motion, forces, and interactions of particles. The method was originally developed by Cundall and Strack [113]

Explicit Numerical Scheme

DEM employs an explicit numerical scheme to integrate the motion of spherical particles. This motion consists of both translational and rotational degrees of freedom (DOF), represented by the following equations of motion

$$m_i \frac{d^2}{dt^2}\mathbf{x_i} = \mathbf{F_i} \tag{3.1}$$

$$I_i \frac{d}{dt}\boldsymbol{\omega}_\mathbf{i} = \mathbf{T_i} \tag{3.2}$$

where m_i represents the mas of particle i, $\mathbf{x_i}$ represents the position vector of the particle and $\mathbf{F_i}$ represents the body force vector on particle i. The rotational equation of motion contains the particles moment of inertia I_i, the particle's angular velocity vector $\boldsymbol{\omega}_\mathbf{i}$, and the total torque vector $\mathbf{T_i}$.

The integration scheme is the typical integration scheme used in explicit codes, the "leapfrog" scheme, which is a variant of the Verlet integration scheme [114, 115]. The name of the scheme is a nod to the scheme's pattern of computing even derivatives at the current time-step, while computing odd derivatives mid-step.

Recall that an integration scheme is needed to compute the updated position of a particle from its current position $\mathbf{x_i}$ using its current acceleration $\ddot{\mathbf{x}}_\mathbf{i} = d^2/dt^2\,(\mathbf{x_i})$. The acceleration is in turn computed from the force $\mathbf{F_i}$ using Newton's first law:

$$\ddot{\mathbf{x}}_\mathbf{i} = \frac{\mathbf{F_i}}{m_i} \tag{3.3}$$

When using a second order finite difference scheme with time-step Δt, Equation (3.3) becomes:

$$\ddot{\mathbf{x}}_{\mathbf{i}}^{\,0} \cong \frac{\mathbf{x}_{\mathbf{i}}^{\,-} - 2\mathbf{x}_{\mathbf{i}}^{\,0} + \mathbf{x}_{\mathbf{i}}^{\,+}}{\Delta t^2} \tag{3.4}$$

where $\ddot{\mathbf{x}}_{\mathbf{i}}^{\,0}$ is the current acceleration, $\mathbf{x}_{\mathbf{i}}^{\,0}$ is the current position, $\mathbf{x}_{\mathbf{i}}^{\,+}$ is the updated position, and $\mathbf{x}_{\mathbf{i}}^{\,-}$ is the previous position. If the updated particle position is required, Equation (3.4) is expressed as:

$$\mathbf{u}^{+} = 2\mathbf{u}^{0} - \mathbf{u}^{-} + \ddot{\mathbf{u}}^{0}\Delta t^2 \tag{3.5}$$

which may be rewritten as:

$$\mathbf{u}^{+} = \mathbf{u}^{0} + \Delta t\left(\frac{\mathbf{u}^{0} - \mathbf{u}^{-}}{\Delta t} + \ddot{\mathbf{u}}^{0}\Delta t\right) \tag{3.6}$$

Note that the first term inside the parentheses of Equation (3.6) represents the mean velocity during the previous step

$$\dot{\mathbf{u}}^{-} \simeq \frac{\mathbf{u}^{0} - \mathbf{u}^{-}}{\Delta t} \tag{3.7}$$

Using Equation (3.7), Equation (3.6) may be written as:

$$\mathbf{u}^{+} = \mathbf{u}^{0} + \Delta t\left(\dot{\mathbf{u}}^{-} + \ddot{\mathbf{u}}^{0}\Delta t\right) \tag{3.8}$$

The algorithm then is succinctly described by Equations (3.9) and (3.10)

$$\dot{\mathbf{u}}^{+} = \dot{\mathbf{u}}^{-} + \ddot{\mathbf{u}}^{0}\Delta t \tag{3.9}$$

$$\mathbf{u}^{+} = \mathbf{u}^{0} + \dot{\mathbf{u}}^{+}\Delta t^2 \tag{3.10}$$

The leapfrog pattern can be clearly discerned here, where the particle positions are known at multiples of Δt, while velocities are known at midsteps $\Delta t \pm \Delta t/2$.

Particle orientation is computed similarly to the position. The current angular acceleration is

$$\dot{\boldsymbol{\omega}}_{\mathbf{i}}^{\mathbf{0}} = \frac{\mathbf{T_i}}{I_i} \tag{3.11}$$

Following the familiar scheme, an expression analogous to Equation (3.9) is obtained

$$\boldsymbol{\omega}^{+} = \boldsymbol{\omega}^{-} + \Delta t \dot{\boldsymbol{\omega}}^{0} \tag{3.12}$$

Contact Model

The contact force used in the discrete element particle model may follow one of two formulations. The first formulation, henceforth referred to as **Hertzian contact**, resembles the Hertz-Mindlin solution [116], which is valid for elastic bodies in contact. The elastic normal force in the Hertzian solution is expressed as

$$F_{n,el} = \frac{4}{3} E^{*} \sqrt{R^{*}} u_n^{3/2} \tag{3.13}$$

Where E^{*} and R^{*} represent the equivalent effective Young's modulus and particle radius, respectively. These are determined from the contacting particle parameters

$$E^{*} = \left(\frac{1-\nu_1^2}{E_1} - \frac{1-\nu_2^2}{E_2} \right)^{-1} \tag{3.14}$$

$$R^{*} = \left(\frac{1}{R_1} + \frac{1}{R_2} \right)^{-1} \tag{3.15}$$

where ν_1^2 and ν_1^2 are the Poisson ratios of the interacting particles.

The shear force is linear with respect to the relative sliding displacement at the contact, assuming the no micro-slip solution of Hertzian contact.

$$F_s = 8G^{*} \sqrt{R^{*} u_n} u_s \tag{3.16}$$

with G^{*} being the equivalent shear modulus. Finally, the normal and tangential contact stiffnesses can be written as

$$k_n = 2E^* \sqrt{R^* u_n} \tag{3.17}$$

$$k_s = 8G^* \sqrt{R^* u_n} \tag{3.18}$$

There are some alternate contact models that bear mentioning. A simple normal contact model is the contact model from the original DEM formulation of Cundall and Strack [113]. This model uses a linear spring formulation for the normal contact stiffness rather than the Hertz formulation of Equation (3.13). On the other side of the complexity spectrum, there are some elasto-plastic contact models that account for hysteresis in un-loading of the grains at contact, such as the Walton and Braun elastoplastic contact law [117], and the Thornton elastic-perfectly plastic contact law [118, 119]. Finally, an often-used alternative tangential contact model is the Mindlin-Deresiewicz model [120], which tries to account for micro-slip of the contact surface.

A frictional dissipation mechanism is included in the current DEM formulation as in most DE simulation packages. This takes the form of the following frictional **Mohr-Coulomb sliding criterion**

$$F_s \le F_{s\max} = \mu F_{n,el} \tag{3.19}$$

where μ is the coefficient of interparticle friction.

Contact damping in both the normal and tangential directions is included in the contact model used herein. This is done using a normal contact viscous force:

$$F_{n,v} = \beta_n v_{n,rel} \tag{3.20}$$

where β_n is the normal contact viscous damping ratio and $v_{n,rel}$ is the normal relative velocity, or the rate of inter-penetration of the contacting particles. Similarly, the tangential contact viscous force used is:

$$F_{s,v} = \beta_s v_{s,rel} \tag{3.21}$$

where β_s is the tangential contact viscous damping ratio and $v_{s,rel}$ is the tangential relative velocity, or the rate of sliding between the contacting particles. The viscous damping ratios are related to the interparticle coefficients of restitution by the following relations:

$$\beta_n = \frac{-\log(e_n)}{\sqrt{\pi^2 + (\log(e_n))^2}} \tag{3.22}$$

$$\beta_s = \frac{-\log(e_s)}{\sqrt{\pi^2 + (\log(e_s))^2}} \tag{3.23}$$

Another important aspect of particle contact modeling is **cohesion** between particles. Sand is typically considered a cohesionless material, and rightly so. However, cohesion may be a good approximation for capillary effects, and for some sands it can accurately model chemical cementation. The cohesion model used herein is the Derjaguin-Muller-Toporov (DMT) model [121]. In the DMT model the contact profile is the same as for Hertzian contact but with the added assumption of adhesion outside the area of contact. The radius of contact between two spheres from DMT theory is

$$a^3 = \frac{3R}{4E^*}(F + 4\gamma\pi R) \tag{3.24}$$

and the pull-off force is

$$F_c = -4\gamma\pi R \tag{3.25}$$

Global Damping Mechanism

The global damping mechanism used in the Yade DEM formulation is a type of artificial numerical damping. Such a mechanism is required to ensure that the quasi-static

assumption is reasonable, by dissipating some of the kinetic energy of particles in the model. In Yade, it is implemented in such a way as to decrease only those forces that increase particle velocities, and conversely to increase those forces that decrease particle velocities. Since this must be done by component, it is clear this damping scheme is non-physical. The damping scheme below was originally proposed by Cundall.

$$\frac{\left(\Delta\mathbf{F}\right)_{dk}}{\mathbf{F}_k} = -\lambda_d \ \mathrm{sgn}\left(\mathbf{F}_k \dot{\mathbf{u}}_k^0\right) \qquad k \in \{x, y, z\} \tag{3.26}$$

where λ_d is the damping coefficient. There are several advantages to formulating numerical damping in this way [122]:

- By acting on accelerations, uniform motion in the model is not constrained.
- All particles are equally damped, regardless of their eigenfrequencies.
- The damping coefficient is dimensionless.

In Yade, an adapted form of Equation (3.26) is used which replaces the midstep velocity $\dot{\mathbf{u}}_k^0$ by an on-step estimate of it.

$$\frac{\left(\Delta\mathbf{F}\right)_{dk}}{\mathbf{F}_k} = -\lambda_d \ \mathrm{sgn}\left[\mathbf{F}_k\left(\dot{\mathbf{u}}_k^- + \frac{\ddot{\mathbf{u}}_k^0 \Delta t}{2}\right)\right] \tag{3.27}$$

This is done in order to prevent oscillation of a particle back and forth when the velocity changes its sign due to the force update at each step.

Weibull Survival Probabilities of Sand Grains

Weibull [123] proposed the following equation for the survival probability P_s for material blocks of volume V_0 under normalized tensile stress:

$$P_s\left(V_0\right) = \exp\left[-\left(\frac{\sigma}{\sigma_0}\right)^m\right] \tag{3.28}$$

where $P_s(V_0)$ is the probability of survival of a particle of volume V_0 under a characteristic stress of $\sigma = F/d^2$, σ is the magnitude of characteristic stress where 37% of the blocks survive, and m is known as the Weibull modulus or the m-modulus. The m-modulus describes variability in strength, a higher m-modulus indicates decreasing variability.

For spherical particles of varying volumes, as pointed out by Nakata [28] Equation (3.28) may be written as:

$$P_s(V) = \exp\left[-\frac{V}{V_0}\left(\frac{\sigma}{\sigma_0}\right)^m\right] \tag{3.29}$$

or, in terms of particle diameters:

$$P_s(D) = \exp\left[-\left(\frac{D}{D_0}\right)^3\left(\frac{\sigma}{\sigma_0}\right)^m\right] \tag{3.30}$$

For a sand grain of diameter D, Equation (3.30) gives the probability that the grain survives intact when subjected to a force equal to $F = \sigma \cdot D^2$.

A more useful quantity for particle aggregate simulations using DEM, is the probability density function (PDF) of grain strengths. This may be obtained as the derivative of the survival probability function which actually is the complement of the cumulative distribution function (CDF).

$$\frac{\partial P_s}{\partial \sigma} = m\left(\frac{D}{D_0}\right)^3\left(\frac{\sigma^{m-1}}{{\sigma_0}^m}\right)\exp\left[-\left(\frac{D}{D_0}\right)^3\left(\frac{\sigma}{\sigma_0}\right)^m\right] \tag{3.31}$$

This PDF of grain strengths may be visualized as a surface dependent on grain stresses and diameters, as illustrated in Figure 0.1 below.

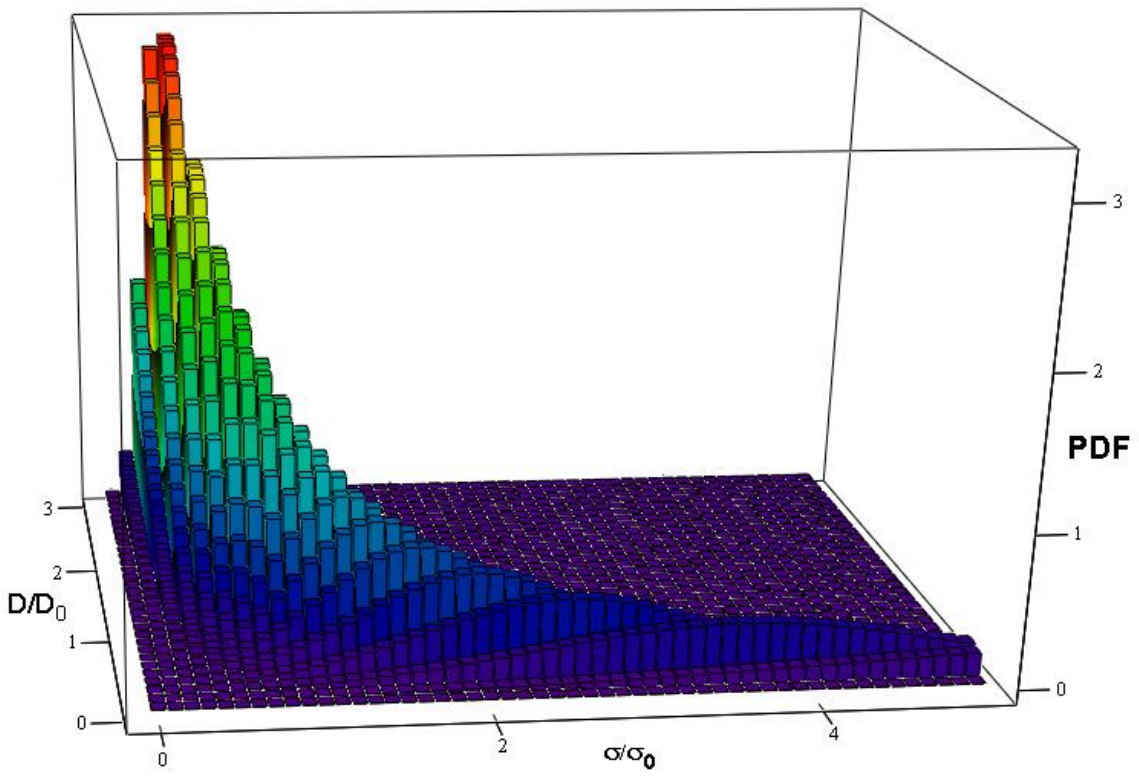

Figure 0.1: Grain probability distribution of normalized strengths for normalized diameters

It should be noted that Equation (3.30) implies a sort of "size-hardening law", whereby the larger the grain the weaker it is expected to be, and vice-versa. This may be qualified by modifying the expression so as to compare the characteristic stresses for D and D_0, which results in the following equation.

$$\sigma_0(D) = \sigma_0(D_0)\left(\frac{D}{D_0}\right)^{\frac{-3}{m}} \tag{3.32}$$

Finally, in order to make Weibull survival usable directly in statistical mechanics mesoscale DE models, an expression for σ is required. Such an expression needs to take into account both the experimental results for characteristic stress, and the stochastic nature

of grain survival. This can be done by solving Equation (3.30) for σ and substituting the survival function P_s with a randomly generated survival probability P_q for particle q

$$\sigma_q = -\sigma_0 \left[\left(\frac{D_0}{D_q} \right)^3 \ln\left(P_q\right) \right]^{1/m} \tag{3.33}$$

where P_q is drawn from the uniform distribution over [0,1]. Equation (3.33) is a match for 2-parameter Weibull random sampling as implemented in NumPy [124]. The scale parameter for 2-parameter Weibull sampling in this case is simply $\lambda = \sigma_0 \left(\frac{D_0}{D_q} \right)^{3/m}$.

Upon crush-up, a spherical particle is replaced by an "Apollonian" spherical packing as shown in Figure 0.2. The use of the Apollonian fractal packing algorithm goes beyond convenience and aesthetic considerations. Experimental observations of the evolution of particle size distributions find a fractal distribution with an exponent of ~2.5 [125]. This agrees remarkably well with the Apollonian packing's fractal number of ~2.47 [126].

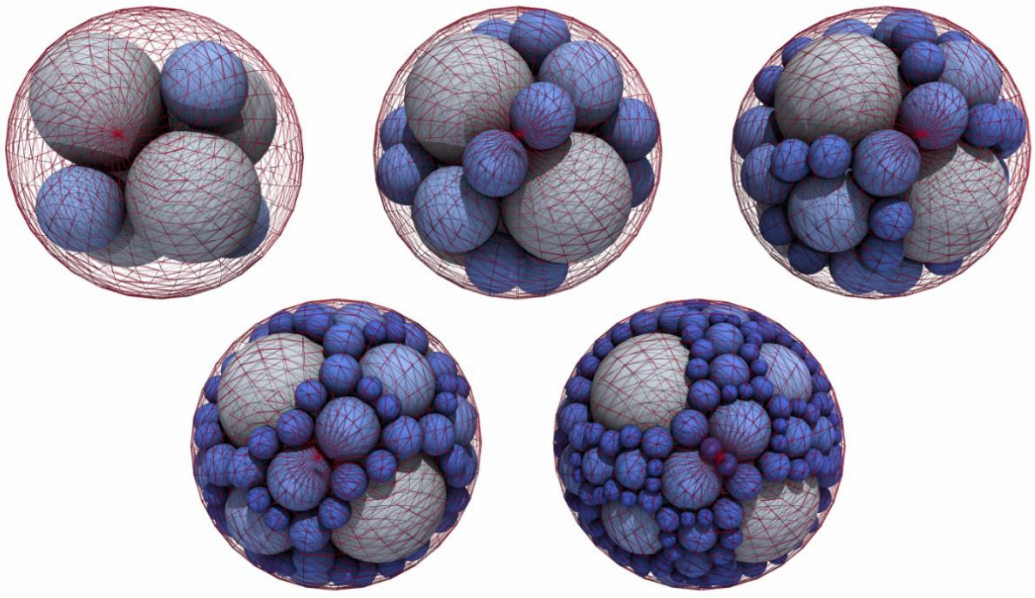

Figure 0.2: Apollonian Sphere Packings at increasing levels of refinement

Brazilian Criterion of Grain Fracture

The crushing criterion used here is the so-called "Brazilian" criterion [127-129]. This criterion derives its name from the use of the distribution of stress in a 1D compression test, also widely known as a Brazilian test. The maximum tensile stress in such a test is:

$$\sigma_t = \frac{\sigma_1 - 3\sigma_3}{2} \tag{3.34}$$

where σ_1 is the major principal stress and σ_3 is the minor principal stress.

A particle that meets the crushing criterion is replaced by an Apollonian packing which has been rotated in 3D space so that the major principal stress bears down on the assumed fracture axis of the fragments. This allows for "blowout" of the packing similar to the blowout fracture seen in a Brazilian test. Figure 0.3 illustrates the loading and blow-out of the Apollonian packing under 1D compression ($\sigma_3 = 0$).

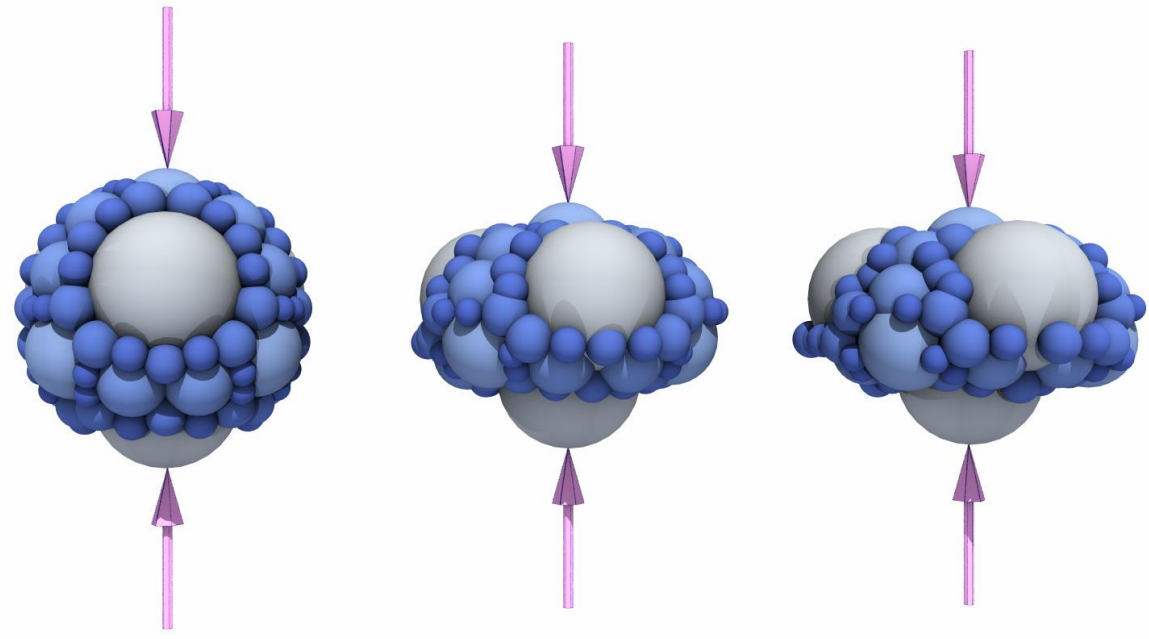

Figure 0.3: Apollonian packing blowout under 1D compression

Hybrid-Elastic-Plastic Models

The hybrid-elastic-plastic (HEP) designation refers to a conglomeration of material model fits rather than a single monolithic model. However, for the sake of conciseness, it will henceforth be usually referred to as the "HEP model". Development of the HEP model was originally carried out by researchers at the Engineer Research and Development Center (ERDC) of the U.S. Army Corps of Engineers. The original goal for the model was calculation of ground shock from conventional weapons for geologic materials [130, 131]. The HEP model was initially implemented in the SABER-PC code [132], a first-principle one-dimensional, spherically-symmetric, Lagrangian finite element code.

In line with the original target of HEP model development, advanced equations of state (EOS) were implemented for the bulk material response. These EOS were judged more important for high confinement applications than a rigorous deviatoric-volumetric behavior coupling. The bulk response in the HEP model is therefore decoupled from the shear response, with a pressure-dependent deviatoric failure surface. Consequently, the HEP model cannot predict dilatation under shear.

The HEP model can simulate complex stress-strain response of geomaterials having been fit to several mechanical tests at high confining pressures. The volumetric response is separated into multiple regions with nonlinear load-unload-reload paths. The failure surface in the HEP model is exponential, non-associative, and elastic-plastic. This exponential failure surface is two-invariant-dependent and has been fit to quasi-static triaxial testing data. The Poisson's ratio scheme typically used is constant but can take different constant values in loading and unloading.

In the intervening years the HEP model from SABER-PC has been adapted for the EPIC Lagrangian Finite Element code [133], which is used in this work as the implementation of the HEP model for response characterization, as well as for calibration and uncertainty quantification. The procedure used to port the HEP model over to EPIC, was similar to the one used to validate it in SABER-PC in the first place [134], and is described below.

1. Carry out controlled ground shock tests with soil backfills carefully placed to tightly controlled and quantified density and water content specifications
2. Carry out uniaxial (UX) and triaxial (TXC) mechanical property tests on specimens of the soil backfill remolded to field-measured densities and moisture contents
3. Analyze the mechanical property data to determine recommended UX stress-strain, pressure-volumetric, and stress-path relations, as well as a TXC failure relation.
4. Fit the HEP model to the recommended properties.
5. Implement these models in SABER/EPIC and simulate the experiments
6. Compare the ground shock measurements with the calculated results to validate the HEP models and overall methodology.

Volumetric Behavior in the HEP Model

The equation of state (EOS) used for the HEP is a modified Tillotson EOS [135, 136], which contains an energy-dependent pressure-volume material response. The EOS is formulated as:

$$P = P_h\left(\mu, \mu_{\max}, \mu_{\min}\right) + P_e\left(e, \rho\right) \tag{3.35}$$

where the pressure P is additively decomposed into an energy independent total hydrostatic triphasic (solid, water, and air) response term P_h as well as an energy-dependent term P_e. The latter is defined as:

$$P_e = \left(a + S\right)\rho e \tag{3.36}$$

with:

$$S = \frac{b}{\frac{e}{e_0 \eta^2} + 1} \tag{3.37}$$

where a, b, and e_0 are constants.

The hydrostatic compressibility term P_h is calculated through an energy-independent hysteretic EOS. This mean the pressure-compression ($P - \mu$) relation is evaluated for loading as well as unloading in both compression and tension. The current value of the compression is defined as:

$$\mu = \frac{\rho}{\rho_0} - 1 \tag{3.38}$$

where ρ is the current density and ρ_0 is the initial density. The hysteresis loop is collapsed into a curve for compression beyond (P_c, μ_c), where c denotes the point of void closure, as illustrated in Figure 0.4.

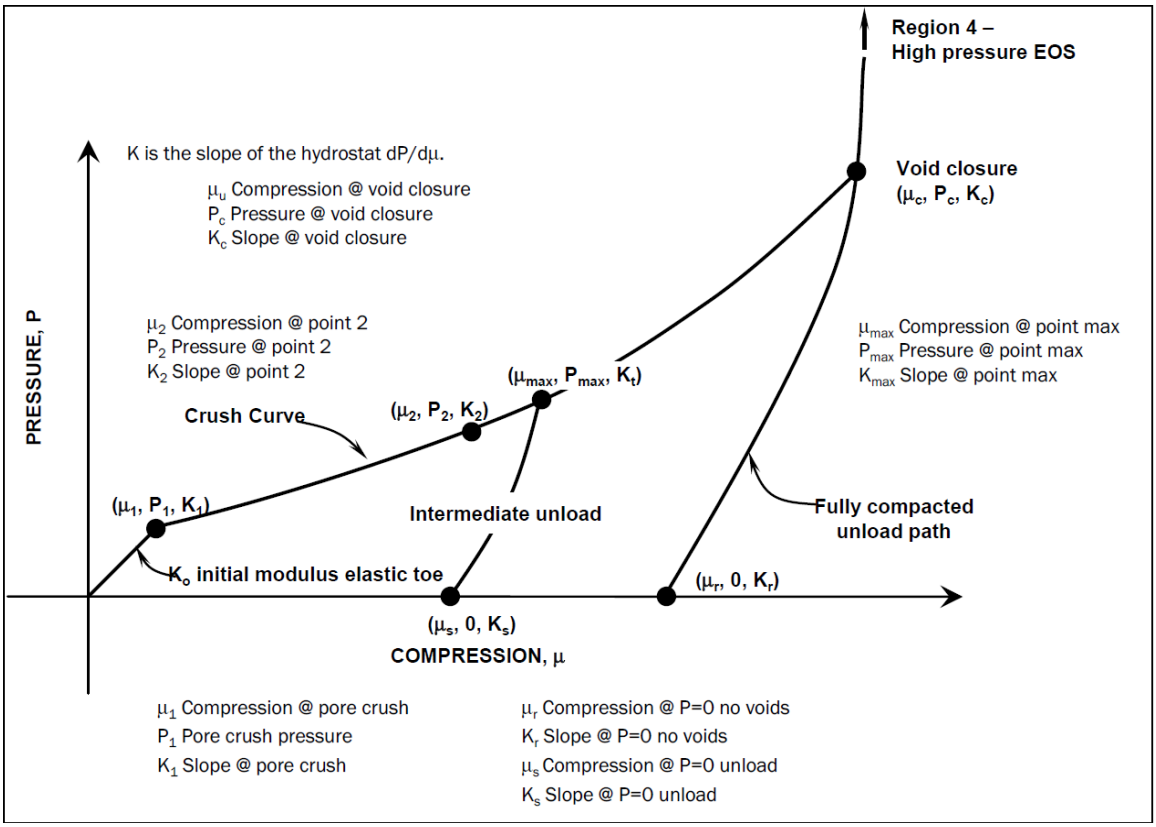

Figure 0.4: Pressure-compression behavior in the HEP model

The EOS, as currently implemented, contains four distinct regions. The initial response is characterized as linear elastic through the "elastic toe" of Region 1 ($\mu \le \mu_1$). Region 2 is identified as a "hysteretic crush-up" region ($\mu_1 < \mu \le \mu_c$). In Region 3, having crossed void closure, the bulk behavior is non-hysteretic ($\mu \ge \mu_c$). Finally, Region 4 is a region of high-pressure pressure response appended to Region 3, which is not used in this work, as it requires the direct use of the SABER code (it has not been ported to EPIC).

For Region 1, the bulk behavior is defined as:

$$P_l = K_0 \mu \tag{3.39}$$

as long as $\mu \le \mu_1$. Note that Region 1 is optional, and may be turned off in the simulation.

Region 2 can be modeled with one of two fit types. In a Region 2 Type 1 fit the bulk behavior is modeled with a single region power fit, with the pressure defined as:

$$P_l = P_1 + K_1\left(\mu - \mu_1\right) + K_\alpha\left(\mu - \mu_1\right)^\alpha \tag{3.40}$$

where:

$$K_\alpha = \frac{P_c - P_1 - K_1\left(\mu_c - \mu_1\right)}{\left(\mu_c - \mu_1\right)^\alpha} \tag{3.41}$$

and:

$$\alpha = \frac{\left(\mu_c - \mu_1\right)\left(K_c - K_1\right)}{P_c - P_1 - K_1\left(\mu_c - \mu_1\right)} \tag{3.42}$$

Note that with the Type 1 fit, it is assumed that $\mu_1 < \mu \le \mu_c$, $\mu_2 = 0$, and $\mu_1 = P_1/K_0$.

For a Region 2 Type 2 fit, two distinct power fit sections are used. The pressure is defined as:

$$P_l = P_i + K_i\left(\mu - \mu_i\right) + K_{\alpha_i}\left(\mu - \mu_i\right)^{\alpha_i} \tag{3.43}$$

where $i = 1$ when $\mu_1 < \mu \le \mu_2$ and $i = 2$ when $\mu_2 < \mu \le \mu_c$. The other variables are as defined below:

$$K_{\alpha_1} = \frac{P_2 - P_1 - K_1\left(\mu_2 - \mu_1\right)}{\left(\mu_2 - \mu_1\right)^{\alpha_1}} \tag{3.44}$$

$$\alpha_1 = \frac{\left(\mu_2 - \mu_1\right)\left(K_2 - K_1\right)}{P_2 - P_1 - K_1\left(\mu_2 - \mu_1\right)} \tag{3.45}$$

$$K_{\alpha_2} = \frac{P_c - P_2 - K_2\left(\mu_c - \mu_2\right)}{\left(\mu_c - \mu_2\right)^{\alpha_2}} \tag{3.46}$$

$$\alpha_2 = \frac{\left(\mu_c - \mu_2\right)\left(K_c - K_2\right)}{P_c - P_2 - K_2\left(\mu_c - \mu_2\right)} \tag{3.47}$$

Note that with the Type 2 fit, it is assumed that $\mu_1 < \mu \le \mu_c$ and $\mu_1 < \mu_2 \ne 0$.

Finally, in Region 3 where $\mu > \mu_c$, a quadratic fit is used for the simple HEP model. The pressure is defined as:

$$P_l = P_c + K_c\left(\mu - \mu_c\right) + B\left(\mu - \mu_c\right)^2 \tag{3.48}$$

where B, μ_c, K_c, and P_c are considered material constants.

Unloading and reloading in the HEP model can be controlled through several options. In the elastic toe of Region 1, unloading and reloading both proceed along the same line as loading.

$$P_u = P_{rl} = K_0\mu \tag{3.49}$$

In Region 2 there are two options for unloading, linear unloading fans or parallel unloading toes. The unloading pressure if choosing nonlinear unloading, is defined as:

$$P_u = K_s\left(\mu - \mu_s\right) + K_\beta\left(\mu - \mu_s\right)^\beta \tag{3.50}$$

where:

$$K_\beta = \frac{P_{\max} - K_s\left(\mu_{\max} - \mu_s\right)}{\left(\mu_{\max} - \mu_1\right)^\beta} \tag{3.51}$$

and:

$$\beta = \frac{\left(\mu_{\max} - \mu_s\right)\left(K_t - K_s\right)}{P_{\max} - K_s\left(\mu_{\max} - \mu_s\right)} \tag{3.52}$$

where K_t is the initial unloading slope with value restricted so that it is greater than or equal to the slope of the virgin loading curve at $\mu_{\max}$. There are also two options for reloading in hysteretic part of Region 2. Option 1 is to match the unloading curve exactly.

Option 2 is to reload to a point between ($P_{\max}, \mu_{\max}$) and ($P_{\min}, \mu_{\min}$). The latter option results in the following expression for the reloading pressure.

$$P_r = P_{\min} + K_r \left(\mu - \mu_{\min} \right) \tag{3.53}$$

where:

$$K_r = \frac{P_{\max} - P_{\min}}{\mu_{\max} - \mu_{\min}} \tag{3.54}$$

and:

$$P_{\min} = P_u \left(\mu_{\min} \right) \tag{3.55}$$

Non-hysteretic unloading and reloading starts upon “full compaction”, that is once $\mu_{\max} > \mu_c$ and $\mu_r < \mu < \mu_c$. The unloading pressure following full compaction is defined as:

$$P_u = K_r \left(\mu - \mu_r \right) + K_\gamma \left(\mu - \mu_r \right)^\gamma \tag{3.56}$$

where:

$$K_\gamma = \frac{P_c - K_r \left(\mu_c - \mu_r \right)}{\left(\mu_c - \mu_r \right)^\gamma} \tag{3.57}$$

and:

$$\gamma = \frac{\left(\mu_c - \mu_r \right)\left(K_c - K_r \right)}{P_c - K_r \left(\mu_c - \mu_r \right)} \tag{3.58}$$

Note that when $\mu \geq \mu_c$, the unloading equations are identical to the loading equations, the region is non-hysteretic.

Deviatoric Behavior in the HEP Model

By comparison with the bulk response, the deviatoric response in the HEP model is rather simple. The HEP model uses an exponential failure surface and constant Poisson's ratios, ν_l for loading and ν_u for unloading. This is illustrated in Figure 0.5.

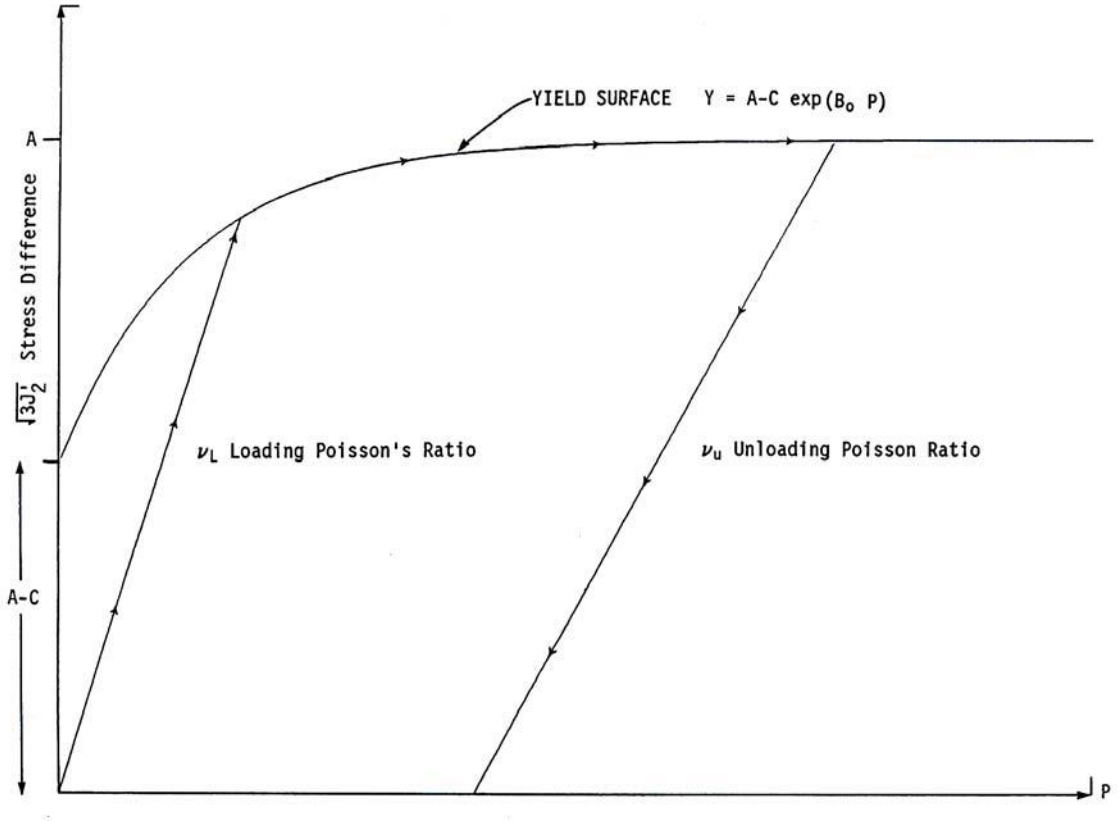

Figure 0.5: Simple HEP deviatoric behavior

The yield surface for the simple HEP (SHEP) model is defined as:

$$Y = A - C\,e^{B_0 P} \tag{3.59}$$

where A, C, and B_0 are constants and Y is in terms of the effective stress or principal stress difference q.

$$q = \sigma_1 - \sigma_3 = \sqrt{3J_2} \tag{3.60}$$

The shear modulus G is defined as:

$$G = \min\left[1.5B\frac{1-2\nu}{1+\nu}, G_{\max}\right] \tag{3.61}$$

where the local bulk modulus B is defined as:

$$B = (1-\mu)\frac{dP}{d\mu} \tag{3.62}$$

Statistical Ensemble Generation and Analysis

Chapter 2 introduced the concept of the statistical ensemble as it pertains to the current study. The section that follows describes the particulars of the integration of mesoscale modeling with the Discrete Element Method within the statistical ensemble formalism. The first part of the section describes the two different types of ensembles used in this study. The rest of the section describes the statistical tools used to quantify the results of the ensemble modeling, including parameter fitting, anomaly detection, and goodness of fit measurements.

Generation of Ab-Initio Realizations for Homogenization

As was previously mentioned, in the current study there are two types of ensembles. Each of these ensembles contains different, though similar realizations. In fact, it is possible, though not very likely, that one or more realizations in the first type is statistically identical to a realization in the second type of ensemble. What differs in the realizations of the second type of ensemble from the first is the starting conditions. The first ensemble is composed of realizations generated “from scratch” (ab-initio) using random sampling of the known Particle Size Distribution (PSD). Each of these Ab-Initio realizations contains the same finite number of particles confined to the same initial uniform isotropic stress. Thus, the ensemble of Ab-Initio mesoscale realizations is not representative of the effective mesoscale statistics of the homogenized medium. The second type of ensemble, presented

in the next section, is drawn directly from the RVE scale and as such is representative of the effective properties of the medium at the mesoscale. Rather, the Ab-Initio realizations are crucial to the determination of the size of the RVE. Ab-Initio realizations of increasing size are created and an ensemble of them used in mesoscale modeling until the Hill-Mandel condition is met. The window size at which the Hill-Condition is finally met, is considered to be the RVE. That realization, a model of the RVE with Discrete Elements, can then be partitioned and the resulting ensemble used for mesoscale effective property distributions of the constitutive behavior of the medium.

The Ab-Initio ensemble is created in four steps as follows.

Step 1 - a massive $1x10^{8}$ particle Discrete Element Model, henceforth called the "source model", is created using the "make cloud" method [137]. The use of the word "cloud" here refers to the fact that the total particle volume is a minuscule fraction of the bounding volume, on the order of $1x10^{-5}$ giving the particle model an effective porosity of greater than 99.999%. The "cloud" in Yade can be generated using several options, including a monodisperse, a polydisperse option with a normal distribution using only the mean and the standard deviation, or given a Particle Size Distribution in histogram format. The last option is used in this study, allowing the source model to mirror the PSD determined using sieve data. The version of "make cloud" used to build the source model in this study is a slightly modified version, with the interference checking (checking a particle is not placed where another already exists) of the main version of Yade disabled. This was done to make it possible to build such a massive DE model in a realistic amount of time, and because with the aforementioned porosity value interference is not an issue.

Step 2 - a random sampling algorithm is used to choose particles from the source model for the realizations required to build the ensembles. The random sampling algorithm used here is the "random choice" module of the NumPy (Numerical Python) library [124]. The random choice method chooses n integers at random from the set of positive integers less than or equal to the size of the source model ($1x10^8$). Here n is the size of the realization for the particular ensemble size. In the mesoscale modeling carried out in this study, ab-initio ensembles consist of realizations of $n=1x10^3$, $n=1x10^4$, $n=1x10^5$, $n=1x10^6$, and $n=5x10^6$ particles. The integer chosen by the sampling algorithm represents a particle index number from the source model. To ensure randomness, particles may be chosen more than once by setting the "Replace" parameter in the random choice method to "True".

Step 3 - each realization DEM is gradually confined to a prescribed average isotropic stress. This is done using the "virtual wall" approach common to most Discrete Element packages and not using the novel surface tracking micromechanical boundaries implemented and described in Chapter 4. The virtual wall approach essentially uses bounding planes to restrict the particles from moving outside the bounded volume. The reason for using this bounding box approach for this step is twofold. First, this approach is robust and computationally very efficient due to the use of so-called "internal compaction". Internal compaction refers to the fact that confinement is not imposed by moving the boundaries, but rather by uniformly and gradually increasing the particle sizes [138]. The second reason for using the bounding box approach in this step, is to create mesoscale models that resemble the continuum mechanical concept of "infinitesimal point or element". This is important because the use of the Cauchy stress tensor as well as deformation gradient carries the underlying assumption of Cartesian geometry. Furthermore, computing ensemble

response results is simpler when the cardinal directions are orthogonal to the principal directions.

Figure 0.6 shows four typical $1x10^4$ particle ab-initio realizations used in the Eglin sand mesoscale modeling carried out in this study.

Figure 0.6 shows these mesoscale realizations as they are confined from the “cloud” state with a porosity of almost unity to an average wall isotropic confinement stress of 5 MPa.

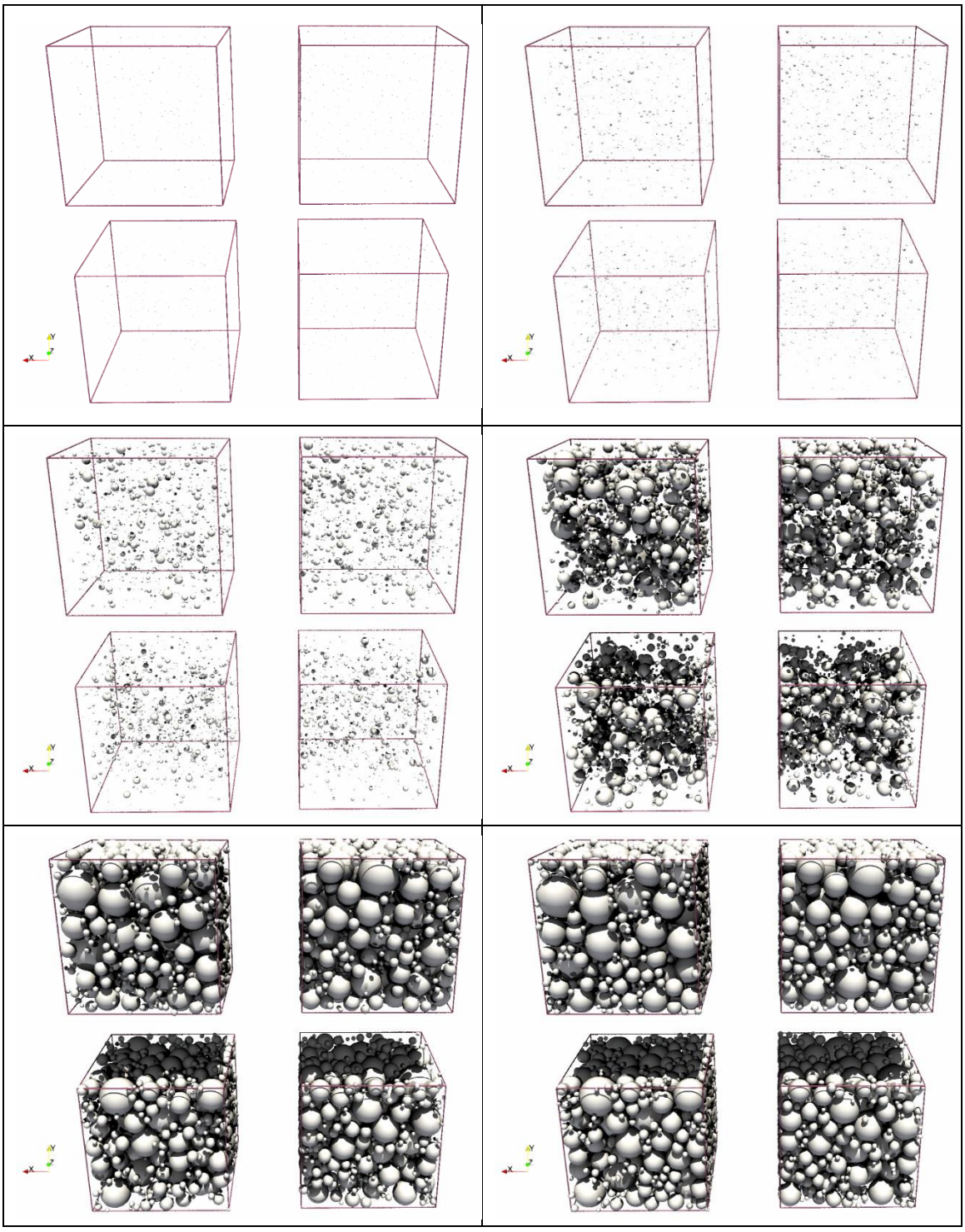

Figure 0.6: Four typical $1x10^4$ particle ab-initio realizations confined to average isotropic stress of 5 MPa in a "bounding box"

Step 4 – each realization is loaded to a uniform isotropic stress using the novel micromechanical boundary described in Chapter 4. First, the typical DEM virtual walls are removed, then the stress tensor $\boldsymbol{\sigma}$ is applied to the realization defined as:

$$\boldsymbol{\sigma} = \sigma_c \mathbf{I} \tag{3.63}$$

where σ_c is the confinement level desired, while $\mathbf{I}$ is the identity tensor. Note that σ_c here is the same as the average isotropic stress imposed in Step 3. When uniform stress is first applied to a realization model, there is a lot of acceleration of boundary particles as the force applied by the virtual walls is typically very different from the force applied when uniform stress is applied using the micromechanical boundaries. To avoid excessive inertial effects in these realization, adaptive damping is applied that forces the average velocity gradient below a certain value as described earlier in the "Quasi-Static Modeling" section of this chapter.

Figure 0.7 shows the same four typical $1x10^4$ particle ab-initio realizations from Figure 0.6 as the virtual walls in the simulation are removed and replaced with the LaGuerre-Voronoi diagrams. The realizations then are gradually loaded to a micromechanical uniform isotropic confinement stress of 5 MPa.

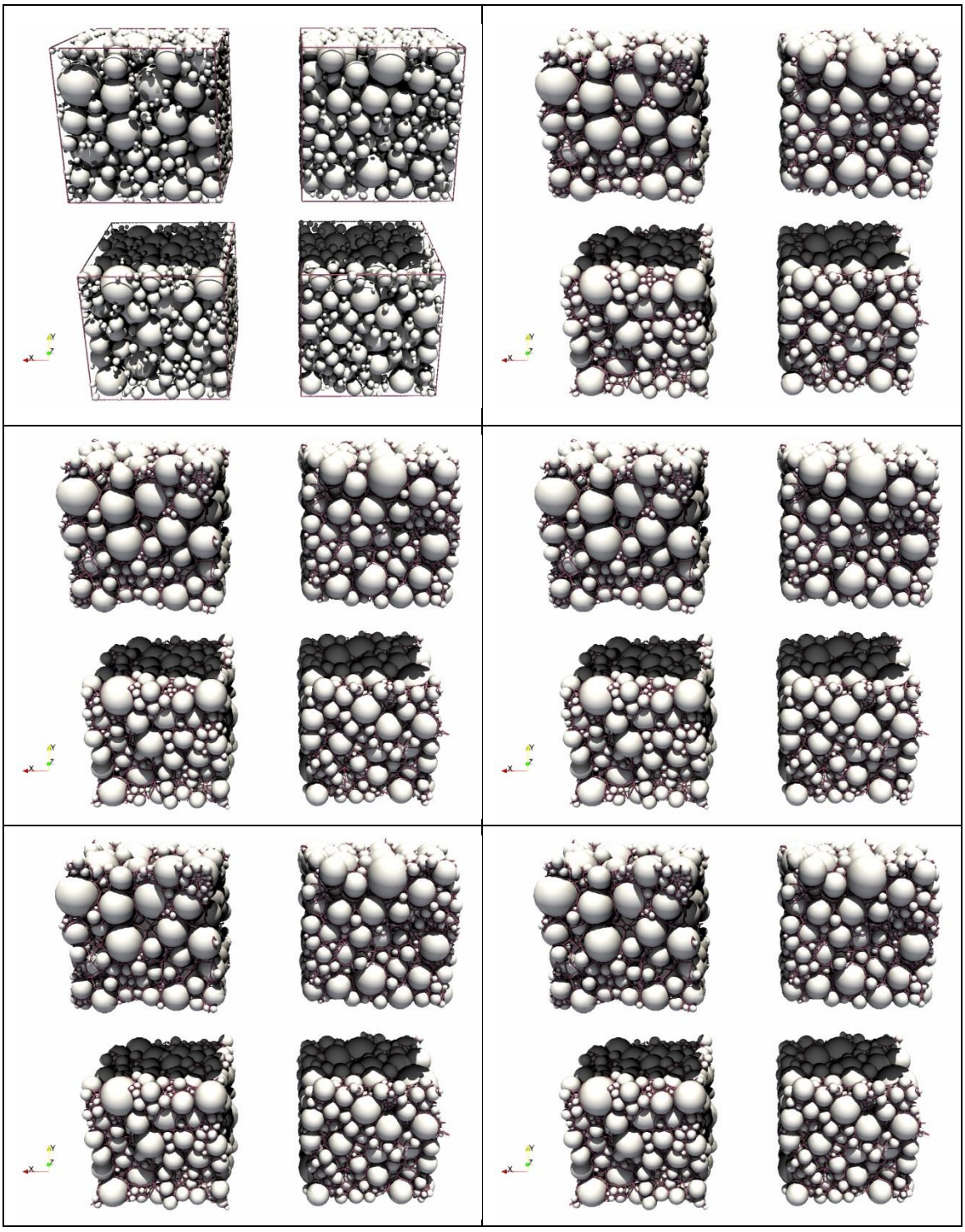

Figure 0.7: Four typical $1x10^4$ particle ab-initio realizations gradually confined to a uniform isotropic micro-stress of 5MPa

Iterative Domain Partitioning for Propagation of Uncertainty

Mesoscale bounds of effective particulate aggregate properties were discussed in Chapter 2, as was propagation of uncertainty at the mesoscale. One of the main objectives of the current study is to use mesoscale models to quantify uncertainty associated with modeling particulate media at scales comparable to the size of the RVE, including scales smaller than the RVE. For particulate media this is not simply a matter of academic and scientific de rigueur. Finite Element meshes of concrete, gravel, sand, rock etc. cannot be expected to have elements whose size is always greater than the RVE. When the element size is smaller than the RVE it is of course necessary to account for the non-determinism present in the system.

The first type of ensemble in this study, the ensemble composed of ab-initio realization, is not representative of the homogenized medium and therefore unsuitable for propagation of uncertainty. What is required is a different ensemble, an ensemble composed of realizations drawn from the homogenized medium, the RVE. This second type of ensemble is constructed in the current study using "iterative domain partitioning" in the sense of Huet [139-143]. Iterative domain partitioning for mesoscale bounds consists of dividing the RVE into increasingly smaller subdomains that can be used as realizations for ensemble averaging. Ostoja-Starzewski showed that these "partition realizations" need not be commensurate [8], so that the number of realizations that can be drawn from the RVE is not restricted. Notwithstanding the latter point, the current study uses commensurate partition realizations, as these can be readily drawn from the RVE using an existing approach, domain decomposition for distributed memory parallel computations with Message Passing Interface (MPI). MPI parallel computation capability is, as of the publication of this study,

still in the process of being implemented in Yade [144]. However, the domain decomposition capability is robust and was adapted for domain partitioning with minor modifications required.

The results of domain partitioning are illustrated in Figure 0.8 and Figure 0.9. A particle DE model is partitioned into a grid of 8x8x8 subdomains in Figure 0.8 and a grid of 17x17x17 subdomains in Figure 0.9 .

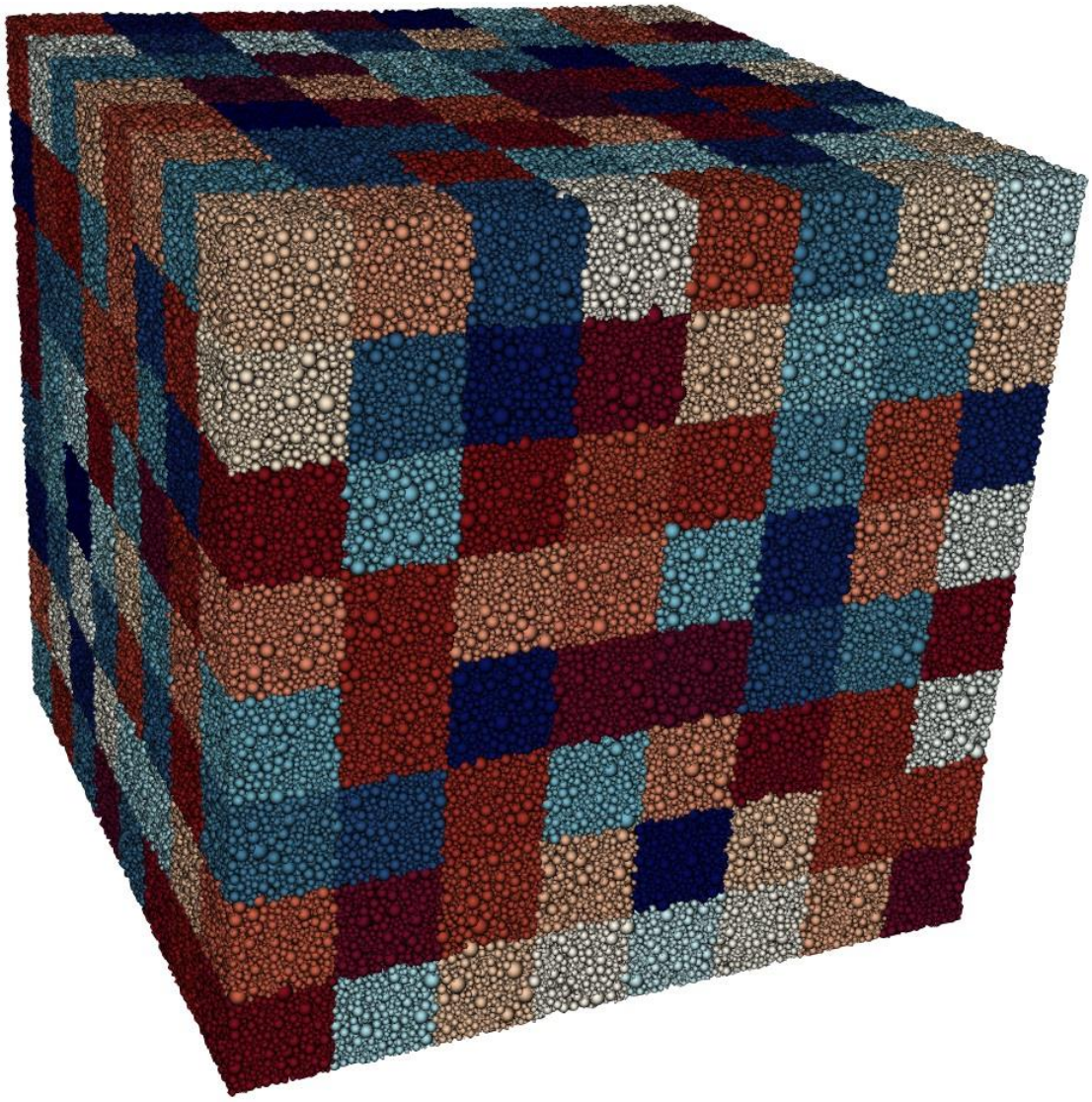

Figure 0.8: RVE-sized $5x10^6$ particle Discrete Element model decomposed into a grid of 8x8x8 subdomains

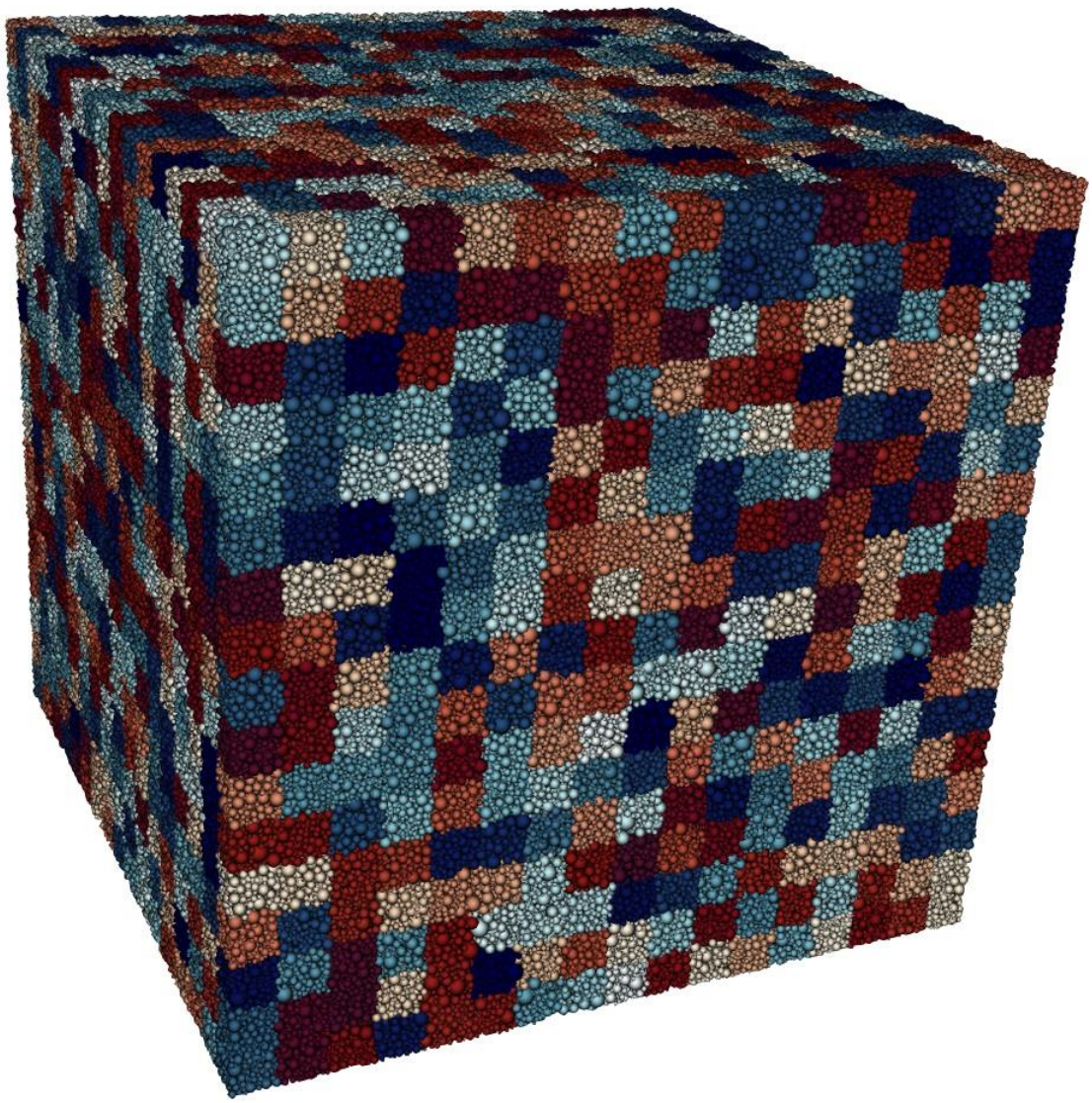

Figure 0.9: RVE-sized $5x10^6$ particle Discrete Element model decomposed into a grid of 17x17x17 subdomains

Anomaly Detection with Grubbs Test for Outliers

One of the difficulties with carrying out large numbers of simulations, such as in the context of statistical ensembles, is that it is virtually impossible to check each simulation to verify its results. If a handful of realizations in an ensemble of hundreds produce anomalous results, they can skew the ensemble averages and lead to erroneous conclusions.

Fortunately, there is a relatively easy to implement test that can detect and filter outliers in statistical data. This the well-known the Grubbs' Test for Outliers [145, 146].

Grubbs' test is also known as the maximum normed residual test. Grubbs' test is used to detect a single outlier in a univariate data set that follows an approximately normal distribution. This outlier is expunged from the dataset and the test is iterated until no outliers are detected.

Grubbs's test is defined for the hypothesis:

- Null: There are no outliers in the data set
- Alternative: There is exactly one outlier in the data set

The Grubbs test statistic is defined as:

$$G = \frac{\max_{i=1,\ldots,N} \left| Y_i - \bar{Y} \right|}{s} \tag{3.64}$$

with Y and s denoting the sample mean and standard deviation, respectively. The Grubbs test statistic is the largest absolute deviation from the sample mean in units of the sample standard deviation.

This is the two-sided version of the test. The Grubbs test can also be defined as a one-sided test. To test whether the minimum value is an outlier, the test statistic is

$$G = \frac{\bar{Y} - Y_{\min}}{s} \tag{3.65}$$

with Y_{min} denoting the minimum value. To test whether the maximum value is an outlier, the test statistic is

$$G = \frac{Y_{\max} - \bar{Y}}{s} \tag{3.66}$$

with Y_{max} denoting the maximum value.

For the two-sided test, the hypothesis of no outliers is rejected at significance level α if

$$G > \frac{N-1}{\sqrt{N}} \sqrt{\frac{t^2_{\alpha/(2N),N-2}}{N-2+t^2_{\alpha/(2N),N-2}}} \tag{3.67}$$

with $t_{\alpha/(2N),N-2}$ denoting the upper critical value of the t-distribution with N − 2 degrees of freedom and a significance level of α/(2N). For the one-sided tests, α/(2N) is replaced with α/N.

Weibull Distribution Fitting of Results

The Weibull distribution is a continuous probability distribution named after Swedish mathematician Waloddi Weibull. He originally proposed the distribution as a model for material breaking strength, but recognized the potential of the distribution in his 1951 paper A Statistical Distribution Function of Wide Applicability [123]. Today, it's commonly used to assess product reliability, analyze life data and model failure times.

Although it is named after Weibull, who described it in detail, the distribution was first identified by Fréchet [147]. It's first application came shortly after that, by Rosin and Rammler [148], in describing a Particle Size Distribution (PSD). In fact, this application is the basis of much of the numerical work described in later chapters of this manuscript. The Weibull distribution was used to describe some of the experimental data used in the mesoscale ensembles here, including the particle size distribution, Young's moduli of sand grains, and the crushing strength of sand grains. It stands to reason then, that the ensemble results of mesoscale simulations are fitted to Weibull distributions.

The probability density function of a Weibull random variable is:

$$f(x;\lambda,k)=\begin{cases}\frac{k}{\lambda}\left(\frac{x}{\lambda}\right)^{k-1}e^{-(x/\lambda)^k} & x\geq 0,\\ 0 & x<0,\end{cases} \tag{3.68}$$

where k > 0 is the shape parameter and λ > 0 is the scale parameter of the distribution. Its complementary cumulative distribution function is a stretched exponential function. The Weibull distribution is related to a number of other probability distributions; in particular, it interpolates between the exponential distribution (k = 1) and the Rayleigh distribution (k = 2 and $\lambda=\sqrt{2}\sigma$).

In engineering mechanics, the shape parameter k of a distribution of strengths is known as the Weibull modulus.

Wasserstein Metric of Statistical Distance

In statistics, the Wasserstein distance, also known as the earth mover's distance (EMD), is a metric of the difference between two probability distribution functions over a region. The EMD moniker comes from an informal interpretation of the histograms as piles of dirt, and the metric as the work required to change one pile into the other. The "work" here is measured as dimensionless amount multiplied by distance. A more detailed definition follows.

A statistical distribution may be represented by a set of clusters, known as a signature. Instead of assigning a distribution to a set of points in $\mathbb{R}^d$, they can be clustered and the point set can be represented in terms of the clusters. Each cluster is then a single point in $\mathbb{R}^d$ while the fraction of the distribution present in that cluster represents the weight of the cluster. The problem to solve here then, is transforming one signature P to another Q with minimum work.

Assuming signature P has m clusters, while Q has n clusters, the signatures can be represented as:

$$\begin{aligned} P &= \{(p_1, w_{p1}), (p_2, w_{p2}), ..., (p_m, w_{pm})\} \\ Q &= \{(q_1, w_{q1}), (q_2, w_{q2}), ..., (q_n, w_{qn})\} \end{aligned} \tag{3.69}$$

where (p_i, q_i) are the cluster representatives and (w_{pi}, w_{qi}) are the weights of the clusters.

The objective here is to solve the transportation problem of finding the flow between p_i and q_j that minimizes the overall cost. This problem is expressed below:

$$F = \min \sum_{i=1}^{m} \sum_{j=1}^{n} f_{i,j} d_{i,j} \tag{3.70}$$

subject to the constraints below:

$$\begin{aligned} & f_{i,j} \geq 0, 1 \leq i \leq m, 1 \leq j \leq n \\ & \sum_{j=1}^{n} f_{i,j} \leq w_{pi}, 1 \leq i \leq m \\ & \sum_{i=1}^{m} f_{i,j} \leq w_{qj}, 1 \leq j \leq m \\ & \sum_{i=1}^{m} \sum_{j=1}^{n} f_{i,j} = \min \left\{ \sum_{i=1}^{m} w_{pi}, \sum_{j=1}^{n} w_{qj} \right\} \end{aligned} \tag{3.71}$$

Hence, the Wasserstein distance is defined as the work normalized by the total flow:

$$EMD(P, Q) = \frac{\sum_{i=1}^{m} \sum_{j=1}^{n} f_{i,j} d_{i,j}}{\sum_{i=1}^{m} \sum_{j=1}^{n} f_{i,j}} \tag{3.72}$$

Mathematical Optimization Algorithms

In Chapter 2 the basic concepts of mathematical optimization were introduced. This section goes into more detail on the specific optimization algorithms used in the current study. There are two algorithms used here and they are both derivative-free, global

optimization methods. In fact, they are both genetic algorithms, which is a type of evolutionary algorithm. The Single-Objective Genetic Algorithm (SOGA) is used to calibrate individual constitutive parameter values in the continuum model to specific Discrete Element ensemble simulations. Thus, in the first stage of calibration the bulk moduli are calibrated to isotropic simulations, while the shear moduli are calibrated to deviatoric simulations. Then, in the second stage the whole parameter space is calibrated to all the available ensemble simulations at once using the Multi-Objective Genetic Algorithm. This ensures the parameters of the FEA model are the best fit to the mesoscale ensemble results.

Single Objective Genetic Algorithm

The aim of genetic algorithms is to emulate the behavior of biological genetics using mathematical operations that model the mechanics of genes. These mathematical operations are typically far less complex than some of the other mathematics used in this study. The power of the genetic algorithms does not come from sophisticated math, rather from simple, easily programmable, random exchanging of number locations in a sequence. In fact, the relevant mathematical operations of genetic algorithms are based on the mechanics of the three basic genetic operations: reproduction, crossover, and mutation.

Here, a search problem is used to explain the way genetic algorithms work. The first step in a search problem would be to use bit strings as representatives of the variable combinations possible. The bit strings here are used as the computational facsimile of chromosomes. Then, a loss function is used to measure how well a specific combination of "chromosomes" does in the search. For a minimization problem, this can be expressed as

$$\min imize \qquad f(x), \qquad x = \{x_1, x_2, x_3, x_4\} \tag{3.73}$$

Here, the variables can be represented as a sequence of bits (bit string), as shown below.

$$\underset{x_1}{1011}\quad \underset{x_2}{11}\quad \underset{x_3}{101}\quad \underset{x_4}{0110} \tag{3.74}$$

The decimal equivalents of the bit strings here are $x_1 = 11$, $x_2 = 3$, $x_3 = 5$, $x_4 = 6$. The ranges for these bit strings are $\{15 \le x_1 \le 0\}$, $\{3 \le x_2 \le 0\}$, $\{7 \le x_3 \le 0\}$, $\{15 \le x_4 \le 0\}$. The bit string representation shown here represents the source of genetic algorithm "magic". Moving from the discrete variables of search algorithms, to the continuous variable space, a population of bit strings emulating chromosomes can capture global solutions. This happens because many points that are possibly local extrema remain in the "gene" pool, so the solution does not get stuck at one of these points.

An optimization using a genetic algorithm proceeds as follows:

1. The population size is chosen, and the variables are assigned random values that correspond to their random bit strings.
2. Reproduction of the population occurs, whereby bit strings with low loss function values are used to form the next "generation" of the variable population. This may be viewed as a computational representation of survival of the fittest.
3. Members of the new generation are paired off randomly. This is done by generating two new "offspring" bit strings from the "parent" bit strings through a random combinatorial process [149].
4. Another genetic concept used in the algorithm is mutation. The reproduction step can yield a new generation with multiple copies of a bit string, or even an entire population of the same string. The mutation step aims to prevent this pitfall by changing a random bit's value in the string [150].

Multi-Objective Genetic Algorithm

Multi-objective optimization means that there are two or more objective functions that need to be optimized simultaneously. Often these are conflicting objectives, such as cost and performance. The answer to a multi-objective problem is usually not a single point. Rather, it is a set of points called the Pareto front. Each point on the Pareto front satisfies the Pareto optimality criterion, which is stated as follows: a feasible vector $\mathbf{X}$ is Pareto optimal if there exists no other feasible vector $\mathbf{X}$ which would improve some objective without causing a simultaneous worsening in at least one other objective. The multi-objective optimization problem can be expressed as:

$$min(f_1(x), f_2(x), \ldots, f_k(x)) \quad x \in X \tag{3.75}$$

where the number of objectives k is at least 2, and $\mathbf{X}$ is the set of feasible decision vectors. The objective function here is vector-valued, and can be defined as:

$$f : X \to \mathbb{R}^k, f(x) = (f_1(x), \ldots, f_k(x))^T \tag{3.76}$$

If a feasible point x^* exists that can be improved on one or more objectives simultaneously, it is not Pareto optimal: it is said to be "dominated" and the points along the Pareto front are said to be "non-dominated." Conversely, the solution $x^* \in X$ and its respective outcome $f(x^*)$ is called Pareto optimal if there does not exist another solution that dominates it. The set of Pareto optimal outcomes is called the Pareto front, Pareto frontier, or Pareto boundary.

CHAPTER 4

MICRO-MECHANICAL BOUNDING OF PARTICLE AGGREGATES

This chapter describes how boundary conditions are typically implemented in particle-based simulations, then introduces a new method for modeling, loading, and quantifying the stress and deformation characteristics of particle aggregates. This method was developed specifically for this study; however, it does fill a known gap in boundary modeling for the broader class of particle-based simulations. As such, it may well have applicability beyond the Discrete Element Method, to other particle-based methods.

A Line in the Sand – Boundaries of Particle Aggregates

In Continuum Mechanics, there are two classical types of boundary conditions: (1) the displacement boundary condition, also known a homogeneous deformation boundary condition, and (2) the traction boundary condition, also known as a uniform stress boundary. These boundaries arise from analogous boundary conditions in Differential Equations; the displacement boundary is the continuum mechanics application of the Dirichlet boundary condition, while the traction boundary is the continuum mechanics application of the Neumann boundary condition. From these classical boundary conditions, two more types of boundary conditions may be defined: mixed orthogonal boundaries, and periodic boundaries. Many authors refer to either, or both, of these boundaries as a third or fourth type of "classical" boundary, and they may certainly be viewed as such. However, in the context of this study, there are two "classical boundaries", those that provide bounds on the response of the medium: the displacement boundary and the traction boundary. The

responses of mixed orthogonal boundaries and periodic boundaries are expected to fall somewhere between the response of those two bounds.

These classical boundary conditions are readily implemented in discretization-based continuum simulation methods such as Finite Element Analysis (FEA). In FEA the Dirichlet boundary is imposed when the final displacement is specified for static models, or when the velocity at the boundary is specified for dynamic models. The Neumann boundary is imposed in FEA by specifying a “pressure” or, more generally, a “stress” on element edges, which is then applied as a prescribed force on the boundary nodes. Similarly, for Finite Difference Analysis, or the Finite Volume Method (FVM), the Dirichlet boundary can be imposed as a flux value at the boundaries. The Neumann boundary condition can be approximated in FVM using extrapolation, or more commonly, using “ghost cells” meant to approximate a flux derivative at the boundary.

In particle methods with discrete bodies, such as the Discrete Element Method, these boundaries have heretofore not been rigorously implemented. Instead of applying the classical boundary conditions from Differential Equations, the discretized forms of the boundaries from Finite Elements have been approximated using particles of infinite radii as boundary “walls”. The positions of these walls in DEM codes are adjusted using either a constant velocity, or some type of numerical servo-like control. Prescribing a constant velocity on the walls is typically used to simulate a “strain rate”, while numerical servo-control is typically used to achieve an average “stress”.

For the majority of applications of the Discrete Element Method in the literature thus far, these approximations of boundary conditions are quite reasonable and sufficient. This is because DEM is typically used as a macro-scale simulation method, rather than as

a micro-scale method within a hierarchical multiscale homogenization framework. The latter requires that upper and lower response bounds be considered, which dictates that the Dirichlet and Neumann boundaries must be implemented.

This last point has been recognized by several other authors in recent years. Dettmar [151] and later Miehe et al [152] implemented micro-mechanical boundaries for Discrete Elements using a penalty method, whereby those particles designated as "boundary particles" receive increasing forces and moments if the boundary conditions are "violated". Liu et al [153] applied micro-mechanical boundaries for 2D Discrete Elements by implementing a servo-control mechanism at each "boundary particle", with special treatment given to "corner particles". A significant limitation of both these approaches is the need for special and permanent designation of "boundary particles".

In fact, if the special designation approach is used for the 3D case, there is a need to partition the particle aggregate domain into four non-alterable particle subdomains: 1) interior particles, 2) single boundary particles, 3) dual boundary or edge boundary particles, and 4) triple boundary or corner boundary particles. This limits the utility of the approach, since particles that are interior particles at the start cannot become boundary particles, nor can single boundary particles become multi-boundary particles or vice-versa. Furthermore, and perhaps most importantly, this approach limits the range of deformation that can be modeled. Finite strains, as opposed to small strains, result in considerable changes in the material structure. These cannot be adequately modeled with a static boundary, since the boundary is an intrinsic part of the material structure. In many geotechnical applications, the assumption of small strains may be reasonable, however this is not so with the finite strain applications typically modeled using hydrocodes. Therefore, the need for a 3D

implementation of micro-mechanical boundaries in the Discrete Element Method is quite clear.

A Novel Approach to Particle Aggregate Boundaries

In the section that follows, a novel approach to micro-mechanical boundary modeling is introduced and described. The approach uses three-dimensional surface reconstruction with weighted alpha shapes to demarcate the boundaries of discrete particle aggregates. Additionally, the reconstructed boundary is partitioned using modified alpha shape weights to construct LaGuerre-Voronoi Diagrams on a model's surface.

Voronoi Diagrams and Delaunay Triangulations

A review of the Voronoi Diagram of points in the Euclidian sense and its dual, the Delaunay Triangulation is in order for a proper introduction to alpha-shapes and Laguerre Diagrams. Both Euclidian and Laguerre diagrams are considered "affine diagrams". Let $\mathcal{P} = \{p_1, \ldots, p_n\}$ be a set of points of $\mathbb{R}^d$. To each p_i is associated its Voronoi region $V(p_i)$

$$V(p_i) = \left\{ x \in \mathbb{R}^d : \|x - p_i\| \leq \|x - p_j\|, \forall j \leq n \right\} \tag{4.1}$$

The region $V(p_i)$ is the intersection of n-1 half-spaces. Each such half-space contains p_i and is bounded by the bisector of p_i and some other point of $\mathcal{P}$. Since the bisectors are hyperplanes, $V(p_i)$ is a convex polyhedron and need not be bounded.

The Euclidean Voronoi diagram of $\mathcal{P}$, denoted here as $Vor(\mathcal{P})$, is the cell complex whose cells are the Voronoi regions and their faces. Equivalently, the Euclidean Voronoi diagram of $\mathcal{P}$ can be defined as the minimization diagram of the distance functions $\delta_i, \ldots, \delta_n$, where

$$\delta_i(x) = \|x - p_i\| \tag{4.2}$$

Another way to describe the Voronoi diagram is in procedural terms. Let each point in the point set is a “generator” point P_k generating a Voronoi polygon R_k. The generator point P_1 generates cell R_1, point P_2 generates polygon R_2 and so on. Then, as noted in [154] "all locations in the Voronoi polygon are closer to the generator point of that polygon than any other generator point in the Voronoi diagram in Euclidean plane". This definition is illustrated in Figure 0.1, where the Voronoi polygon generated by each point can be clearly discerned.

Next, it is important to assert the graph theory concept of a “dual graph”. Consider two cell complexes V and D. Each complex may be considered as the dual of the other if there is an involutive relationship between the faces of V and the faces of D such that the inclusions are reversed. That is to say that for any two faces f and g of V, their dual faces f^* and g^* satisfy Equation (4.3)

$$f \subset g \Rightarrow g^* \subset f^* \tag{4.3}$$

This may also be interpreted asserting that D is a graph that has a vertex for each face of V. The dual graph D has an edge whenever two faces of V are separated from each other by an edge, and a self-loop when the same face appears on both sides of an edge. Thus, each edge e of V has a corresponding dual edge, whose endpoints are the dual vertices corresponding to the faces on either side of e.

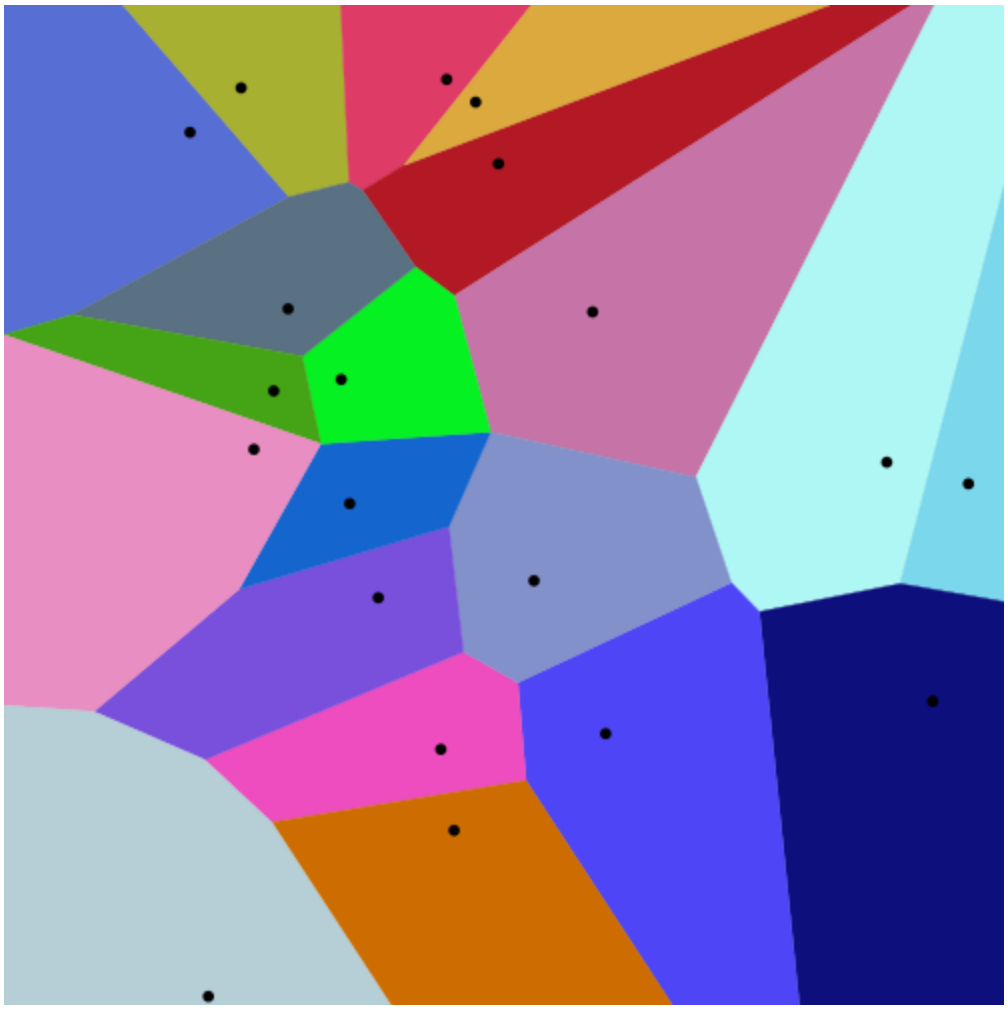

Figure 0.1: A set of 20 points and their Voronoi polygons (https://commons.wikimedia.org/wiki/File:Euclidean_Voronoi_diagram.svg)

The dual graph of the Voronoi graph is the **Delaunay triangulation** of a point set. The triangulation is also most concisely defined using its dual relation to the Voronoi graph. Again, let $\mathcal{P} = \{p_1, \ldots, p_n\}$ be a set of points of $\mathbb{R}^d$ and let f be a face of $Vor(\mathcal{P})$. Any point inside face f can be shown to have the exact same subset $\mathcal{P}_f$ of closest points from $\mathcal{P}$. Next consider that the dual of face f according to the definition provided in the preceding paragraph has to be a face defined by the subset $\mathcal{P}_f$, specifically its convex hull.

$Del(\mathcal{P})$, the Delaunay triangulation of $\mathcal{P}$ is simply the cell complex consisting of all the dual faces defined by the convex hulls of each and every closest point subset in $Vor(\mathcal{P})$. Because points of $\mathcal{P}$ are assumed to be in general position, all the faces of $Del(\mathcal{P})$ are simplices and $Del(\mathcal{P})$ is a simplicial complex. Common algorithms for finding the Delaunay triangulation of a point set include flip algorithms [155], incremental algorithms [156, 157], divide-and-conquer [158, 159], and sweephull [160].

Surface Reconstruction with Alpha-Shapes

The definition of a boundary for free-floating particles in space, also known as a "point cloud", requires some sort of surface reconstruction algorithm. Serendipitously, surface reconstruction from point clouds has been an area of intensive research and progress in recent years. This has been spurred by rapid developments in 3D scanning and photogrammetry. There are several approaches used to extract an exterior surface from a point cloud. These can be divided into three broad categories: explicit surface reconstruction techniques, implicit surface reconstruction techniques, and computer vision techniques. Two types of explicit reconstruction techniques are Parametric Surface fitting such as B-splines and NURBS, and Triangulated Surfaces using Delaunay Triangulation and Voronoi Diagrams. Implicit surface reconstruction techniques include: the Least Square Method, Poisson Reconstruction, the Partial Differential Equation (PDE) Method, and the Level Set Method. The two classical Computer Vision Techniques are Shape-from-Shading (SFS) and Photometric Stereo (PMS).

The surface reconstruction method used here is a method based on the concept of alpha-shapes, introduced and developed by Edelsbrunner et al. [161] [162]. The alpha-shape technique relies upon triangulation of surfaces through Delaunay Triangulation and

its dual, the Voronoi Diagram. The alpha-shape technique may be considered a generalization of the concept of a “convex hull”, which is the smallest convex set that contains all points of interest in a Euclidian plane. For the 2-dimensional case, the alpha-shape concept may be described using a disk of radius $1/\alpha$ as follows:

- If $\alpha = 0$, it is a closed half-plane (convex hull)
- If $\alpha > 0$, it is closed disk of radius $1/\alpha$
- If $\alpha < 0$, it is the closure of the complement of a disk of radius $-1/\alpha$

While this a simple idea on its surface, it is a concept that can enable surface reconstruction of complex shapes. Consider the point cloud shown in Figure 0.2. The leftmost illustration shows the result of boundary reconstruction using the convex hull approach, while the middle illustration shows what is possible using the alpha-shape approach.

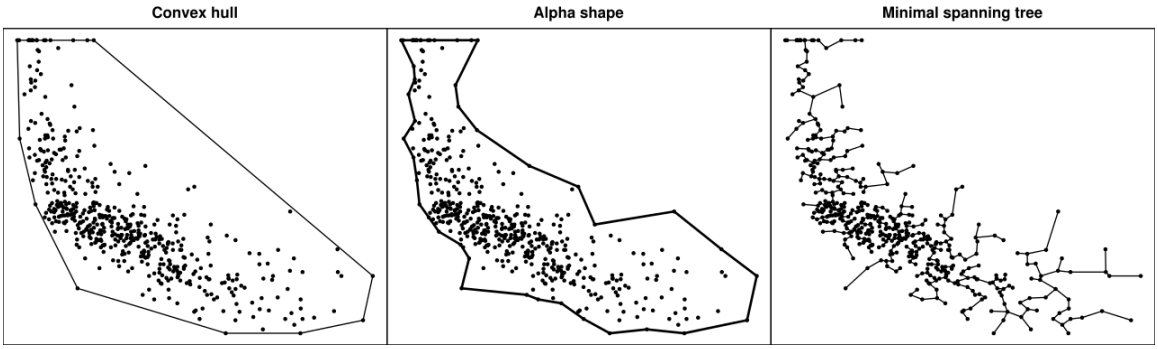

Figure 0.2: Alpha-shape reconstruction of a 2D point set boundary

A sublime intuitive visualization of the technique was offered in that original paper by Edelsbrunner's and Mucke [161]. The α-shape may be conceived of as a huge mass of ice-cream making up the space $\mathbb{R}^d$ and containing the points S as harder pieces, perhaps nuts, chocolate, or cookie dough. Using an ice-cream spoon with a spherical hollow, it is possible to carve out all parts of the ice-cream block that may be reached without bumping into the hard pieces, thereby even carving out holes in the inside (e.g. parts not reachable

by simply moving the spoon from the outside). This process will eventually result in an object bounded by caps, arcs and points. If, instead, all these “round" faces are straightened to triangles and line segments, the resulting mass of ice-cream and pieces represents an intuitive description of what is called the α-shape of S. An example for this process in 2D is shown in Figure 0.3 (where the ice-cream spoon is “flattened” and is simply a circle):

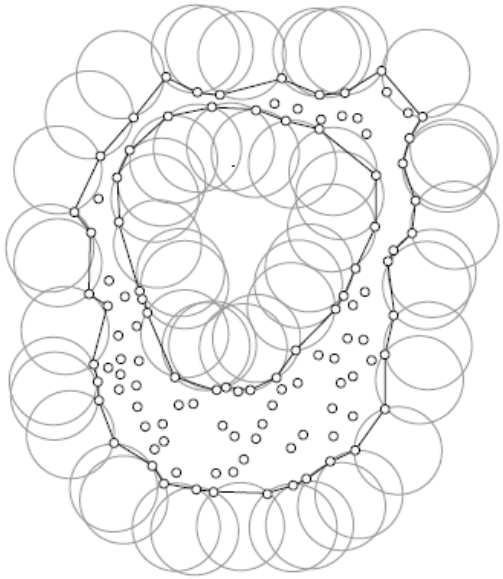

Figure 0.3: Alpha-shape reconstruction of a 2D point set boundary

Figure 0.3 makes it trivial to understand what the α of an α-shape is, it is merely the radius of the concave cavity used to carve the domain around a point set. Notice that all the circles in Figure 0.3 are the same size.

Having described the technique in broad terms and physical metaphors, a more technical and succinct definition follows.

First, consider a set of points $\mathcal{S}$ in $\mathbb{R}^d$ in general position. Here “general position” is a computational geometry term that refers to the genericity of the set of points, which distinguishes it from certain special circumstances. In the current context, general

position implies that no 4 points of $\mathcal{S}$ lie on a common plane, and no 5 points lie on the surface of a common sphere. The Delaunay triangulation of the pointset $\mathcal{S}$ is $DT(\mathcal{S})$.

Next, consider a sphere (or circle for 2D) of radius α. A simplex Δ is designated as α-exposed if there exists such a sphere that is empty. This is also known as an empty circumsphere. A circumsphere of a simplex in $DT(\mathcal{S})$ is a sphere passing through the vertices of this simplex. A circumsphere is said to be empty if it encloses no vertex of the triangulation $DT(\mathcal{S})$.

One additional concept must be introduced to properly explain the alpha-shape of $\mathcal{S}$, the alpha-complex. The alpha-complex $AC(\mathcal{S},\alpha)$ includes all Delaunay simplices which have an empty circumsphere with square radius not bigger than α. Let Δ_T be a simplex of $DT(\mathcal{S})$ with a circumsphere of radius σ_T centered at μ_T. For the point set $\mathcal{S}$, the alpha-complex $\mathcal{C}_\alpha(\mathcal{S})$ of $\mathcal{S}$ is the simplicial subcomplex that meets the following criterion.

A simplex Δ_T is in $\mathcal{C}_\alpha(\mathcal{S})$ if and only if it meets either of the conditions below:

- $\sigma_T < \alpha$ and the circumsphere is empty
- Δ_T is a face of another simplex in $\mathcal{C}_\alpha(\mathcal{S})$.

The alpha-shape is just the domain covered by simplices of the alpha-complex. It should be noted at this point that the alpha-complex and the shape it describes, bounds only the centers of the boundary particles. If it is desired to bound the particles themselves, this must be done through some additional computational geometry “magic”. In

this work, the "magic" takes the form of LaGuerre-Voronoi Diagrams, also known as Power Diagrams

LaGuerre-Voronoi Diagrams on Particle Aggregate Boundaries

Laguerre-Voronoi diagrams, also known as power diagrams in the literature are fundamentally constructions similar to the Euclidean Voronoi diagrams of points and their dual Delaunay triangulations. The main difference lies in replacing the point set $\mathcal{P}$ with a set of hyperspheres $\mathcal{S}$. "Hyperspheres" here implies circles in 2 dimensions and spheres in 3 dimensions. The distance function of a point x to a hypersphere σ is referred to as the "power" of x to σ, which is the source of one of the names of its eponymous diagram. The power of a point x to hypersphere σ with center c and radius r is defined as:

$$\sigma(x) = (x-c)^2 - r^2 \tag{4.4}$$

Let $\mathcal{S} = \{\sigma_1, \ldots, \sigma_n\}$ be a set of hyperspheres in $\mathbb{R}^d$. The hyperspheres of $\mathcal{S}$ have centers c_i, radii r_i, and power functions $\sigma_i(x) = (x-c_i)^2 - r_i^2$. As for the Voronoi case, consider a region within $\mathbb{R}^d$ consisting of all points with power to σ_i smaller than or equal to their power to the other hyperspheres in $\mathcal{S}$. Denoting this region $Pow(\sigma_i)$

$$Pow(\sigma_i) = \{x \in \mathbb{R}^d : \sigma_i(x) \le \sigma_j(x), 1 \le j \le n\} \tag{4.5}$$

There is a set of points that has equal powers to the hyperspheres σ_i and σ_j. This set of points defines a hyperplane π_{ij}. This hyperplane is orthogonal to a line joining c_i to c_j and is called the "radical hyperplane" of σ_i and σ_j. This radical hyperplane partitions $\mathbb{R}^d$ into two half-spaces, with half-space π_{ij}^i belonging to hypersphere σ_i and consisting

of all points whose power to σ_i is smaller than their power to σ_j. The region $Pow(\sigma_i)$ is a convex polyhedron consisting of the intersection of all π_{ij}^i, where $i \neq j$.

From the above definition, it follows that there is a cell complex consisting of cells which are the power regions of $\mathcal{S}$ and their faces. This cell complex is denoted as $Pow(\mathcal{S})$ and termed a "power diagram" of $\mathcal{S}$. Note that if all the hyperspheres have identical radii, the power diagram is identical to the Voronoi diagram of the hypersphere centers. Figure 0.4 shows a simple 2D power diagram of four circles.

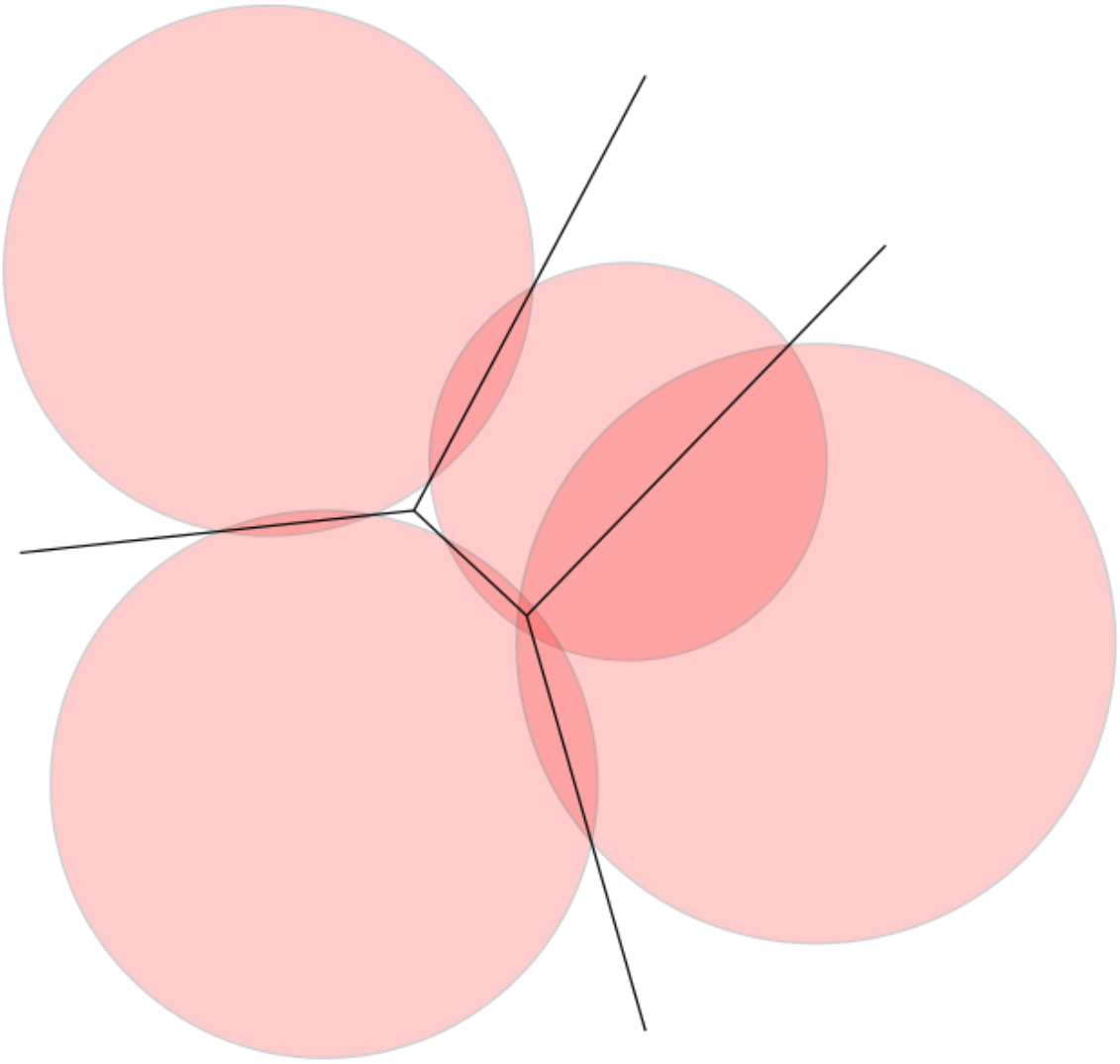

Figure 0.4: 2-dimensional Power Diagram of 4 Circles
(https://commons.wikimedia.org/wiki/File:Power_diagram.svg)

Ancillary Surface Mapping with Regular Grids

As previously noted, the surface reconstruction algorithm presented in this section returns both a list of the boundary particles, as well as their respective area vectors. However, obtaining strain and stress measures requires that the particle positions, and their area vectors need to be computed both for the reference, as well as for the current configuration.

A highlight of this novel micromechanical boundary implementation is that the boundary particles may become interior particles and vice-versa. While this makes micro-mechanical boundaries more versatile, it does increase computation complexity for original-to-deformed mapping schemes such as the deformation gradient. This complexity is herein resolved by introducing into the computation a fixed rectangular grid which is "fitted" to the particle aggregate boundary at either configuration. Figure 0.5 illustrates the different surface types described. On the left can be seen the Laguerre diagram surface consisting of polyhedral quasi-polygons, while on the right can be seen the ancillary rectangular grid surface interpolated to the Laguerre diagram.

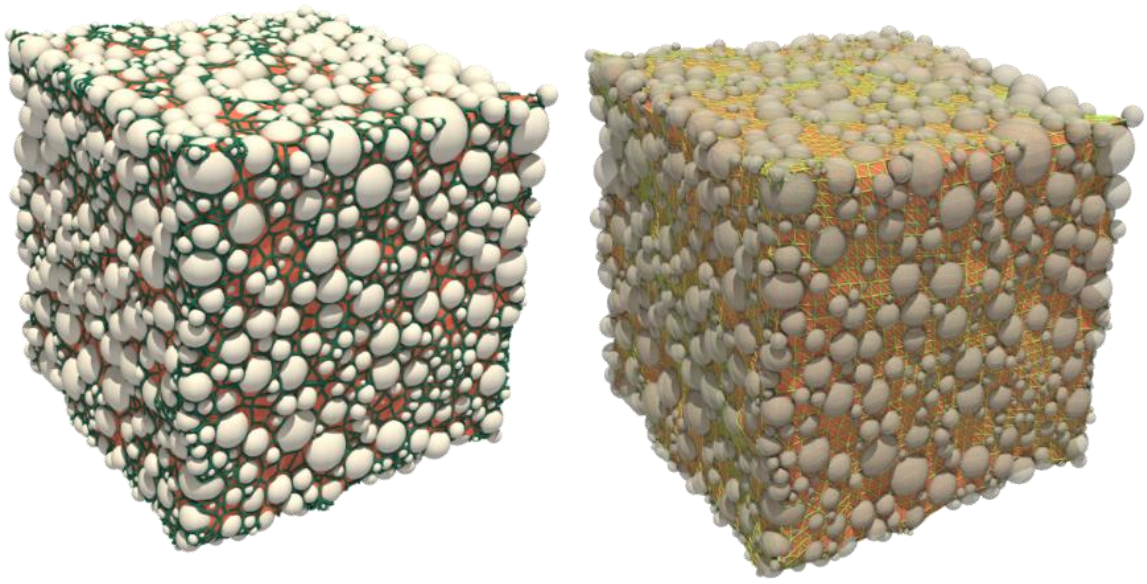

Figure 0.5: The two types of boundary surfaces considered: a) the power diagram polygonal boundary surface, and b) the ancillary regular grid boundary surface

The interpolation of the ancillary rectangular grid is carried out in two stages. In the initial stage, the ancillary grid is stretched and rotated according to the deformation of

the particle aggregate as defined from the particle centers. Essentially, this means applying a deformation map in the form of a deformation tensor to a tessellated unit cube.

$$\mathbf{x_i} = \bar{\mathbf{F}} \cdot \mathbf{X_i} \tag{4.6}$$

Here $\mathbf{x_i}$ represents the position of each grid point in the current configuration, i.e. after deformation. Meanwhile, $\mathbf{X_i}$ represents the position of each grid point in the original configuration, i.e. on the unit cube. Figure 0.6 shows the initial tessellated unit cube, as well as the surface grid of the unit cube after this first stage of interpolation.

Additional details on how a deformation tensor can be obtained from the particle aggregate model, can be found further down in this chapter under the section “Particle Kinematics and the Deformation Gradient Tensor”.

In the second stage, the ancillary surface grid is stretched to the surface defined by the LaGuerre-Voronoi diagram. This is done using the simple linear barycentric interpolation of Eq

$$f(x) \approx \sum_{i=1}^{3} \alpha_i f(x_i) \tag{4.7}$$

where x_i represents the vertices in the triangulation of the LaGuerre-Voronoi diagram closest to x, α_i represent their barycentric coordinates, and $f(x)$ represents the function to be interpolated. In this case, it is desired to simply stretch the surface grid points, so $f(x)$ is the radial distance of x from the center of mass of the particle aggregate. Figure 0.7 shows again the surface grid of the unit cube after the first stage of interpolation, and then after the linear barycentric interpolated stretching on the LaGuerre-Diagram.

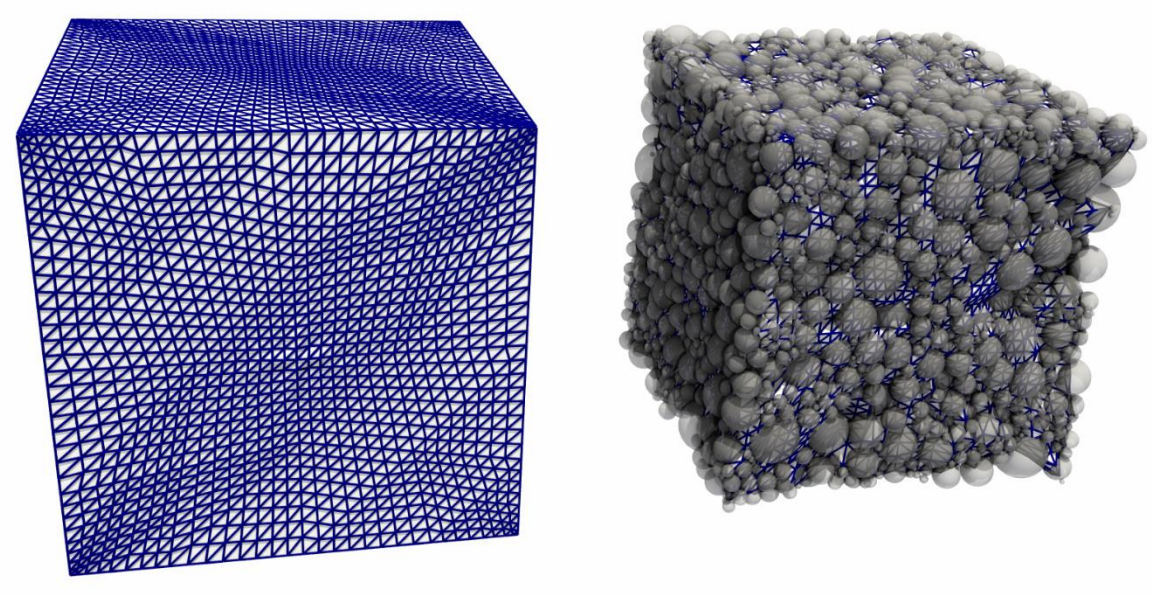

Figure 0.6: First stage of ancillary surface grid interpolation stage a) tessellated unit cube, b) interpolated to centers of boundary particles

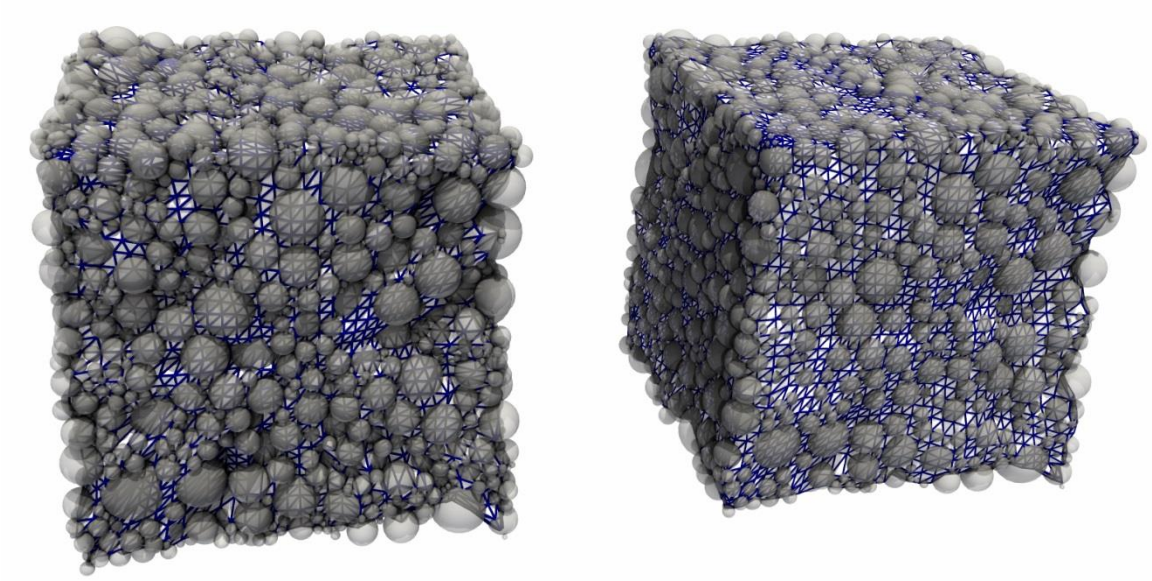

Figure 0.7: Second stage of ancillary surface grid interpolation stage a) interpolated to centers of boundary particles, b) interpolated to LaGuerre-Voronoi diagram

Numerical Implementation of Boundary Conditions

This section provides a brief review of the Uniform Boundary Conditions that satisfy the Hill macrohomogeneity condition. These are the Neumann, a.k.a. traction, natural, or static uniform boundary condition (SUBC), and the Dirichlet , a.k.a. displacement, essential, or kinematic uniform boundary condition (KUBC). A mixed-orthogonal uniform boundary condition also can satisfy the Hill condition provided certain restrictions.

Kinematic Uniform Boundaries

The displacement boundary condition in solid mechanics is based upon the Dirichlet boundary condition for both ordinary and partial differential equations. This boundary condition specifies the value of a solution at the boundary. For an ordinary differential equation (ODE) such as:

$$y'' + y = 0 \tag{4.8}$$

the Dirichlet boundary condition on the interval $[a,b]$ may take the form:

$$y(a) = \alpha, \quad y(b) = \beta \tag{4.9}$$

where α and β are known values.

Similarly, for a partial differential equation (PDE) such as:

$$\nabla^2 y + y = 0 \tag{4.10}$$

where ∇^2 denotes the Laplace operator, the Dirichlet boundary condition on a domain $\Omega \subset \mathbb{R}^n$ assumes the form:

$$y(x) = f(x) \quad \forall x \in \partial\Omega \tag{4.11}$$

where $f(x)$ is a known function on the domain boundary $\partial\Omega$.

To see how to apply the KUBC to a particle aggregate boundary, consider again the nonlinear deformation map of Equation (4.30). The KUBC requires that the boundary displacement be set by the applied deformation tensor with no particle rotations.

$$\mathbf{x}_q = \mathbf{F} \cdot \mathbf{X}_q, \quad \mathbf{Q}_q = \mathbf{I} \text{ on } \partial V \tag{4.12}$$

where, for the sake of clarity, the bar denoting an average has been omitted. It is understood that all effective macroscale deformation and stress metrics henceforth imply an averaging of the microscale quantities.

Due to the explicit nature of the Discrete Element Method, it is necessary to reformulate the expression of Equation (4.12) in terms of velocities. To that effect consider the time derivative of the first part of Equation (4.13):

$$\dot{\mathbf{x}}_q = \dot{\mathbf{F}} \cdot \mathbf{X}_q \tag{4.13}$$

where $\dot{\mathbf{F}}$ is the time derivative of the deformation gradient. Equation (4.13) describes how the KUBC affects the boundary of the particle aggregate, however it is not a useful expression for implementation of the boundary. This is due to a limitation that has been described repeatedly in this chapter, the flux of particles through the boundary makes deformation mapping from particle positions impossible. Fortunately, there is a way to impose the KUBC instantaneously through the velocity gradient tensor, which can be done on the boundary particles at the current rather than the reference configuration. The velocity gradient tensor may be rewritten in index notation form as:

$$\mathbf{L_{ij}} = \frac{\partial \mathbf{v_i}}{\partial \mathbf{x_j}} \tag{4.14}$$

or, using gradient notation as:

$$\mathbf{L} = \nabla \mathbf{v} \tag{4.15}$$

Furthermore, the velocity gradient can be related to the time derivative of the deformation tensor. Consider that

$$\dot{\mathbf{F}}_{\mathbf{ij}} = \frac{\partial \mathbf{v}_{\mathbf{i}}}{\partial \mathbf{X}_{\mathbf{j}}} \tag{4.16}$$

Applying the chain rule:

$$\dot{\mathbf{F}}_{\mathbf{ij}} = \frac{\partial \mathbf{v}_{\mathbf{i}}}{\partial \mathbf{x}_{\mathbf{j}}} \frac{\partial \mathbf{x}_{\mathbf{i}}}{\partial \mathbf{X}_{\mathbf{j}}} \tag{4.17}$$

from which it can be seen that:

$$\dot{\mathbf{F}} = \mathbf{L} \cdot \mathbf{F} \tag{4.18}$$

and that

$$\mathbf{L} = \dot{\mathbf{F}} \cdot \mathbf{F}^{-1} \tag{4.19}$$

Hence, the KUBC may be applied directly on the current list of boundary particles using the following expression:

$$\mathbf{v}_q = \mathbf{L} \cdot \mathbf{x}_q^{LG} \tag{4.20}$$

where $\mathbf{x}_q^{LG}$ denotes the position vector of the centroid of the Laguerre-Voronoi power region of boundary particle q.

Static Uniform Boundaries

The traction boundary condition in solid mechanics is based upon the Neumann boundary condition for both ordinary and partial differential equations. This boundary condition specifies the derivative of a solution at the boundary. For an ordinary differential equation (ODE) such as that of Equation (4.8) the Neumann boundary condition on the interval $[a,b]$ may take the form:

$$y'(a) = \alpha, \quad y'(b) = \beta \tag{4.21}$$

where α and β are known values.

Similarly, for a partial differential equation (PDE) such as that of Equation (4.10) the Neumann boundary condition on a domain $\Omega \subset \mathbb{R}^n$ assumes the form:

$$\frac{\partial y}{\partial \mathbf{n}}(\mathbf{x}) = f(\mathbf{x}) \quad \forall \mathbf{x} \in \partial\Omega \tag{4.22}$$

where $\mathbf{n}$ denotes the normal to the boundary, while $f(x)$ is a known function on the domain boundary $\partial\Omega$.

Application of the SUBC to a particle aggregate is relatively simple. The "hard work" has already been done in finding the Laguerre-Voronoi diagram of the boundary. Given the area vector $\mathbf{A}_q$ of any particle q on the boundary of the particle aggregate, the microscale body force applied on that particle is the product of the Cauchy stress tensor with $\mathbf{A}_q$

$$\mathbf{f}_q = \boldsymbol{\sigma} \cdot \mathbf{A}_q \tag{4.23}$$

Use of the Cauchy stress tensor here makes application of the SUBC simple, since the Cauchy stress is defined in the current deformed configuration. However, computation of the deformation gradient tensor can be easily carried out as described in the previous section. This means that other measures of stress can be easily applied by simply carrying out a frame transformation. Additional discussion on different measures of deformation and stress can be found in the following section on work-conjugate measures.

Periodic Boundaries

The concept of the periodic boundary condition (PBC) in computational mechanics is essentially undistinguishable from the concept of a unit cell. PBCs enforce a

displacement field on a domain that mirrors its opposite extremum, effectively representing an endlessly repeating cell. In terms of the deformation gradient this may be expressed as:

$$\left[\psi - \bar{\mathbf{F}} \cdot \mathbf{X}\right] : \textit{periodic} \quad \textit{on} \quad \partial\Omega \tag{4.24}$$

Furthermore, because of resulting antiperiodicity of boundary normals, boundary tractions are antiperiodic. This can be expressed as:

$$\left[t - \bar{\mathbf{P}} \cdot \mathbf{N}\right] : \textit{antiperiodic} \quad \textit{on} \quad \partial\Omega \tag{4.25}$$

In the specific case of particle methods like Discrete Elements, Equation (4.25) is applied through boundary particle displacements as shown below:

$$\mathbf{x}_q^+ - \mathbf{x}_q^- = \bar{\mathbf{F}} \cdot \left(\mathbf{X}_q^+ - \mathbf{X}_q^-\right), \qquad \mathbf{Q}_q^+ - \mathbf{Q}_q^- = 0 \qquad \textit{on } \partial V \tag{4.26}$$

where the superscripts + and – are used to denote particles on opposite extrema of the realization model bounding box. As mentioned above and required by equilibrium, forces and moments on opposite boundaries need to be antiperiodic as shown below:

$$\mathbf{f}_q^+ + \mathbf{f}_q^- = 0, \qquad \mathbf{m}_q^+ + \mathbf{m}_q^- = 0 \qquad \textit{on } \partial V \tag{4.27}$$

In particle methods, PBCs are easily implemented by making the simulation space itself periodic. By restricting the particle coordinates to the limits of the cell domain and effectively “wrapping” the simulation space, periodic displacements and antiperiodic forces are seamlessly applied by the contact implementation in the model.

In the Yade implementation of periodic space, a parallelepiped-shaped cell is effectively repeated to create the periodic boundary conditions [137]. The deformation of the cell can then be obtained as a velocity gradient representing a homogeneous velocity field. This velocity gradient is integrated automatically over time, resulting in the tensor-valued stepwise deformation gradient shown below:

$$\mathbf{F}^{+} = \left(\mathbf{I} + \nabla\mathbf{v}\,\Delta t\right)\mathbf{F}^{0} \tag{4.28}$$

where $\nabla\mathbf{v}$ represents the velocity gradient of the simulation cell, $\mathbf{F}^{+}$ represents the deformation gradient at the end of the timestep, while $\mathbf{F}^{0}$ represents the initial deformation gradient. The initial deformation gradient can be reset to the identity tensor at any time, allowing for arbitrary reference configurations in the simulation.

Loading of the periodic unit cell is carried out by altering the matrix representing the base vectors of the unit cell parallelepiped. This may be viewed as "shrinking" or "expanding" the periodic space so that the contact forces at the unit cell boundaries increase or decrease. Using this simple but very powerful method allows stress-average or strain rate loading of the unit cell as required by the simulation parameters.

Finite Strain Stress and Deformation of Particle Aggregates

Of imperative importance to the multiscale utility of particle aggregate boundary modeling, is the ability to extract equivalent macroscale metrics of stress and deformation. In continuum mechanics, the averages of stress and strain are readily defined by volume integrals, however these averages need to be defined for the discrete setting.

Particle Kinematics and the Deformation Gradient Tensor

The motion of a body may be described as a transformation ψ defined by:

$$\mathbf{x} = \psi\left(\mathbf{X}, t\right) \tag{4.29}$$

where **x** represents the current location of a given material point at time t, while **X** represents the material point in the reference configuration. If the concept of a "material point" is then extended to a discrete material particle, the transformation may then be defined as a non-linear deformation map to the current configuration:

$$\psi_i\left(\mathbf{X}\right) = \mathbf{x}_\mathbf{i} + \mathbf{Q}_\mathbf{i} \cdot \left(\mathbf{X} - \mathbf{X}_\mathbf{i}\right) \quad for \quad i = 1\ldots, P+Q \tag{4.30}$$

where $\mathbf{Q_i}$ is the second-order particle transformation tensor, P are the interior particles in the aggregate, and Q are the boundary particles in the aggregate. The current positions of the particles may then be expressed as:

$$\mathbf{x_i} = \bar{\mathbf{F}} \cdot \mathbf{X_i} + \mathbf{w_i} \tag{4.31}$$

where $\bar{\mathbf{F}}$ is the macroscopic deformation gradient, while $\mathbf{w_i}$ represents the displacement of particle i with respect to the macroscale current or deformed configuration.

The macroscopic deformation gradient is defined by the volume average of the macro-scale deformation:

$$\bar{\mathbf{F}} = \frac{1}{V}\int_V \mathbf{F} dv \tag{4.32}$$

Recall that the deformation gradient is defined as:

$$\mathbf{F} = \frac{\partial \boldsymbol{\psi}}{\partial \mathbf{X}} \tag{4.33}$$

which may be rewritten in index notation form as:

$$\mathbf{F_{ij}} = \frac{\partial \mathbf{x_i}}{\partial \mathbf{X_j}} \tag{4.34}$$

or, using gradient notation as:

$$\mathbf{F} = \nabla \mathbf{x} \tag{4.35}$$

Substitution of Equation (4.35) into Equation (4.32) followed by application of the divergence theorem, gives:

$$\bar{\mathbf{F}} = \frac{1}{V}\int_{\partial V} \mathbf{x} \otimes \mathbf{N} ds \tag{4.36}$$

where $\mathbf{N}$ is the unit normal vector at the outer boundary for the reference configuration.

If $\mathbf{A_q}$ is the area vector defined as:

$$\mathbf{A_q} = \int_{\partial V} \mathbf{N} ds \tag{4.37}$$

then, for a discrete setting, Equation (4.36) is equivalent to:

$$\bar{\mathbf{F}} = \frac{1}{V} \sum_{q=1}^{Q} \mathbf{x}_q \otimes \mathbf{A_q} \tag{4.38}$$

which may be described as the volume average of the tensor products of the area vectors in the reference configuration and the particle position vectors in the current configuration.

Love-Weber Average of the Cauchy Stress Tensor

Before delving into the vagaries of the definition of stress as pertains a system of discrete particles, consideration is given to the definition of the stress average in continuum mechanics. In continuum mechanics, instead of a discrete particle, the fundamental analysis unit is the, presumably infinitesimal, "material point". A fundamental definition of the Cauchy stress for a material point arises naturally from the balance of momentum equation:

$$\nabla \bullet \boldsymbol{\sigma} + \boldsymbol{\gamma} = \rho \dot{\mathbf{v}} \tag{4.39}$$

where $\boldsymbol{\sigma}$ denotes the Cauchy stress tensor, $\mathbf{v}$ is the velocity, $\boldsymbol{\gamma}$ is the body force density, and ρ is the mass density.

The volume average of the Cauchy stress tensor may be defined as:

$$\bar{\boldsymbol{\sigma}} = \frac{1}{V} \int_V \boldsymbol{\sigma} dv \tag{4.40}$$

Rewriting Equation (4.40) in indicial notation and noting that $\boldsymbol{\sigma}_{\mathbf{ij}} = \boldsymbol{\sigma}_{\mathbf{ik}} \delta_{kj}$ where δ_{kj} is the Kronecker delta:

$$\bar{\boldsymbol{\sigma}}_{ij} = \frac{1}{V} \int_V \boldsymbol{\sigma}_{\mathbf{ik}} \delta_{kj} dv \tag{4.41}$$

Furthermore, since $\delta_{kj} = \partial x_j / \partial x_k$ Equation (4.41) may be rewritten as:

$$\bar{\boldsymbol{\sigma}}_{ij} = \frac{1}{V}\int_V \boldsymbol{\sigma}_{\mathbf{ik}} \frac{\partial \mathbf{x}_{\mathbf{k}}}{\partial \mathbf{x}_{\mathbf{j}}} dv \tag{4.42}$$

Using the chain rule, Equation (4.42) may be written as:

$$\bar{\boldsymbol{\sigma}}_{ij} = \frac{1}{V}\int_V \left[\frac{\partial\left(\boldsymbol{\sigma}_{\mathbf{ik}} \mathbf{x}_{\mathbf{j}}\right)}{\partial \mathbf{x}_{\mathbf{k}}} - \frac{\partial \boldsymbol{\sigma}_{\mathbf{ik}}}{\partial \mathbf{x}_{\mathbf{k}}} \mathbf{x}_{\mathbf{j}} \right] dv \tag{4.43}$$

Applying the divergence theorem to the first term in the integral of Equation (4.43) gives:

$$\bar{\boldsymbol{\sigma}}_{ij} = \frac{1}{V}\int_{\partial V} \boldsymbol{\sigma}_{ik} \mathbf{x}_j \mathbf{N}_k dS - \frac{1}{V}\int_V \frac{\partial \boldsymbol{\sigma}_{ik}}{\partial \mathbf{x}_k} \mathbf{x}_j dv \tag{4.44}$$

Taking Equation (4.39) into account gives:

$$\bar{\boldsymbol{\sigma}}_{ij} = \frac{1}{V}\int_{\partial V} \boldsymbol{\sigma}_{ik} \mathbf{x}_j \mathbf{N}_k dS - \frac{1}{V}\int_V \left(\rho \dot{\mathbf{v}}_i - \boldsymbol{\gamma}_i\right) \mathbf{x}_j dv \tag{4.45}$$

Furthermore, since at all points on the boundary $\mathbf{f}_i^{ext} = \boldsymbol{\sigma}_{ik}\mathbf{N}_k$, where $\mathbf{f}_i^{ext}$ is the exterior force, then:

$$\bar{\boldsymbol{\sigma}}_{ij} = \frac{1}{V}\int_{\partial V} \mathbf{f}_i^{ext} \mathbf{x}_j dS - \frac{1}{V}\int_V \left(\rho \dot{\mathbf{v}}_i - \boldsymbol{\gamma}_i\right) \mathbf{x}_j dv \tag{4.46}$$

where it becomes obvious that the average Cauchy stress tensor is composed of two parts.

The first integral on the right side of Equation (4.46) represents the static component of the stress, involving the forces applied at the boundary. The second integral is an inertial term, representing the acceleration of each material point. For static and quasi-static analyses, the second term may be ignored, however it needs to be considered for transient dynamic analyses.

For the case of a particle aggregate with P interior particles and Q boundary particles, Equation (4.46) may be written as:

$$\bar{\boldsymbol{\sigma}}_{ij} = \frac{1}{V}\sum_{q=1}^{Q} \mathbf{f}_i^{ext,q} \mathbf{x}_j^q - \frac{1}{V}\sum_{q=1}^{P+Q}\int_{V_q} \left(\rho \dot{\mathbf{v}}_i - \boldsymbol{\gamma}_i\right) \mathbf{x}_j dV \tag{4.47}$$

For a particle aggregate under in equilibrium when subjected to external forces $\mathbf{f}_i^{ext,q}$ the second term vanishes, giving the classical Love-Weber formula of the average Cauchy stress tensor [163-166]:

$$\bar{\boldsymbol{\sigma}}_{ij}^{LW} = \frac{1}{V}\sum_{q=1}^{Q}\mathbf{f}_i^{ext,q}\mathbf{x}_j^q \tag{4.48}$$

Work-Conjugate Measures of Stress and Strain

It was mentioned that different measures of stress and strain may be obtained using the particle aggregate boundary conditions and averaging procedures described in this chapter. In describing these measures and their relations, a note is in order about which measures are energetic conjugates of each other. The fundamental metrics of stress and strain here are the Cauchy stress tensor and the deformation gradient tensor, respectively. However, these measures are not actually energetic conjugates of each other. Work conjugate measures of stress and strain are those measures whose product gives the strain work density. It must be stated that energy-conjugate measures need not be used exclusively in pairs, in fact this is far from the most common way to pair stress-strain measures. However, work-conjugacy must be taken into account if thermomechanics are considered, such as when computing strain energy and when considering work potentials and plastic dissipation.

Starting with the Cauchy stress, it is well-established that its work-conjugate strain measure is the true strain, better known in the full 3D configuration as the Hencky strain. It is given by:

$$\mathbf{H} = \ln\left(\mathbf{U}\right) \tag{4.49}$$

where $\mathbf{U}$ is the right stretch tensor. The right stretch tensor $\mathbf{U}$ arises from polar decomposition of the deformation gradient tensor:

$$\mathbf{F} = \mathbf{R} \cdot \mathbf{U} = \mathbf{V} \cdot \mathbf{R} \tag{4.50}$$

where $\mathbf{V}$ is the left stretch tensor and $\mathbf{R}$ is the rotation tensor. The right stretch tensor $\mathbf{U}$ is itself work-conjugate to the Biot stress, which is also known as the Jaumann stress and is given by:

$$\mathbf{T} = J\mathbf{R}^T \cdot \boldsymbol{\sigma} \cdot \mathbf{F}^{-T} \tag{4.51}$$

where J is the Jacobian.

Next of immediate interest is the stress measure that is work-conjugate to the deformation gradient tensor. This measure is known as the First Piola-Kirchoff stress tensor, or more succinctly as the Nominal stress. The Nominal stress tensor is given by:

$$\mathbf{P} = J\boldsymbol{\sigma} \cdot \mathbf{F}^{-T} \tag{4.52}$$

It should be noted that the nominal stress/deformation gradient pair will be the work-conjugate pair used in this work to compute the strain energy. This is a fairly common way to compute the strain energy, and is certainly convenient given that the Cauchy stress tensor and deformation gradient tensor are computed frequently in the particle aggregate simulations carried out using the framework described in this chapter.

As a matter of completeness, there is another work-conjugate stress-strain pair sometimes used to compute the strain energy. This is the Green-Lagrange strain/Second Piola-Kirchoff stress-strain pair. The Green-Lagrange strain is often used in mechanics application for the simple reason that it can be additively decomposed into small strain terms and higher order terms. This is useful when making the transition from infinitesimal strain theory to finite strains. The Green-Lagrange strain is given by:

$$\mathbf{E} = \frac{1}{2}(\mathbf{F}^{-T} \cdot \mathbf{F} - \mathbf{I}) \tag{4.53}$$

while the Second Piola-Kirchoff stress, also known as the Material stress, is given by:

$$\mathbf{T} = J\mathbf{F}^{-1} \cdot \boldsymbol{\sigma} \cdot \mathbf{F}^{-T} \tag{4.54}$$

CHAPTER 5

EGLIN SAND MESOSCALE ENSEMBLE SIMULATIONS AND RESULTS

This chapter describes the multitude of mesoscale simulations and results thereof, carried out using the methods described in the preceding chapters of this document. First, the experimental micromechanical parameters used in these simulations are presented. Next, the ensemble homogenization results are presented for realizations at confinements up to 20 MPa, prior to grain fracture and the resulting comminution becoming significant.

The results of the grain crushing simulations and the evolution of the PSD with increasing isotropic stress are presented in the following section. Next, ensemble homogenization results are presented for the higher confinements levels, taking into account the comminuted size distribution. With homogenization carried out at the various confinement levels, mesoscale bounds on the Lame constants are established from the iterative domain partition of the RVE. Mesoscale bounds for large strain bulk and deviatoric responses are established using the periodic unit cell approach, shown to be statistically equivalent to the iterative domain partition approach for window sizes higher than $1/8^{th}$ the RVE size.

Finally some thermomechanical statistics of the unit cell simulations are presented. Energy dissipation due to friction and grain comminution, as well as the amount of recoverable strain energy, are quantified along with the associated uncertainty. These thermomechanical results further show the versatility of the framework presented here. The HEP Model used as the continuum model in this study is phenomenological model. However,

there several work-based particulate medium models, which can greatly benefit from a micromechanical source for energy density evolution data.

Micromechanical Parameters

The micromechanical parameters used here for Eglin sand, were obtained from experimental testing results. For Eglin sand there have been several micromechanical experiments carried out in recent years, enabling a near-complete description of the required Discrete Element parameters from experimental data. These are shown in Table 0.1, while the histogram of the Particle Size Distribution is shown in Figure 0.1.

Table 0.1: Eglin sand parameters used in mesoscale modeling

Parameter	Distribution Type	Shape/StDev	Scale/Mean
Particle Size [34]	Weibull	2.59	0.428 (mm)
Young's Modulus [167]	Weibull	5.48	95.9 (GPa)
Density [34, 168]	Scalar Constant	-	2.72 (g/cm^3)
Shear Stiffness [169, 170]	Scalar Constant	-	0.17
Angle of Friction [171, 172]	Normal	5.7 (deg)	19.1 (deg)
Crush Strength * [171]	Scalar Constant	-	36 (MPa)
Fail. Ref. Diameter [171]	Scalar Constant	-	1.36 (mm)
Weibull Modulus [171]	Scalar Constant	-	2.5

* Crush Strength is the characteristic stress at 37% survival

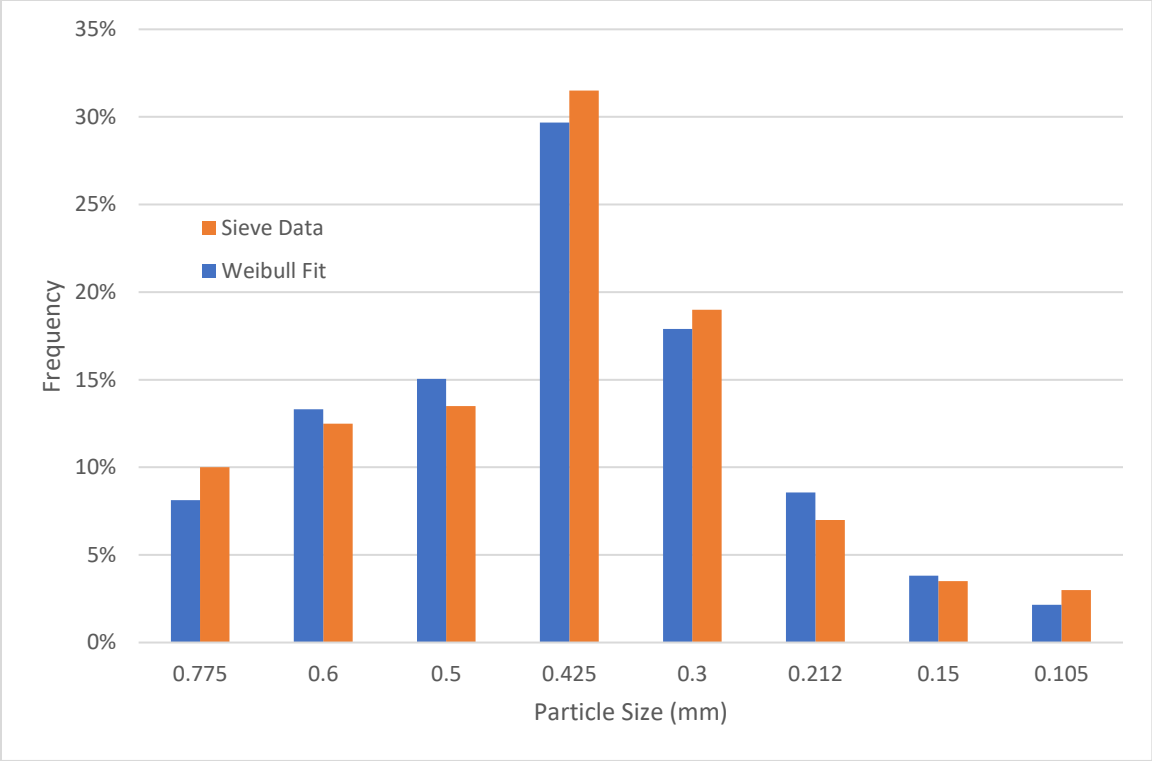

Figure 0.1: Eglin Sand PSD from the sieve data as well as the Weibull fit

Computational Homogenization without Fragmentation

Homogenization results for Eglin sand at relatively low confinements are presented in this section. The results are presented at three confinement levels, specifically 1 MPa, 5 MPa, and 20 MPa. At confinements higher than 20 MPa, use of the virgin Particle Size Distribution curve is not physically realistic. In fact, comminution is also relevant for confinement of 20 MPa, however this is used as an opportunity to compare homogenization of Eglin sand at 20 MPa with and without the comminution of crush-up behavior.

The histograms of the elastic moduli from the ensemble results can be found in Appendix A Figure 0.1 through Figure 0.36. Figure 0.2 through Figure 0.7 show the ratios of the upper bound average to the lower bound average as they converge to unity (Hill condition)

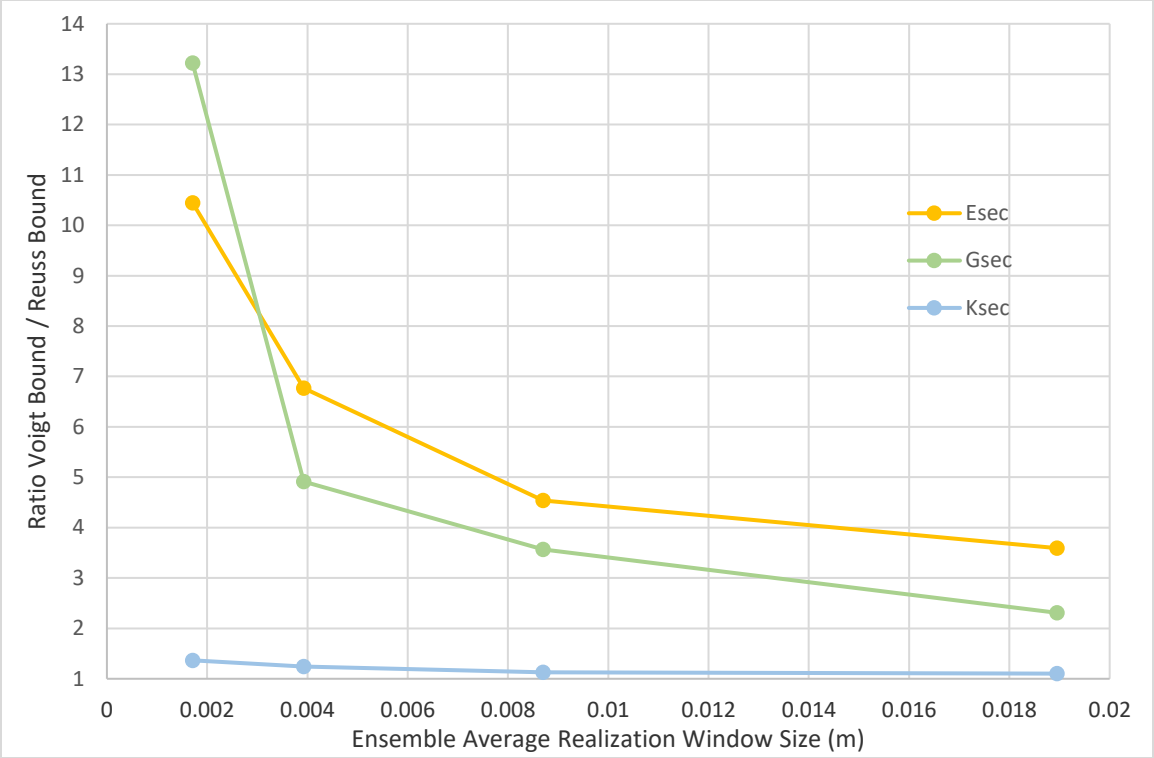

Figure 0.2: Ratios of elastic moduli Voigt to Reuss bounds at 1 MPa confinement

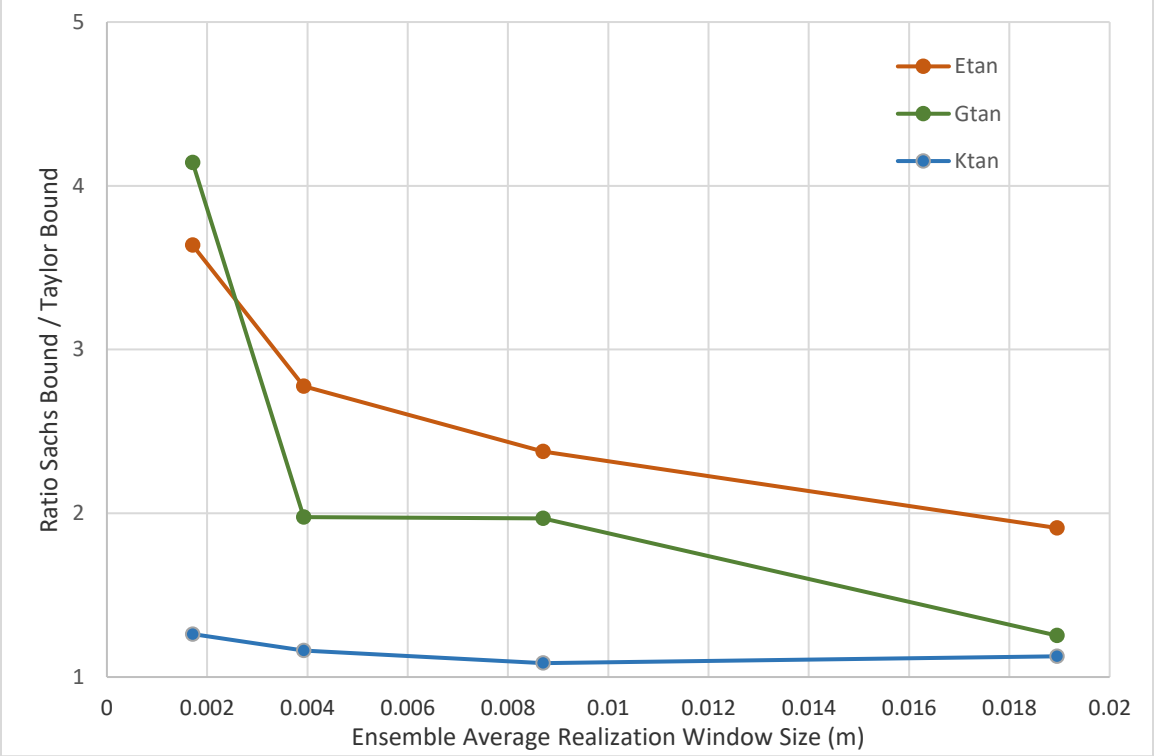

Figure 0.3: Ratios of elastic moduli Sachs to Taylor bounds at 1 MPa confinement

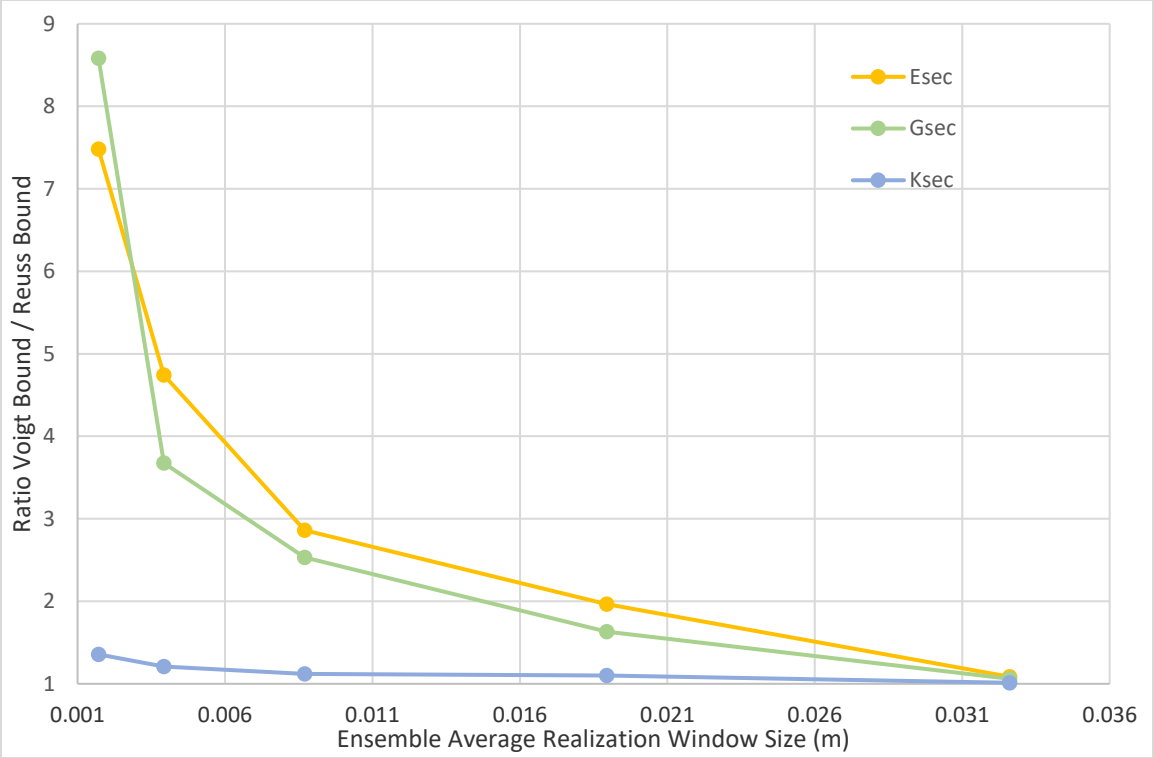

Figure 0.4: Ratios of elastic moduli Voigt to Reuss bounds at 5 MPa confinement

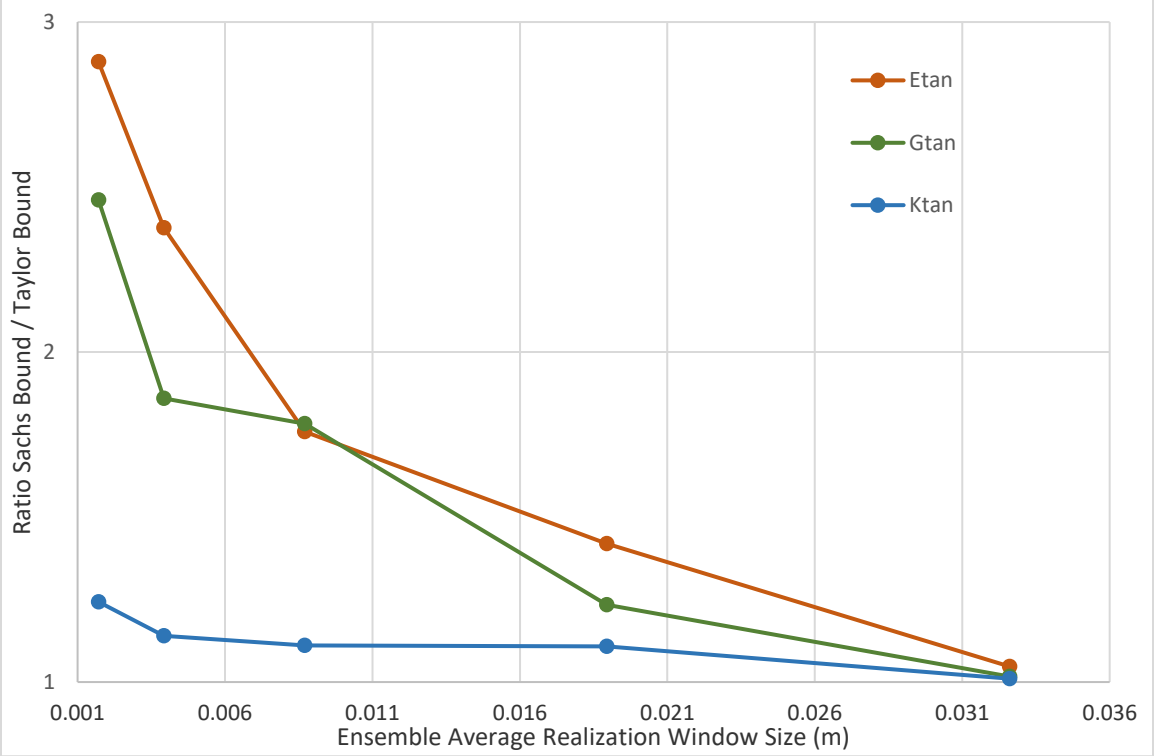

Figure 0.5: Ratios of elastic moduli Sachs to Taylor bounds at 5 MPa confinement

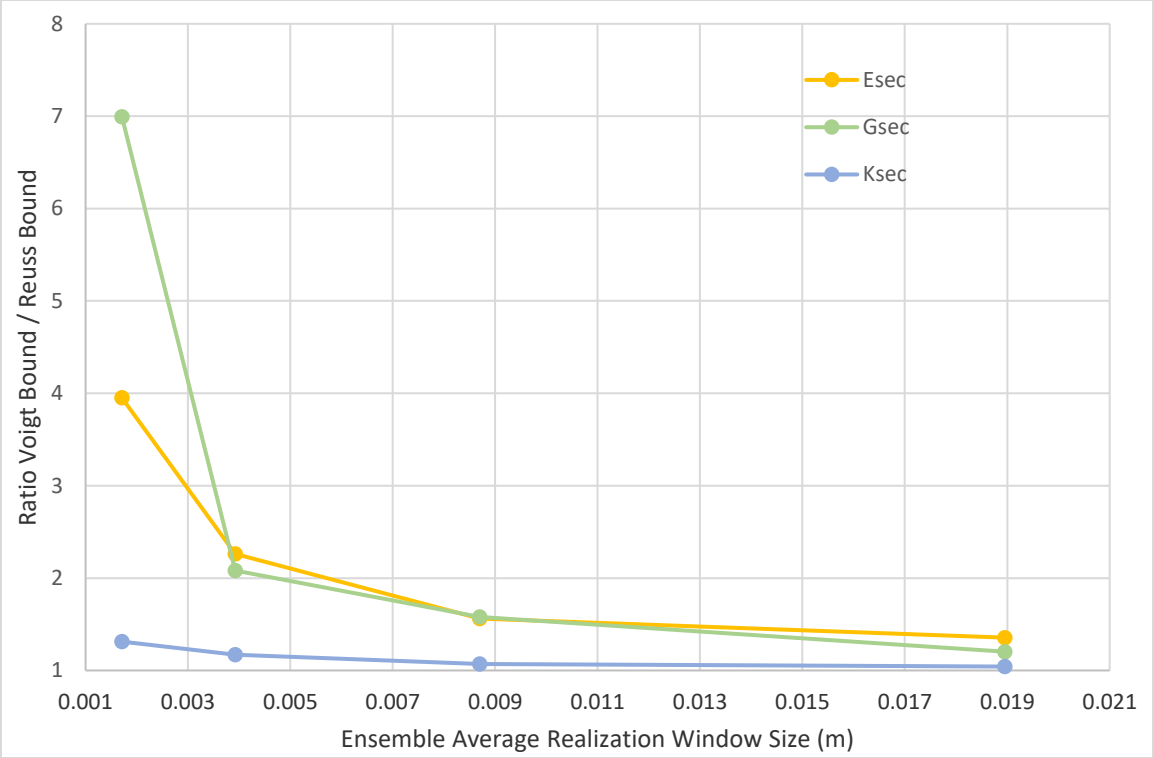

Figure 0.6: Ratios of elastic moduli Voigt to Reuss bounds at 20 MPa confinement

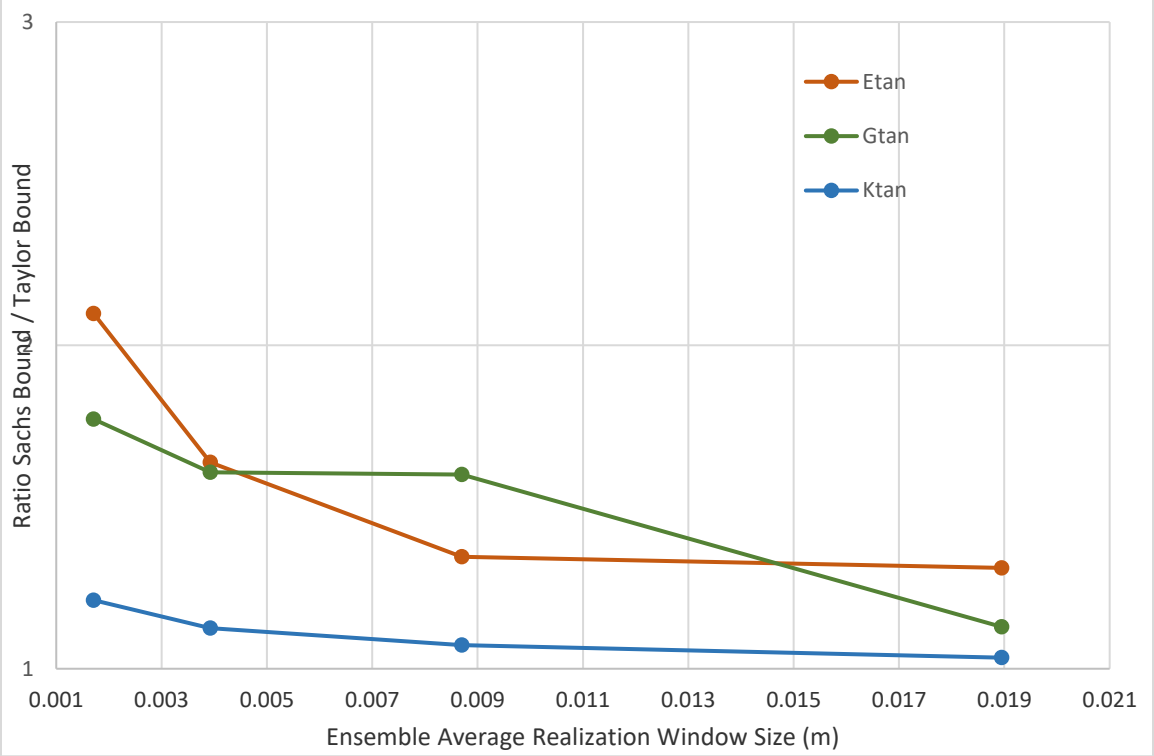

Figure 0.7: Ratios of elastic moduli Sachs to Taylor bounds at 20 MPa confinement

Comminution due to Grain Fragmentation

Shown in this section are ensemble average results of mesoscale simulations of the crush-up behavior of Eglin sand. Figure 0.8 shows the evolution of the particle size distribution (PSD) of Eglin sand found from the cumulative behavior of the mesoscale model ensemble compared with that from experimental PSD evolution. The experimental data in this figure is represented by three different data series. First, the data series titled "Weibull Initial" is the Weibull distribution fit for the "as-received" PSD.

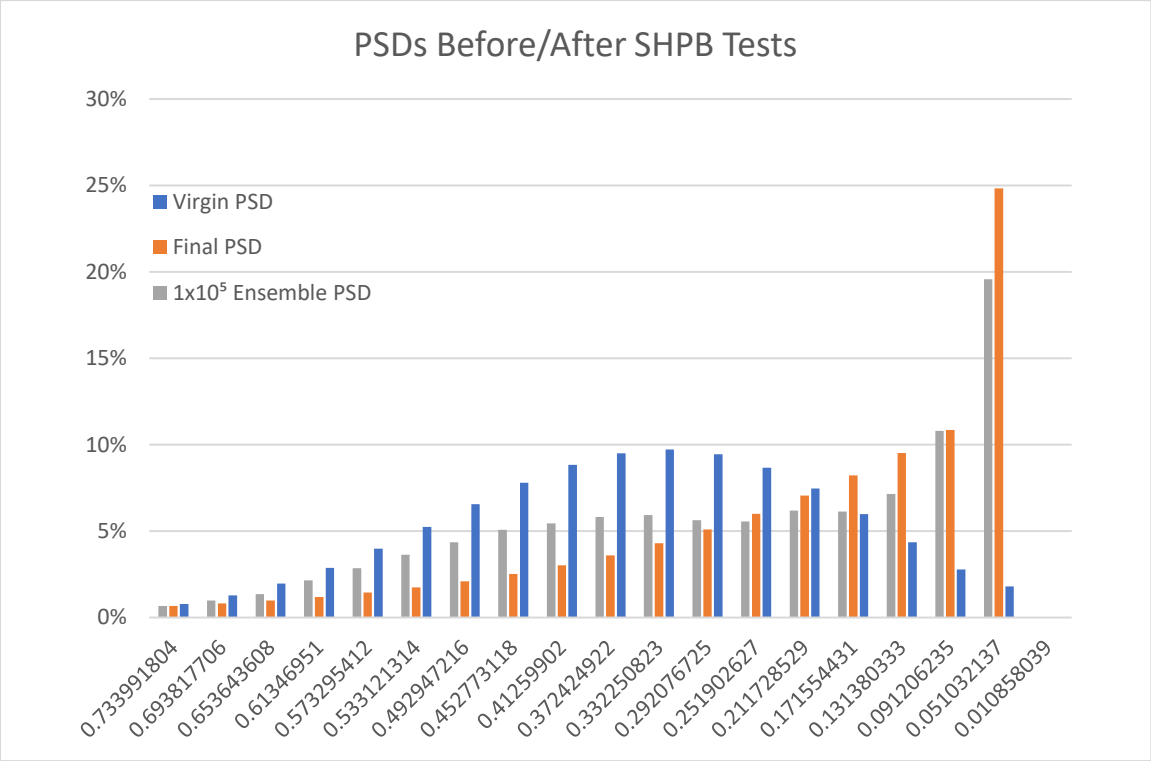

Figure 0.8: Eglin Sand PSD evolution during crush-up for compression up to 200 MPa

The fit here is almost perfect, so the discrete data points for each sieve are not shown. The series titled "Sieves Final" shows the experimental sieve data points for the sand after crush-up [34] [34]. The "Weibull Final" series shows the Weibull distribution fit for the sieve data points. The fit is still quite good, though not as perfect as the fit for the initial PSD. Next, the series titled "m=2.5" represents the mesoscale simulation

ensemble cumulative PSD using a Weibull modulus of 2.5 for the Weibull grain survival model described in this paper.

The fit of Figure 0.8 is remarkable for one very important reason: no calibration or optimization has been carried out to obtain the computational results shown. Only experimental data has been used for the mesoscale ensemble simulations of grain crush-up. So, what is remarkable is that this Discrete Element paradigm, wherein sand grains are modeled as prefect spheres, can with no calibration use lab data to approximate the complex, non-deterministic behavior of sand using fractal geometry to discretize the comminution of macrograins.

Next, the evolving particle size distribution is shown at increasing confinement stresses in Figure 0.9 through 4.20. Figure 0.9 shows the PSD at 20 MPa with minor comminution, while Figure 0.13 shows the severely comminuted PSD at 400 MPa.

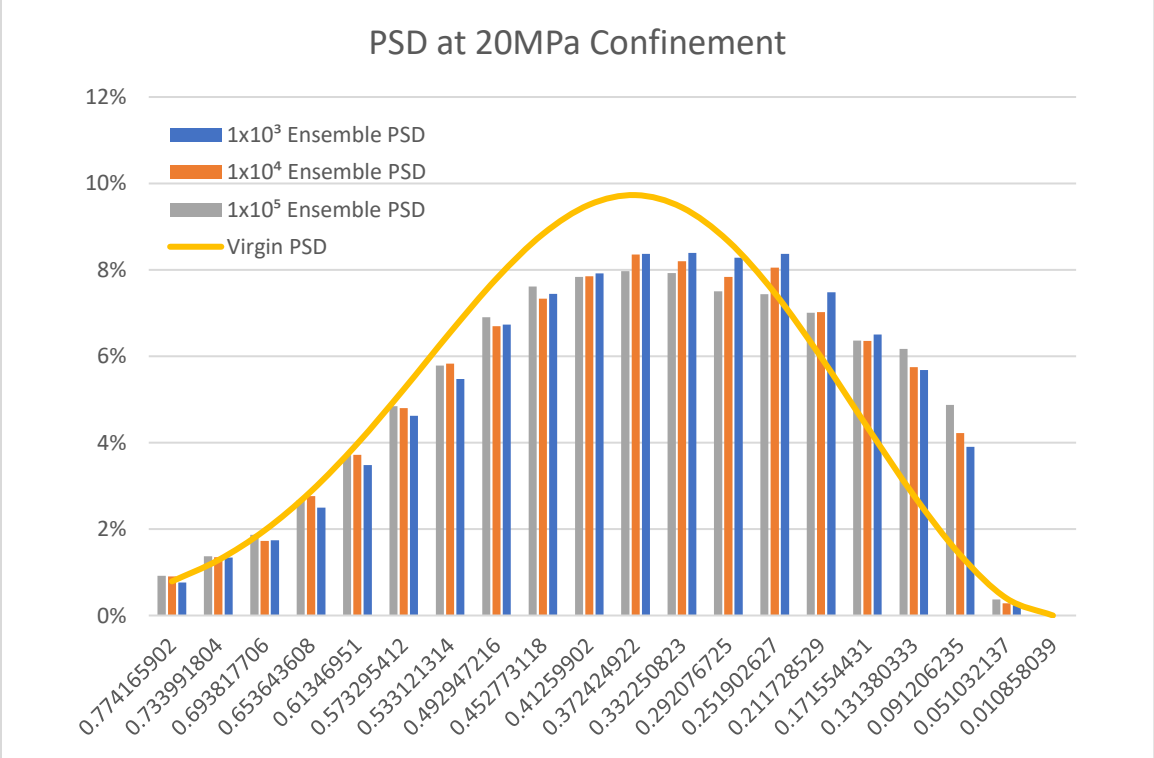

Figure 0.9: Comminuted PSDs of the Statistical Ensembles at 20 MPa Confinement

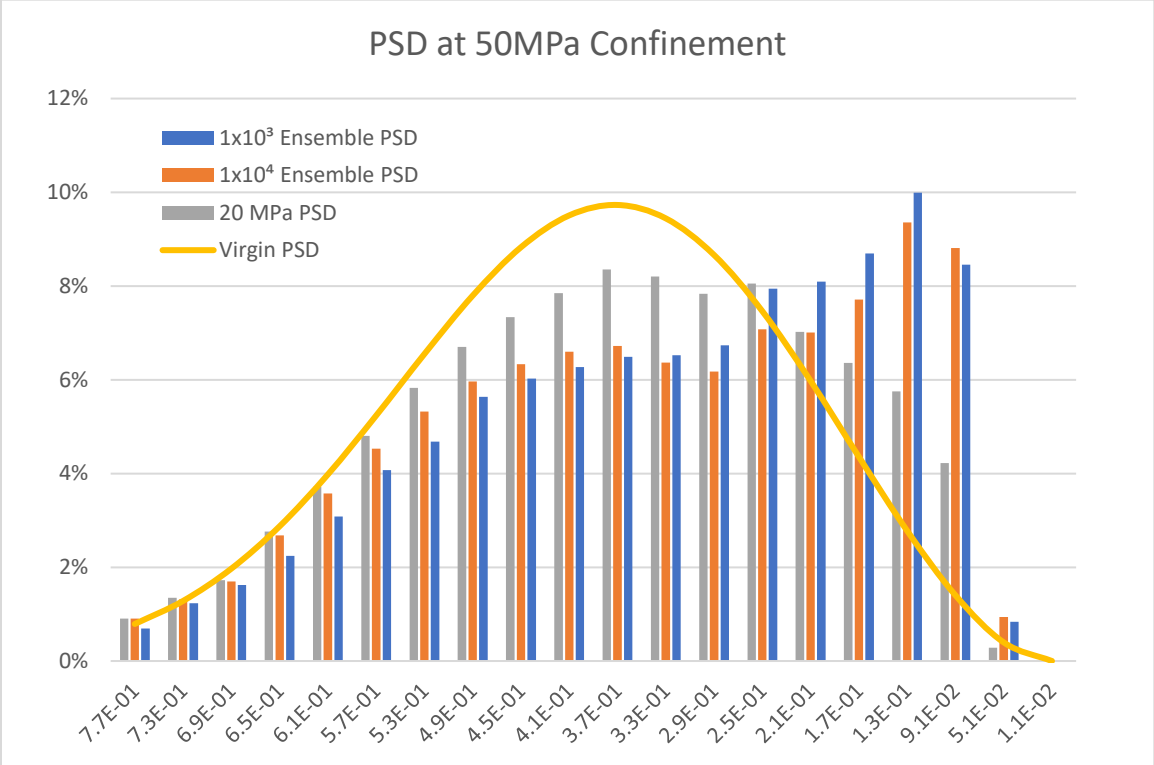

Figure 0.10: Comminuted PSDs of the Statistical Ensembles at 50 MPa Confinement

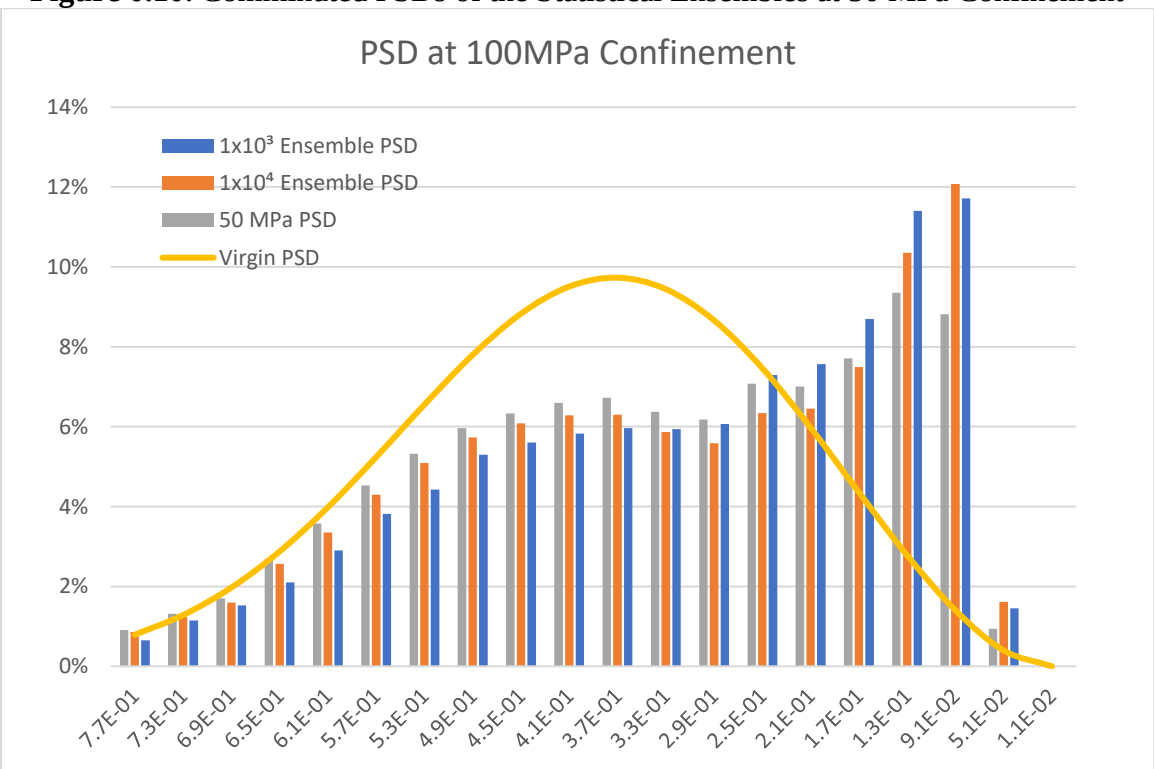

Figure 0.11: Comminuted PSDs of the Statistical Ensembles at 100 MPa Confinement

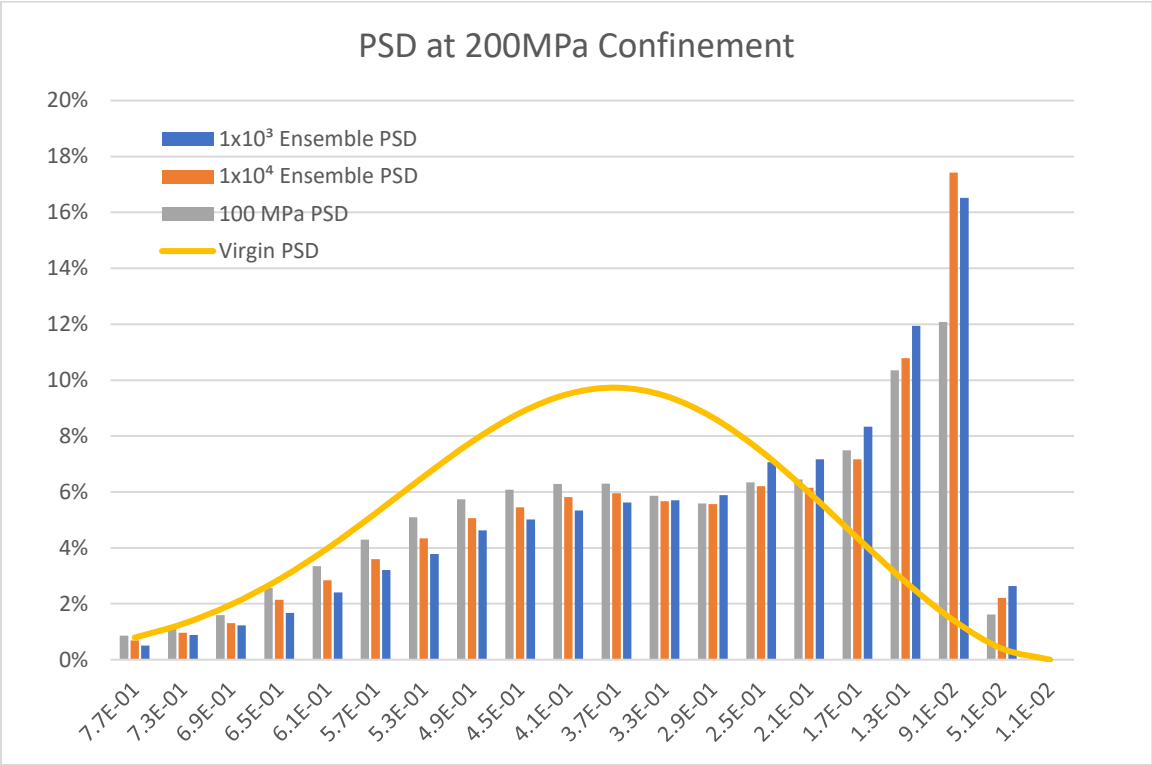

Figure 0.12: Comminuted PSDs of the Statistical Ensembles at 200 MPa Confinement

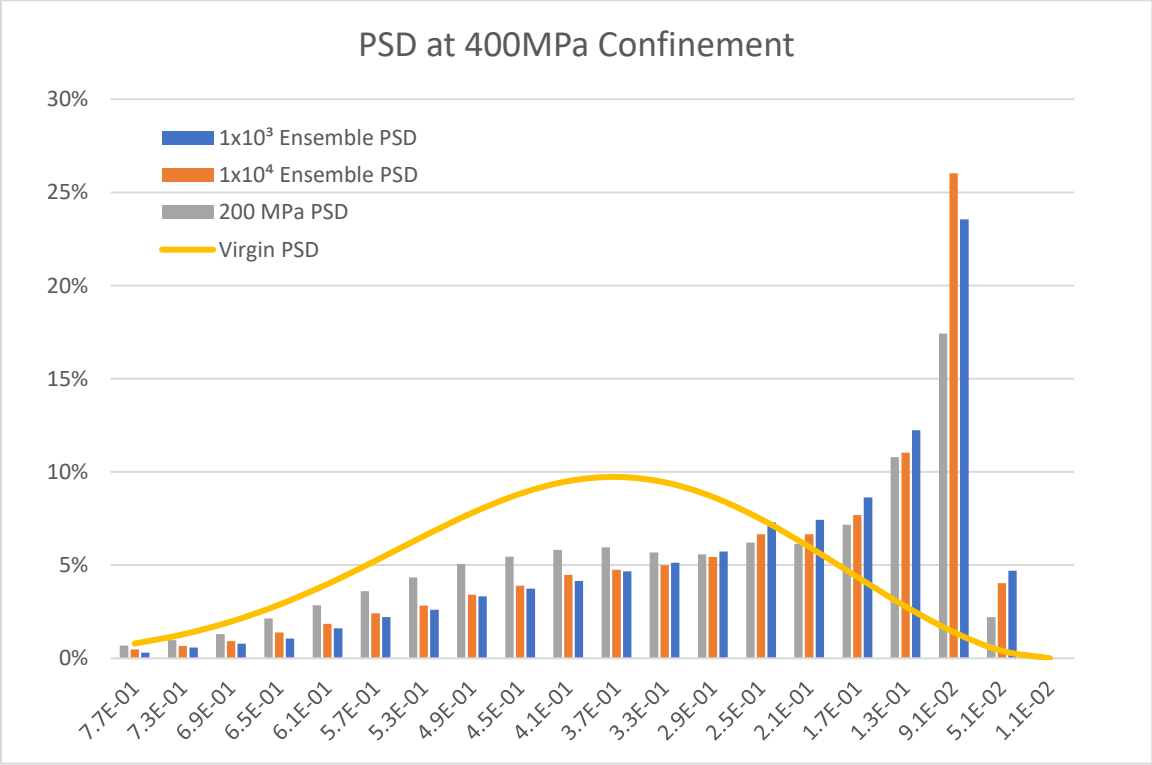

Figure 0.13: Comminuted PSDs of the Statistical Ensembles at 400 MPa Confinement

Table 0.2 shows the normalized Wasserstein distances between the comminuted PSDs for ensembles of realizations with different particle number. The difference between comminuted size distributions is negligible between realizations of a thousand (10^3) and ten thousand (10^4) particles, and even more so between realizations of ten thousand (10^4) and hundred thousand (10^5) particles.

Table 0.2: Wasserstein distance between comminuted PSDs of ensembles of different sizes

10^3 vs 10^4 Ensemble PSDs at 20 MPa	1.4%
10^4 vs 10^5 Ensemble PSDs at 20 MPa	0.9%
10^3 vs 10^5 Ensemble PSDs at 20 MPa	1.7%
10^3 vs 10^4 Ensemble PSDs at 50 MPa	3.5%
10^3 vs 10^4 Ensemble PSDs at 100 MPa	3.9%
10^3 vs 10^4 Ensemble PSDs at 200 MPa	3.7%
10^3 vs 10^4 Ensemble PSDs at 400 MPa	2.4%

Mesoscopic Physical Characteristics of the Ensembles

This section is concerned with describing equivalent physical characteristics of the discrete model ensembles. The ab-initio realizations used here for homogenization and up-scaling are models of a set scale based on the number of particles. However, number of particles is not a very useful metric for describing particulate materials. What is truly useful, is to have an equivalent window size in units of length for the mesoscale models. This can be done by finding the mean dimension of the bounding box for each realization and computing the ensemble average of the realization window sizes.

In the previous section, the evolution of the PSD of Eglin sand due to crush-up was discussed and results presented. The comminution shown there is also relevant to the physical characteristics of the ensembles at the confinement levels where crush-up is relevant. A realization that contains 10 000 particles at 5MPa, can become a Discrete Element model with 200 000 particles or more once comminution up to isotropic stress magnitude of 400 MPa is simulated. Homogenization at the higher confinement is then again carried out using set particle number ensembles, but this time the PSD is based on the comminuted results shown in Figure 0.1 through Figure 0.13. The equivalent physical window sizes for these ensembles need to also be computed. The computed ensemble averages of realization window sizes, along with equivalent porosities for each realization size and particle size distribution is shown in Figure 0.14 through Figure 0.25

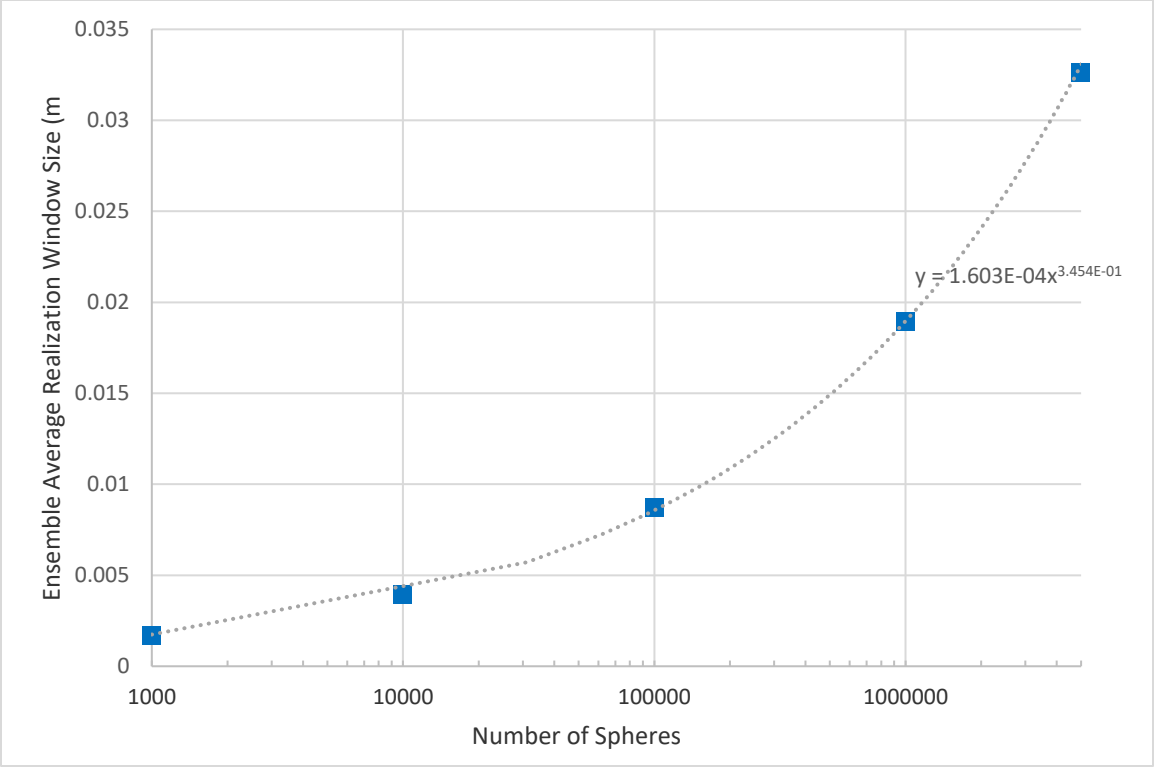

Figure 0.14: Average realization window size of ensembles with virgin PSD

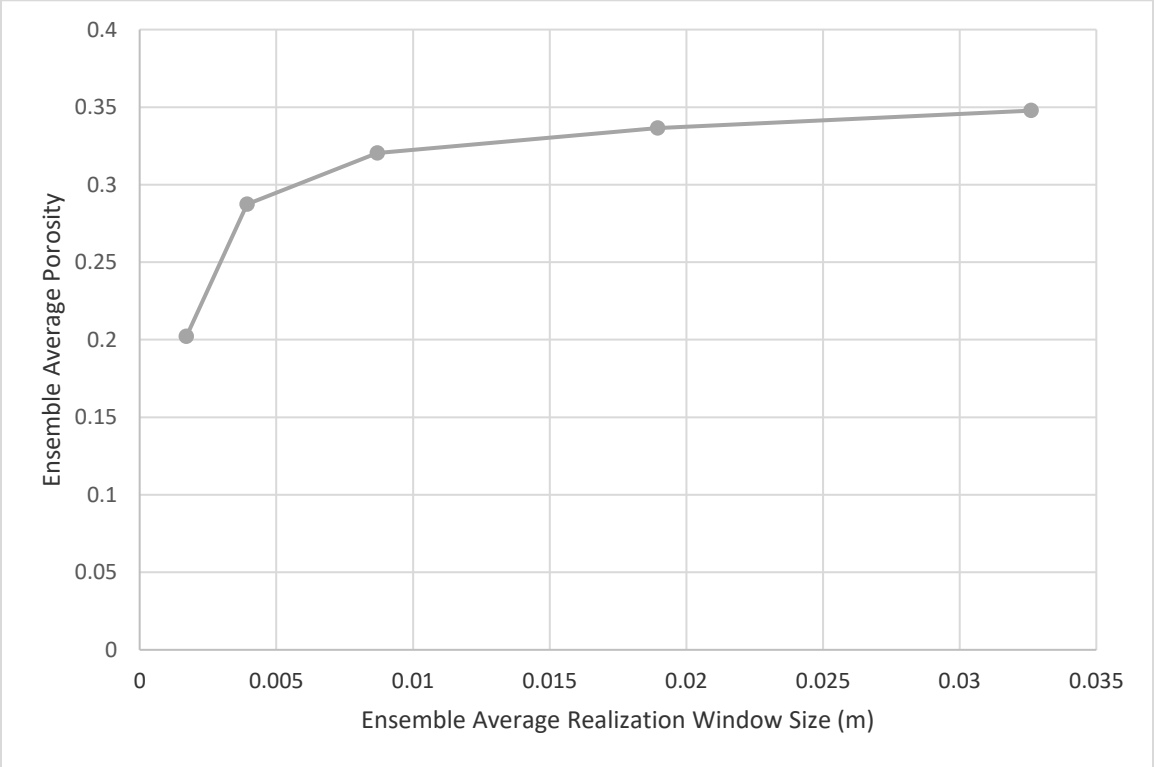

Figure 0.15: Average realization porosity of ensembles with virgin PSD

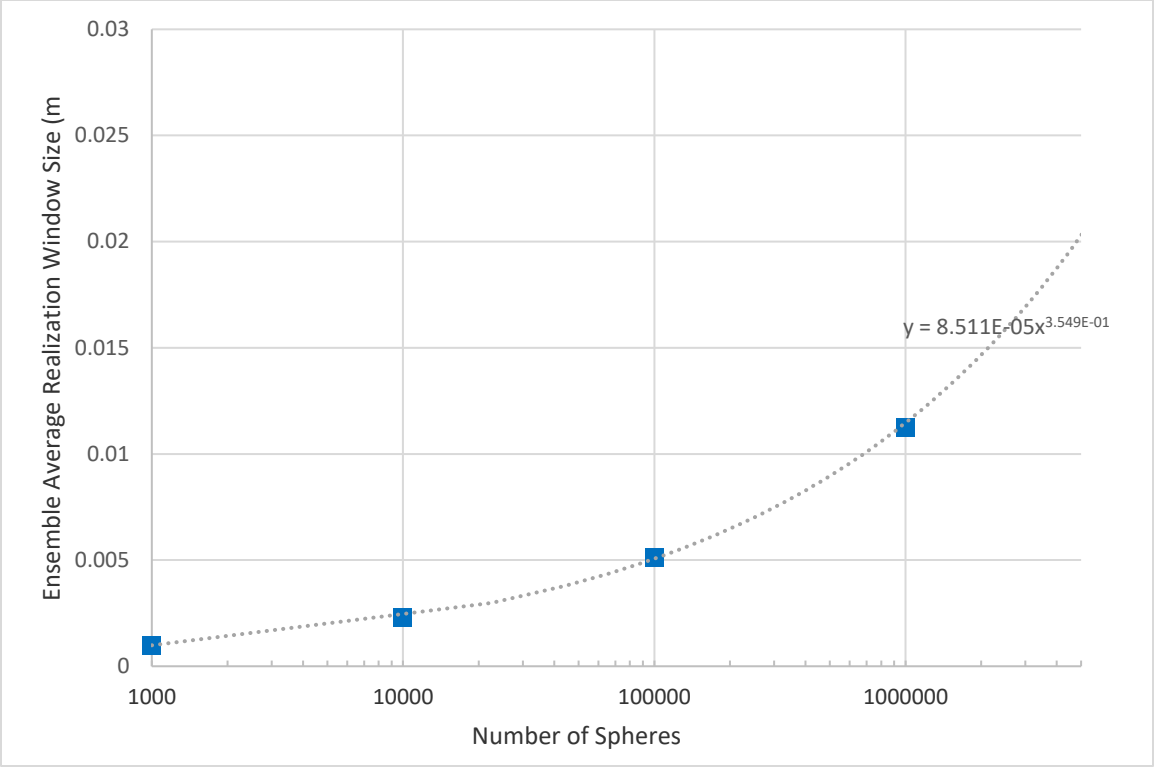

Figure 0.16: Average window size of ensembles with comminuted PSD at 20 MPa

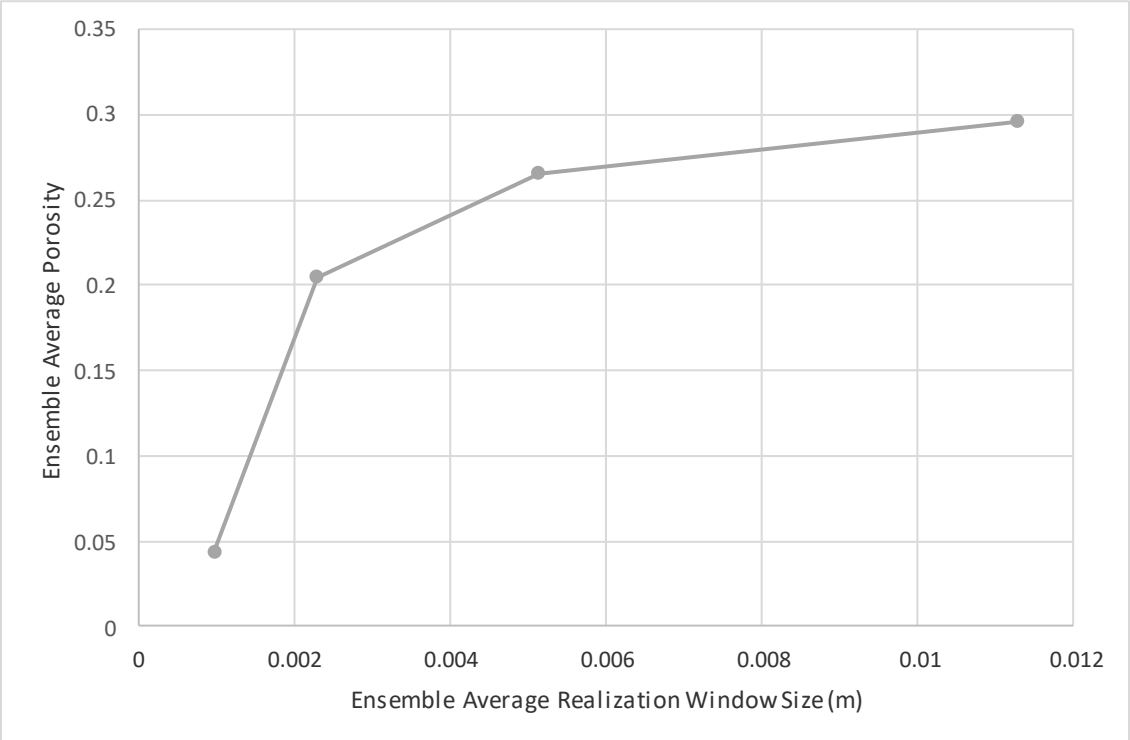

Figure 0.17: Average porosity of ensembles with comminuted PSD at 20 MPa

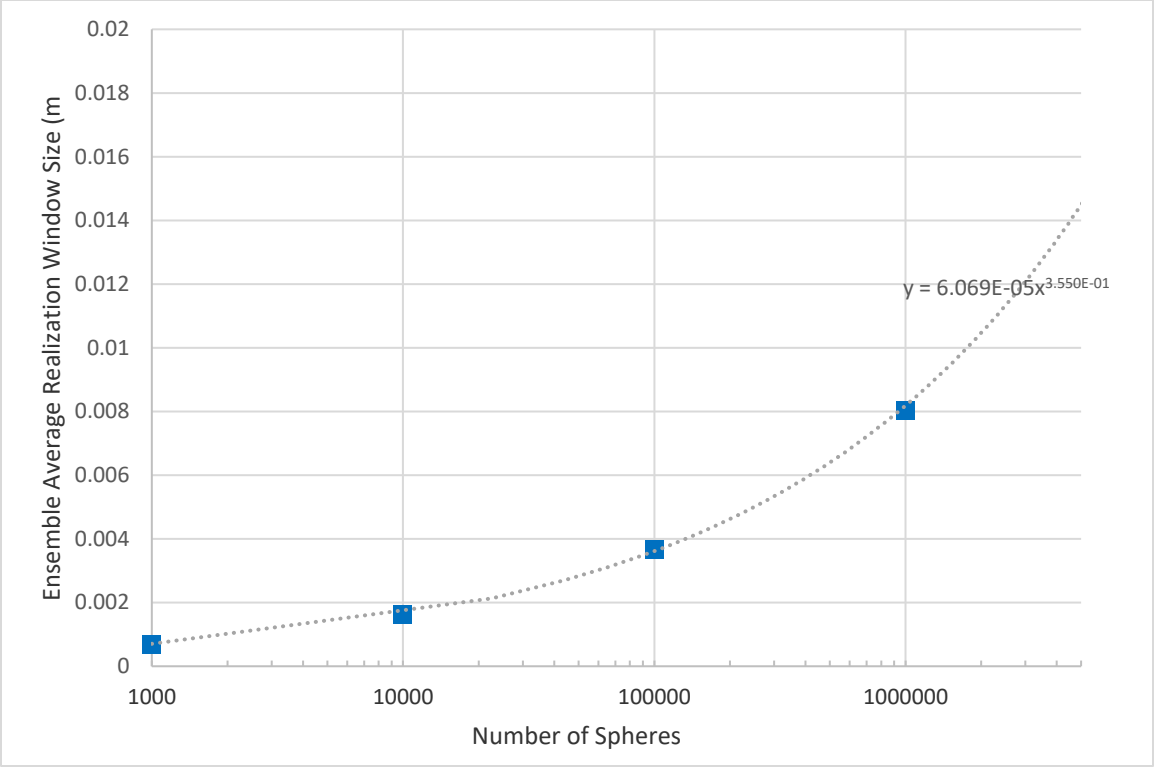

Figure 0.18: Average window size of ensembles with comminuted PSD at 50 MPa

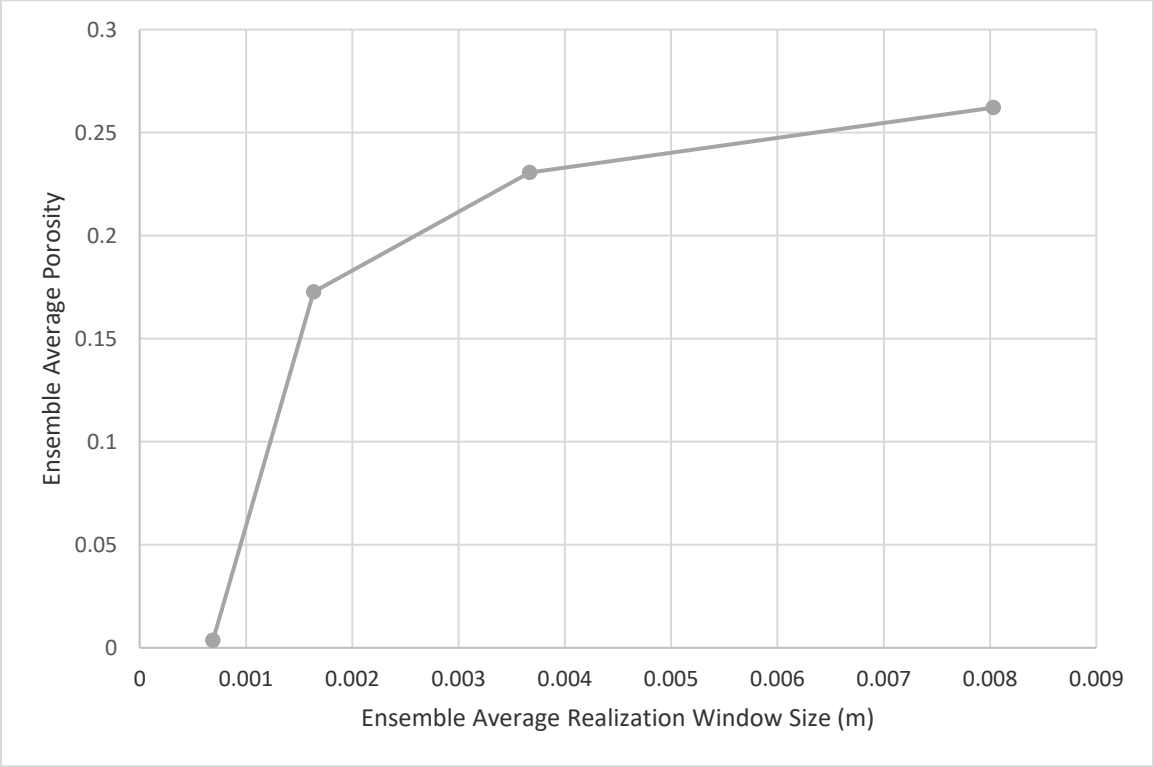

Figure 0.19: Average porosity of ensembles with comminuted PSD at 50 MPa

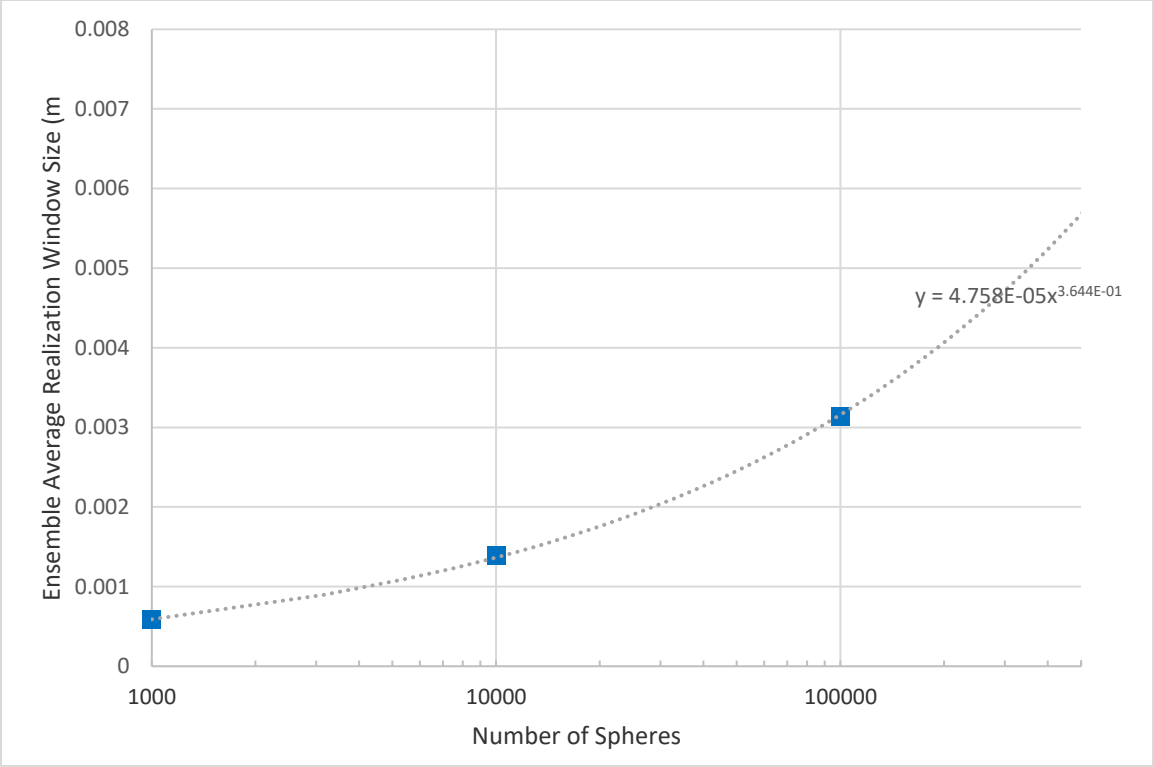

Figure 0.20: Average window size of ensembles with comminuted PSD at 100 MPa

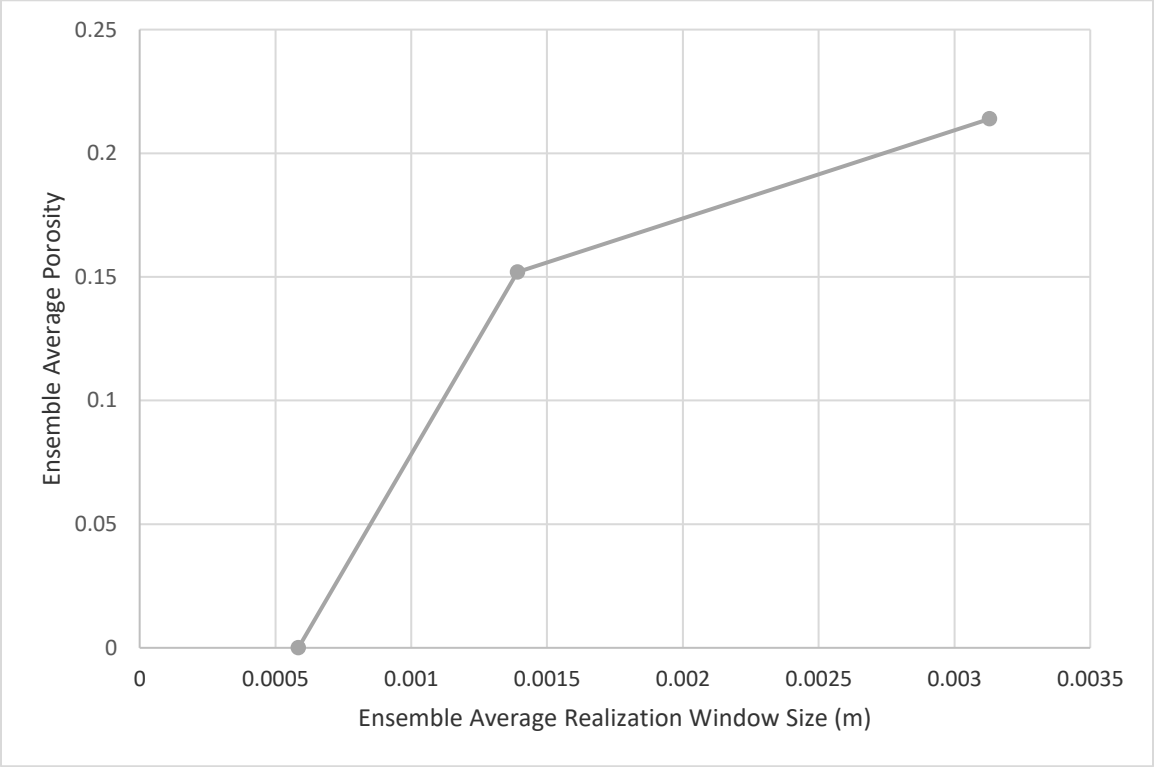

Figure 0.21: Average porosity of ensembles with comminuted PSD at 100 MPa

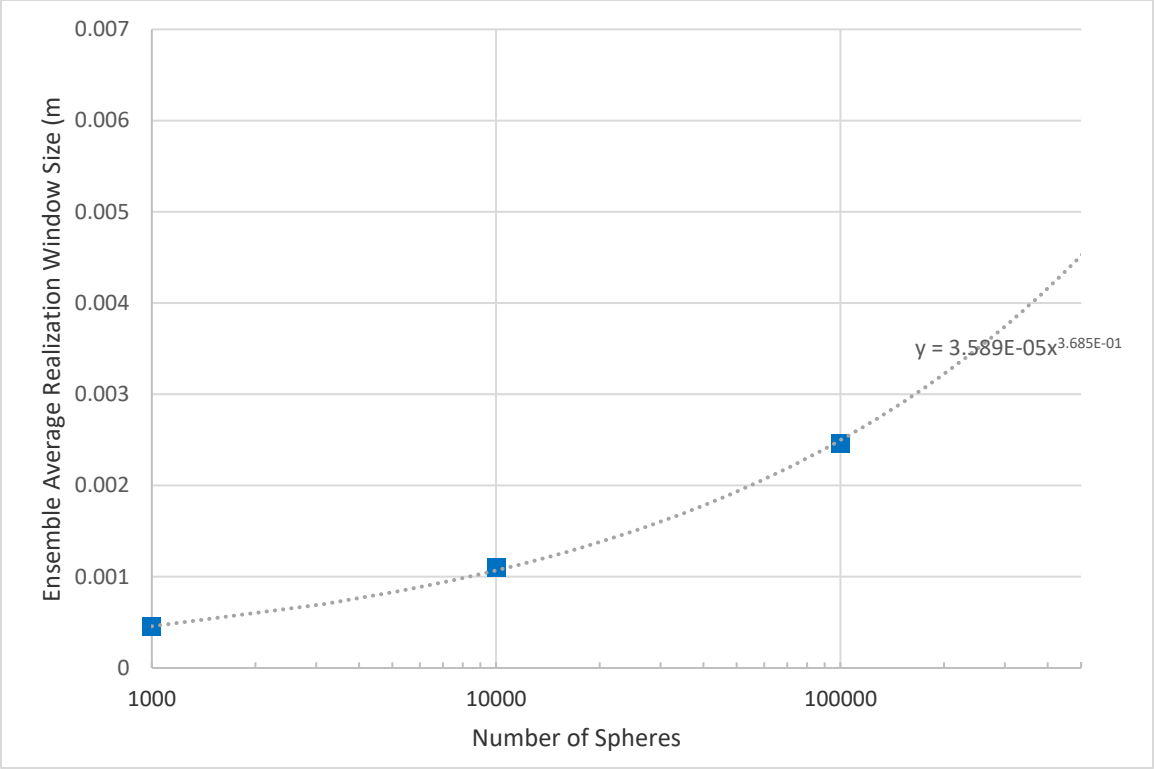

Figure 0.22: Average window size of ensembles with comminuted PSD at 200 MPa

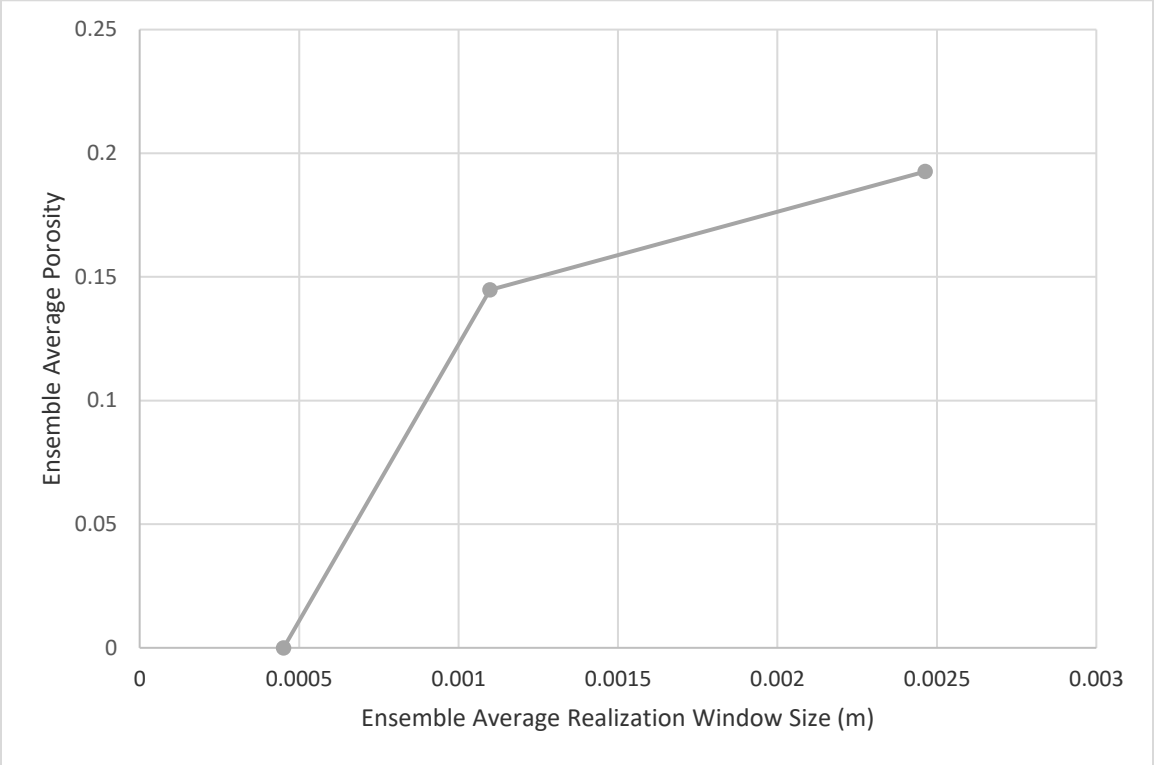

Figure 0.23: Average porosity of ensembles with comminuted PSD at 200 MPa

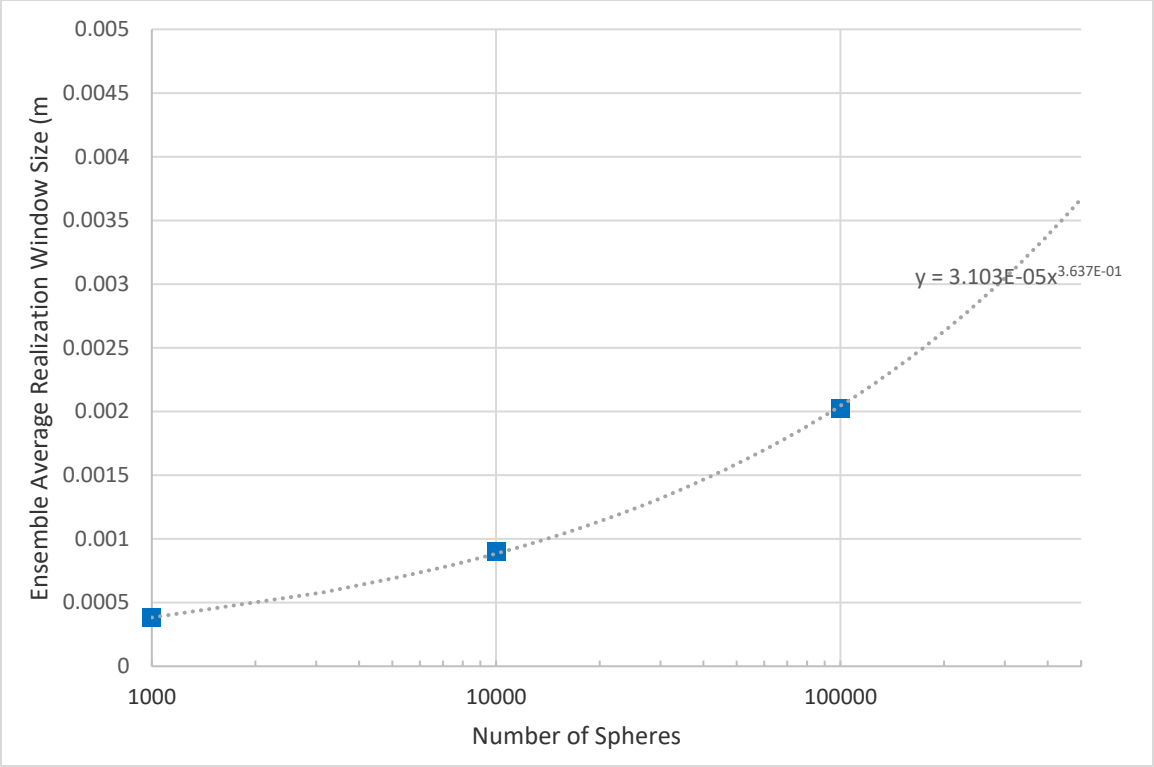

Figure 0.24: Average window size of ensembles with comminuted PSD at 400 MPa

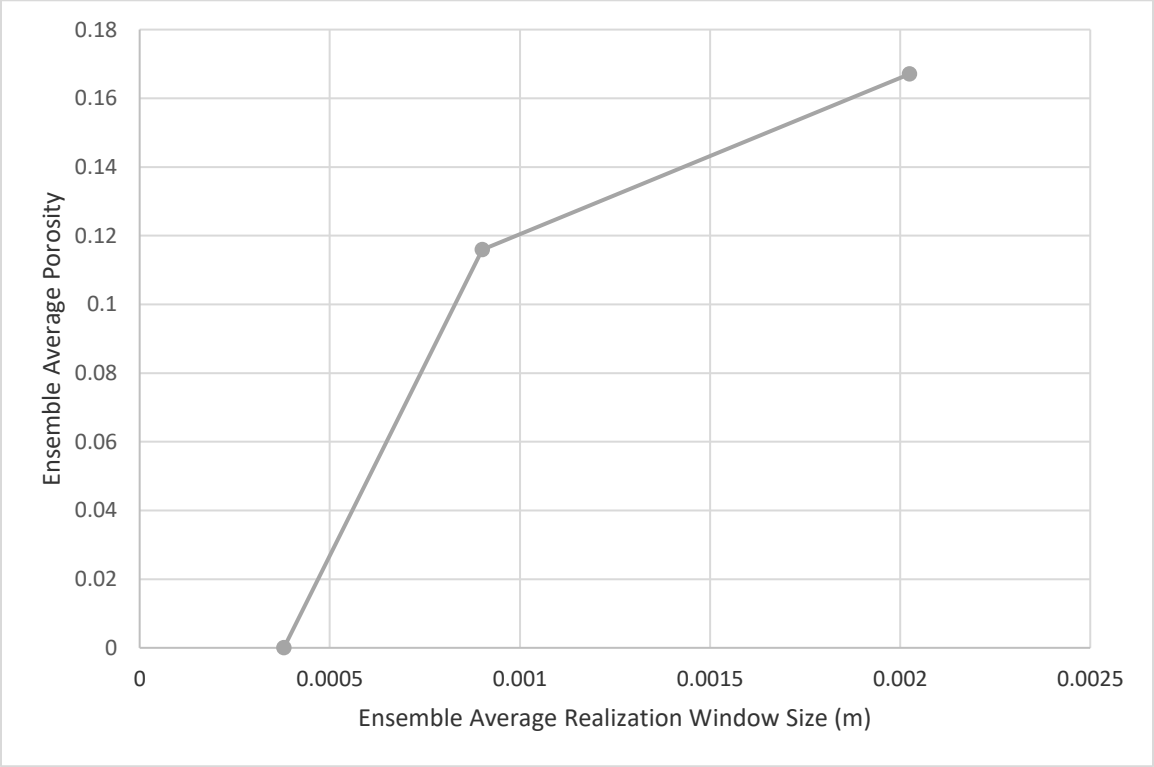

Figure 0.25: Average porosity of ensembles with comminuted PSD at 400 MPa

Computational Homogenization with Comminution

Homogenization results for Eglin sand at relatively low confinements were presented in an earlier section of this chapter. Then, comminution due to crush-up was simulated and described in a subsequent section. In this section, homogenization of Eglin sand proceeds for the higher confinements where comminution is considered.

The histograms of the elastic moduli from the ensemble results can be found in Appendix B Figure 0.1 through Figure 0.36. Figure 0.2 through Figure 0.7 show the ratios of the upper bound average to the lower bound average as they converge to unity (Hill condition)

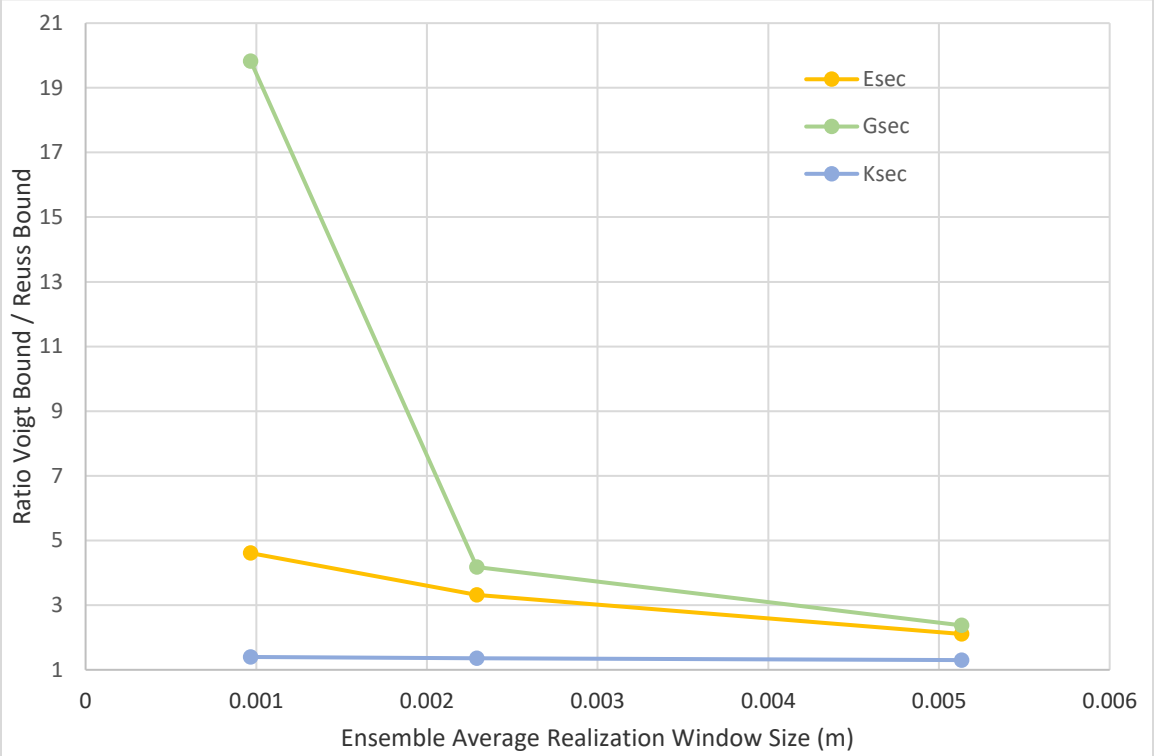

Figure 0.26: Ratios of elastic moduli Voigt to Reuss bounds at 20 MPa confinement

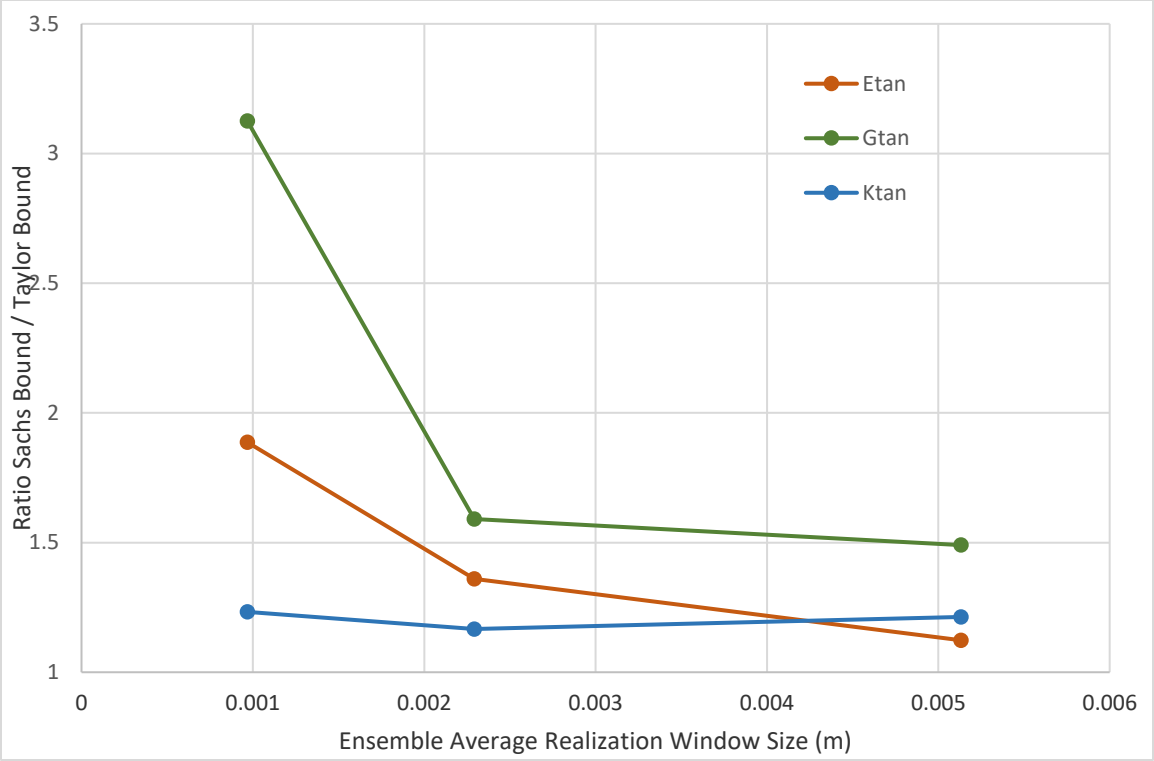

Figure 0.27: Ratios of elastic moduli Sachs to Taylor bounds at 20 MPa confinement

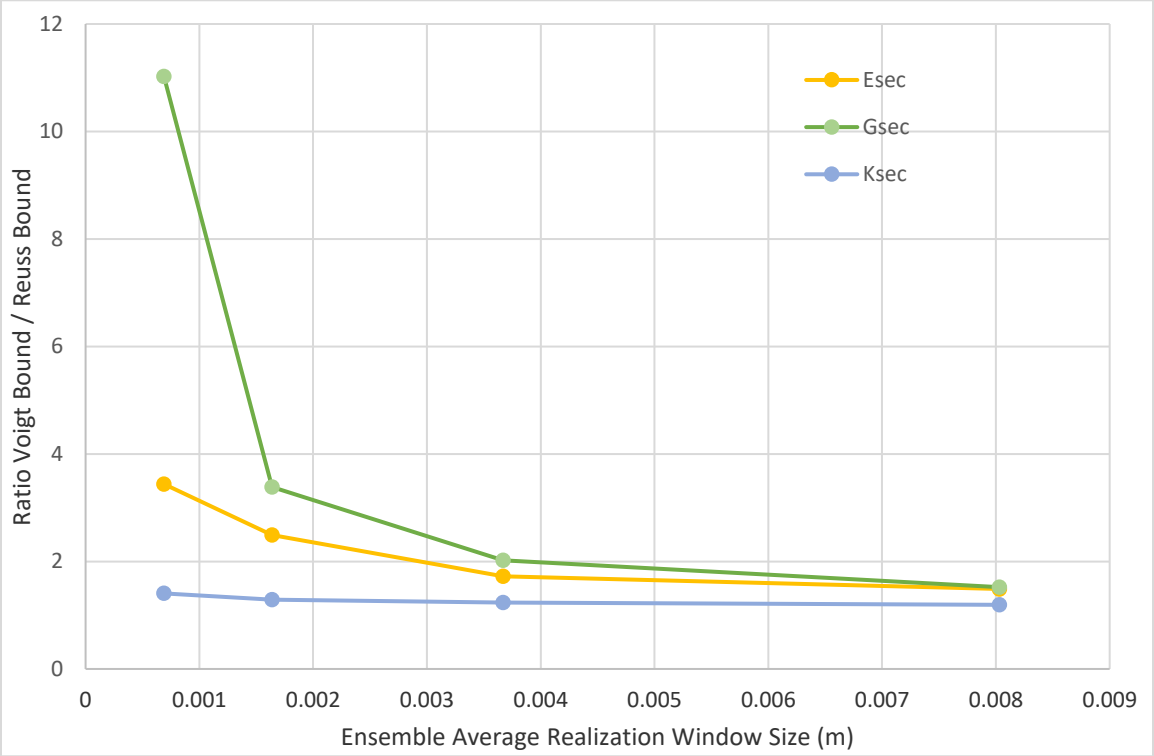

Figure 0.28: Ratios of elastic moduli Voigt to Reuss bounds at 50 MPa confinement

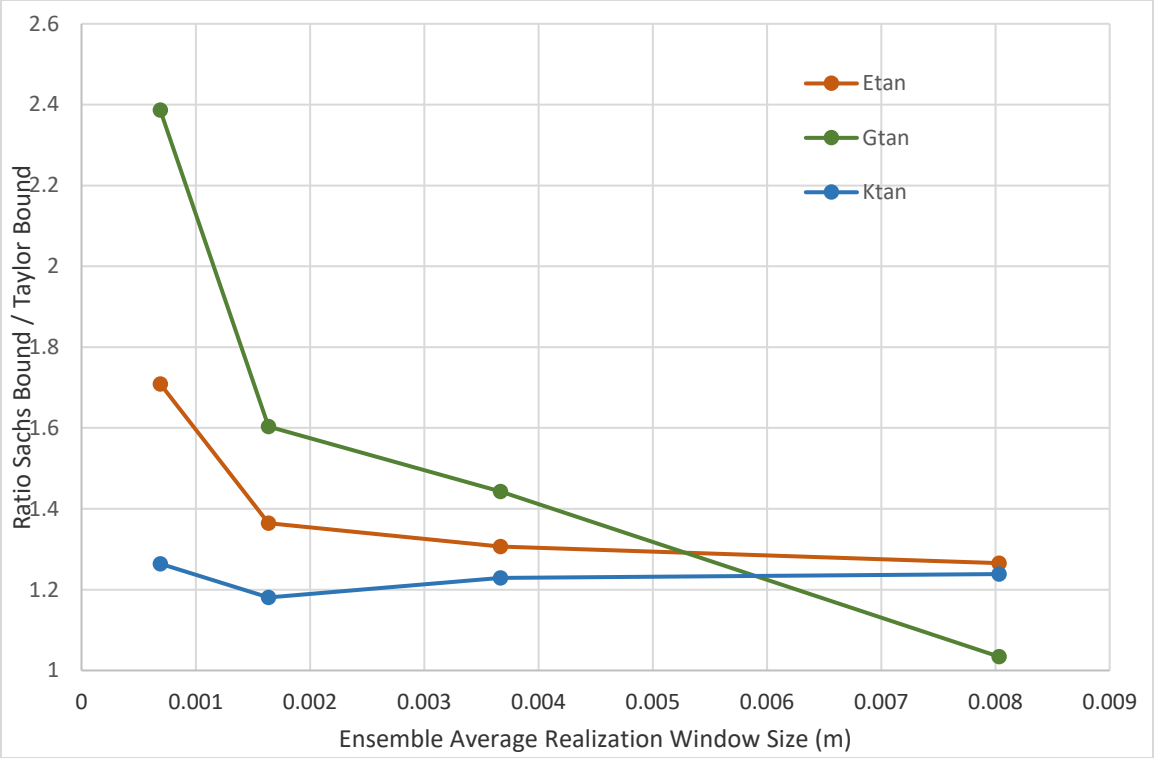

Figure 0.29: Ratios of elastic moduli Sachs to Taylor bounds at 50 MPa confinement

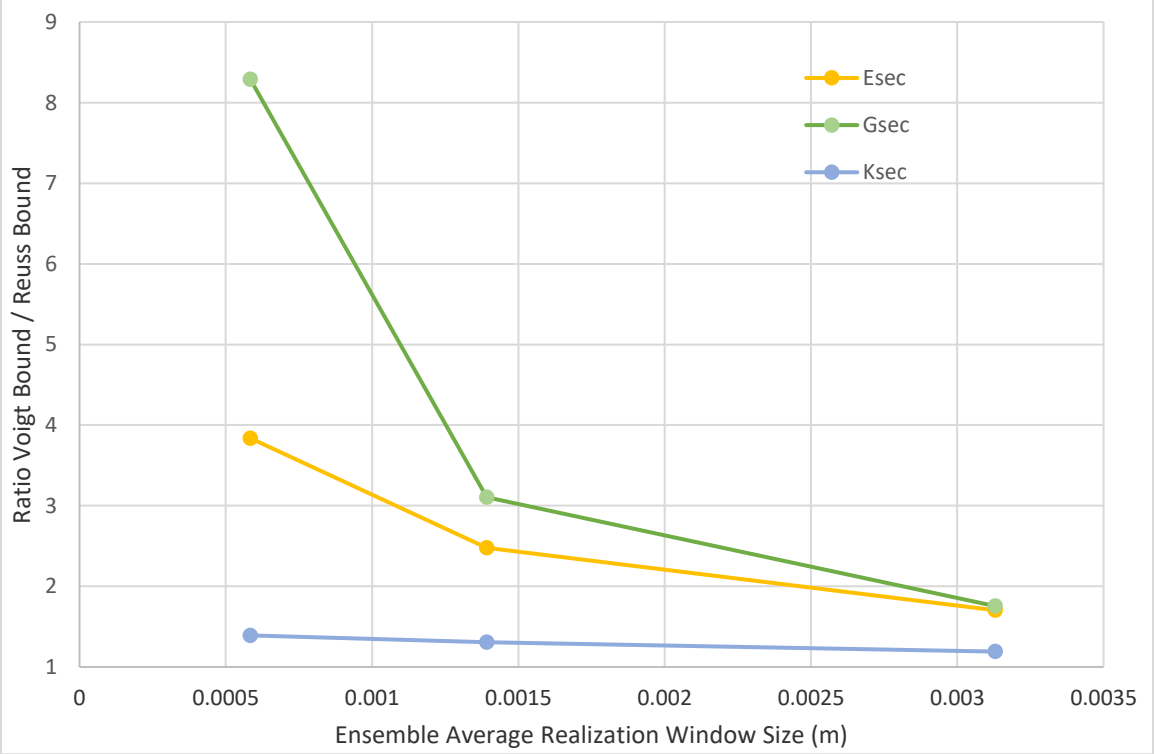

Figure 0.30: Ratios of elastic moduli Voigt to Reuss bounds at 100 MPa confinement

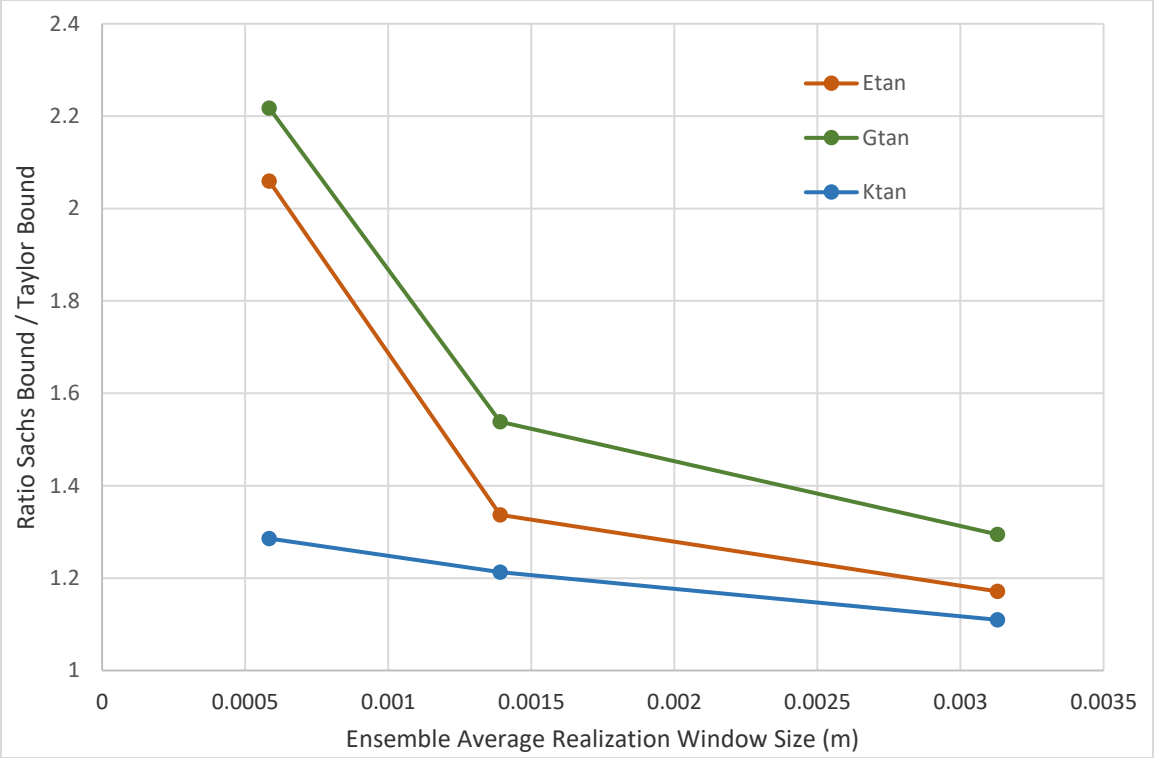

Figure 0.31: Ratios of elastic moduli Sachs to Taylor bounds at 100 MPa confinement

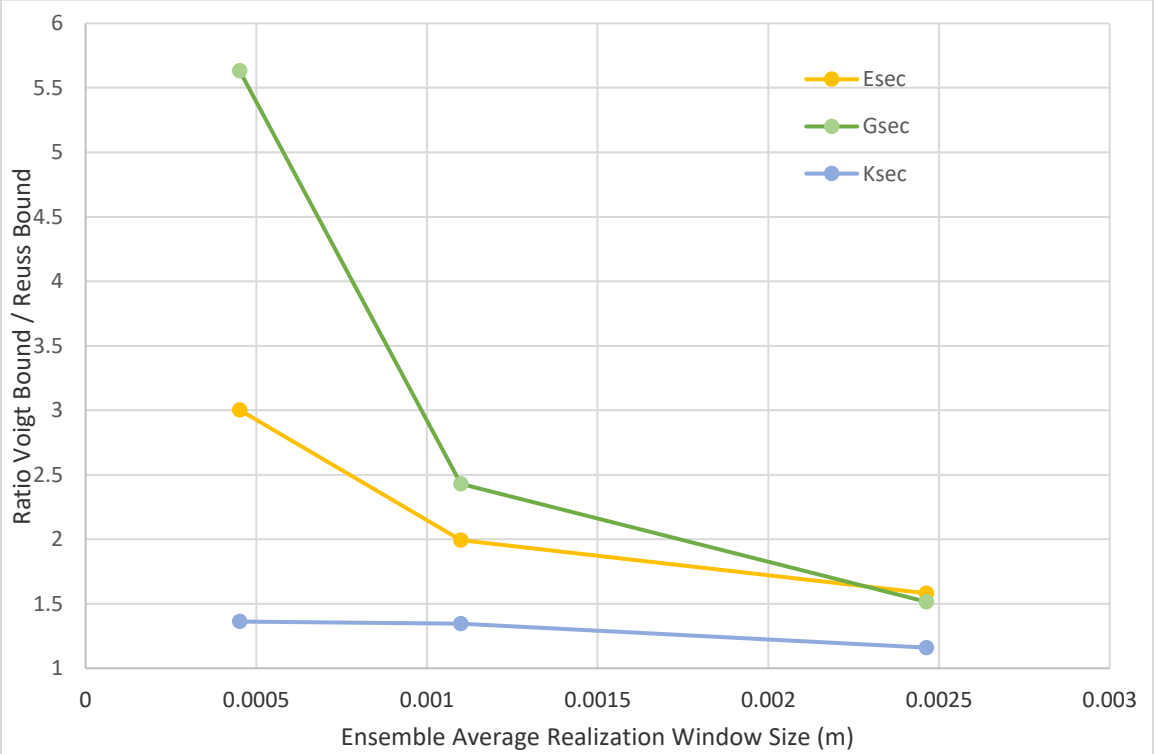

Figure 0.32: Ratios of elastic moduli Voigt to Reuss bounds at 200 MPa confinement

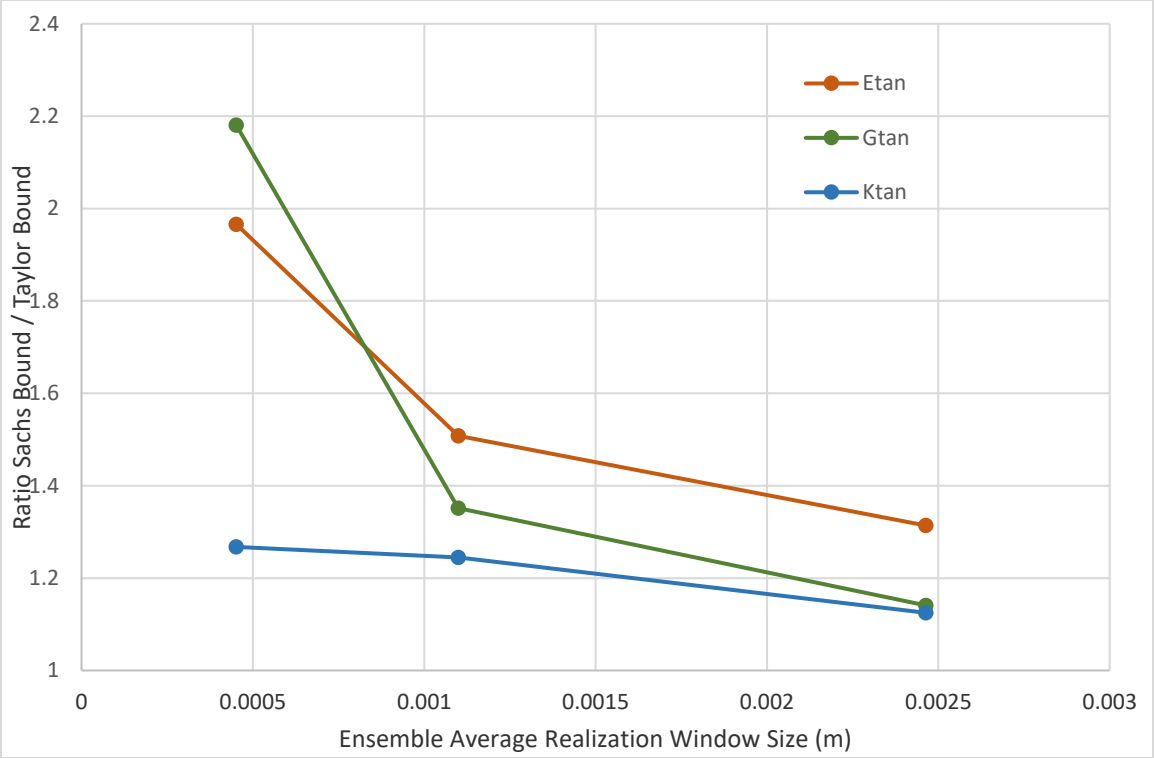

Figure 0.33: Ratios of elastic moduli Sachs to Taylor bounds at 200 MPa confinement

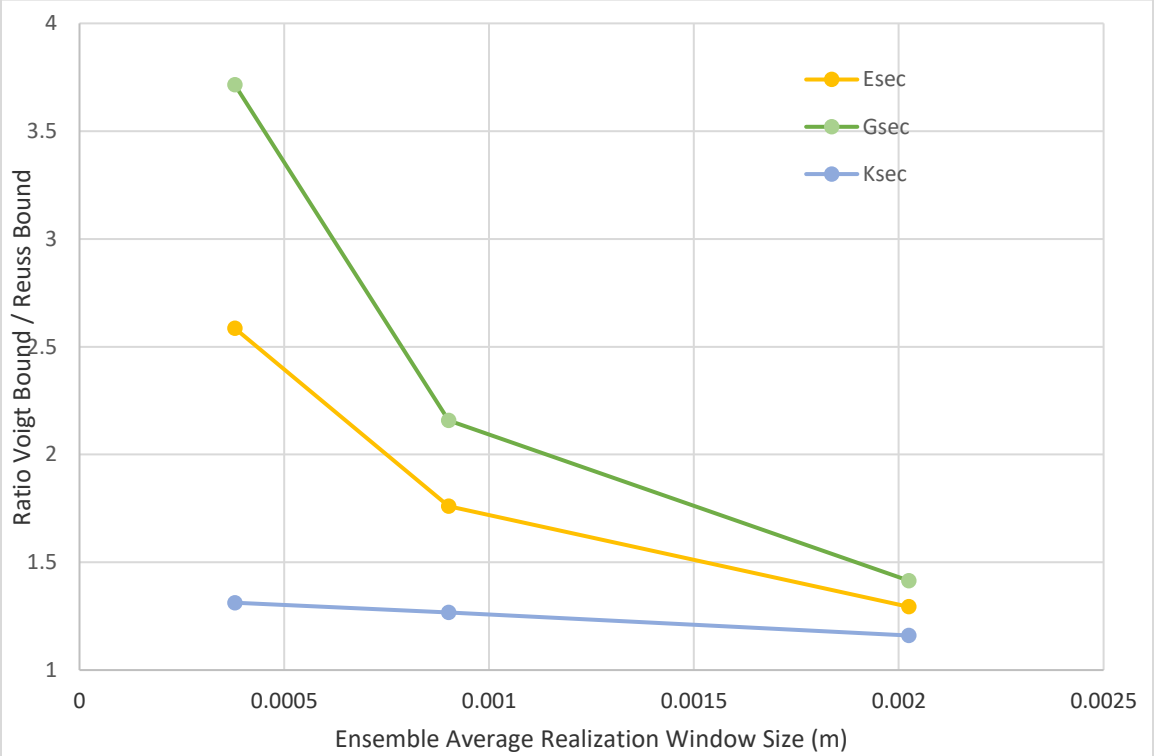

Figure 0.34: Ratios of elastic moduli Voigt to Reuss bounds at 400 MPa confinement

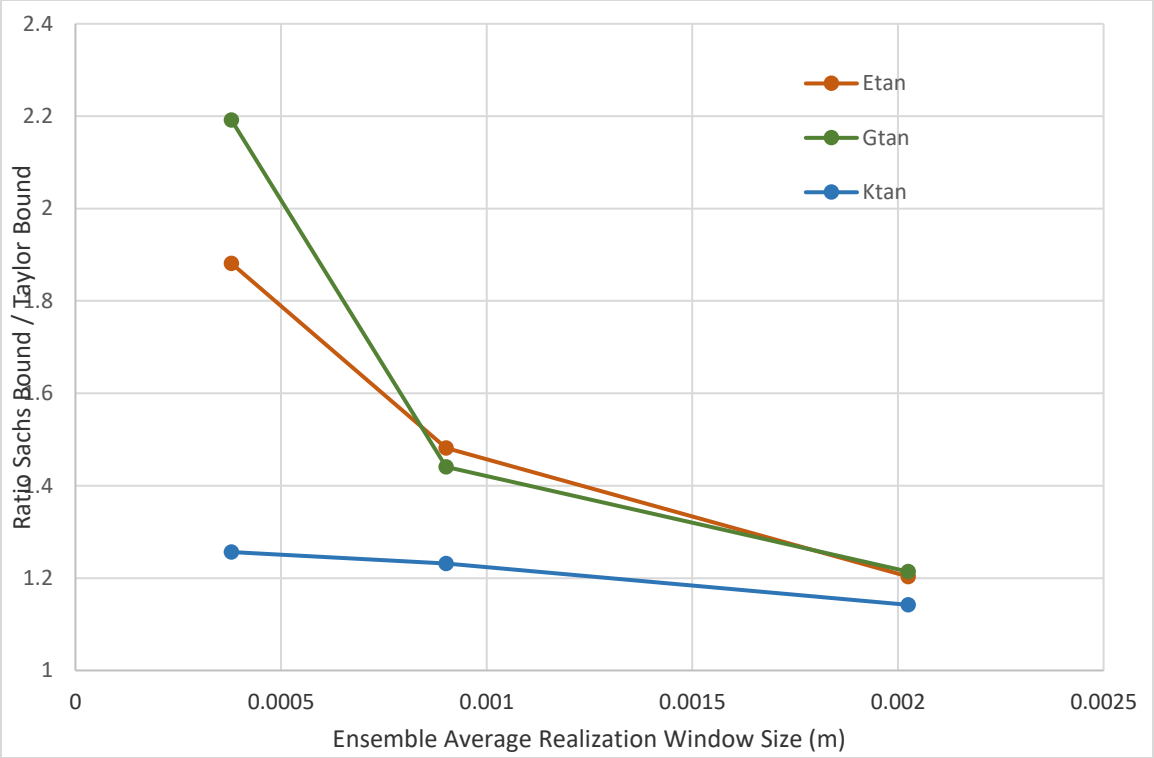

Figure 0.35: Ratios of elastic moduli Sachs bound to Taylor bound at 400 MPa confinement

Ensemble Averaged Finite Strain Response

In the previous sections, a homogenization study of Eglin sand was carried out using the novel surface-tracked microboundaries introduced in this framework. Implementation of these microboundaries allows evaluation of the linear Reuss and Voigt bounds, as well as the nonlinear Sachs and Taylor bounds. The microboundary surface tracking is very robust and has worked to perfection in the tens of thousands of simulations whose results have been presented thus far. They are also capable of applying large strains and capturing those deformation and stresses. As an example, Figure 0.36 shows isotropic compression of an ensemble of $1x10^4$ particles to volumetric strains of approximately 24% using both Static Uniform (SUBC) and Kinematic Uniform (KUBC) boundaries.

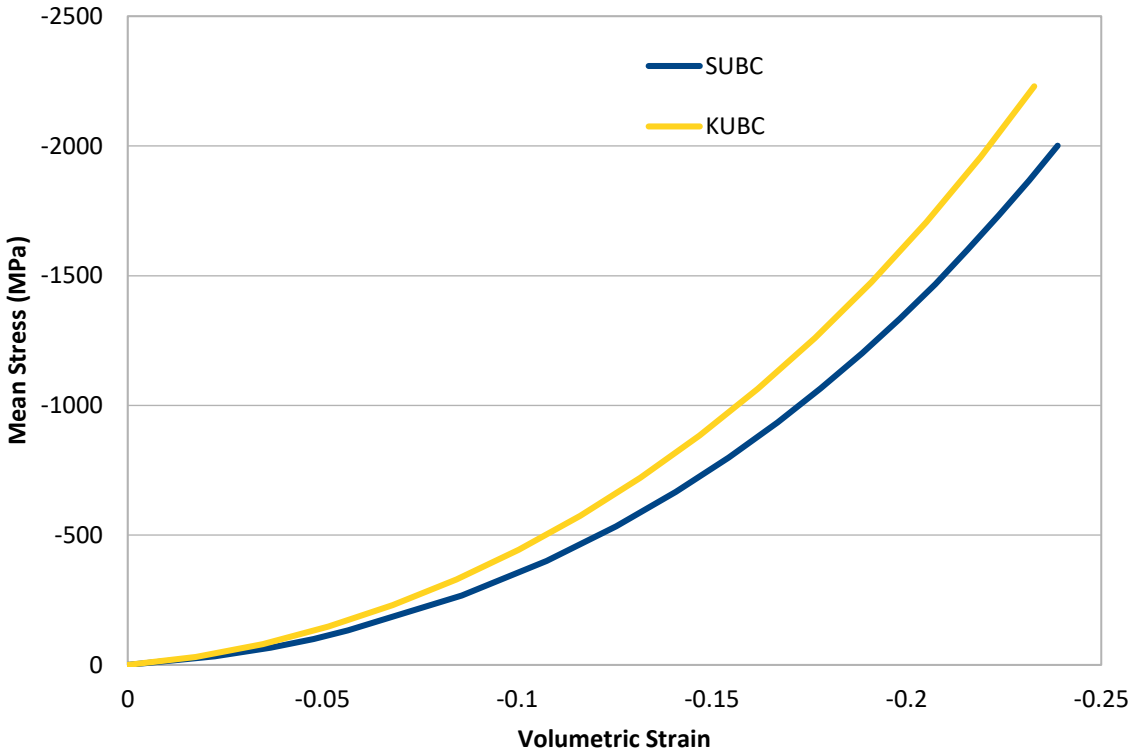

Figure 0.36: Isotropic compression of Eglin sand using SUBC and KUBC

However, there is an additional wrinkle when crush-up is taken into account. The computational cost of applying the surface-tracking algorithm while also continuously replacing grains with Apollonian spherical packings, is simply too great. Even the smallest realizations must run continuously for at least a month to achieve the magnitude of deformations that are of interest here. Fortunately, as was shown in the previous section, using Periodic Boundaries (PBC) yields an ensemble response distribution that converges to the response distribution found when partitioning the RVE. This implies PBCs can be used to simulate the ensemble response at finite strains with grain crush-up modeled continuously.

Figure 0.37 presents the ensemble average results of isotropic compression with PBCs alongside the volumetric stress-strain curve from the triaxial testing of Martin and Cazacu [168]. It has been the goal of this current study to propagate the microscale and mesoscale data through mesoscale simulation without making any arbitrary assumptions

on behavior other than those present in the Discrete Element Method. While much is known about the microscale characteristics of Eglin sand, there are some things that are not known that are relevant to the current framework. One such missing piece is whether fragmentation of the sand grains results in any additional air voids being created. This is sometimes referred to as intra-granular porosity, or double porosity. In Figure 0.37, three different mesoscale ensemble simulations are presented, with internal porosities of 0, 0.1, and 0.2. Note that the concept of double porosity does not necessarily apply only to air voids present within the grain prior to fracture. If crush-up is not completely dominated by fragmentation, but undergoes abrasion and attrition, this will result in a significant volume of ultra-fine particles.

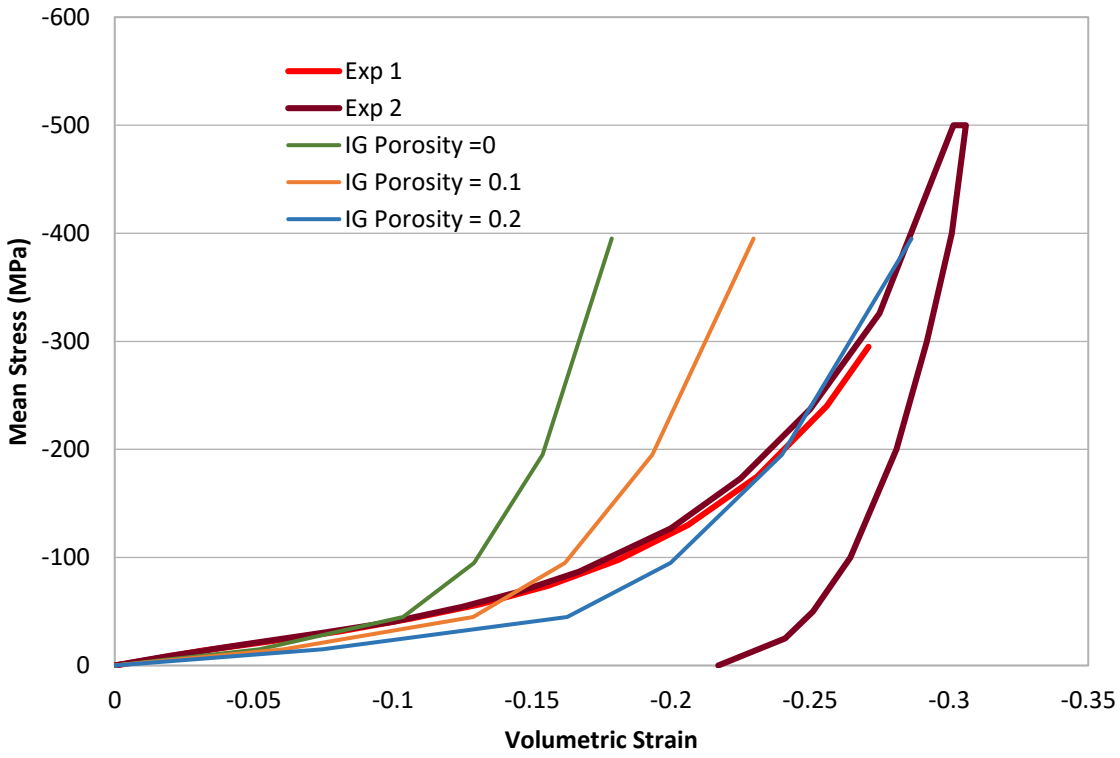

Figure 0.37: Eglin Sand volumetric compression response at mean stress up to 400 MPa

The response of the mesoscale ensemble simulations captures the "shape" of the experimental testing quite well. It is clear that some double porosity should be assumed,

however this only comes about at higher confinements. A linear interpolation is shown in Figure 0.38 along with unloading points at each of the confinement levels treated in this study. Note that the bulk response curve shows load-unload points. The paths are linear representations of the difference between the points, the actual loading path was not computed between those points and is not going to be linear if computed.

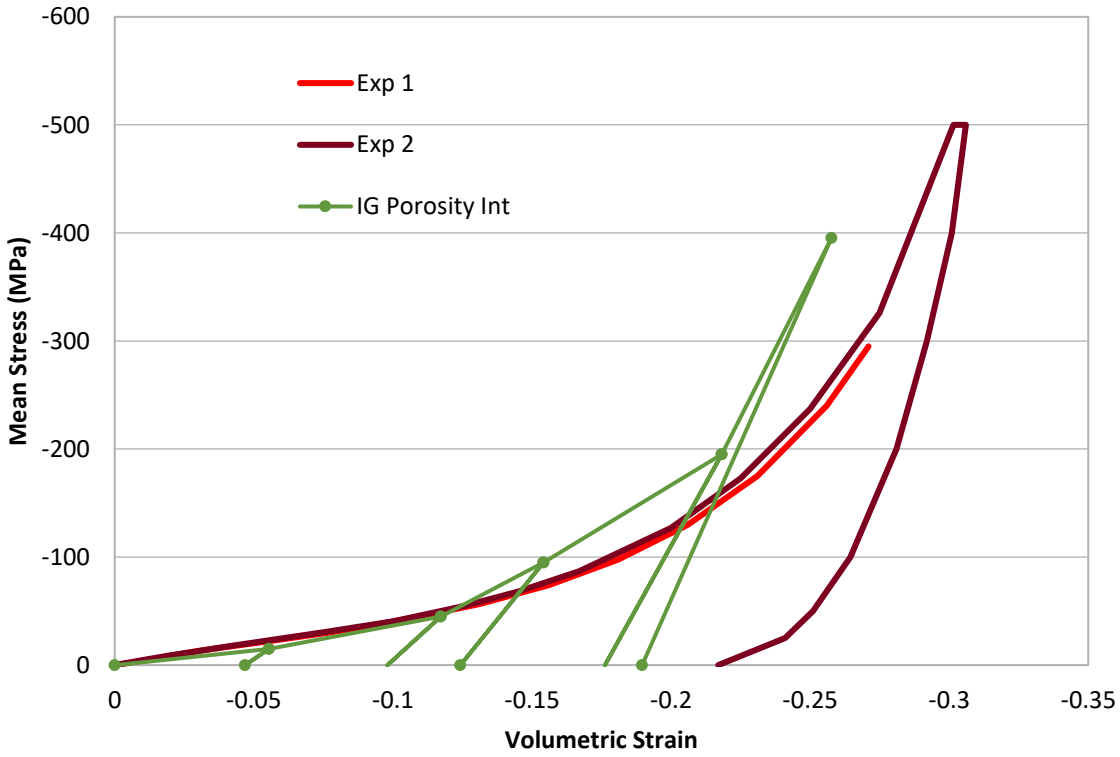

Figure 0.38: Volumetric response with interpolated double porosity

Next, the finite strain response under the simulated deviatoric loading paths of confined triaxial compression tests (CTC) is presented. The deviatoric phase of the CTC tests consists of maintaining lateral confinement while increasing the axial strain.

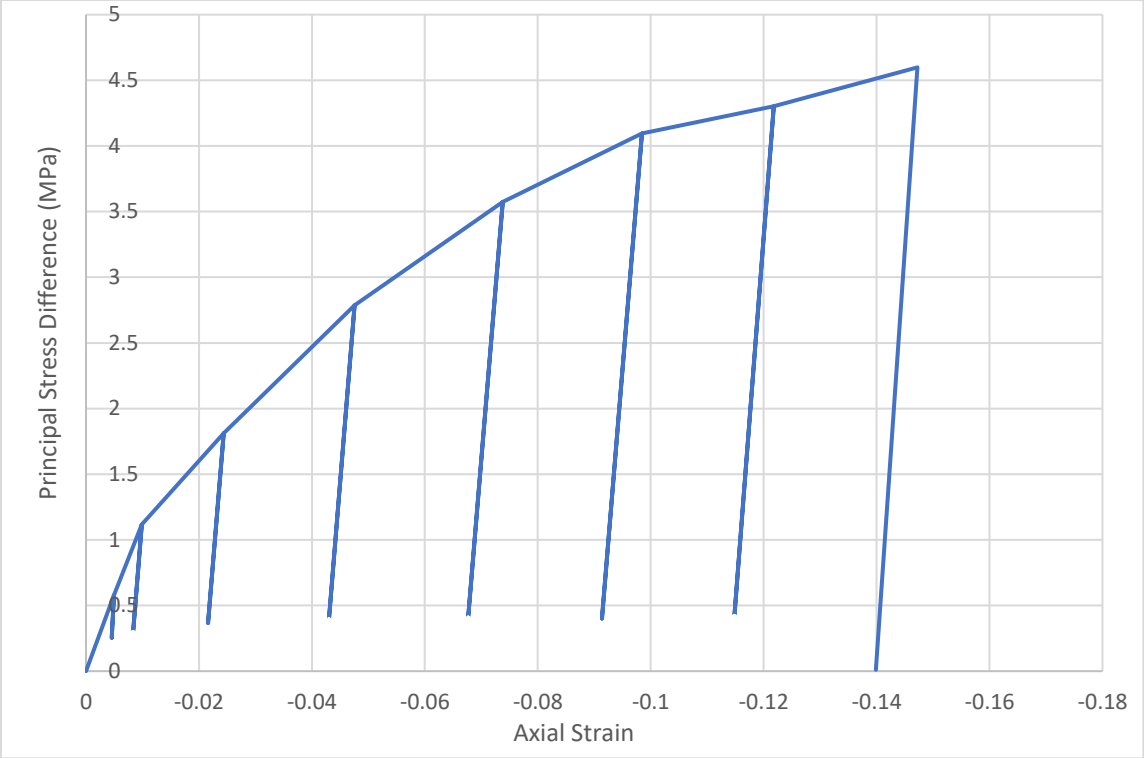

Figure 0.39: Deviatoric response of CTC axial loading at 20 MPa confinement

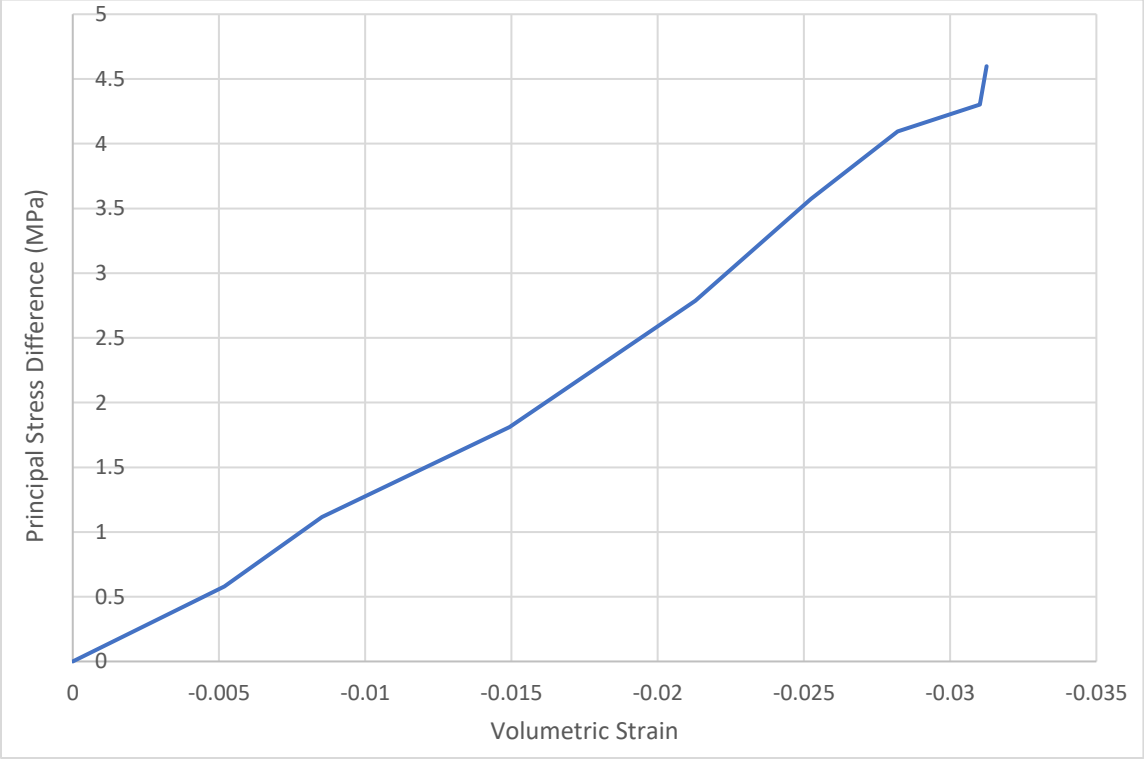

Figure 0.40: Volumetric response of CTC axial loading at 5 MPa confinement

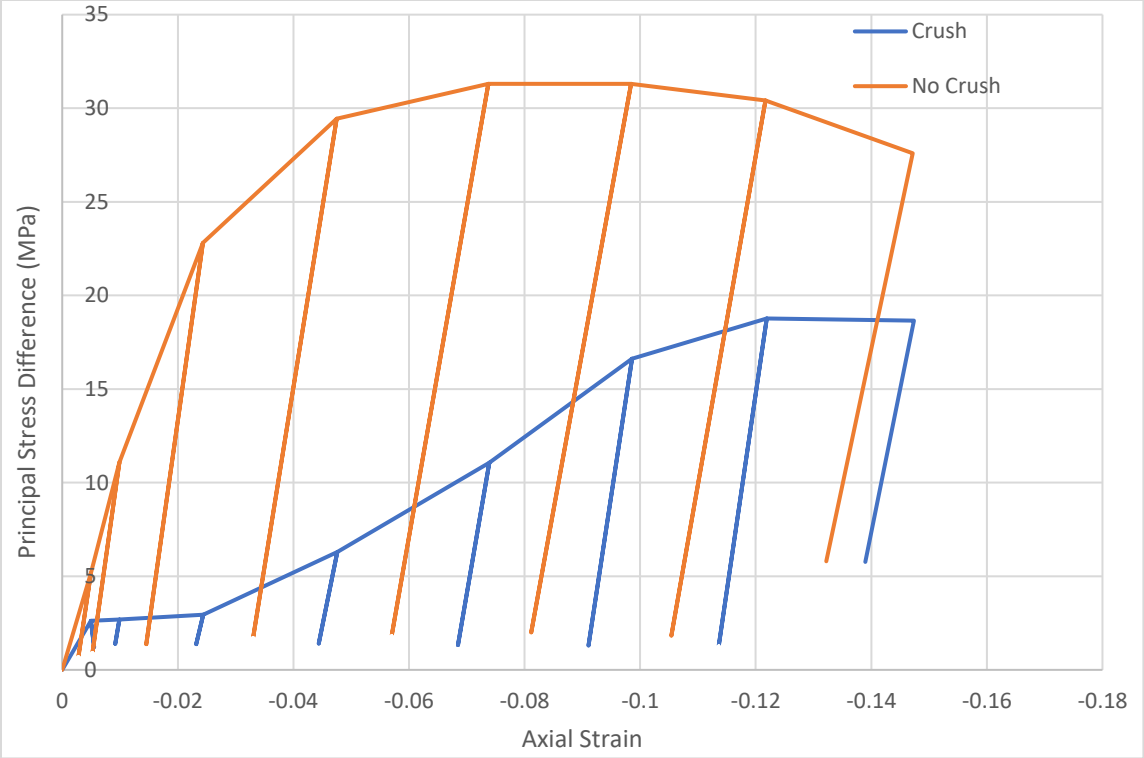

Figure 0.41: Deviatoric response of CTC axial loading at 20 MPa confinement

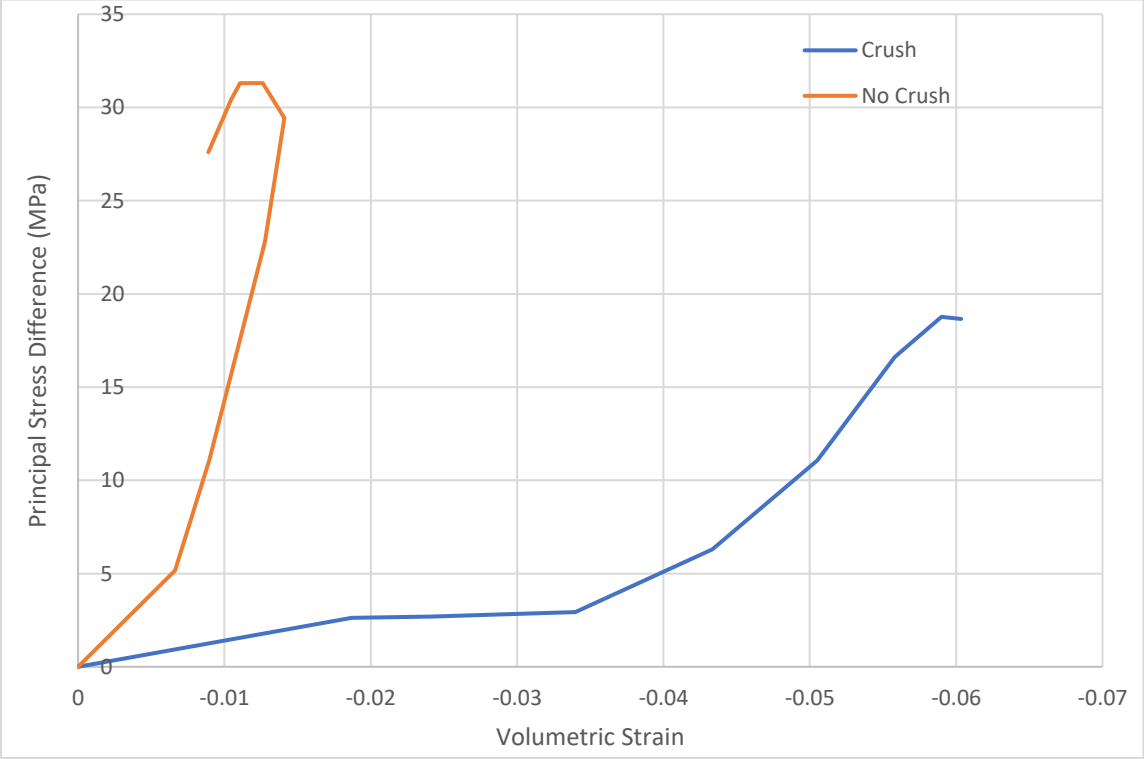

Figure 0.42: Volumetric response of CTC axial loading at 20 MPa confinement

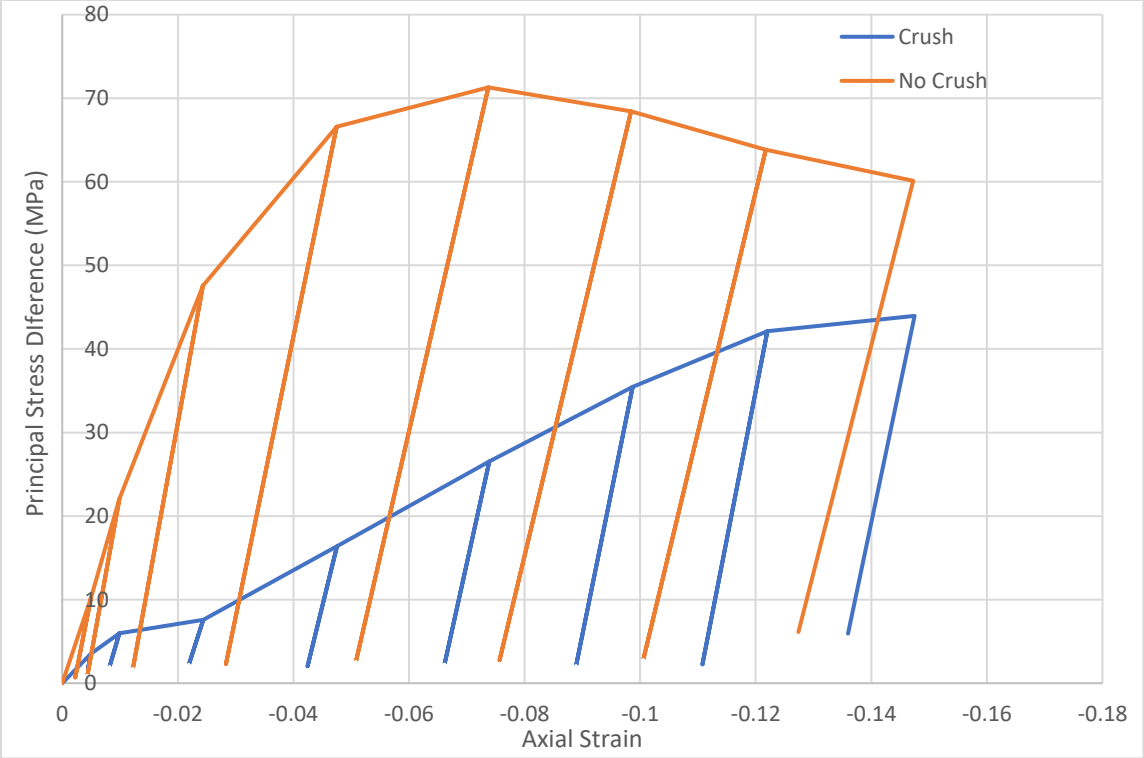

Figure 0.43: Deviatoric response of CTC axial loading at 50 MPa confinement

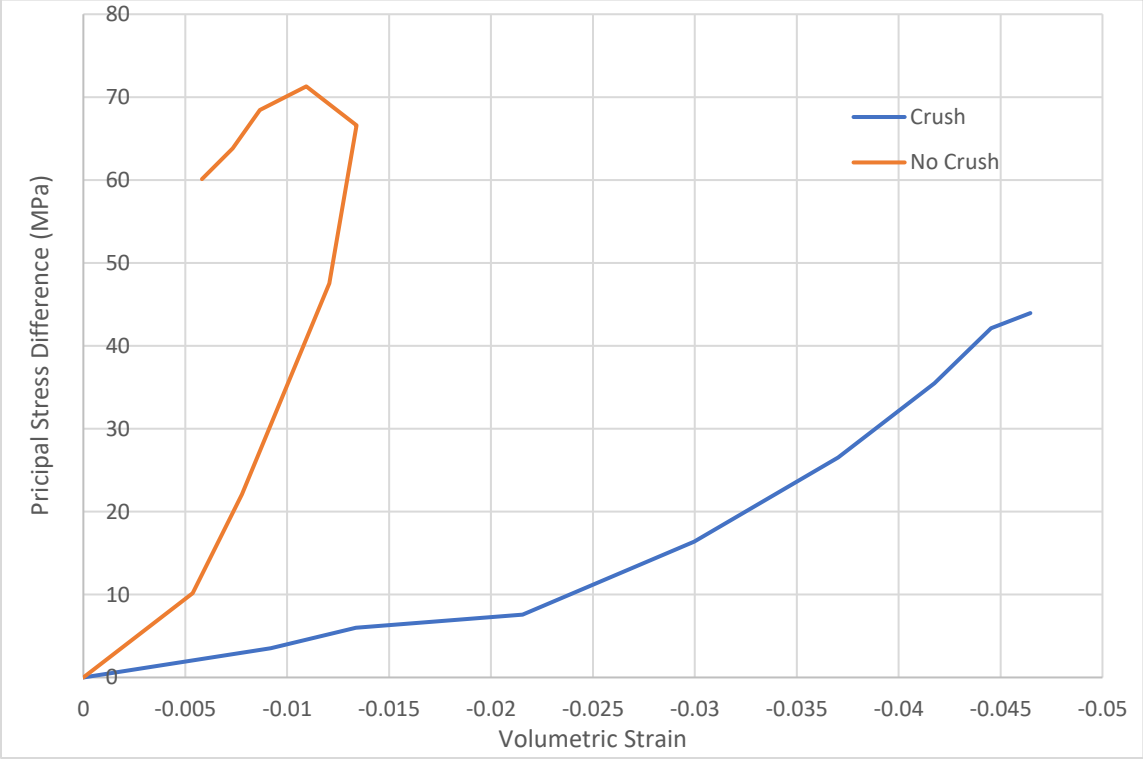

Figure 0.44: Volumetric response of CTC axial loading at 50 MPa confinement

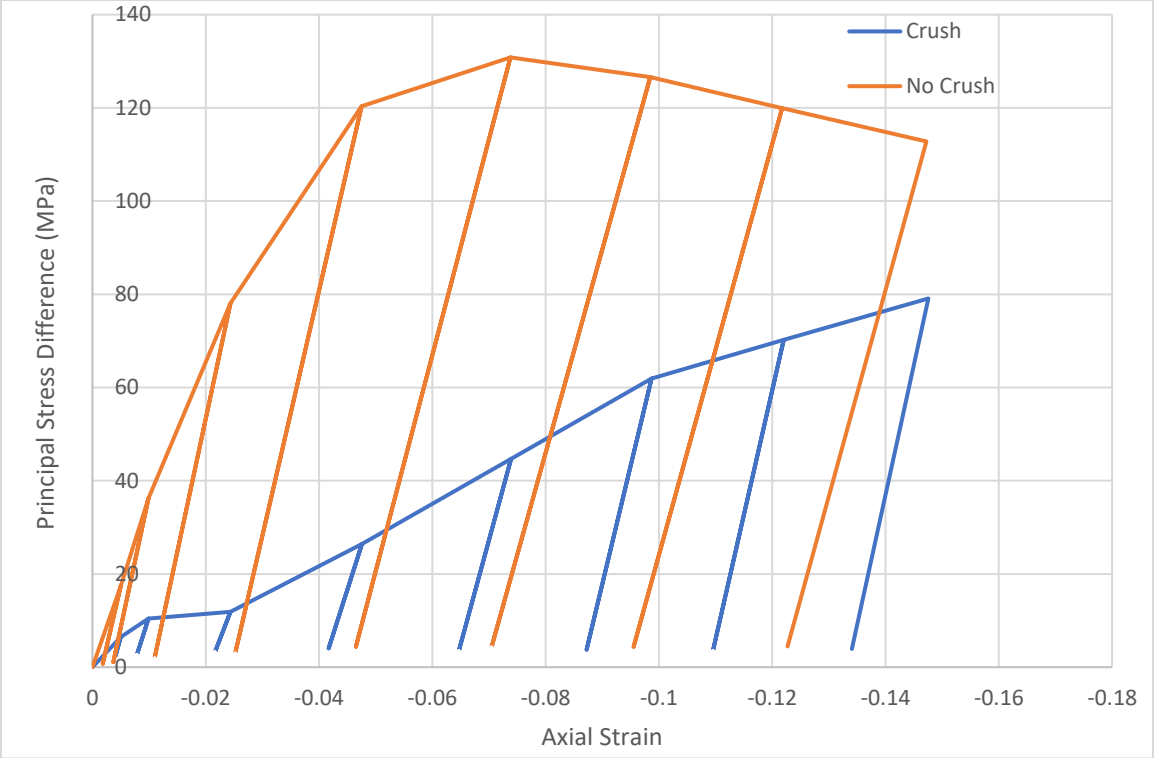

Figure 0.45: Deviatoric response of CTC axial loading at 100 MPa confinement

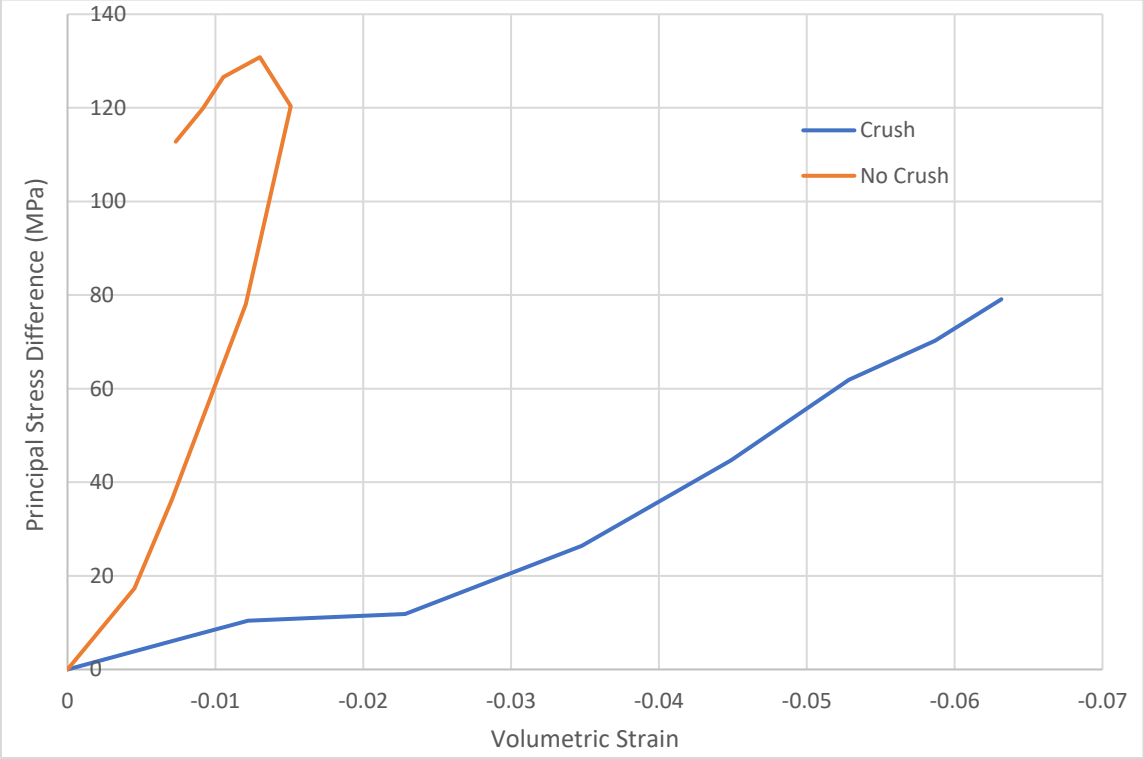

Figure 0.46: Volumetric response of CTC axial loading at 100 MPa confinement

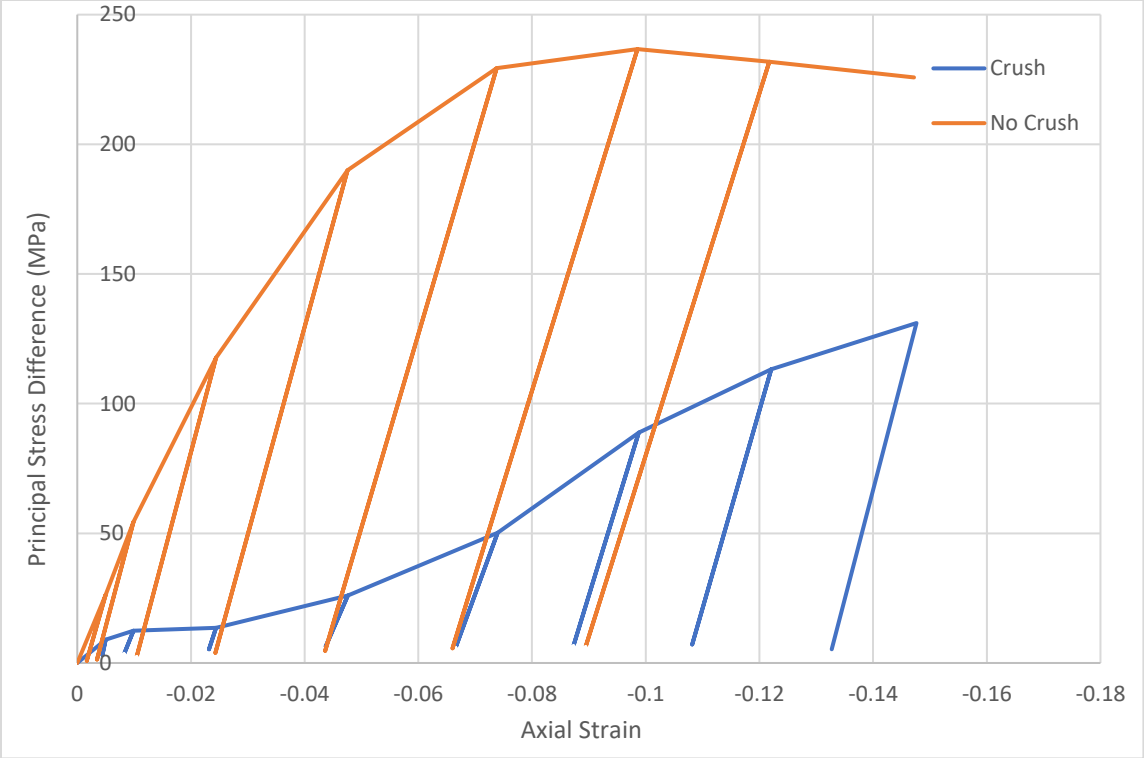

Figure 0.47: Deviatoric response of CTC axial loading at 200 MPa confinement

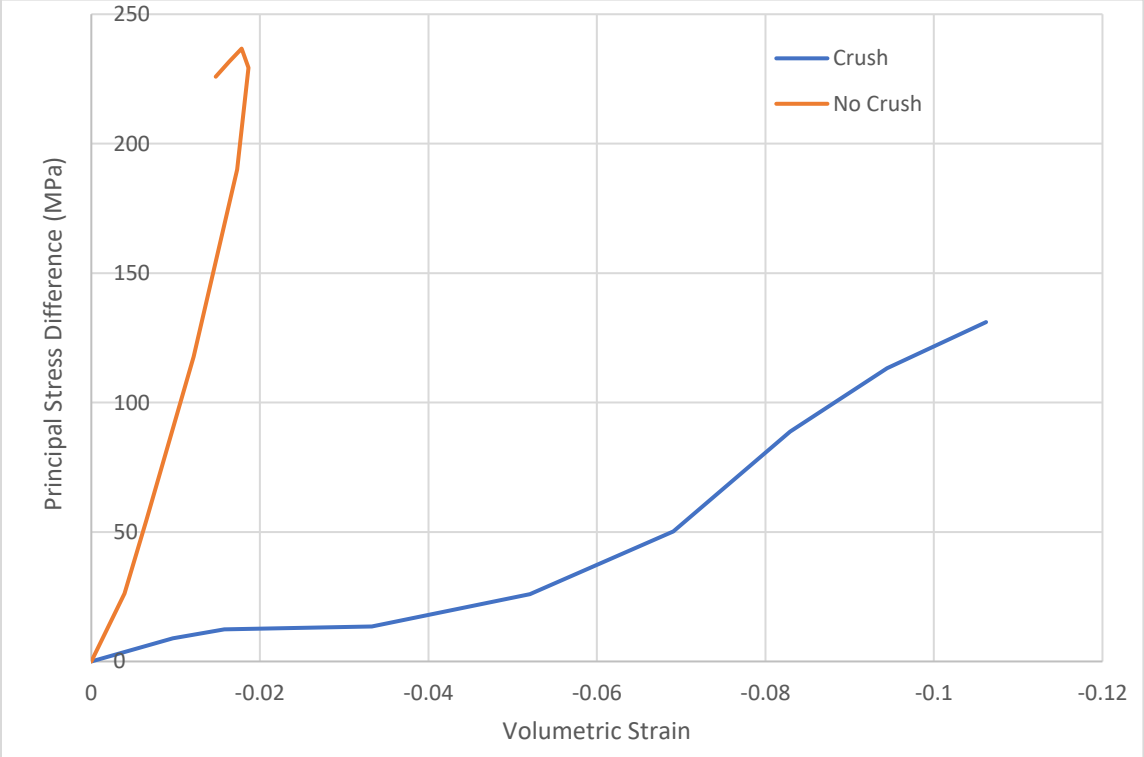

Figure 0.48: Volumetric response of CTC axial loading at 200 MPa confinement

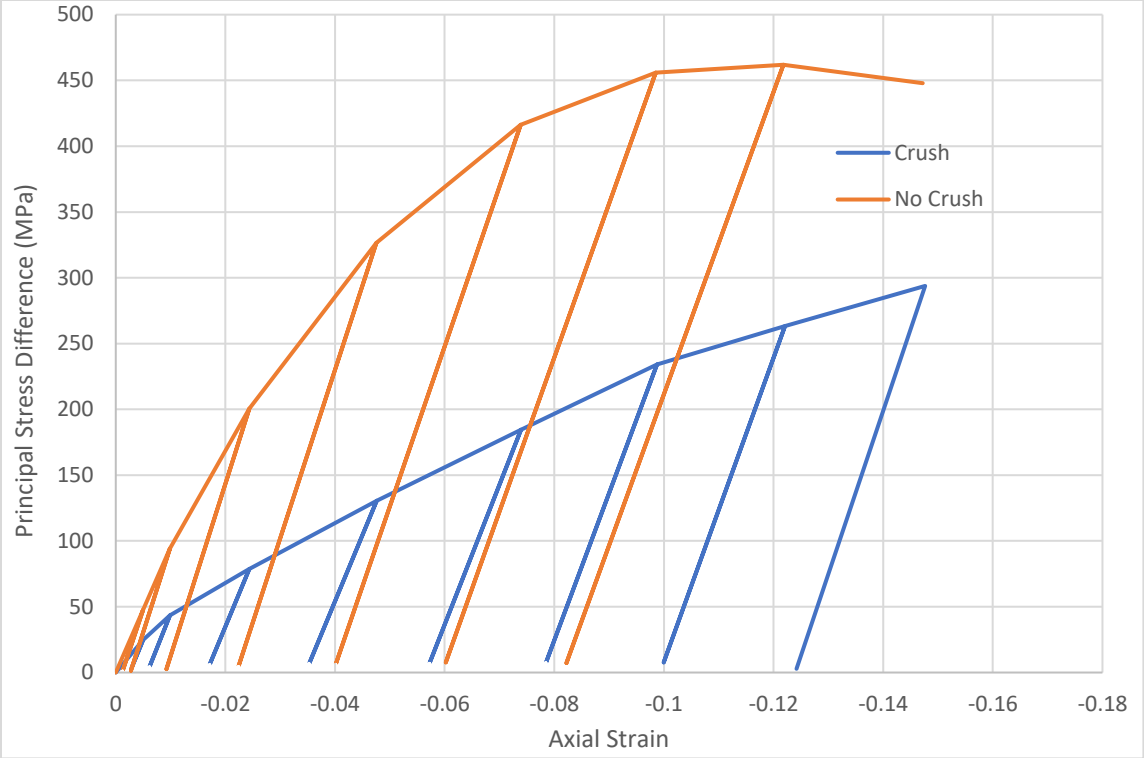

Figure 0.49: Deviatoric response of CTC axial loading at 400 MPa confinement

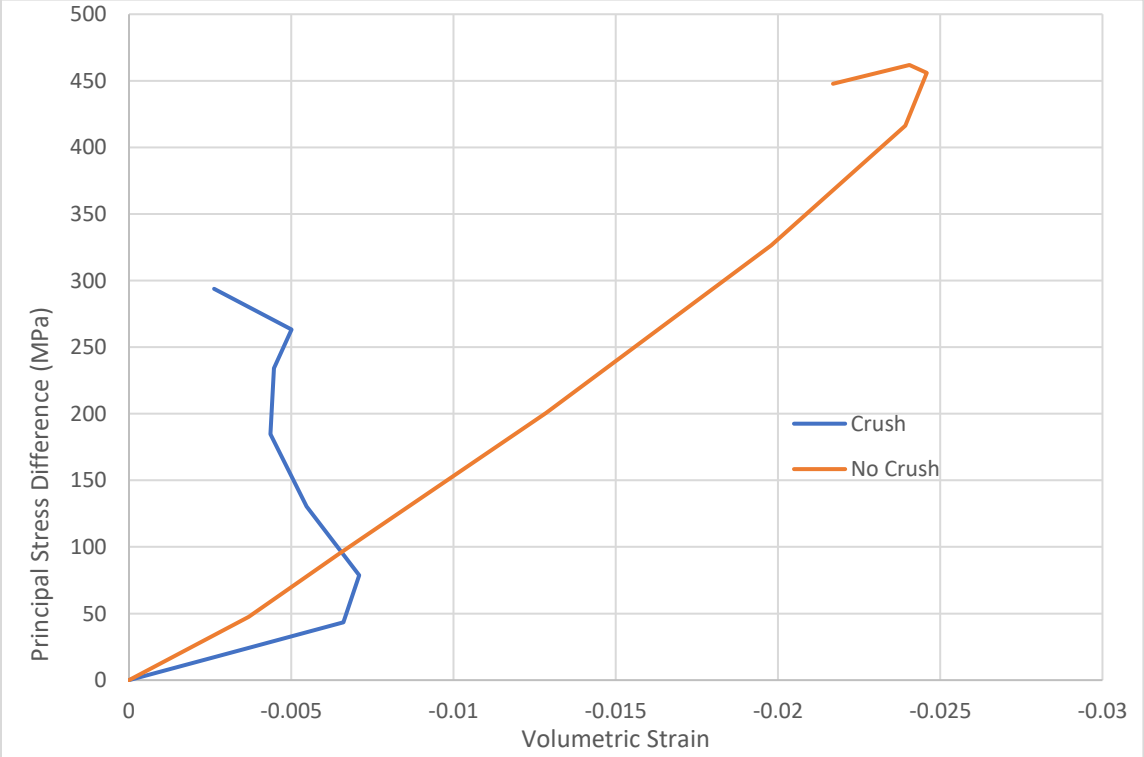

Figure 0.50: Volumetric response of CTC axial loading at 400 MPa confinement

Ensemble Thermomechanical Statistics of Eglin Sand

The mesoscale ensemble simulations can clearly be used to evaluate the response of particulate media along many different loading paths and at various scales up to and including the macroscale. However, there is an additional bonus to explicitly modeling the response and evolution of a particulate material with discrete particles. The strain energy can be monitored during simulation, giving insight into the internal variable evolution. If the virtual work done in a simulation is monitored, its components can be readily extracted. Loading a realization to a certain stress tensor, then unloading it can be used to obtain the 1) total work done during loading, 2) recoverable elastic and plastic free energy during unloading 3) total plastic dissipation. For a thorough review of the thermomechanical statistics considered here, the reader is pointed to the work of Yang et al. [173].

Figure 0.51 shows the total work during the loading phase of the ensemble simulation, the total energy recovered during unloading, as well as the energy dissipated due to particle sliding as well as crushing. The energy recovered here is made up of both elastic energy and plastic free energy that can be recovered.

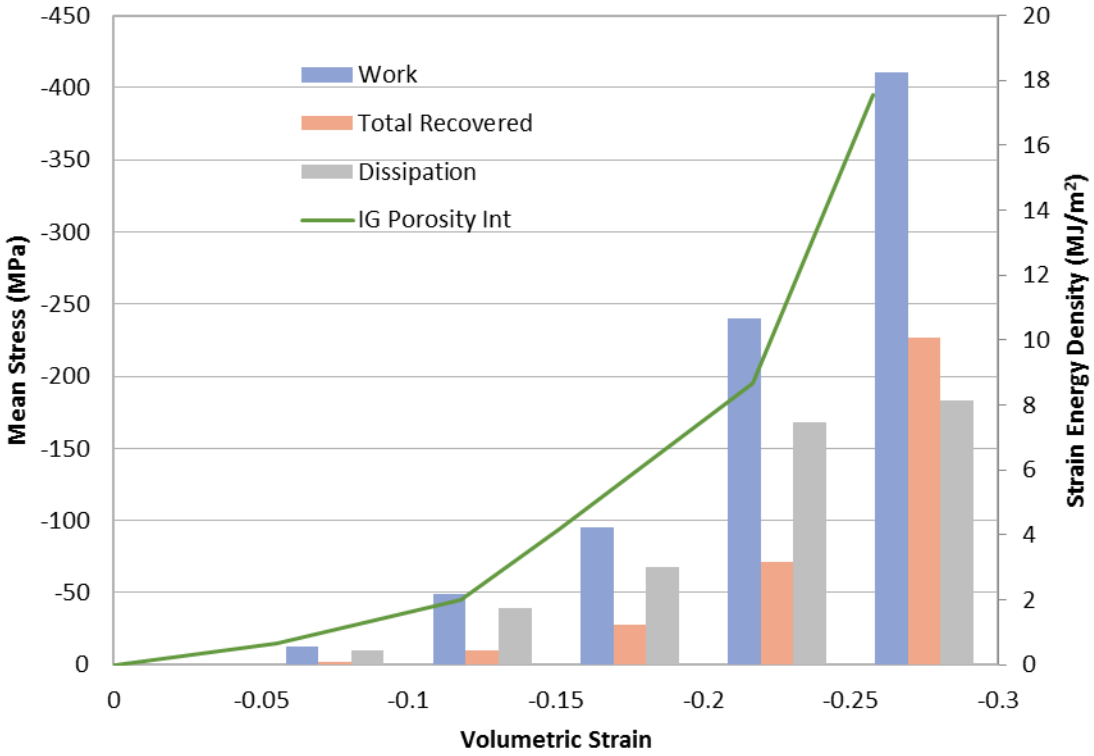

Figure 0.51: Work and energy dissipation during volumetric loading

Next, the work done during the deviatoric loading phases of the CTC tests are is presented. The deviatoric phase of the CTC tests consists of maintaining lateral confinement while increasing the axial strain. For each deviatoric loading test, two charts are presented, one showing the response and strain energy density for the case where crush-up is allowed to occur during the deviatoric phase, and one with no crush-up. For deviatoric loading at 5 MPa confinement, only one chart is shown, since crush-up is virtually non-existent until higher mean stresses are reached.

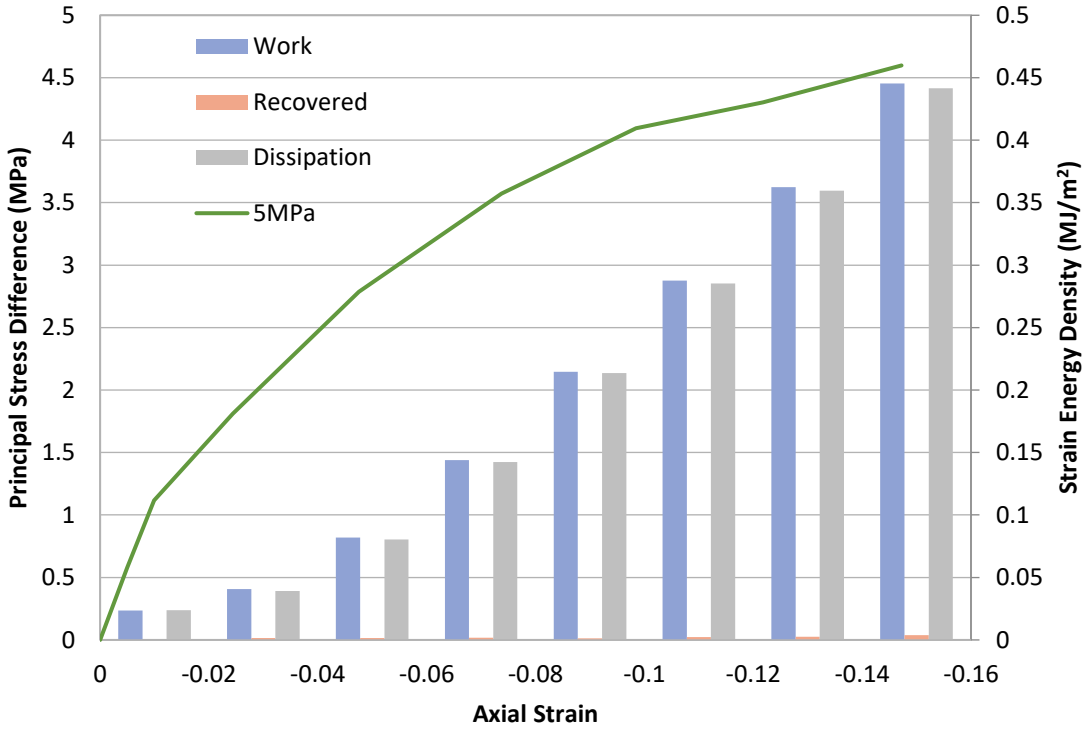

Figure 0.52: Work and dissipation during CTC axial loading at 5 MPa confinement

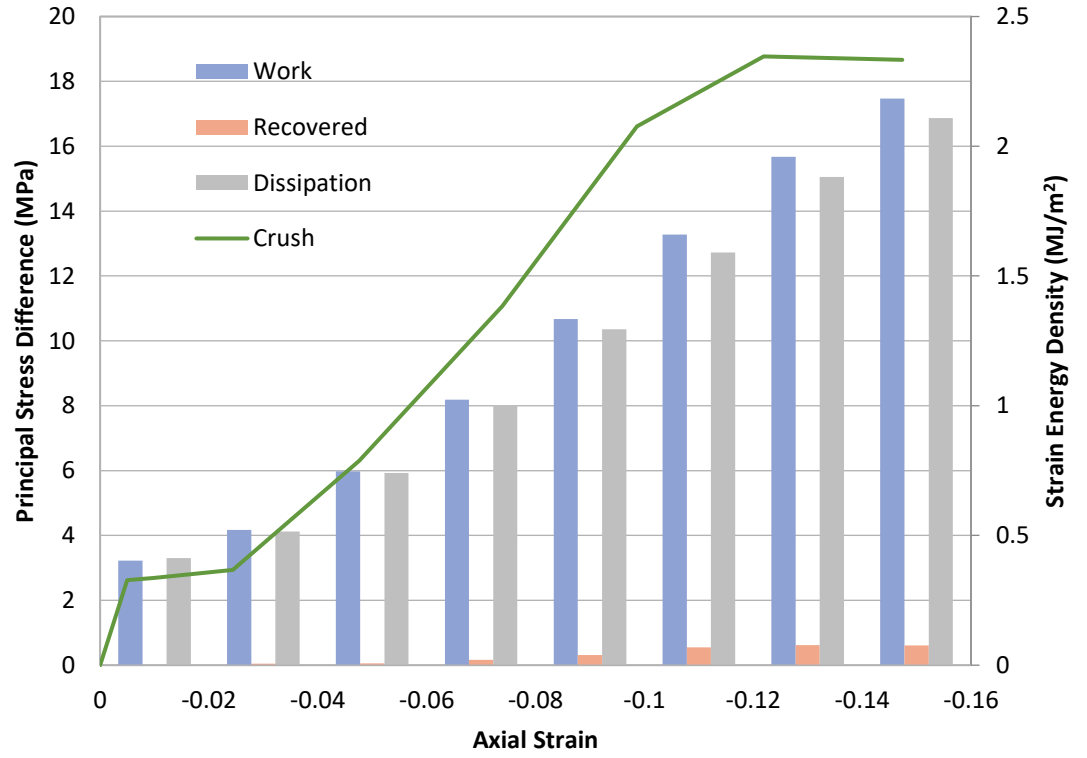

Figure 0.53: Work and dissipation during CTC axial loading at 20 MPa with crush-up

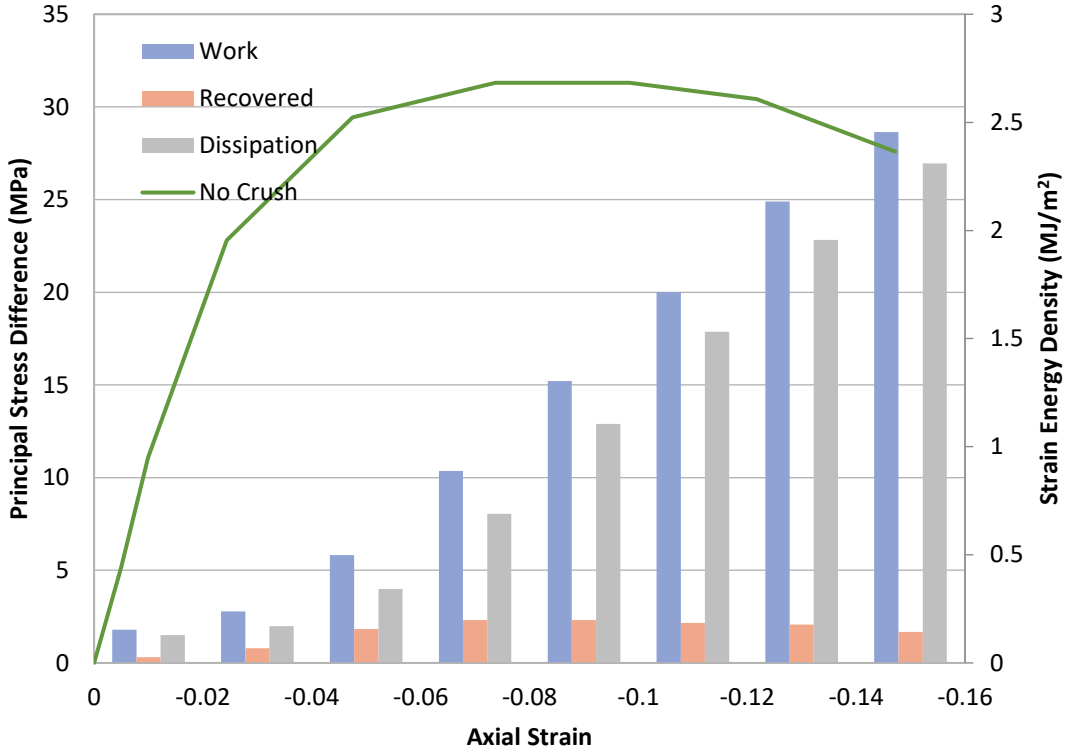

Figure 0.54: Work and dissipation during CTC axial loading at 20 MPa without crush-up

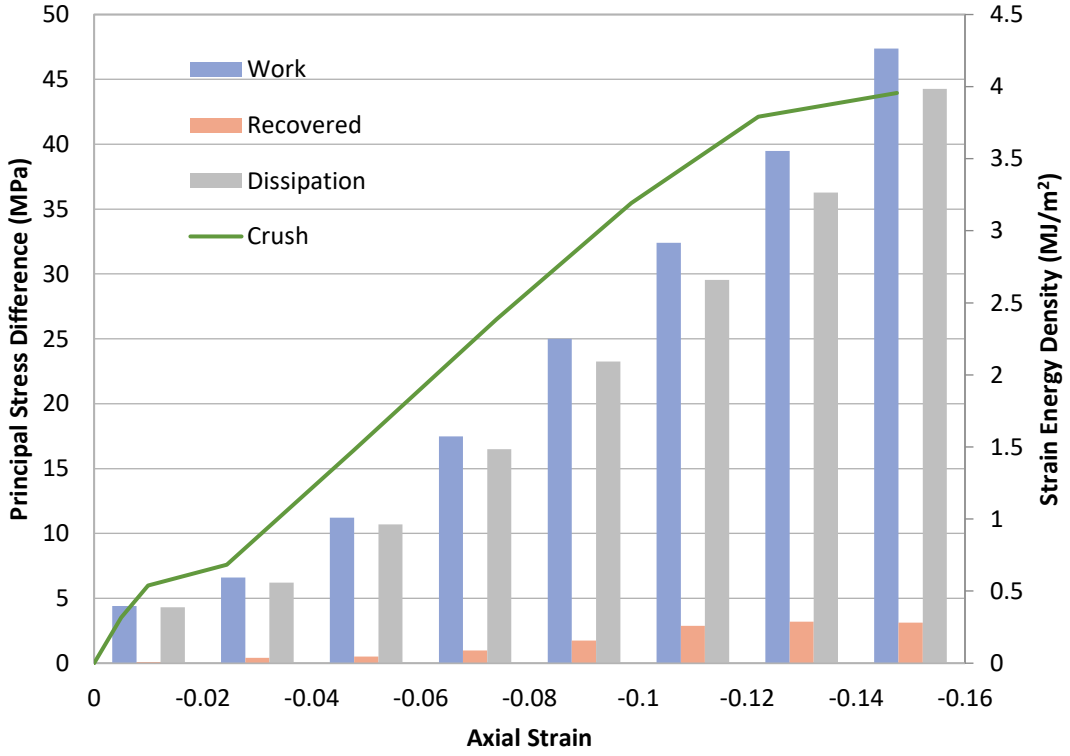

Figure 0.55: Work and dissipation during CTC axial loading at 50 MPa with crush-up

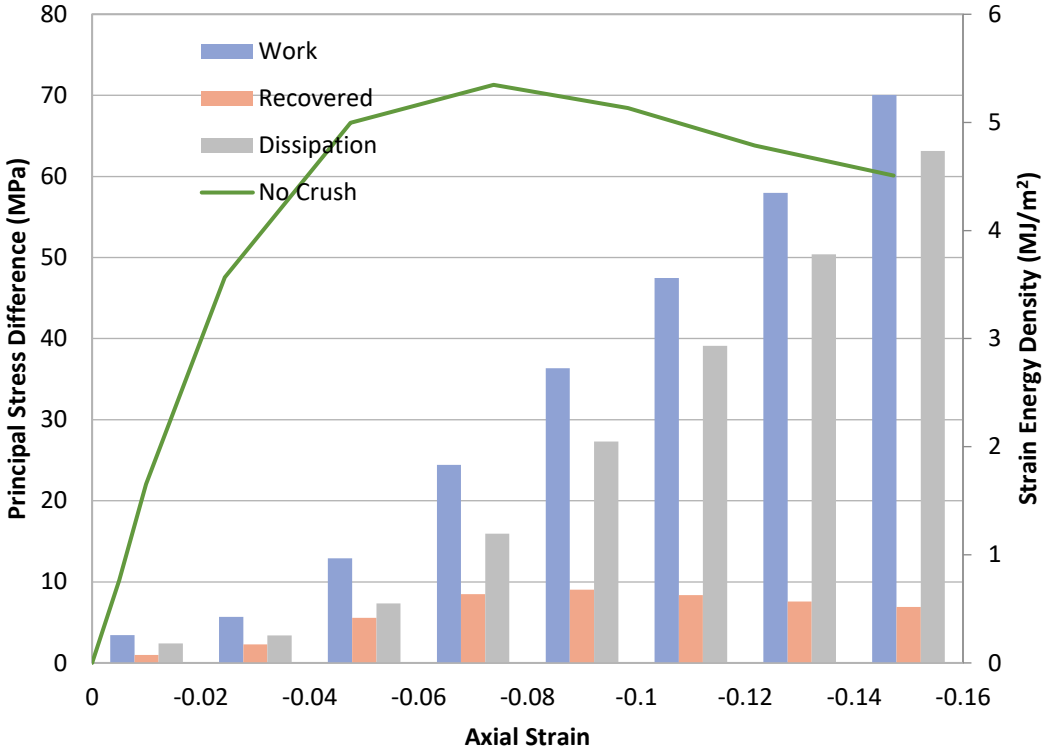

Figure 0.56: Work and dissipation during CTC axial loading at 50 MPa without crush-up

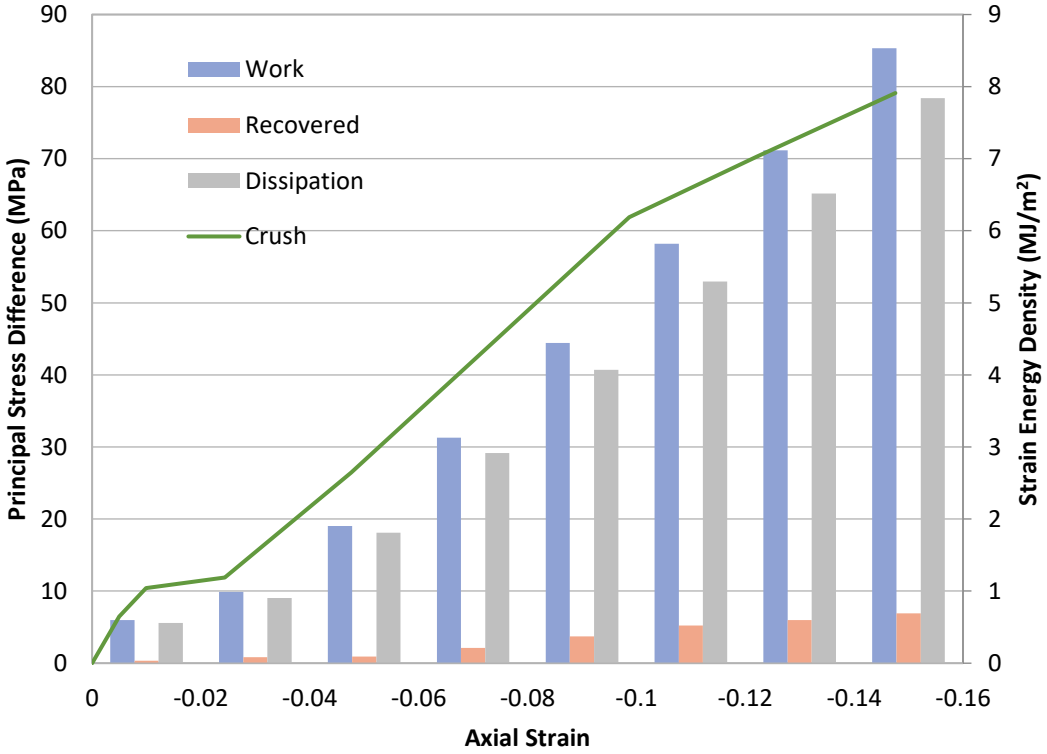

Figure 0.57: Work and dissipation during CTC axial loading at 100 MPa with crush-up

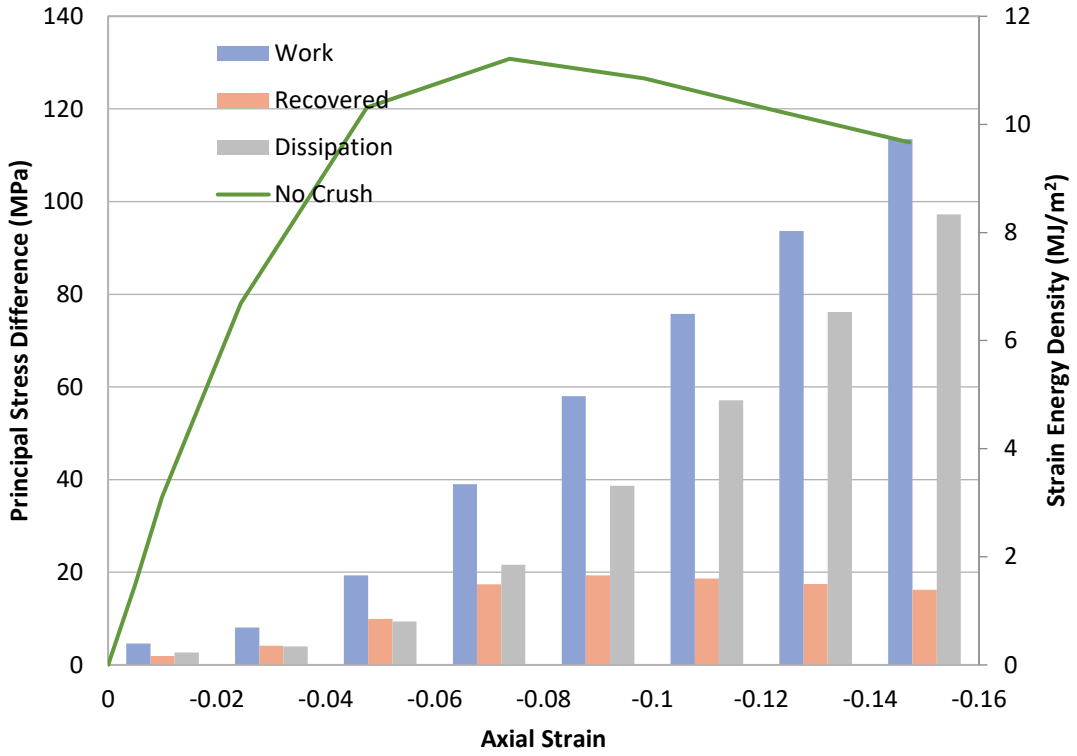

Figure 0.58: Work, dissipation during CTC axial loading at 100 MPa without crush-up

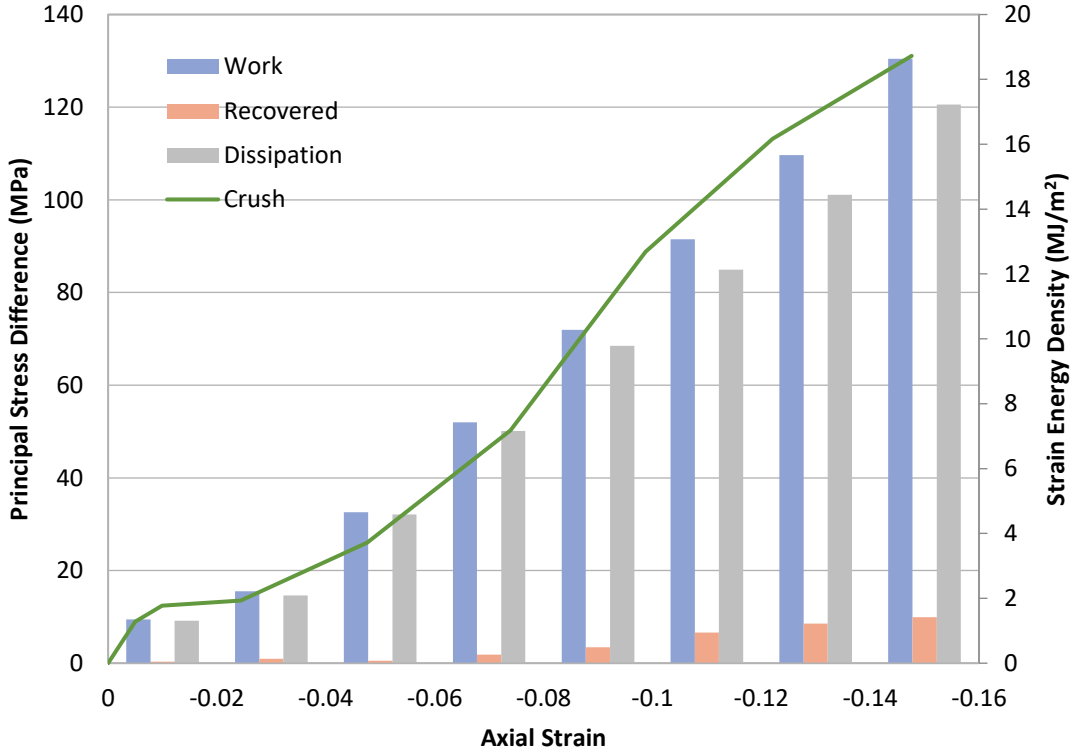

Figure 0.59: Work and dissipation during CTC axial loading at 200 MPa with crush-up

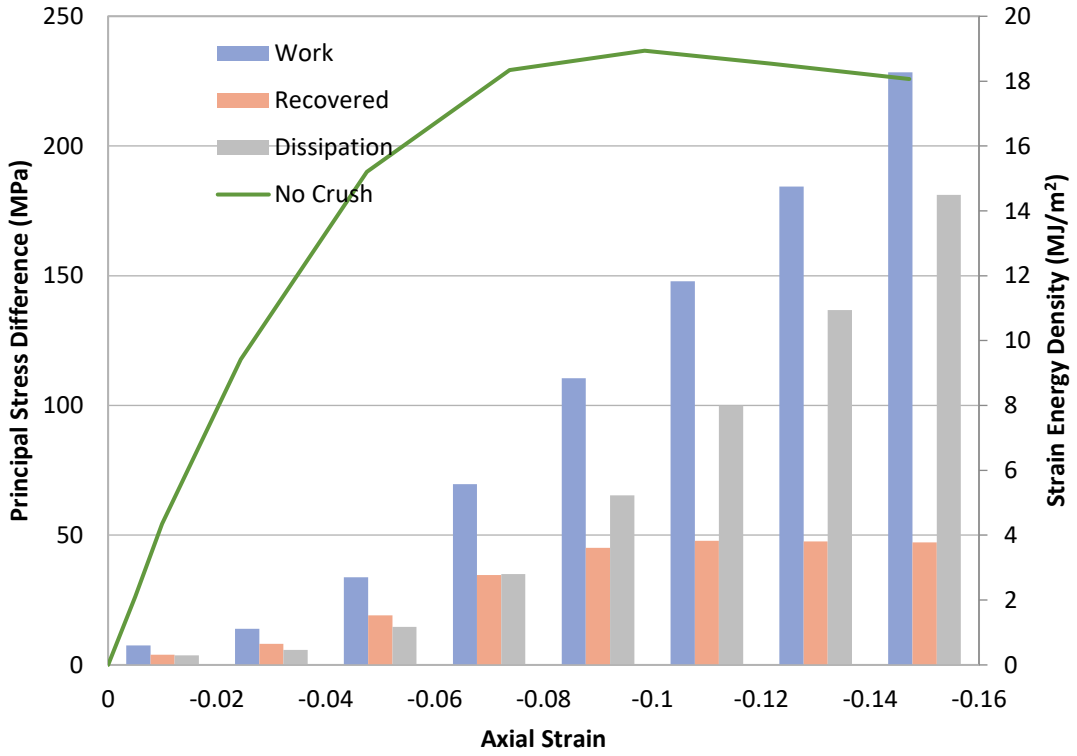

Figure 0.60: Work, dissipation during CTC axial loading at 200 MPa without crush-up

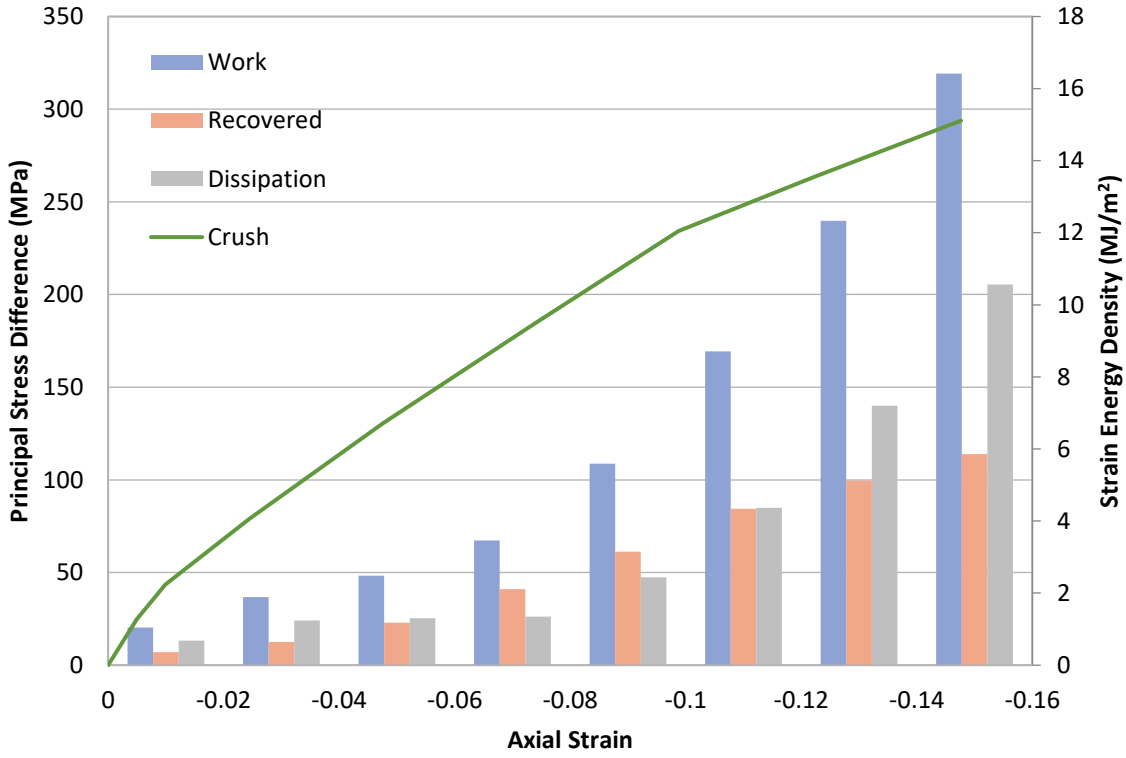

Figure 0.61: Work and dissipation during CTC axial loading at 400 MPa with crush-up

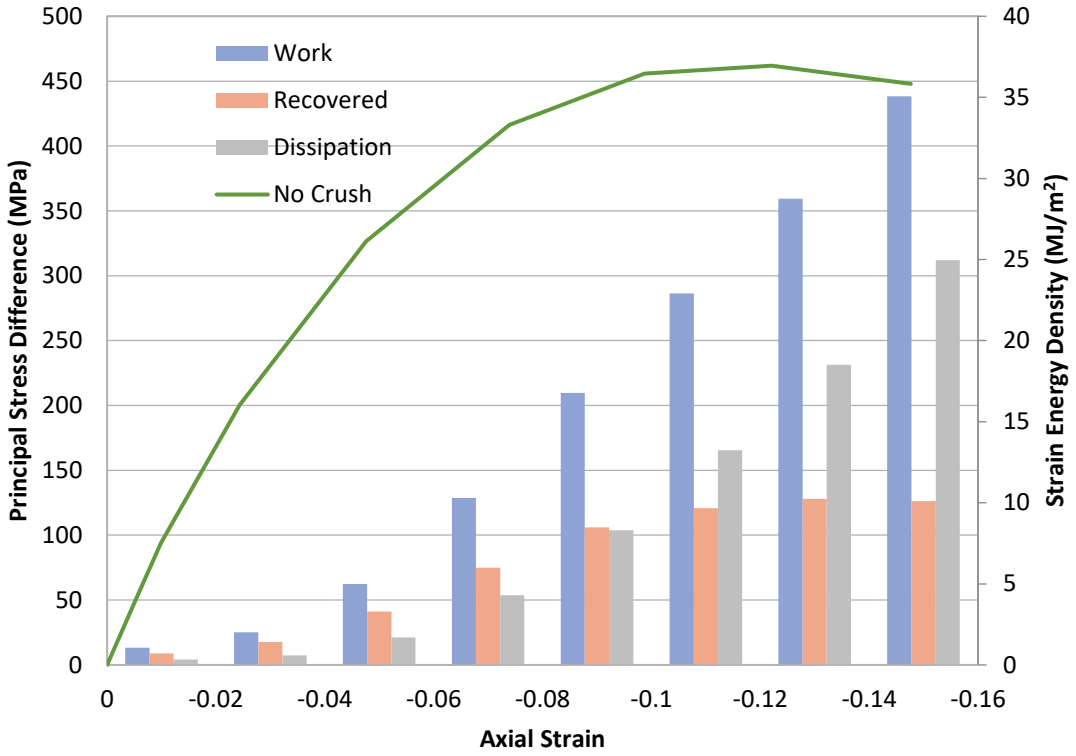

Figure 0.62: Work, dissipation during CTC axial loading at 400 MPa without crush-up

Summary and Discussion of Mesoscale Results

The first important goal of this research study is to formulate a framework for evaluation of the Hill-Mandel homogenization criterion for particulate materials via discrete modeling of the mesoscale. To that effect, hundreds of thousands of simulations have been carried out using the Discrete Element Method in the context of statistical ensembles. If the computational homogenization aspect of the study were reduced to a question and answer, that question would be “what is the size of the RVE”, and the answer would be a resounding “it depends”.

Having reduced the Hill condition to a ratio of upper bounds to lower bounds, which must converge to unity, it can be seen that this approach to unity depends on a few factors for particulate media. Two important observation about approaching the RVE size:

- The size of the RVE in particulate media appears to depend on the confinement stress level in the aggregate. More highly confined aggregates seem to approach homogeneity more rapidly.
- The upper bound to lower bound ratio is lower at the mesoscale for certain loading paths than other. The bulk modulus under uniform strain micro-loading does not differ greatly from the bulk modulus under uniform stress loading even at smaller mesoscales. The shear modulus ratio is high at lower scales but seems to converge more quickly than the Young's modulus ratio.

These observations may appear to be unrelated at first blush, however they result from the same underlying principle. The underlying principle is that in particulate media dissipation due to frictional sliding is the main source of response heterogeneity and the primary driver of the discrepancy between the upper bound response and the lower bound response.

A method that evaluates the Hill condition in frictional particulate media must allow sliding of the boundary particles with respect to each other. It is with the introduction of the surface tracking micro-boundaries here that this is finally possible. Allowing this frictional sliding of grains at the boundary gives insight into just how important frictional dissipation is to the homogenization of particulate media. At higher confinement levels the grains are packed more tightly together, allowing for far less movement therefore less dissipation. This is partly the reason for the apparently smaller RVE at the higher confinements. The other reason is that there are more particles at the higher confinements due to comminution. Frictional dissipation at the boundaries is also responsible for the bound ratios being lower under bulk and shear mesoscale loading to obtain the eponymous moduli

than for uniaxial loading to obtain the Young's modulus. Under uniaxial loading in a CTC simulation, the static uniform boundary condition allows sliding at the boundaries due to the deviatoric micro-forces in the model while the kinematic uniform boundary condition fixes the velocities of particles at the boundaries so that they are less able to slide relative to each other. The contrast is far smaller in bulk loading due to less frictional dissipation under the static uniform boundary. The contrast also fades quicker under pure deviatoric loading due to relative velocities being imposed on the boundary particles for the kinematic uniform boundary condition.

It seems clear the RVE size depends on the type of loading and level of confinement. Still a qualitative determination can be made on its approximate size for Eglin sand based on the mesoscale simulations carried out here. The RVE has clearly been reached at a confinement level of 5 MPa for the DE model of five million ($5x10^6$) particles. This is equivalent to a physical window size of approximately 3.3 cm. The bound ratios for other confinement levels seems to follow a similar convergence pattern based on the number of particles in the model, except for confinement levels in excess of 100 MPa where less particles are required.

Figure 0.63 shows the apparent RVE size for Eglin sand based on the mesoscale simulations carried out herein. Two curves are shown in Figure 0.63. One shows the RVE size based on minimum number of particles being five million. The second curve shows the RVE size taking into account the faster convergence at higher levels of confinement.

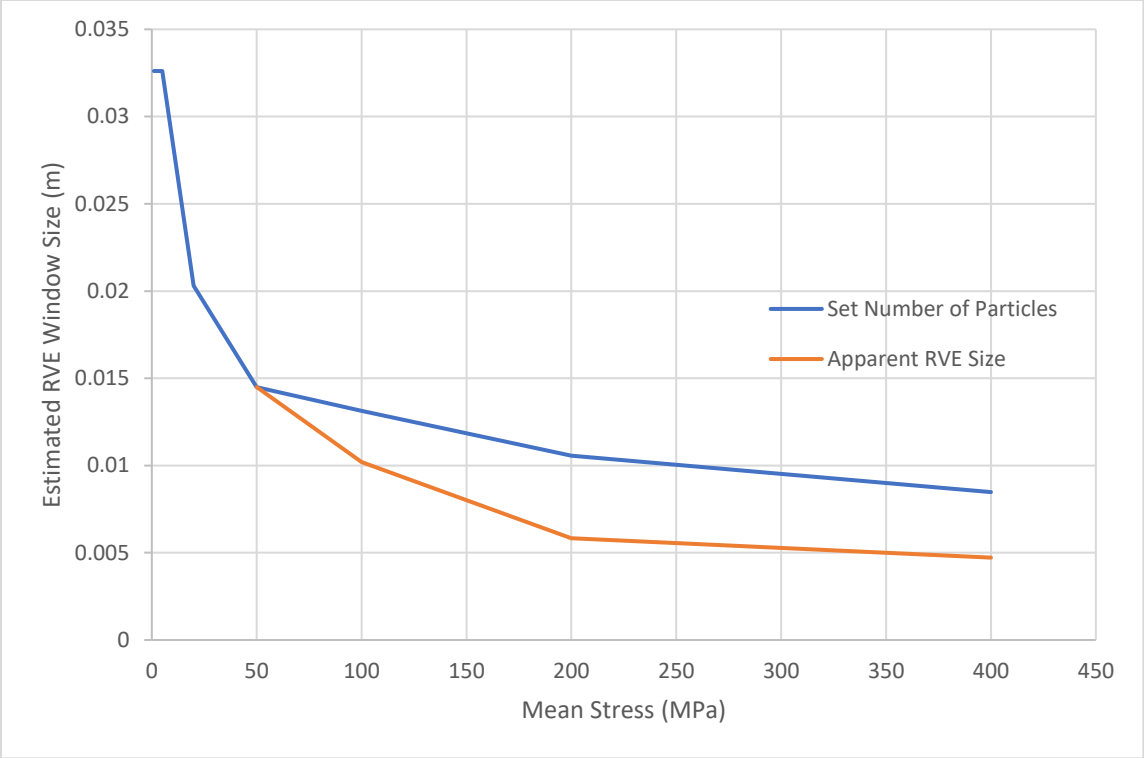

Figure 0.63: RVE size for Eglin sand based on mesoscale simulations

Next, the effective moduli computed with the mesoscale ensemble results are summarized. The moduli computed using mesoscale simulations follow the trend from experimental data, though their magnitudes are lower. Additional calibration of the particle model to the triaxial experiments would certainly produce a better fit to the experimental data, however such a calibration is beyond the immediate scope of the framework. Herein, only experimental micromechanical distributions and the uncertainty associated with them, has been used for forward propagation using Discrete Elements.

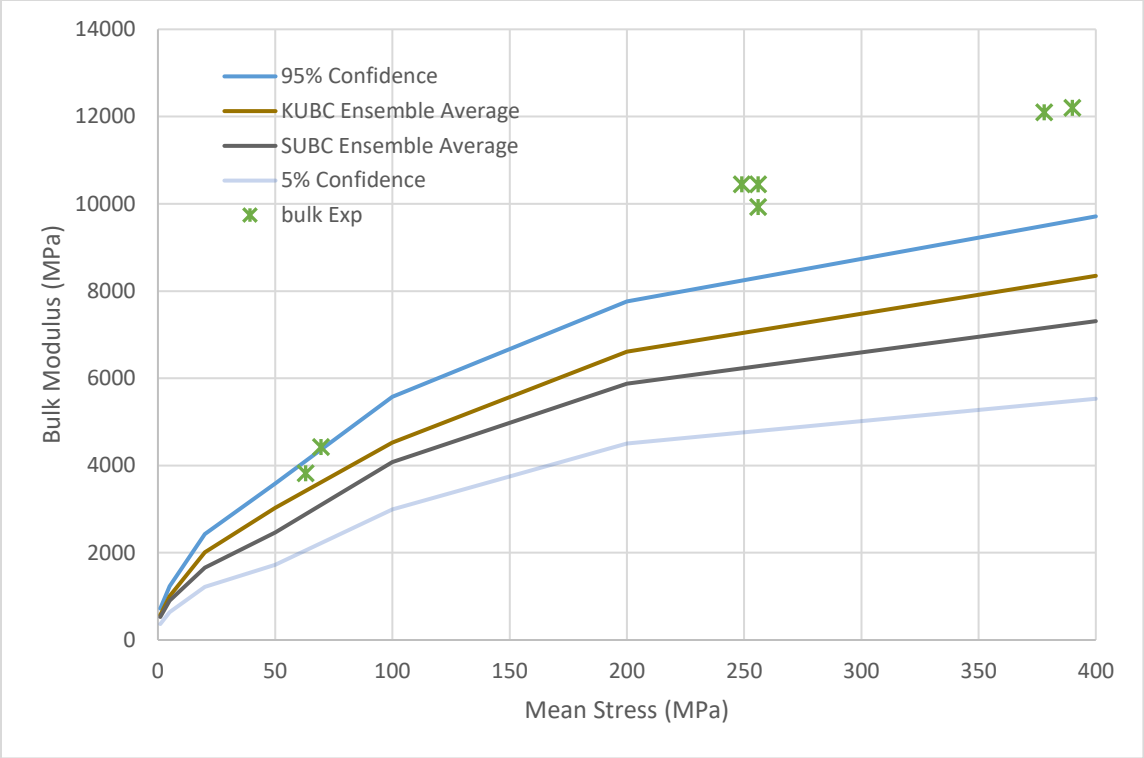

Figure 0.64: Effective bulk moduli for $1x10^5$ particle ensembles

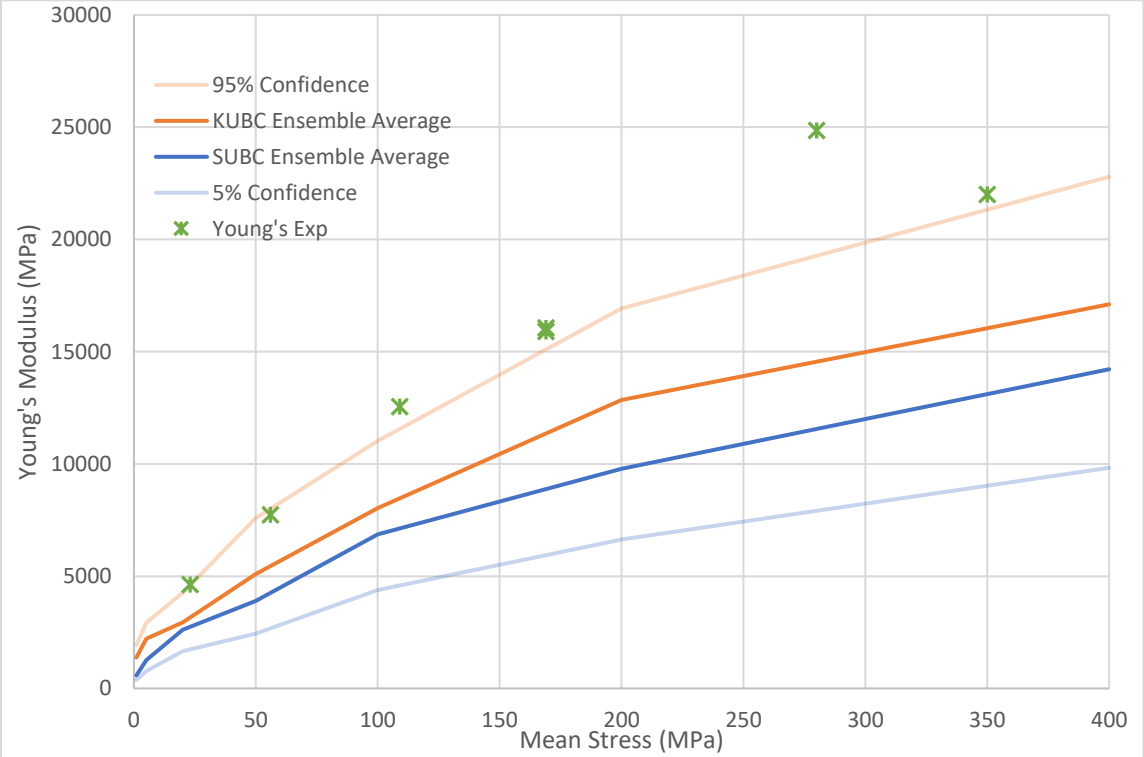

Figure 0.65: Effective Young's moduli for $1x10^5$ particle ensemble

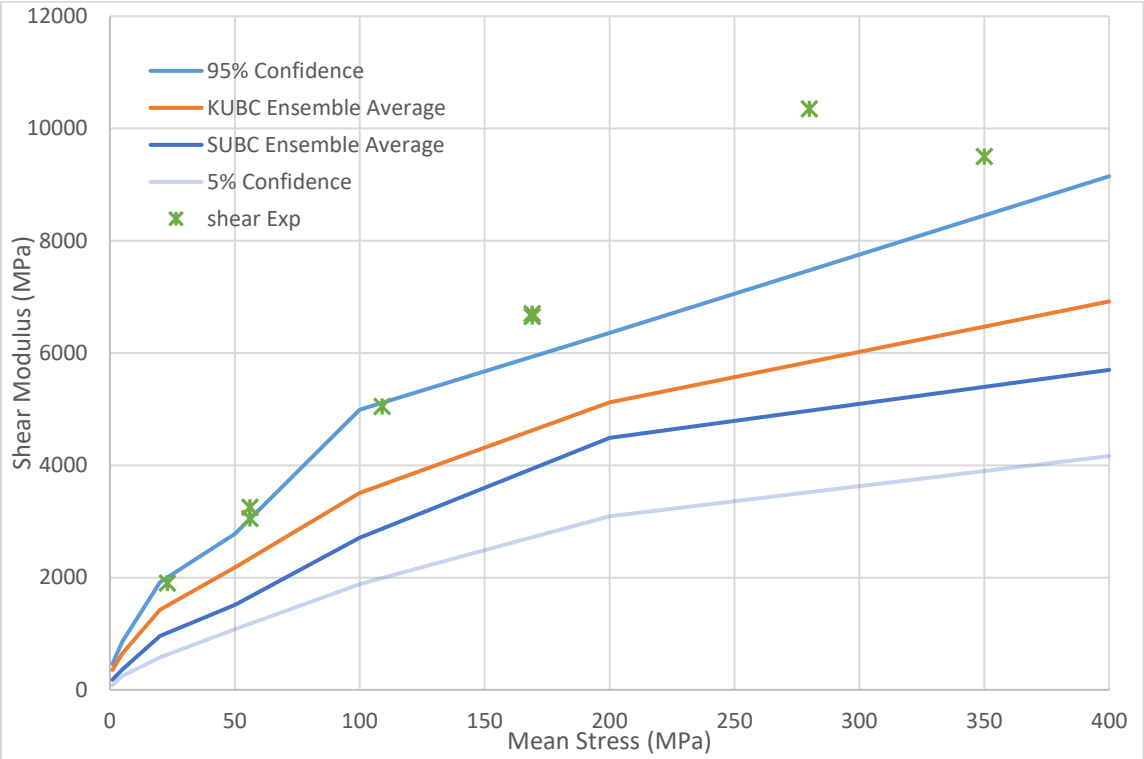

Figure 0.66: Effective shear moduli for $1x10^5$ particle ensemble

CHAPTER 6

MESOSCALE-BASED MODELING AND UQ WITH THE HEP MODEL

It has been stressed throughout this manuscript that the objectives of this research study are manifold. Chapter 5 presented results for the meso-to-macro aspect of the study, namely homogenization and constitutive response evolution at different mesoscopic scales. This chapter presents results for the propagation of the discrete simulations results to the continuum mechanics computational paradigm. Virtually all Lagrangian Finite Element codes, their Eulerian Finite Volume counterparts, and the coupled or adaptive combination thereof, use continuum mechanical constitutive models for particulate media like sand. Identification of parametric values for these models, is far from an exact science. Discrete modeling efforts like the ones presented in the current framework, can provide an additional path towards that goal. Furthermore, when ensemble modeling is used to quantify the variability of the mesoscopic response, that uncertainty can be propagated to the continuum model.

In this chapter, Finite Element modeling of Eglin sand is carried out using the Discrete Element results documented in Chapter 5. In the first section the typical response of an HEP model using built-in library parameters for HEP sand are shown. Next, parameter calibration of the HEP model is carried out using mathematical optimization. The HEP parameters are optimized to the discrete model results, rather than experimental data. This is done initially to the ensemble average response of the DE simulations, then individually

to different ensemble realizations, effectively propagating the uncertainty to the HEP model. Finally, Finite Element simulations of triaxial testing with the HEP model are carried out using the parameters obtained from the optimization of the previous section.

Confined Triaxial Simulations with Library HEP Model

The HEP model in the Epic code comes with several pre-calibrated material parameters. These materials have been passed down to Epic from the initial implementation of the SABER-PC code discussed in Chapter 3 and are based on extensive experimental testing and computational calibration. In this section, the response of one of these materials is described under several triaxial loading scenarios. The specific material model used here is Material 123 in the Epic HEP library, described as "DSOIL3 – Clayey Sand 26.5% AFV". This is a rather stiff sand with a porosity of 26.5%, and was chosen to illustrate the response here simply due to the fact that its response range extends into the high confinement range of the experimental testing of Eglin sand. The default values of the HEP model constants relevant to the response are shown in Table 0.1 of the next section.

The response of HEP Material 123 under isotropic compression is shown in Figure 0.2. Note that several unload-reload cycles have been carried out at specific isotropic stress levels corresponding to the confinement levels where the Eglin sand's mesoscale response has been simulated, namely 5 MPa, 20 MPa, 50 MPa, 100 MPa, 200 MPa, and 400 MPa. The isotropic compression response as well as the deviatoric responses shown further in this section, are extracted from "single element" simulations in Epic. A single hexahedral (brick) element with unit dimensions has been loaded to the prescribed path. Figure 0.1 shows this single hexahedron at 400 MPa.

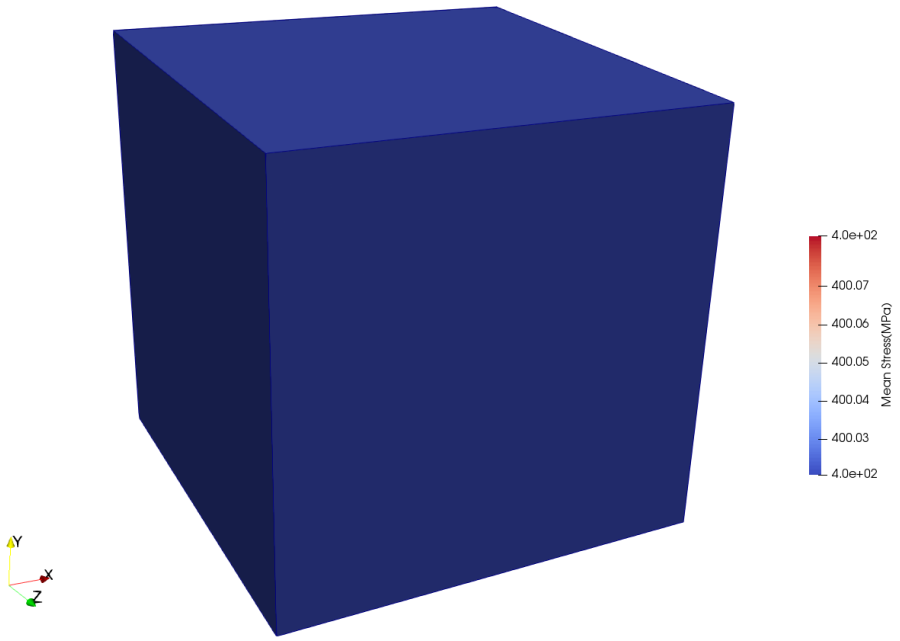

Figure 0.1: Hexahedral single element in Epic

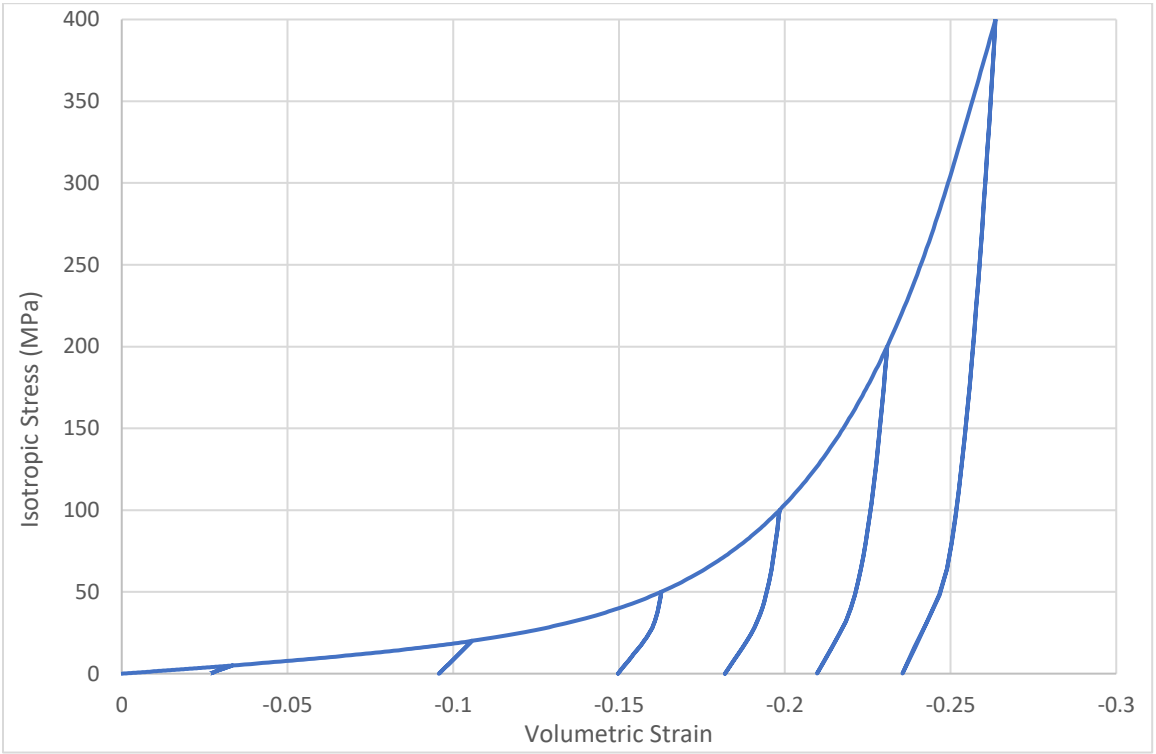

Figure 0.2: Isotropic response of library sand material

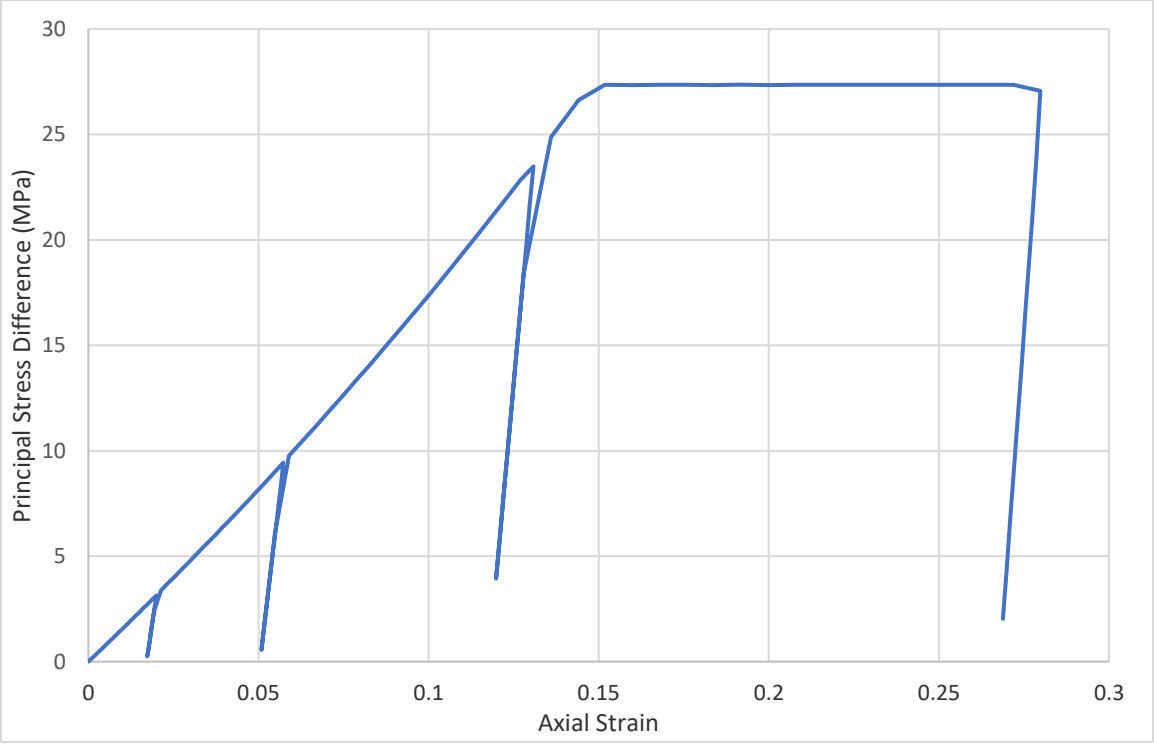

Figure 0.3: Axial loading response of library sand material at 5 MPa confinement

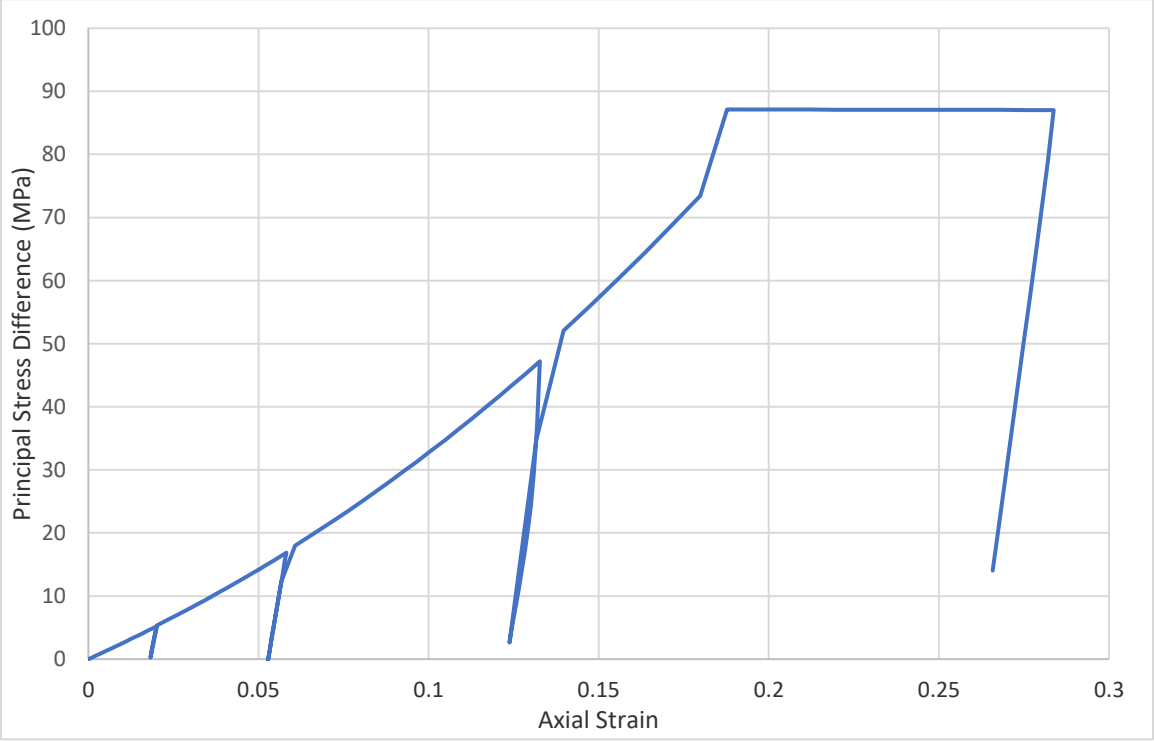

Figure 0.4: Axial loading response of library sand material at 20 MPa confinement

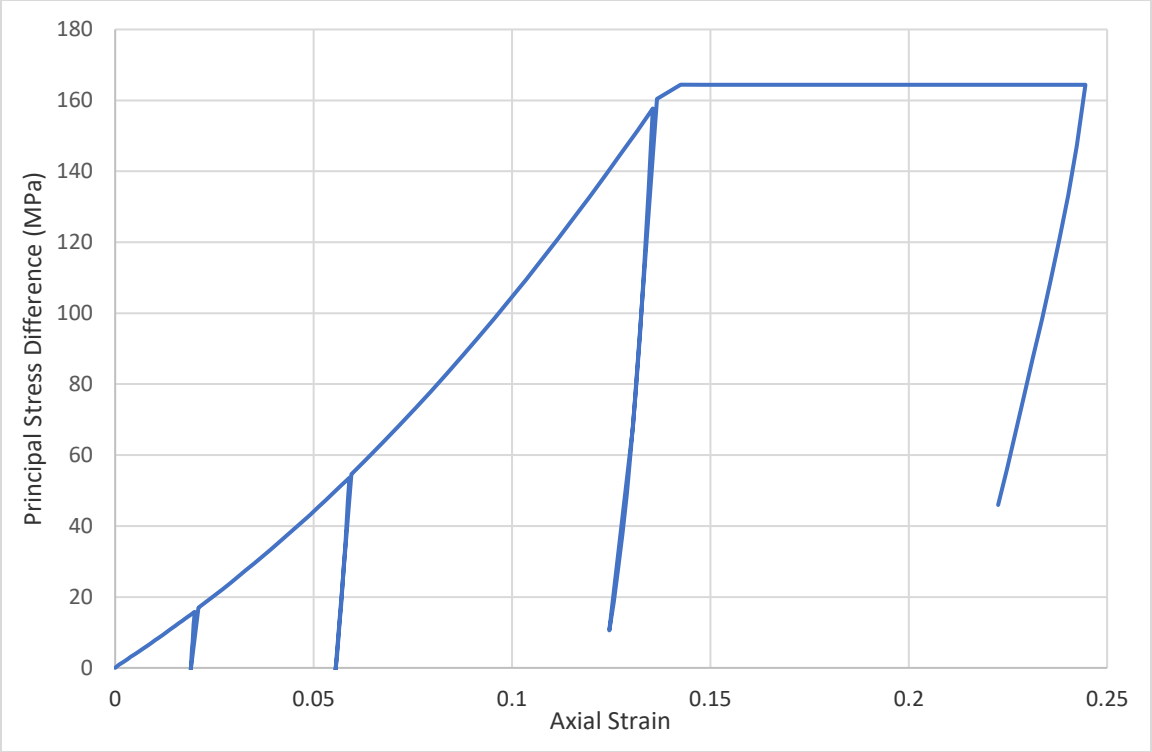

Figure 0.5: Axial loading response of library sand material at 50 MPa confinement

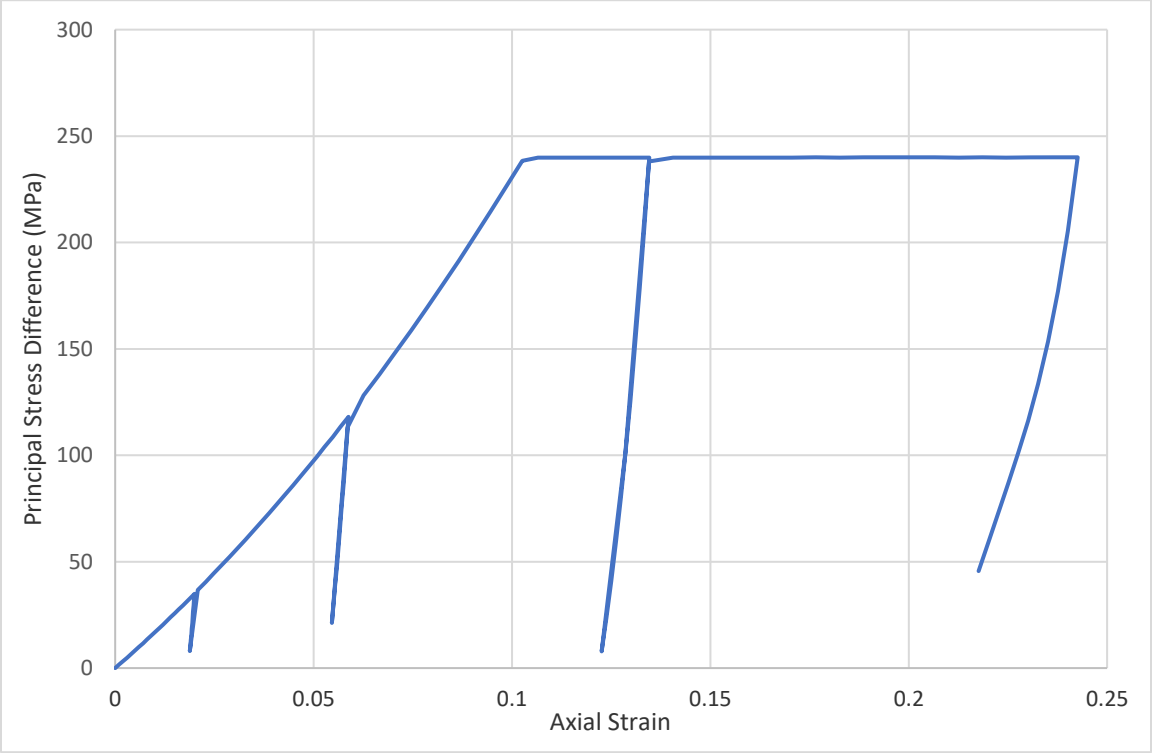

Figure 0.6: Axial loading response of library sand material at 100 MPa confinement

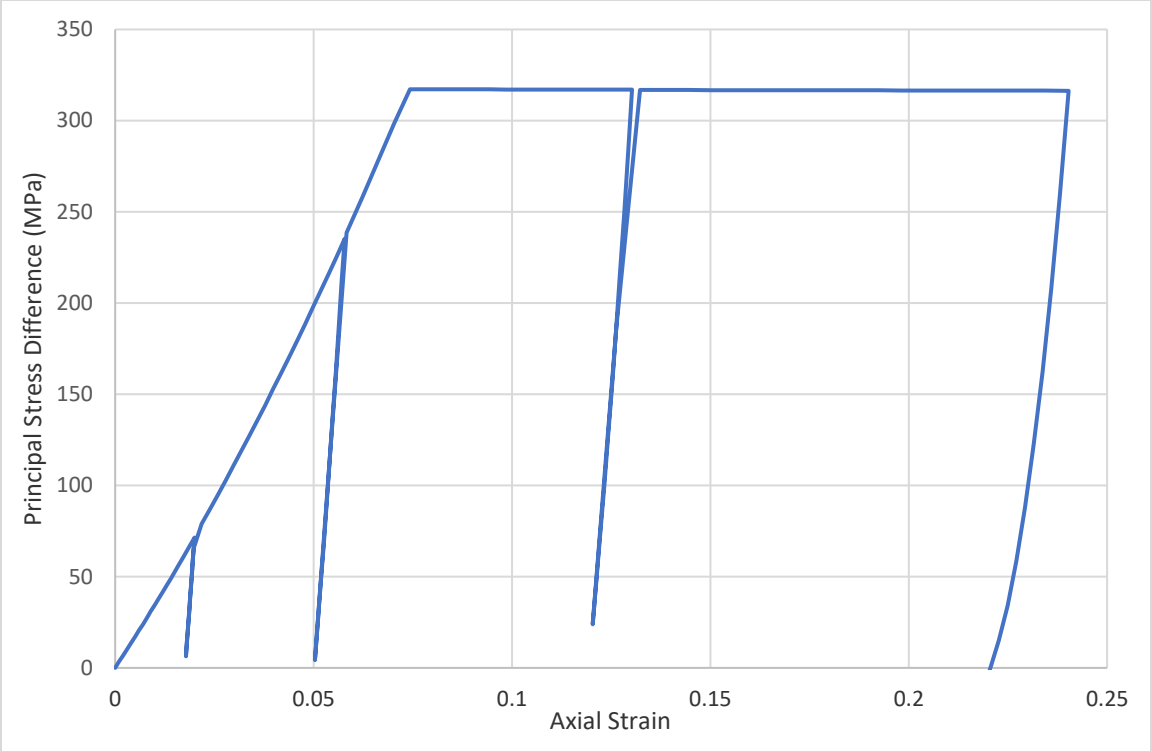

Figure 0.7: Axial loading response of library sand material at 200 MPa confinement

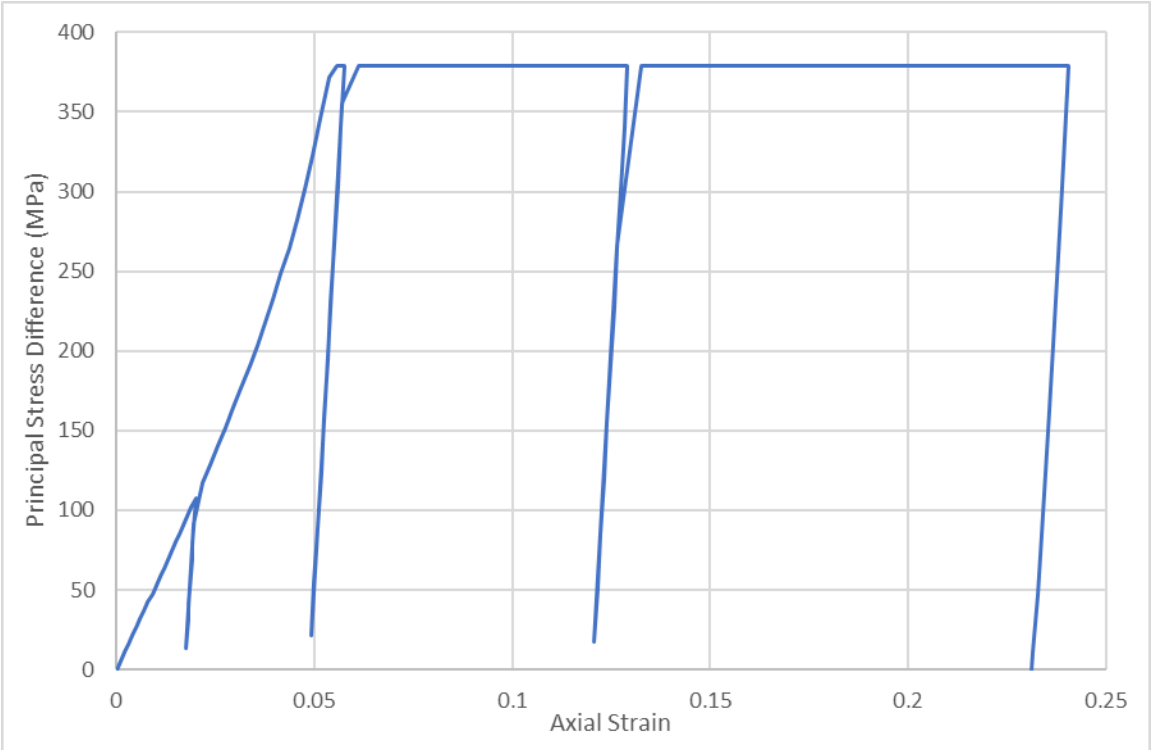

Figure 0.8: Axial loading response of library sand material at 400 MPa confinement

Calibration of the HEP Model from Discrete Modeling

Table 0.1 shows the Simple HEP model constants that are varied in this parametric optimization study along with the units used in the model and a brief description of their function. Also shown in the table, is the optimization method used to calibrate the material parameters. The library HEP material here, the DSOIL3 fit used to illustrate the response in the previous section, is used merely as a starting point for the optimization algorithm as it seeks to minimize the loss function, or the relative error between the ensemble average response and the HEP fit.

Table 0.1: Simple HEP model variables relevant to optimization study

Opt. Method	Name	Lib. Value	Units	Description
SOGA	ASUBC	0.206	Mb	Bulk Modulus at void closure
SOGA	ASUB0	0.0109	Mb	Initial Bulk Modulus
SOGA	ASUB1	0.0014	Mb	Bulk Modulus at Point 1
SOGA	PSUBC	0.00502	Mb	Pressure at Void Closure
SOGA	PSUB1	0.0	Mb	Pressure at Point 1
SOGA	USUBC	0.385	-	Bulk Strain at Void Closure
SOGA	ASUB2	0.032	Mb	Bulk Modulus at Point 2
SOGA	PSUB2	0.00259	Mb	Pressure at Point 2
SOGA	USUB2	0.333	-	Bulk Strain at Point 2
SOGA/MOGA	VCURL	0.327	-	Loading Poisson's Ratio
SOGA/MOGA	SHRMAX	1.0	Mb	Maximum Shear Modulus
SOGA/MOGA	ASUB1	0.0041	Mb	Maximum Yield Stress
SOGA/MOGA	BSUB0	-489.0	Mb^{-1}	Yield Curve transition rate

For all the bulk response variables Single Objective Genetic Algorithm (SOGA) was used. First two parameters at a time were varied, and the objective function is plotted as contours in their parametric optimization space. Then the optimization was carried out on all bulk response parameters simultaneously. For the deviatoric response parameters, a SOGA optimization was carried out for axial loading at each confinement level. This was followed by a Multi-Objective Genetic Algorithm (MOGA) optimization considering deviatoric loading at all different confinement levels simultaneously.

Figure 0.9 through Figure 0.13 show the SOGA objective function contours for different couples of bulk parameters. Table 0.2 shows the optimum volumetric response parameters identified by SOGA on all parameters simultaneously.

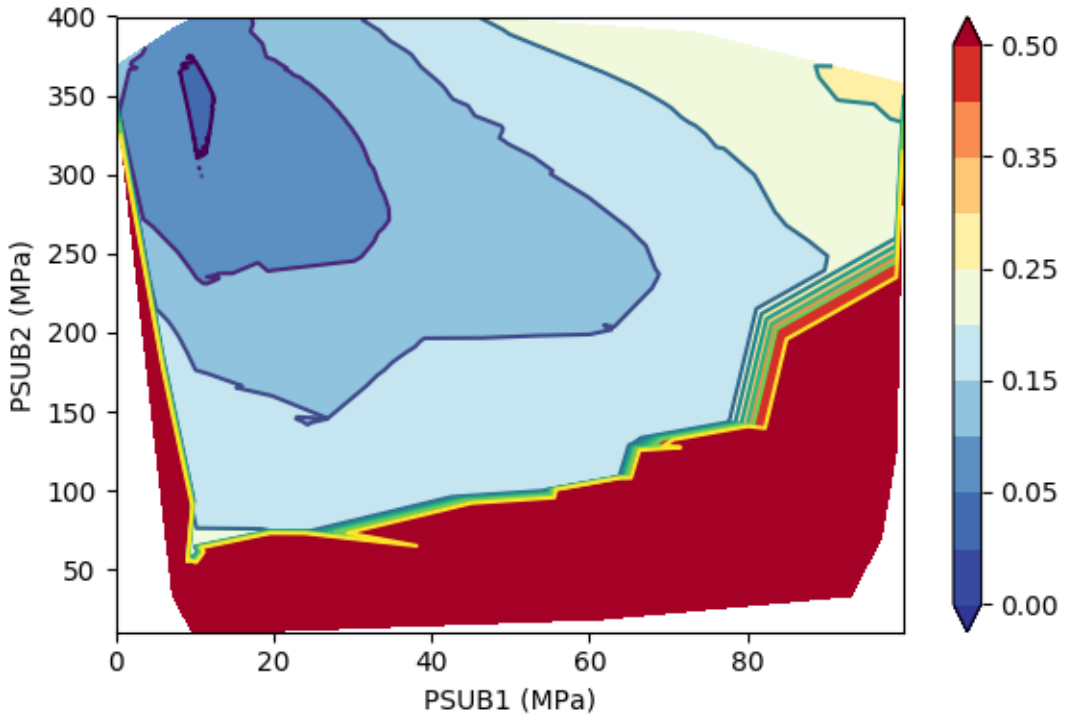

Figure 0.9: Objective function contours for parametric optimization of PSUB1 vs. PSUB2

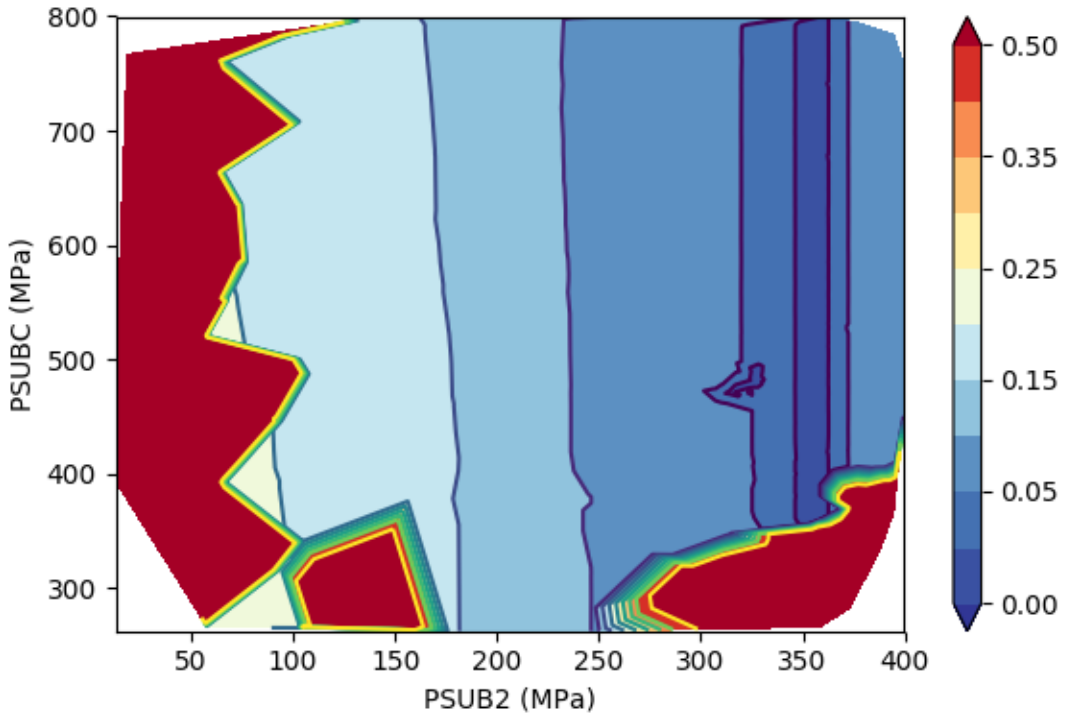

Figure 0.10: Objective contours for parametric optimization of PSUB2 vs. PSUBC

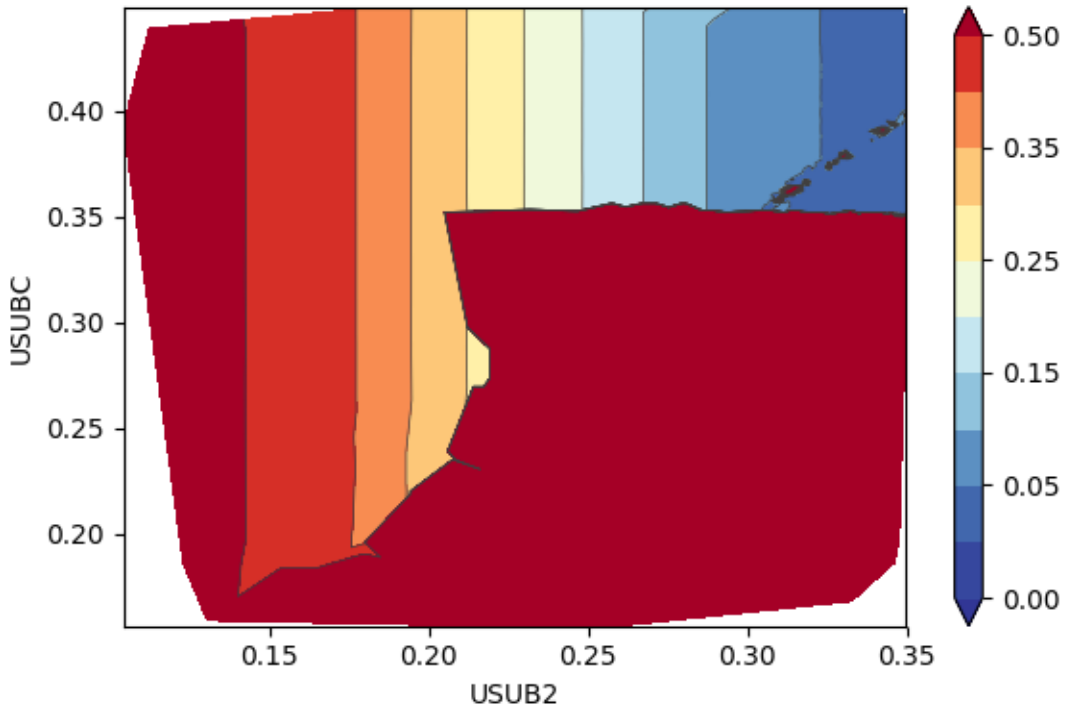

Figure 0.11: Objective contours for parametric optimization of USUB2 vs. USUBC

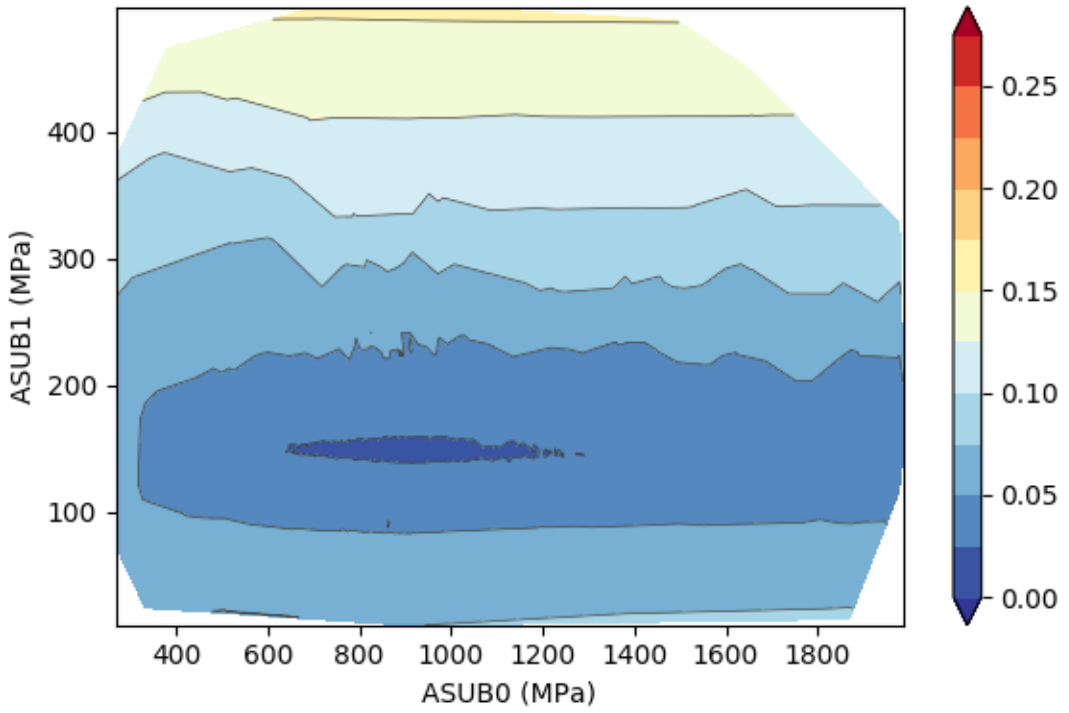

Figure 0.12: Objective contours for parametric optimization of ASUB0 vs. ASUB1

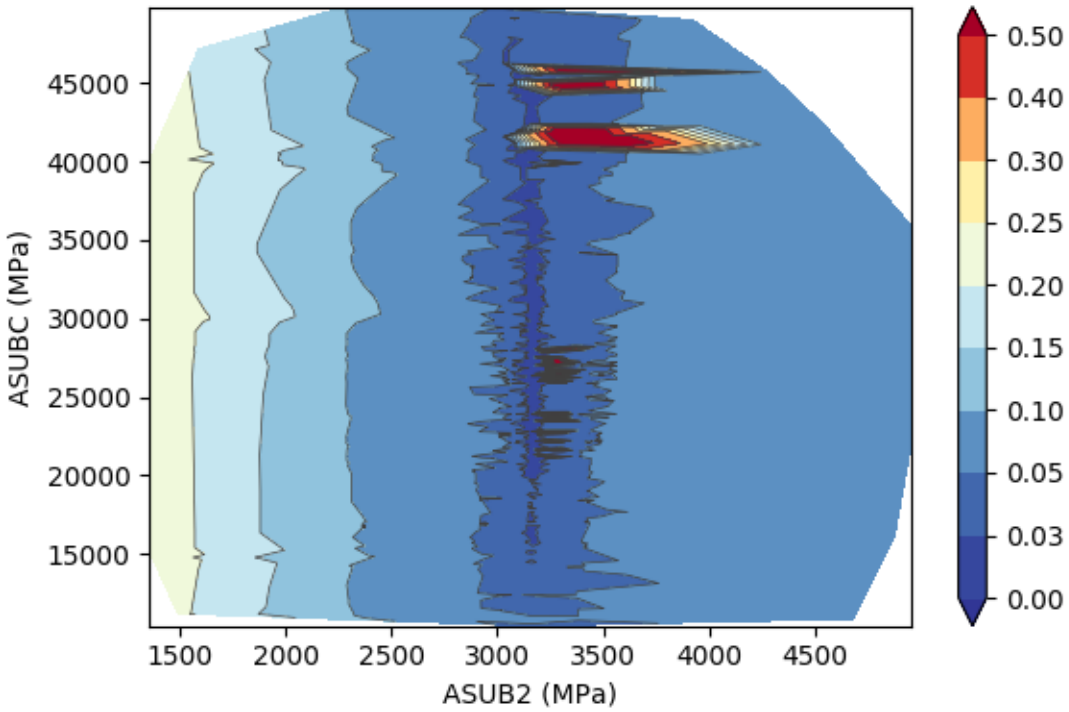

Figure 0.13: Objective contours for parametric optimization of ASUB0 vs. ASUB1

Table 0.2: Optimized simple HEP model bulk response variables

Name	Lib. Value	Ensemble Average Opt. Value	Units
ASUBC	20600	18228	MPa
ASUB0	1090	730.1	MPa
ASUB1	140	70.8	MPa
PSUBC	502	572.2	MPa
PSUB1	0.0	12.8	MPa
USUBC	0.385	0.365	-
ASUB2	3200	1993	MPa
PSUB2	259	306.2	MPa
USUB2	0.333	0.362	-

Table 0.2 shows the bulk parameters of the HEP model optimized to the mesoscale ensemble average of the volumetric loading response. These parameters can also be optimized specifically to each different realization in the ensemble. In doing so, the distribution of the mesoscale response and the uncertainty associated with it are effectively being propagated to the continuum model. This is a very important aspect of the framework, as it represents the level of the upscaling that is accessible to most mechanicians using a continuum method such as Finite Elements to simulate the material response.

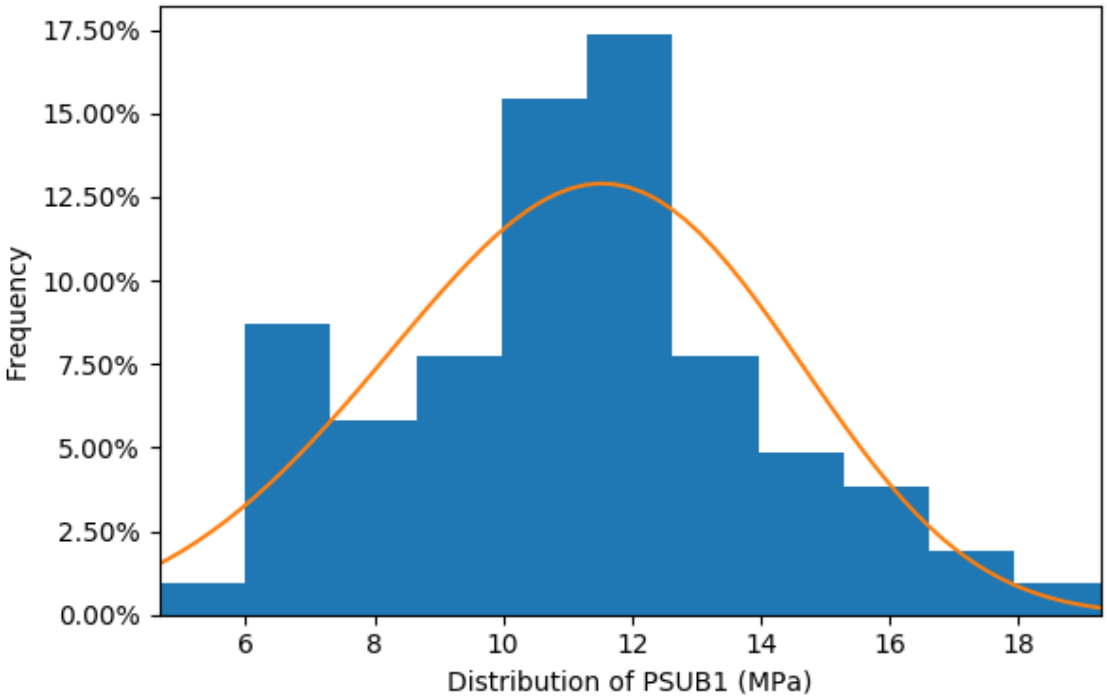

Figure 0.14: Histogram of PSUB1 optimized to each realization

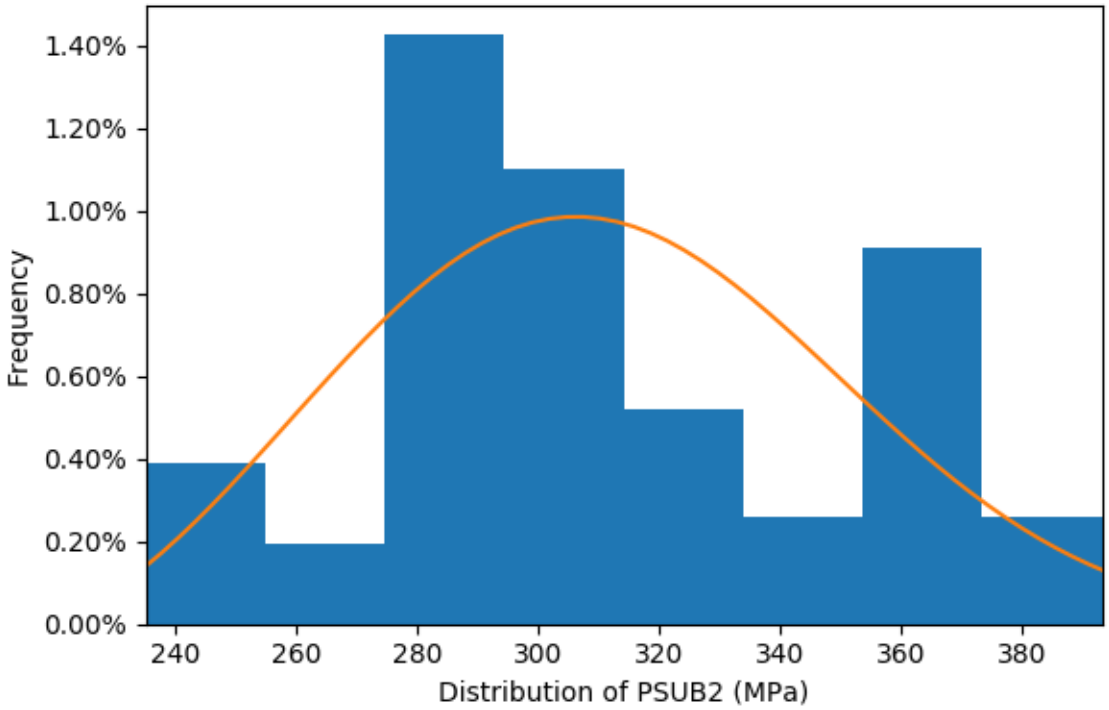

Figure 0.15: Histogram of PSUB2 optimized to each realization

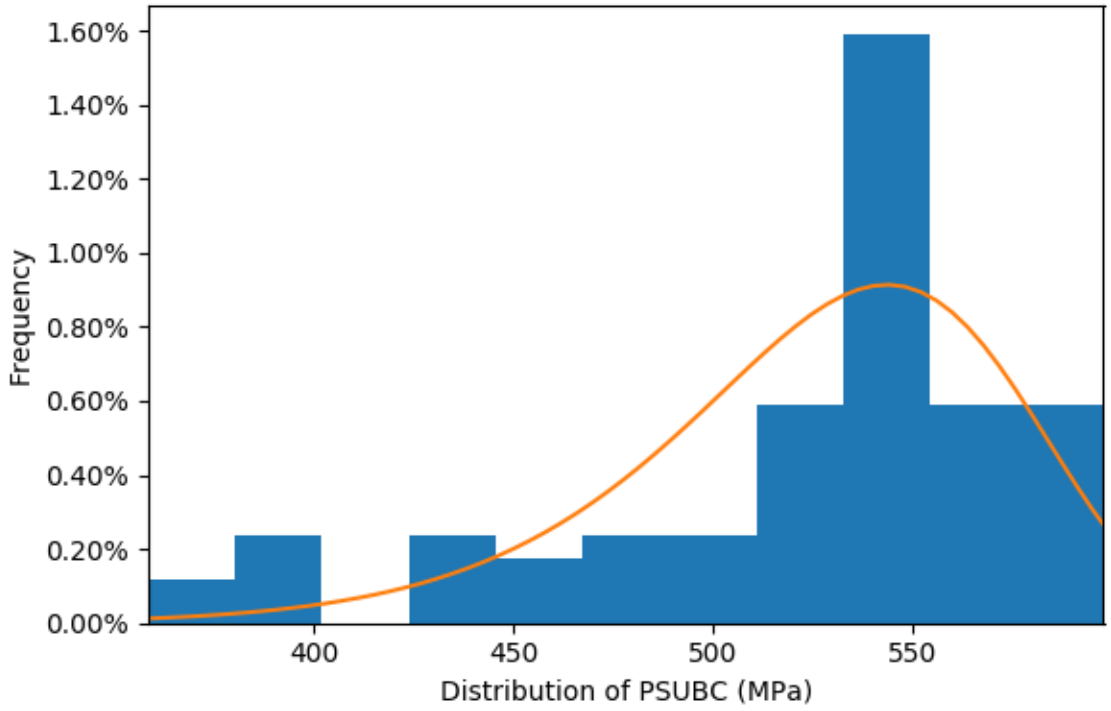

Figure 0.16: Histogram of PSUBC optimized to each realization

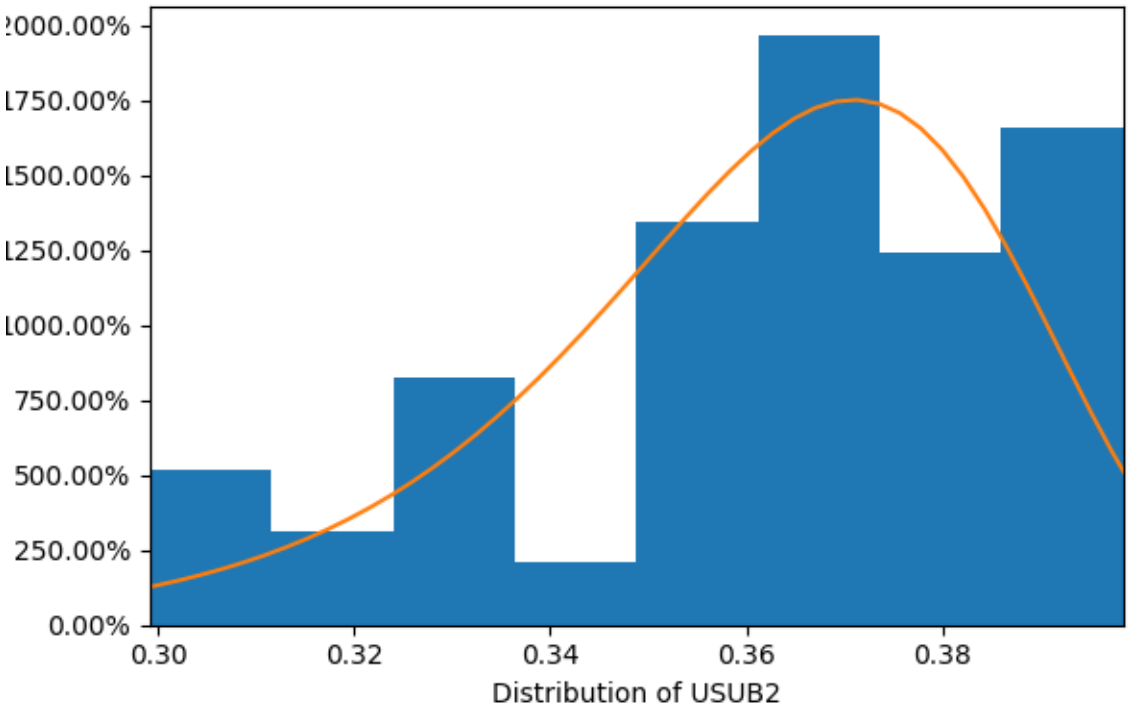

Figure 0.17: Histogram of USUB2 optimized to each realization

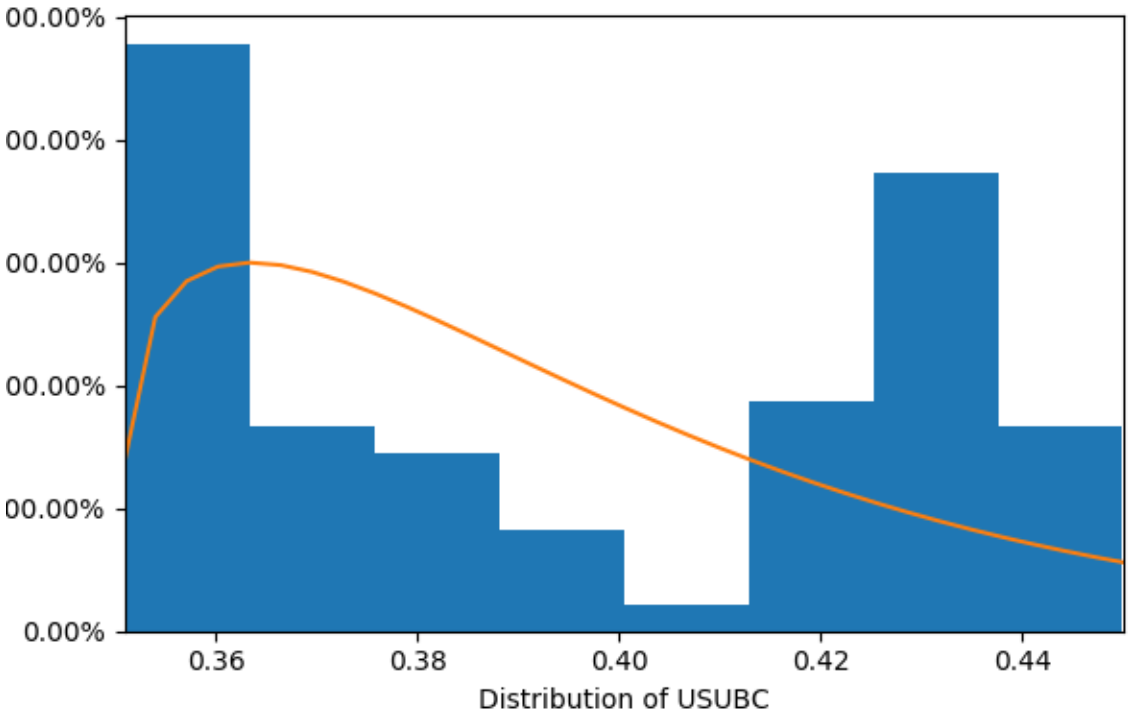

Figure 0.18: Histogram of USUBC optimized to each realization

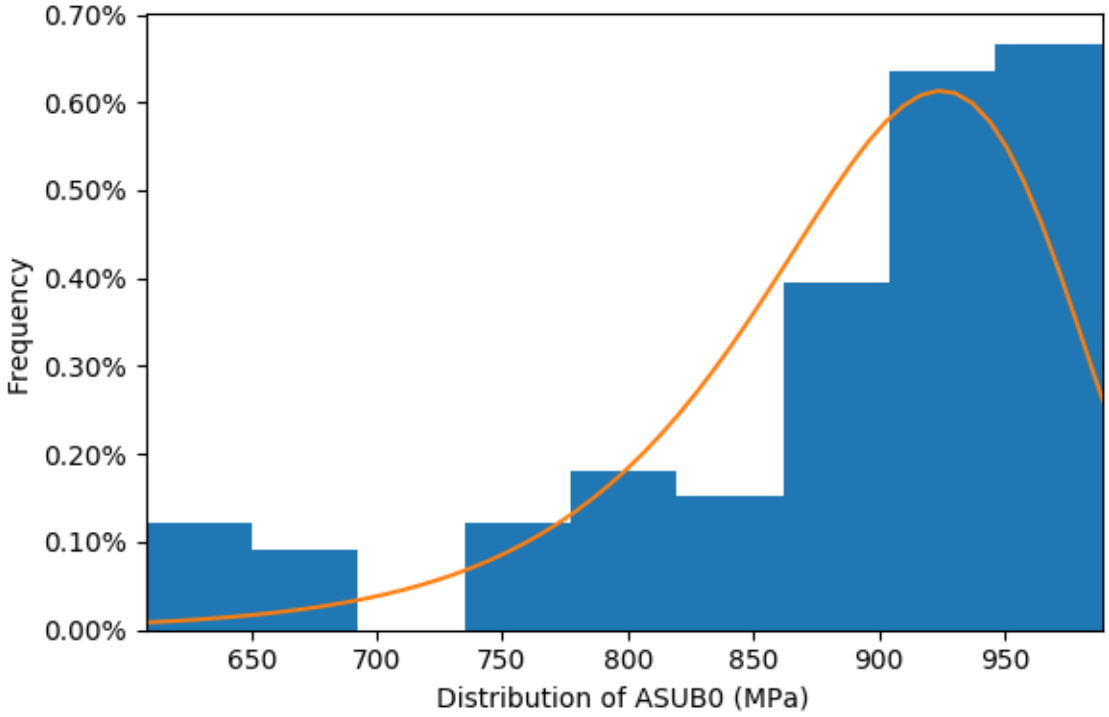

Figure 0.19: Histogram of ASUB0 optimized to each realization

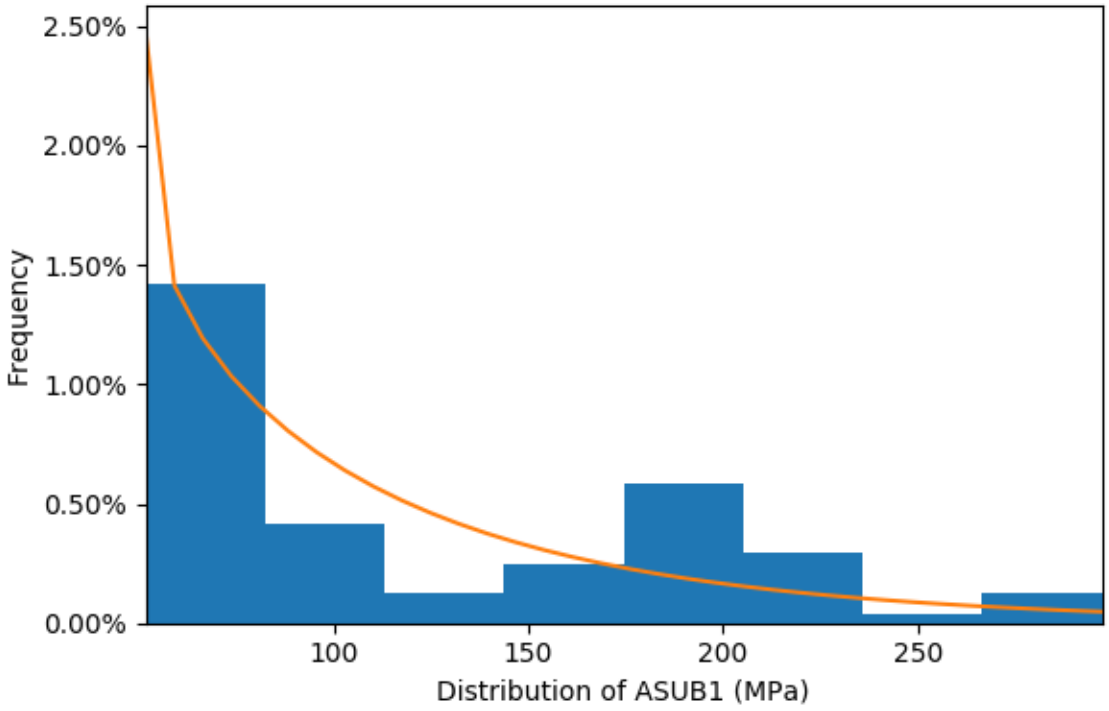

Figure 0.20: Histogram of ASUB1 optimized to each realization

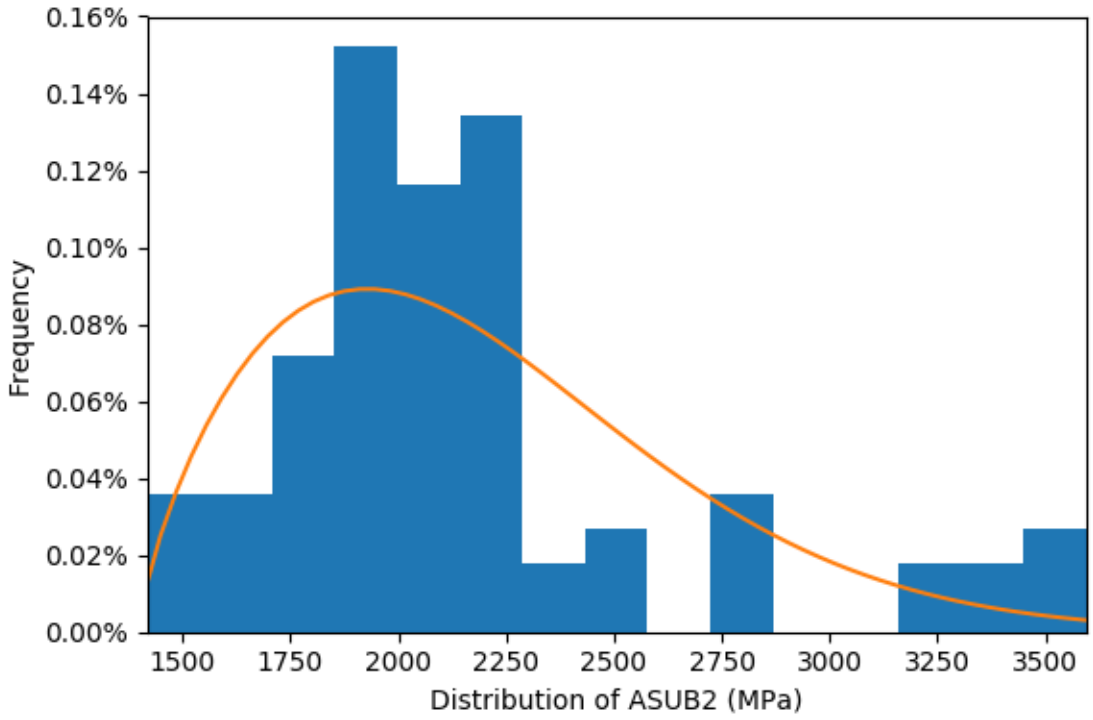

Figure 0.21: Histogram and fit of ASUB2 optimized to each realization

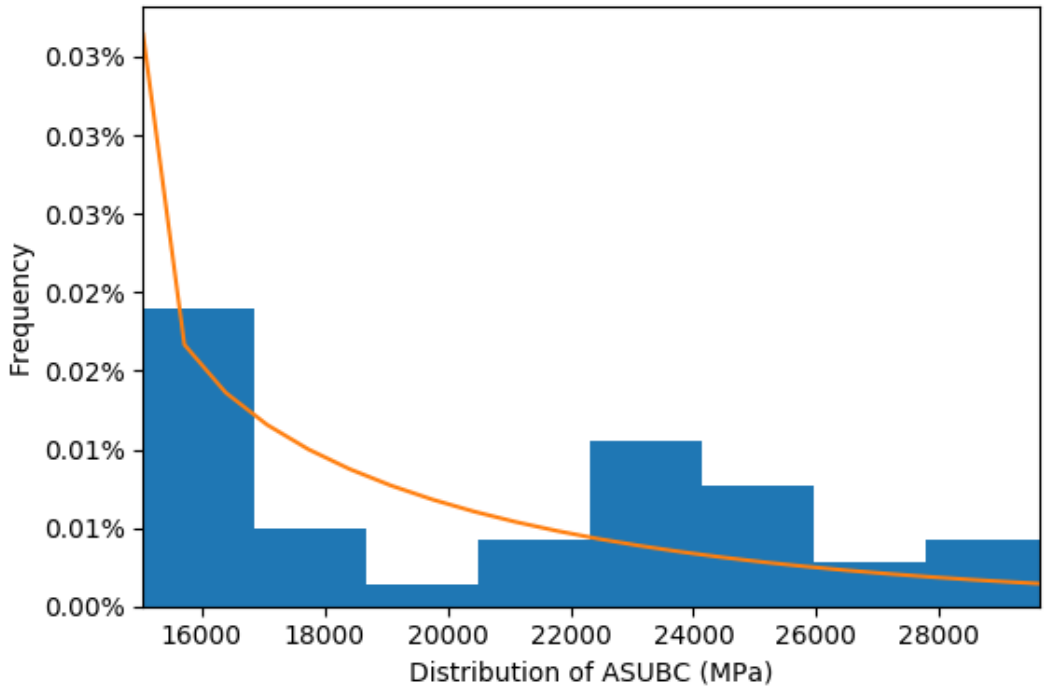

Figure 0.22: Histogram of ASUBC optimized to each realization

Finally, Table 0.3 shows values of the deviatoric variables optimized to the deviatoric phase of each confined triaxial compression test.

Table 0.3: Optimized simple HEP model deviatoric response variables

Name	Lib. Value	Ensemble Average Opt. Value						Units
		5 MPa	20 MPa	50 MPa	100 MPa	200 MPa	400 MPa	
ASUB1	410	370.6	356.1	348.0	366.3	352.8	303.0	MPa
BSUB0	-489.0	-4.85	-55.1	-19.7	-33.2	-15.4	-53.3	/Mb
VCURL	0.327	0.272	0.267	0.303	0.154	0.404	0.168	MPa
SHEARMAX	100000	82000	238000	200000	176000	266000	14207	MPa

CHAPTER 7

CONCLUSIONS

A recently developed method for imposing micro-boundaries on particle aggregates, as well as for obtaining the stress and deformation tensors for heterogeneous particle aggregates was used in this work to evaluate mesoscale bounds.

Hundreds of thousands of simulations were carried out using random samples of spherical particles with the Discrete Element formulation. The Cauchy stress tensor and the deformation tensor were successfully obtained for the ensemble using two different surface reconstruction methods, along nine distinct loading paths, subjected to two different boundary conditions. The ensemble distributions of the elastic moduli were successfully obtained and compare favorably with experimental values.

This is an important development, as it clears an important hurdle for utilization of DE models in the context of mesoscale modeling of particle aggregates. As such, and along with the statistical mechanics perspective herein, it represents a powerful tool in the multiscale modeling of particulate media.

Additionally, a method for simulating the particle size distribution (PSD) evolution of particle aggregates during grain crush-up was devised and presented in this work. It was demonstrated that through this approach, the evolution of Discrete Element Models of particle aggregates can be modeled during large stress loading and the resulting comminution approximated using the available experimental testing and data.

. The PSD evolution and constitutive response were successfully obtained for the ensemble under loading conditions simulating lab testing, including a Split-Hopkinson Pressure bar and triaxial loading.

Future Work

This framework opens several possibilities for further research. Some of these are discussed here, but there are many others yet to be considered.

The main thrust of this research is to improve constitutive characterization of particulate media, especially soils, when using solid mechanics simulation tools. Of particular interest are explicit dynamic applications that depend on evolution, loading path, and time-history of the particulate medium. In these dynamic applications, propagation of stress waves and shock response can be important. The mesoscale-based framework devised here is useful for modeling of the quasi-static response, however dynamic/shock response is also very important in hydrocode modeling. The immediate next step in this research would be to extend the meso-to-macro framework here to transient applications, including propagation of stress waves and shock response.

Another logical next step in continuing this mesoscale research, is to carry out this type of study with different particulate media. This can be another sand specimen, or perhaps a different type of soil entirely. Modeling of other types of soils are likely to require different physics to be considered. For example, if clay is prevalent, electrochemical interactions need to be modeled. Additionally, the non-cohesive sand considered here was only considered in the kiln-dried condition. However, for most soils two-phase flow is very important and can alter the response of the particulate medium significantly. There is a great deal of research being done in unsaturated fluid flow with Discrete Elements. If this

cutting-edge research is integrated into this mesoscale-based framework, it can yield a way to model soil mechanical response with evolving water-air interface flow.

Once a sufficient number of mesoscale studies are carried out on a large enough number of soils, it is conceivable that a large enough database of material results will exist to enable machine-learning algorithms to be able to sort through and make predictions for soil behavior in continuum modeling, but also possibly for in-situ applications.

Another place where this research could be very fruitful, would be in concrete research. Discrete Elements have been used to model concrete successfully in many applications. Using this type of ensemble mesoscale modeling would be very useful if it could be used for propagation of knowledge and uncertainty to the structural response of the concrete. Much of concrete practice currently is based on the principle that there needs to be a sufficient number of conservative assumptions in the design with the material. However, concrete practice stands to benefit from having some better-established confidence levels. This requires that the uncertainty inherent in material heterogeneity be established, which requires some sort of analysis like the one presented in the current framework.

REFERENCES

[1] D.C. Drucker, R.E. Gibson, D.J. Henkel, Soil mechanics and work hardening theories of plasticity, Transactions of the American Society of Civil Engineers 122 (1957).

[2] K. Roscoe, A. Schofield, A. Thurairajah, Yielding of clays in states wetter than critical, Geotechnique 13(3) (1963) 211-240.

[3] K. Terzaghi, Theory of Consolidation, Wiley Online Library1943.

[4] A. Bishop, The effective stress principle, Teknisk Ukeblad 39 (1959) 859-863.

[5] J.Q. Ehrgott Jr, Tactical Wheeled Vehicle Survivability: Results of Experiments to Quantify Aboveground Impulse, DTIC Document, 2010.

[6] C. Kloss, C. Goniva, LIGGGHTS–open source discrete element simulations of granular materials based on Lammps, Supplemental Proceedings: Materials Fabrication, Properties, Characterization, and Modeling, Volume 2 (2011) 781-788.

[7] S. Plimpton, P. Crozier, A. Thompson, LAMMPS-large-scale atomic/molecular massively parallel simulator, Sandia National Laboratories 18 (2007).

[8] M. Ostoja-Starzewski, Microstructural randomness and scaling in mechanics of materials, CRC Press2007.

[9] K. Sett, B. Jeremić, M.L. Kavvas, Stochastic elastic–plastic finite elements, Computer Methods in Applied Mechanics and Engineering 200(9) (2011) 997-1007.

[10] G. Stefanou, The stochastic finite element method: past, present and future, Computer Methods in Applied Mechanics and Engineering 198(9) (2009) 1031-1051.

[11] R. Hill, Elastic properties of reinforced solids: some theoretical principles, Journal of the Mechanics and Physics of Solids 11(5) (1963) 357-372.

[12] C. Coulomb, An attempt to apply the rules of maxima and minima to several problems of stability related to architecture, Mémoires de l'Académie Royale des Sciences 7 (1776) 343-382.

[13] H.P.G. Darcy, Les Fontaines publiques de la ville de Dijon. Exposition et application des principes à suivre et des formules à employer dans les questions de distribution d'eau, etc, V. Dalamont1856.

[14] G. Stokes, Cambridge Phl Soc, Trans 9 (1856) 5.

[15] W.J.M. Rankine, II. On the stability of loose earth, Philosophical transactions of the Royal Society of London (147) (1857) 9-27.

[16] J. Boussinesq, Application des potentiels à l'étude de l'équilibre et du mouvement des solides élastiques, Gauthier-Villars, Imprimeur-Libraire1885.

[17] A. Atterberg, Die plastizitat der Tone, Intern mitt. boden. (1911) 4-37.

[18] W. Fellenius, Statens jarnjvagars geoteknniska commission, Stockholm Sweden, 1922.

[19] K. Terzaghi, Erdbaumechanik auf bodenphysikalischer Grundlage, (1925).

[20] R. Proctor, Fundamental principles of soil compaction, Engineering news-record 111(13) (1933).

[21] A. Casagrande, The determination of pre-consolidation load and it's practical significance, Proc. Int. Conf. Soil Mech. Found. Eng. Cambridge, Mass., 1936, 1936, p. 60.

[22] D.W. Taylor, Fundamentals of soil mechanics, LWW1948.

[23] R.B. Peck, Advantages and limitations of the observational method in applied soil mechanics, Geotechnique 19(2) (1969) 171-187.

[24] A. Skempton, The bearing capacity of clays, Selected Papers on Soil Mechanics (1951) 50-59.

[25] L. Bjerrum, Engineering geology of Norwegian normally-consolidated marine clays as related to settlements of buildings, Geotechnique 17(2) (1967) 83-118.

[26] H.B. Seed, I.M. Idriss, Simplified procedure for evaluating soil liquefaction potential, Journal of Soil Mechanics & Foundations Div (1971).

[27] É. Guyon, J.-P. Troadec, Du sac de billes au tas de sable, Odile Jacob1994.

[28] A. Nakata, M. Hyde, H. Hyodo, Murata, A probabilistic approach to sand particle crushing in the triaxial test, Géotechnique 49(5) (1999) 567-583.

[29] B. Hopkinson, X. A method of measuring the pressure produced in the detonation of high, explosives or by the impact of bullets, Philosophical Transactions of the Royal Society of London. Series A, Containing Papers of a Mathematical or Physical Character 213(497-508) (1914) 437-456.

[30] H. Kolsky, An investigation of the mechanical properties of materials at very high rates of loading, Proceedings of the physical society. Section B 62(11) (1949) 676.

[31] G. Gray, Classic split Hopkinson pressure bar technique ASM V8 mechanical testing, Materials Park, Ohio: ASM International (1999) 17-20.

[32] A. Gilat, Y. Pao, High-rate decremental-strain-rate test, Experimental mechanics 28(3) (1988) 322-325.

[33] A.B. Shemirani, R. Naghdabadi, M. Ashrafi, Experimental and numerical study on choosing proper pulse shapers for testing concrete specimens by split Hopkinson pressure bar apparatus, Construction and Building Materials 125 (2016) 326-336.

[34] H. Luo, W.L. Cooper, H. Lu, Effects of particle size and moisture on the compressive behavior of dense Eglin sand under confinement at high strain rates, International Journal of Impact Engineering 65 (2014) 40-55.

[35] A. Bragov, A. Lomunov, I. Sergeichev, K. Tsembelis, W. Proud, Determination of physicomechanical properties of soft soils from medium to high strain rates, International Journal of Impact Engineering 35(9) (2008) 967-976.

[36] R.B. Brinkgreve, Selection of soil models and parameters for geotechnical engineering application, Soil constitutive models: Evaluation, selection, and calibration2005, pp. 69-98.

[37] M. Goldscheider, True triaxial tests on dense sand, Workshop on Constitutive Relations for Soils, 1982, pp. 11-54.

[38] D.C. Drucker, W. Prager, Soil mechanics and plastic analysis or limit design, Quarterly of applied mathematics 10(2) (1952) 157-165.

[39] F.L. DiMaggio, I.S. Sandler, Material model for granular soils, Journal of the Engineering Mechanics Division 97(3) (1971) 935-950.

[40] J.B. BURLAND, The yieding and dilation of clay, correspondence, Geotechnique 15(1) (1965) 211-214.

[41] D.M. Wood, Soil behaviour and critical state soil mechanics, Cambridge university press1990.

[42] I.S. Sandler, Review of the development of cap models for geomaterials, Shock and Vibration 12(1) (2005) 67-71.

[43] I. Sandler, M. Baron, Recent developments in the constitutive modelling of geological materials, Proceedings of the 3rd Conference on Numerical Methods in Geomechanics, Aachen, Wittke (ed), Balkema/Rotterdam, 1979, pp. 363-376.

[44] J. Isenberg, D. Vaughan, I. Sandler, Nonlinear soil-structure interaction, Final Report Weidlinger Associates, Menlo Park, CA. (1978).

[45] H. Levine, A two-surface plastic and microcracking model for plain concrete, ASME1982.

[46] J.C. Mould Jr, H.S. Levine, A rate-dependent three invariant softening model for concrete, Studies in Applied Mechanics, Elsevier1994, pp. 11-37.

[47] D. Pelessone, A modified formulation of the cap model, Gulf Atomics Report GA-C19579 to the Defense Nuclear Agency (1989).

[48] M. Rubin, Simple, convenient isotropic failure surface, Journal of engineering mechanics 117(2) (1991) 348-369.

[49] L.E. Schwer, Y.D. Murray, Continuous surface cap model for geomaterial modeling: A new LS-DYNA material type, Seventh International LSDYNA Users Conference. Dearborn. Michigan, LSTC& ETA, 2002, pp. 16-35.

[50] B. Loret, N. Khalili, A three-phase model for unsaturated soils, International journal for numerical and analytical methods in geomechanics 24(11) (2000) 893-927.

[51] A.W. Bishop, G. Blight, Some aspects of effective stress in saturated and partly saturated soils, Geotechnique 13(3) (1963) 177-197.

[52] P.-A. Guidault, O. Allix, L. Champaney, J.-P. Navarro, A two-scale approach with homogenization for the computation of cracked structures, Computers & structures 85(17-18) (2007) 1360-1371.

[53] S. Eckardt, C. Könke, Adaptive damage simulation of concrete using heterogeneous multiscale models, Journal of Algorithms & Computational Technology 2(2) (2008) 275-298.

[54] O. Lloberas-Valls, D. Rixen, A. Simone, L. Sluys, Multiscale domain decomposition analysis of quasi-brittle heterogeneous materials, International Journal for Numerical Methods in Engineering 89(11) (2012) 1337-1366.

[55] T. Hettich, A. Hund, E. Ramm, Modeling of failure in composites by X-FEM and level sets within a multiscale framework, Computer Methods in Applied Mechanics and Engineering 197(5) (2008) 414-424.

[56] S. Loehnert, T. Belytschko, A multiscale projection method for macro/microcrack simulations, International Journal for Numerical Methods in Engineering 71(12) (2007) 1466-1482.

[57] S. Ghosh, K. Lee, P. Raghavan, A multi-level computational model for multi-scale damage analysis in composite and porous materials, International Journal of Solids and Structures 38(14) (2001) 2335-2385.

[58] F. Larsson, K. Runesson, On two-scale adaptive FE analysis of micro-heterogeneous media with seamless scale-bridging, Computer Methods in Applied Mechanics and Engineering 200(37-40) (2011) 2662-2674.

[59] I. Temizer, P. Wriggers, An adaptive multiscale resolution strategy for the finite deformation analysis of microheterogeneous structures, Computer Methods in Applied Mechanics and Engineering 200(37-40) (2011) 2639-2661.

[60] J.T. Oden, K. Vemaganti, N. Moës, Hierarchical modeling of heterogeneous solids, Computer Methods in Applied Mechanics and Engineering 172(1-4) (1999) 3-25.

[61] N. Takano, M. Zako, M. Ishizono, Multi-scale computational method for elastic bodies with global and local heterogeneity, Journal of computer-aided materials design 7(2) (2000) 111.

[62] J. Fish, W. Chen, Discrete-to-continuum bridging based on multigrid principles, Computer Methods in Applied Mechanics and Engineering 193(17-20) (2004) 1693-1711.

[63] H. Zhang, J. Wu, J. Lv, A new multiscale computational method for elasto-plastic analysis of heterogeneous materials, Computational mechanics 49(2) (2012) 149-169.

[64] L.A. Bitencourt Jr, O.L. Manzoli, P.G. Prazeres, E.A. Rodrigues, T.N. Bittencourt, A coupling technique for non-matching finite element meshes, Computer methods in applied mechanics and engineering 290 (2015) 19-44.

[65] W. Voigt, Ueber die Beziehung zwischen den beiden Elasticitätsconstanten isotroper Körper, Annalen der physik 274(12) (1889) 573-587.

[66] A. Reuß, Berechnung der fließgrenze von mischkristallen auf grund der plastizitätsbedingung für einkristalle, ZAMM-Journal of Applied Mathematics and Mechanics/Zeitschrift für Angewandte Mathematik und Mechanik 9(1) (1929) 49-58.

[67] I. Babuška, Homogenization approach in engineering, Computing methods in applied sciences and engineering, Springer1976, pp. 137-153.

[68] G.I. Taylor, Plastic strain in metals, J. Inst. Metals 62 (1938) 307-324.

[69] G. Sachs, Zur ableitung einer fliessbedingung, Mitteilungen der deutschen Materialprüfungsanstalten, Springer1929, pp. 94-97.

[70] Z. Hashin, S. Shtrikman, A variational approach to the theory of the elastic behaviour of multiphase materials, Journal of the Mechanics and Physics of Solids 11(2) (1963) 127-140.

[71] Z. Hashin, S. Shtrikman, A variational approach to the theory of the effective magnetic permeability of multiphase materials, Journal of applied Physics 33(10) (1962) 3125-3131.

[72] L. Walpole, On bounds for the overall elastic moduli of inhomogeneous systems—I, Journal of the Mechanics and Physics of Solids 14(3) (1966) 151-162.

[73] G.W. Milton, R.V. Kohn, Variational bounds on the effective moduli of anisotropic composites, Journal of the Mechanics and Physics of Solids 36(6) (1988) 597-629.

[74] R.W. Zimmerman, Hashin-Shtrikman bounds on the Poisson ratio of a composite material, Mechanics research communications 19(6) (1992) 563-569.

[75] B.W. Rosen, Z. Hashin, Effective thermal expansion coefficients and specific heats of composite materials, International Journal of Engineering Science 8(2) (1970) 157-173.

[76] S. Nemat-Nasser, N. Yu, M. Hori, Bounds and estimates of overall moduli of composites with periodic microstructure, Mechanics of materials 15(3) (1993) 163-181.

[77] J.D. Eshelby, The determination of the elastic field of an ellipsoidal inclusion, and related problems, Proceedings of the royal society of London. Series A. Mathematical and physical sciences 241(1226) (1957) 376-396.

[78] T.I. Zohdi, P. Wriggers, Computational micro-macro material testing, Archives of Computational Methods in Engineering 8(2) (2001) 131-228.

[79] O. Pierard, C. Friebel, I. Doghri, Mean-field homogenization of multi-phase thermo-elastic composites: a general framework and its validation, Composites Science and Technology 64(10-11) (2004) 1587-1603.

[80] T. Mori, K. Tanaka, Average stress in matrix and average elastic energy of materials with misfitting inclusions, Acta metallurgica 21(5) (1973) 571-574.

[81] R. Hill, A self-consistent mechanics of composite materials, Journal of the Mechanics and Physics of Solids 13(4) (1965) 213-222.

[82] Y. Huang, K. Hu, X. Wei, A. Chandra, A generalized self-consistent mechanics method for composite materials with multiphase inclusions, Journal of the Mechanics and Physics of Solids 42(3) (1994) 491-504.

[83] R. McLaughlin, A study of the differential scheme for composite materials, International Journal of Engineering Science 15(4) (1977) 237-244.

[84] M. Hori, S. Nemat-Nasser, Double-inclusion model and overall moduli of multi-phase composites, Mechanics of Materials 14(3) (1993) 189-206.

[85] R. Hill, On constitutive macro-variables for heterogeneous solids at finite strain, Proceedings of the Royal Society of London. A. Mathematical and Physical Sciences 326(1565) (1972) 131-147.

[86] R. Ogden, On the overall moduli of non-linear elastic composite materials, Journal of the Mechanics and Physics of Solids 22(6) (1974) 541-553.

[87] P. Ponte Castaneda, J.R. Willis, On the overall properties of nonlinearly viscous composites, Proceedings of the Royal Society of London. A. Mathematical and Physical Sciences 416(1850) (1988) 217-244.

[88] P. Suquet, Overall potentials and extremal surfaces of power law or ideally plastic composites, Journal of the Mechanics and Physics of Solids 41(6) (1993) 981-1002.

[89] T. Olson, Improvements on Taylor's upper bound for rigid-plastic composites, Materials Science and Engineering: A 175(1-2) (1994) 15-20.

[90] D. Talbot, J. Willis, Some simple explicit bounds for the overall behaviour of nonlinear composites, International journal of solids and structures 29(14-15) (1992) 1981-1987.

[91] P.P. Castañeda, The effective mechanical properties of nonlinear isotropic composites, Journal of the Mechanics and Physics of Solids 39(1) (1991) 45-71.

[92] P.P. Castañeda, New variational principles in plasticity and their application to composite materials, Journal of the Mechanics and Physics of Solids 40(8) (1992) 1757-1788.

[93] G. DeBotton, P.P. Castañeda, Elastoplastic constitutive relations for fiber-reinforced solids, International journal of solids and structures 30(14) (1993) 1865-1890.

[94] T. Christman, A. Needleman, S. Suresh, An experimental and numerical study of deformation in metal-ceramic composites, Acta Metallurgica 37(11) (1989) 3029-3050.

[95] V. Tvergaard, Analysis of tensile properties for a whisker-reinforced metal-matrix composite, Acta metallurgica et materialia 38(2) (1990) 185-194.

[96] G. Bao, J. Hutchinson, R. McMeeking, Particle reinforcement of ductile matrices against plastic flow and creep, Acta metallurgica et materialia 39(8) (1991) 1871-1882.

[97] O. van der Sluis, P. Schreurs, H. Meijer, Effective properties of a viscoplastic constitutive model obtained by homogenisation, Mechanics of Materials 31(11) (1999) 743-759.

[98] J. Mandel, Plasticité classique et viscoplasticité: course held... Udine, September-October 1971, Springer, 1972.

[99] Z. Hashin, Analysis of composite materials, J. appl. Mech 50(2) (1983) 481-505.

[100] M. Ostoja-Starzewski, From Random Fields to Classical or Generalized Continuum Models, Procedia IUTAM 6 (2013) 31-34.

[101] S. Torquato, H. Haslach Jr, Random heterogeneous materials: microstructure and macroscopic properties, Appl. Mech. Rev. 55(4) (2002) B62-B63.

[102] K. Huang, Statistical mechanics, stme (1987) 512.

[103] M. Kardar, Statistical physics of particles, Cambridge University Press2007.

[104] J. Sethna, Statistical mechanics: entropy, order parameters, and complexity, Oxford University Press2006.

[105] J.W. Gibbs, The collected works of J. Willard Gibbs, Yale Univ. Press, 1948.

[106] W.F. Brown Jr, Solid mixture permittivities, The Journal of Chemical Physics 23(8) (1955) 1514-1517.

[107] M.J. Beran, Statistical continuum theories, American Journal of Physics 36(10) (1968) 923-923.

[108] J.J. McCOY, On the displacement field in an elastic medium with random variations of material properties, Recent Advances in Engineering Sciences 5 (1970) 235-254.

[109] S. Torquato, Effective stiffness tensor of composite media—I. Exact series expansions, Journal of the Mechanics and Physics of Solids 45(9) (1997) 1421-1448.

[110] T.J. Sullivan, Introduction to uncertainty quantification, Springer2015.

[111] S. Boyd, L. Vandenberghe, Convex optimization, Cambridge University Press2004.

[112] B.M. Adams, W. Bohnhoff, K. Dalbey, J. Eddy, M. Eldred, D. Gay, K. Haskell, P.D. Hough, L. Swiler, DAKOTA, a multilevel parallel object-oriented framework for design optimization, parameter estimation, uncertainty quantification, and sensitivity analysis: version 5.0 user's manual, Sandia National Laboratories, Tech. Rep. SAND2010-2183 (2009).

[113] P.A. Cundall, O.D. Strack, A discrete numerical model for granular assemblies, Geotechnique 29(1) (1979) 47-65.

[114] L. Verlet, Computer" experiments" on classical fluids. ii. equilibrium correlation functions, Physical Review 165(1) (1968) 201.

[115] R.D. Skeel, Variable step size destabilizes the Störmer/leapfrog/Verlet method, BIT Numerical Mathematics 33(1) (1993) 172-175.

[116] R. Mindlin, Compliance of elastic bodies in contact, Journal of applied mechanics 16 (1949).

[117] O.R. Walton, R.L. Braun, Viscosity, granular-temperature, and stress calculations for shearing assemblies of inelastic, frictional disks, Journal of rheology 30(5) (1986) 949-980.

[118] C. Thornton, Coefficient of restitution for collinear collisions of elastic-perfectly plastic spheres, Journal of Applied Mechanics 64(2) (1997) 383-386.

[119] C. Thornton, S.J. Cummins, P.W. Cleary, An investigation of the comparative behaviour of alternative contact force models during inelastic collisions, Powder Technology 233 (2013) 30-46.

[120] R.D. Mindlin, Elastic spheres in contact under varying oblique forces, J. Applied Mech. 20 (1953) 327-344.

[121] B.V. Derjaguin, V.M. Muller, Y.P. Toporov, Effect of contact deformations on the adhesion of particles, Journal of Colloid and interface science 53(2) (1975) 314-326.

[122] S. Hentz, F.V. Donzé, L. Daudeville, Discrete element modelling of concrete submitted to dynamic loading at high strain rates, Computers & structures 82(29-30) (2004) 2509-2524.

[123] W. Weibull, A statistical distribution function of wide applicability, Journal of applied mechanics 18(3) (1951) 293-297.

[124] S. Van Der Walt, S.C. Colbert, G. Varoquaux, The NumPy array: a structure for efficient numerical computation, Computing in Science & Engineering 13(2) (2011) 22.

[125] K. Sato, H. Kitajima, M. Takahashi, T. Matsushima, Bilinear log n-log p relation and critical power-law grain size distribution of crushable aggregates under compression and shear, arXiv preprint arXiv:1706.00910 (2017).

[126] M. Borkovec, W. De Paris, R. Peikert, The fractal dimension of the Apollonian sphere packing, Fractals 2(04) (1994) 521-526.

[127] O. Tsoungui, D. Vallet, J.-C. Charmet, Numerical model of crushing of grains inside two-dimensional granular materials, Powder technology 105(1-3) (1999) 190-198.

[128] M. Todisco, W. Wang, M. Coop, K. Senetakis, Multiple contact compression tests on sand particles, Soils and Foundations 57(1) (2017) 126-140.

[129] W. Zheng, D.D. Tannant, Grain breakage criteria for discrete element models of sand crushing under one-dimensional compression, Computers and Geotechnics 95 (2018) 231-239.

[130] S. Akers, M. Adley, J. Cargile, Comparison of constitutive models for geologic materials used in penetration and ground shock calculations, Proceedings of the 7th International Symposium on Interaction of the Effects of Munitions with Structures, Mannheim, Germany, 1995.

[131] H. Zimmerman, M. Wagner, J. Carney, Y. Ito, Effects of site geology on ground shock environments: Report 1, constitutive models for materials i2, i3, and w1-w10, Technical Rep. No. SL-87-19, US Army Engineer Waterways Experiment Station, Vicksburg, Miss (1987).

[132] H.D. Zimmerman, R. Shimano, Y. Ito, Early-time ground shock from buried conventional explosives: user's guide for SABER-PC/CWE, US Army Engineer Waterways Experiment Station1992.

[133] G. Johnson, R. Stryk, S. Beissel, User instructions for the 2011 version of the EPIC code, Alliant Techsystems Inc., Hopkins, MN. Distribution authorized to US government agencies and their contractors (2011).

[134] H.D. Zimmerman, Geological Constitutive Model & Equation of State Upgrade: Code Implementation and Documentation Guide, ERDC, 2009.

[135] J.H. Tillotson, Metallic equations of state for hypervelocity impact, GENERAL DYNAMICS SAN DIEGO CA GENERAL ATOMIC DIV, 1962.

[136] A.L. Brundage, Implementation of Tillotson equation of state for hypervelocity impact of metals, geologic materials, and liquids, Procedia Engineering 58 (2013) 461-470.

[137] V. Šmilauer, Reference Manual. In Yade Documentation 2nd ed., The Yade Project, DOI 10.5281/zenodo.34045, http://yade-dem.org/doc/, 2015.

[138] A.-T. Tong, E. Catalano, B. Chareyre, Pore-scale flow simulations: model predictions compared with experiments on bi-dispersed granular assemblies, Oil & Gas Science and Technology–Revue d'IFP Energies nouvelles 67(5) (2012) 743-752.

[139] C. Huet, Universal conditions for assimilation of a heterogeneous material to an effective continuum, Mechanics research communications 9(3) (1982) 165-170.

[140] C. Huet, On the definition and experimental determination of effective constitutive equations for assimilating heterogeneous materials, Mechanics Research Communications 11(3) (1984) 195-200.

[141] C. Huet, Application of variational concepts to size effects in elastic heterogeneous bodies, Journal of the Mechanics and Physics of Solids 38(6) (1990) 813-841.

[142] C. Huet, An integrated micromechanics and statistical continuum thermodynamics approach for studying the fracture behaviour of microcracked heterogeneous materials with delayed response, Engineering Fracture Mechanics 58(5-6) (1997) 459-556.

[143] C. Huet, Coupled size and boundary-condition effects in viscoelastic heterogeneous and composite bodies, Mechanics of Materials 31(12) (1999) 787-829.

[144] B. Chareyre, Caulk, R.A., Chèvremont, W., Guntz, T., Kneib, F., Kunhappen, D., Pourroy, J., Calcul distribué MPI pour la dynamique de systèmes particulaires, Yade Technical Archive, 2019.

[145] F.E. Grubbs, Procedures for detecting outlying observations in samples, Technometrics 11(1) (1969) 1-21.

[146] W. Stefansky, Rejecting outliers in factorial designs, Technometrics 14(2) (1972) 469-479.

[147] M. Fréchet, Sur les ensembles compacts de fonctions mesurables, Fundamenta Mathematicae 9(1) (1927) 25-32.

[148] W.K. Brown, K.H. Wohletz, Derivation of the Weibull distribution based on physical principles and its connection to the Rosin–Rammler and lognormal distributions, Journal of Applied Physics 78(4) (1995) 2758-2763.

[149] L. Booker, Improving search in genetic algorithms, Genetic algorithms and simulated annealing (1987) 61-73.

[150] D.E. Goldberg, Genetic algorithms, Pearson Education India2006.

[151] J.P. Dettmar, Static and dynamic homogenization analyses of discrete granular and atomistic structures on different time and length scales, 2006.

[152] C. Miehe, J. Dettmar, D. Zäh, Homogenization and two-scale simulations of granular materials for different microstructural constraints, International Journal for Numerical Methods in Engineering 83(8-9) (2010) 1206-1236.

[153] J. Liu, E. Bosco, A. Suiker, Formulation and numerical implementation of micro-scale boundary conditions for particle aggregates, Granular Matter 19(4) (2017) 72.

[154] Q.T. Tran, D. Taniar, M. Safar, Reverse k nearest neighbor and reverse farthest neighbor search on spatial networks, Transactions on large-scale data-and knowledge-centered systems I, Springer2009, pp. 353-372.

[155] F. Hurtado, M. Noy, J. Urrutia, Flipping Edges in Triangulations, Discrete & Computational Geometry 22(3) (1999) 333-346.

[156] L.J. Guibas, D.E. Knuth, M. Sharir, Randomized incremental construction of Delaunay and Voronoi diagrams, Algorithmica 7(1) (1992) 381-413.

[157] H. Edelsbrunner, N.R. Shah, Incremental topological flipping works for regular triangulations, Algorithmica 15(3) (1996) 223-241.

[158] S. Peterson, Computing constrained Delaunay triangulations in the plane, University of Minnesota Undergraduate (1998).

[159] P. Cignoni, C. Montani, R. Scopigno, DeWall: A fast divide and conquer Delaunay triangulation algorithm in Ed, Computer-Aided Design 30(5) (1998) 333-341.

[160] D. Sinclair, S-hull: a fast radial sweep-hull routine for Delaunay triangulation, arXiv preprint arXiv:1604.01428 (2016).

[161] H. Edelsbrunner, D. Kirkpatrick, R. Seidel, On the shape of a set of points in the plane, IEEE Transactions on information theory 29(4) (1983) 551-559.

[162] H. Edelsbrunner, E.P. Mücke, Three-dimensional alpha shapes, ACM Transactions on Graphics (TOG) 13(1) (1994) 43-72.

[163] A.E.H. Love, A treatise on the mathematical theory of elasticity, at the University Press1920.

[164] J. Weber, Recherches concernant les contraintes intergranulaires dans les milieux pulvérulents, Bulletin de Liaison des Ponts-et-chaussées 20 (1966) 1-20.

[165] J. Christoffersen, M. Mehrabadi, S. Nemat-Nasser, A micromechanical description of granular material behavior, Journal of applied mechanics 48(2) (1981) 339-344.

[166] M.M. Mehrabadi, S. Nemat-Nasser, M. Oda, On statistical description of stress and fabric in granular materials, International Journal for Numerical and Analytical Methods in Geomechanics 6(1) (1982) 95-108.

[167] F. Wang, B. Fu, H. Luo, S. Staggs, R.A. Mirshams, W.L. Cooper, S.Y. Park, M.J. Kim, C. Hartley, H. Lu, Characterization of the Grain-Level Mechanical Behavior of Eglin Sand by Nanoindentation, Experimental Mechanics 54(5) (2014) 871-884.

[168] B. Martin, O. Cazacu, Experimental and theoretical investigation of the high-pressure, undrained response of a cohesionless sand, International Journal for Numerical and Analytical Methods in Geomechanics 37(14) (2013) 2321-2347.

[169] K. Senetakis, M.R. Coop, M.C. Todisco, The inter-particle coefficient of friction at the contacts of Leighton Buzzard sand quartz minerals, Soils and Foundations 53(5) (2013) 746-755.

[170] C. Sandeep, K. Senetakis, Grain-scale mechanics of quartz sand under normal and tangential loading, Tribology International 117 (2018) 261-271.

[171] V. Nardelli, M. Coop, J. Andrade, F. Paccagnella, An experimental investigation of the micromechanics of Eglin sand, Powder Technology 312 (2017) 166-174.

[172] D.M. Cole, Laboratory observations of frictional sliding of individual contacts in geologic materials, Granular Matter 17(1) (2015) 95-110.

[173] H. Yang, S.K. Sinha, Y. Feng, D.B. McCallen, B. Jeremić, Energy dissipation analysis of elastic–plastic materials, Computer Methods in Applied Mechanics and Engineering 331 (2018) 309-326.

APPENDIX A

HISTOGRAMS OF MESOSCALE ELASTIC MODULI OF EGLIN SAND WITHOUT COMMINUTION

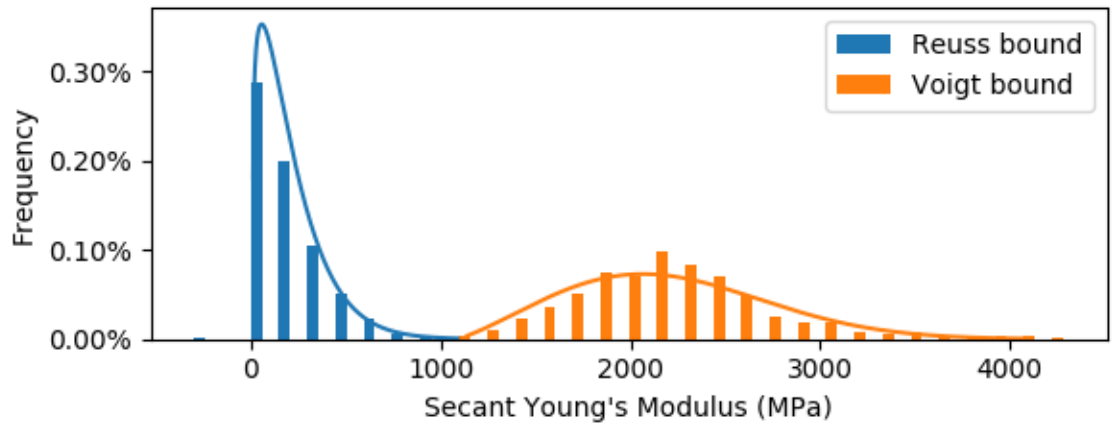

Figure 0.1: Secant Young's Modulus for $1x10^3$ Particle Ensemble at 1MPa

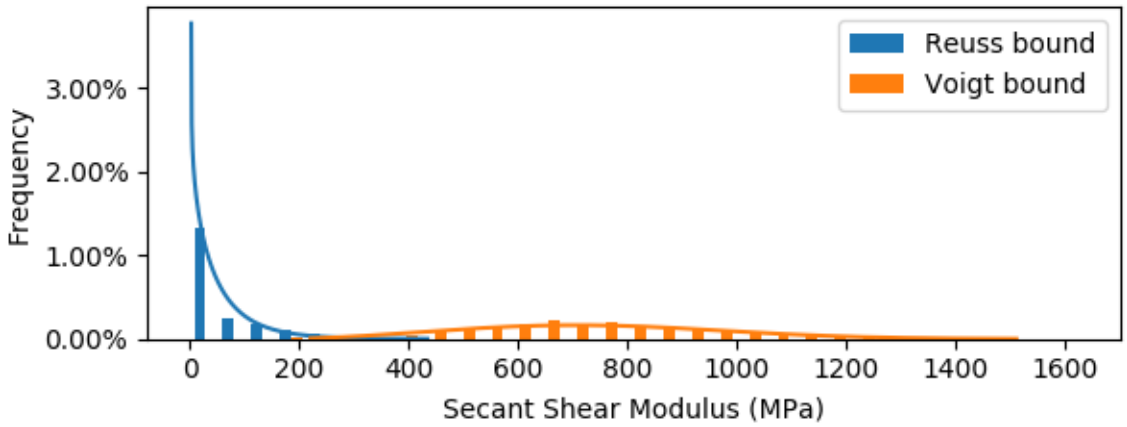

Figure 0.2: Secant Shear Modulus for $1x10^3$ Particle Ensemble at 1MPa

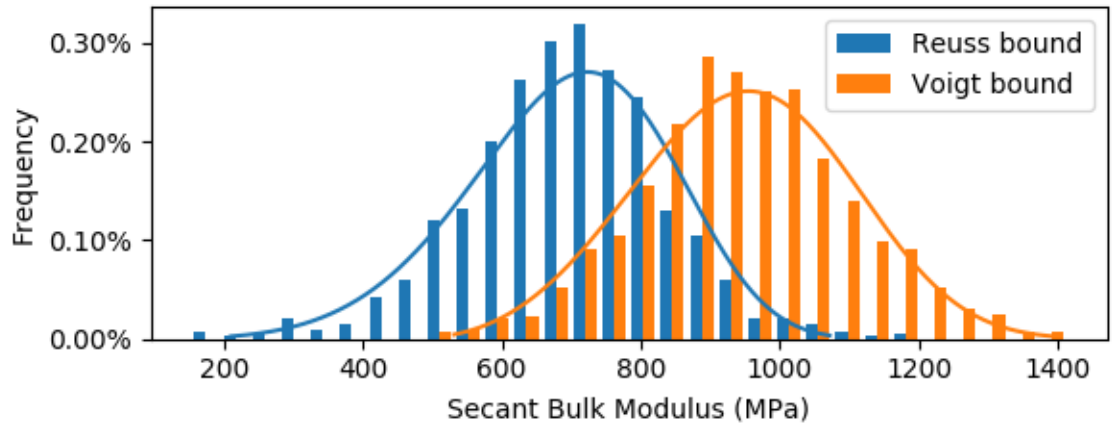

Figure 0.3: Secant Bulk Modulus for $1x10^3$ Particle Ensemble at 1MPa

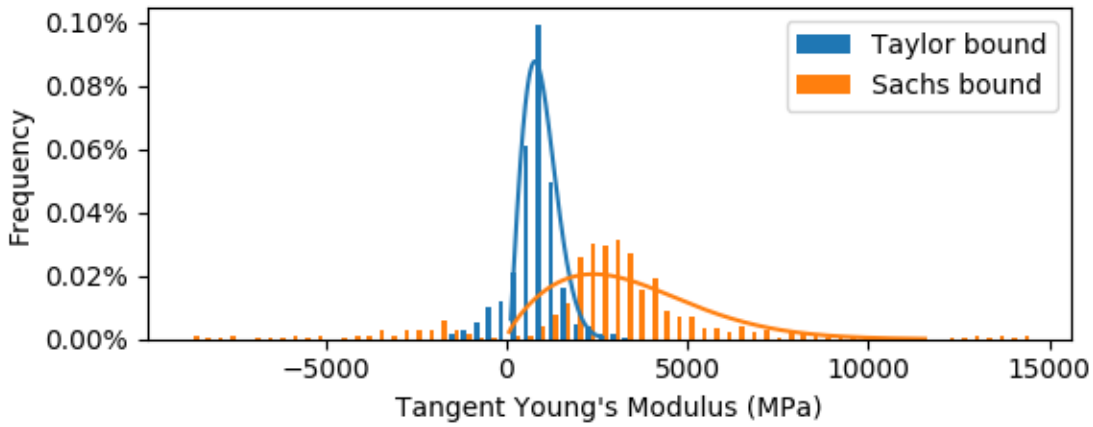

Figure 0.4: Tangent Young's Modulus for $1x10^3$ Particle Ensemble at 1MPa

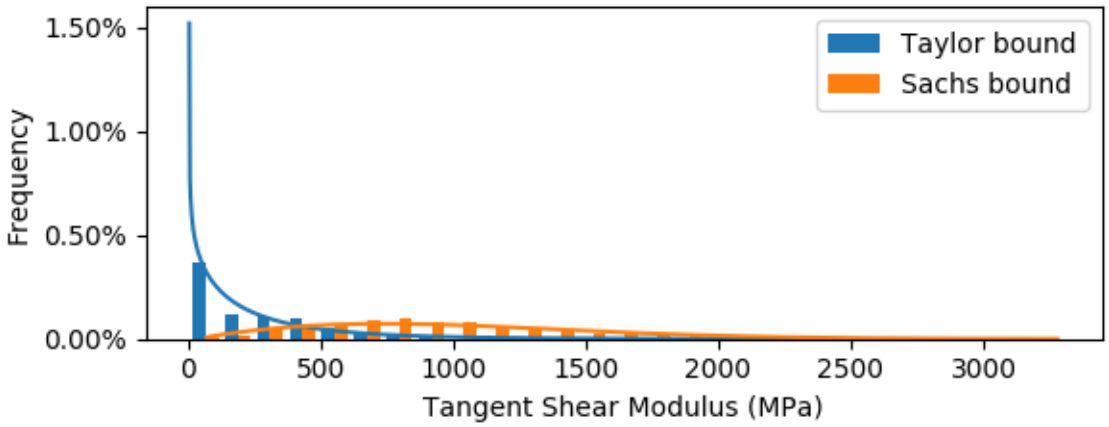

Figure 0.5: Tangent Shear Modulus for $1x10^3$ Particle Ensemble at 1MPa

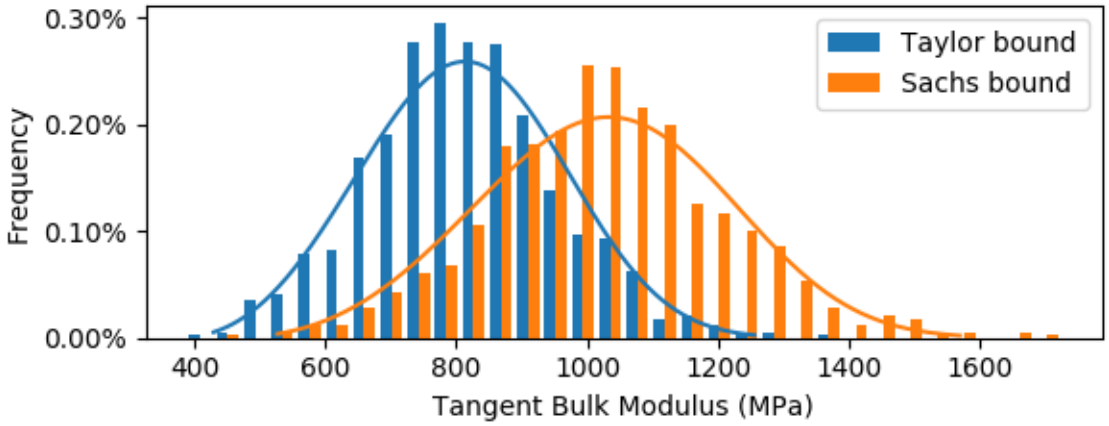

Figure 0.6: Tangent Bulk Modulus for $1x10^3$ Particle Ensemble at 1MPa

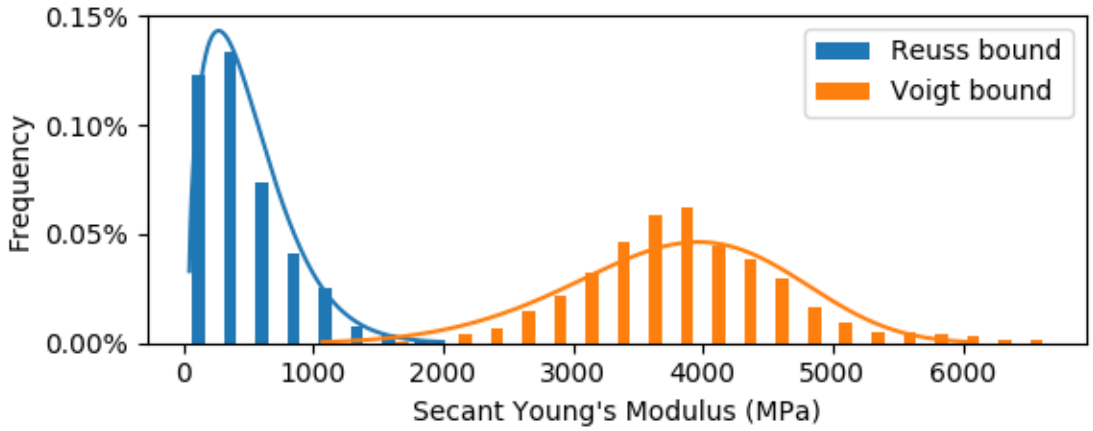

Figure 0.7: Secant Young's Modulus for $1x10^3$ Particle Ensemble at 5MPa

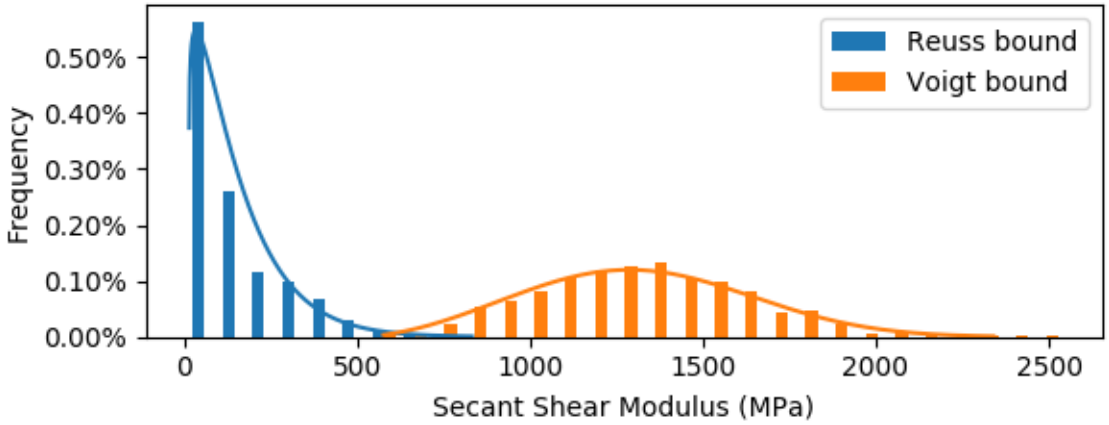

Figure 0.8: Secant Shear Modulus for $1x10^3$ Particle Ensemble at 5MPa

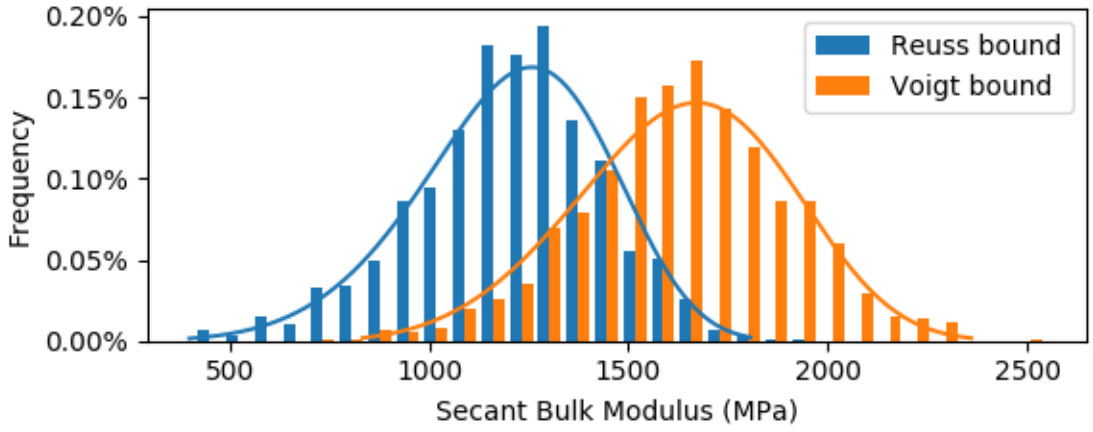

Figure 0.9: Secant Bulk Modulus for $1x10^3$ Particle Ensemble at 5MPa

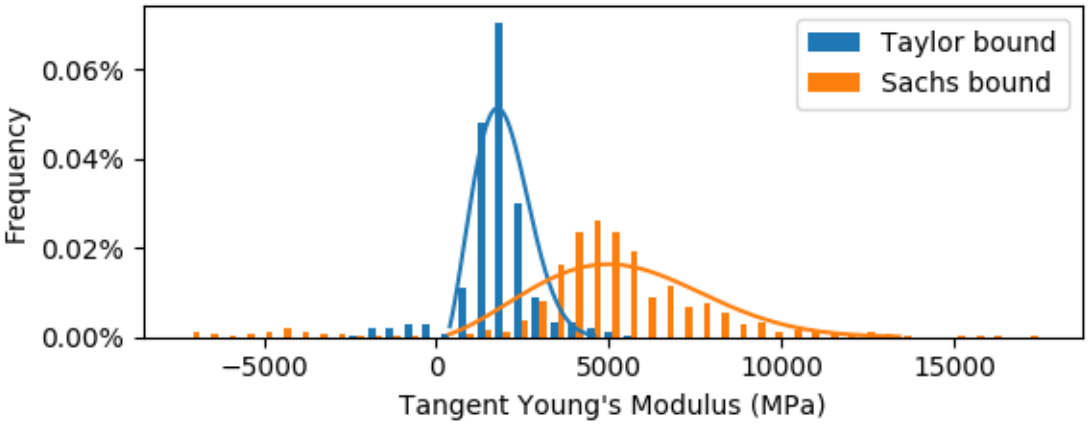

Figure 0.10: Tangent Young's Modulus for $1x10^3$ Particle Ensemble at 5MPa

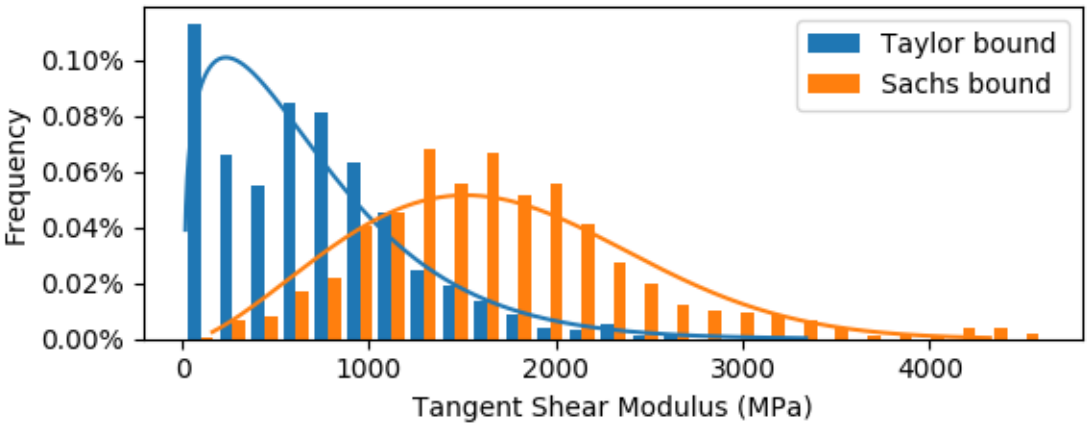

Figure 0.11: Tangent Shear Modulus for $1x10^3$ Particle Ensemble at 5MPa

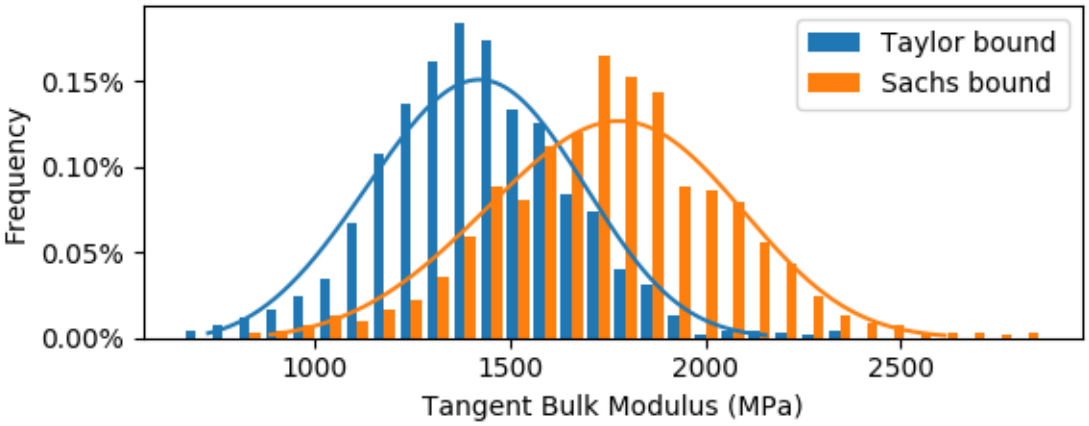

Figure 0.12: Tangent Bulk Modulus for $1x10^3$ Particle Ensemble at 5MPa

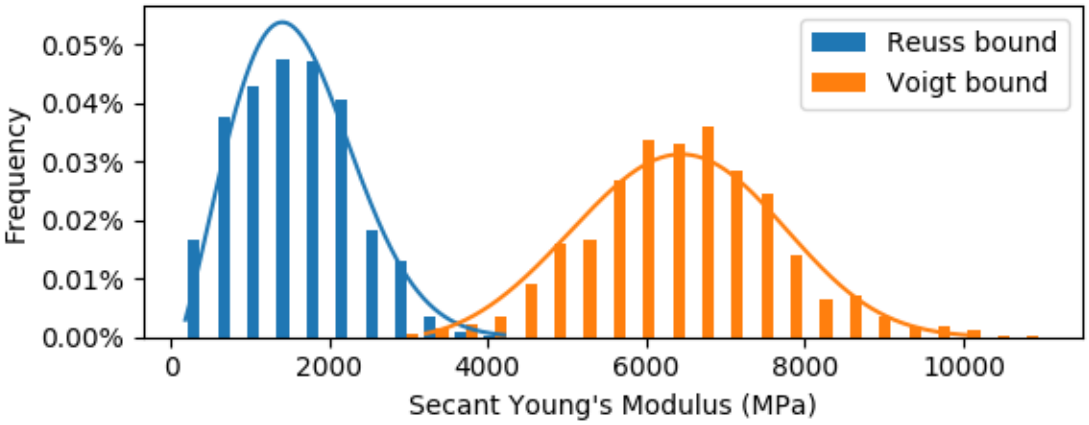

Figure 0.13: Secant Young's Modulus for $1x10^3$ Particle Ensemble at 20MPa

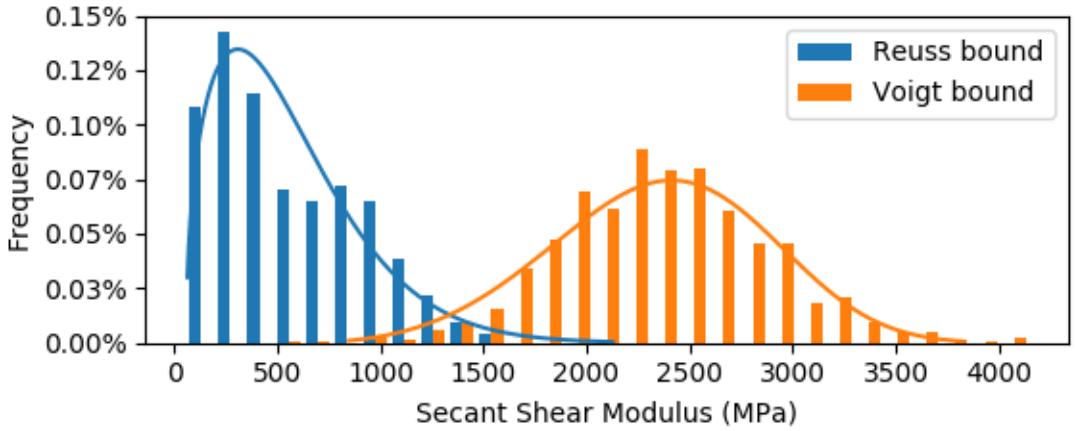

Figure 0.14: Secant Shear Modulus for $1x10^3$ Particle Ensemble at 20MPa

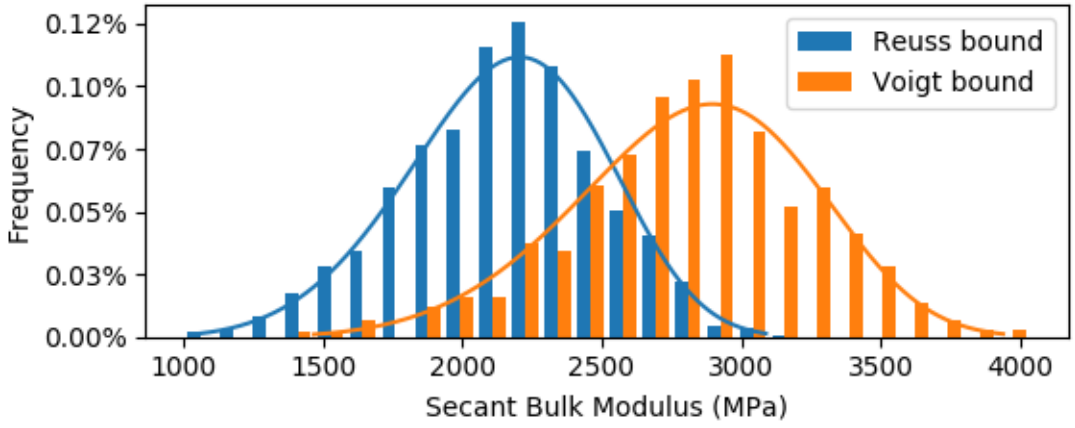

Figure 0.15: Secant Bulk Modulus for $1x10^3$ Particle Ensemble at 20MPa

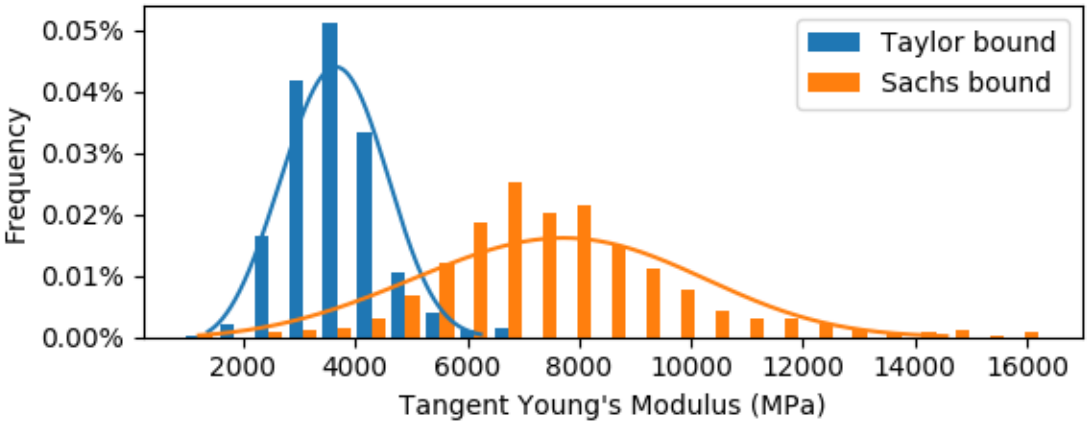

Figure 0.16: Tangent Young's Modulus for $1x10^3$ Particle Ensemble at 20MPa

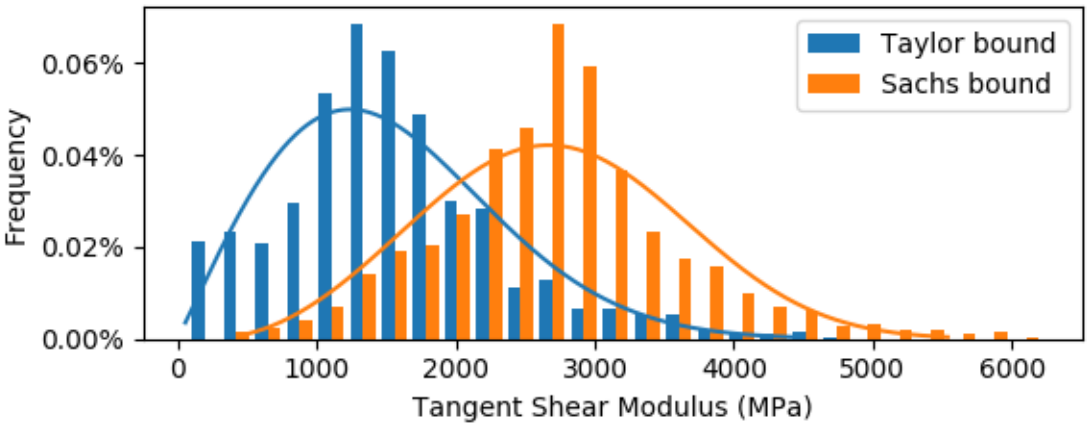

Figure 0.17: Tangent Shear Modulus for $1x10^3$ Particle Ensemble at 20MPa

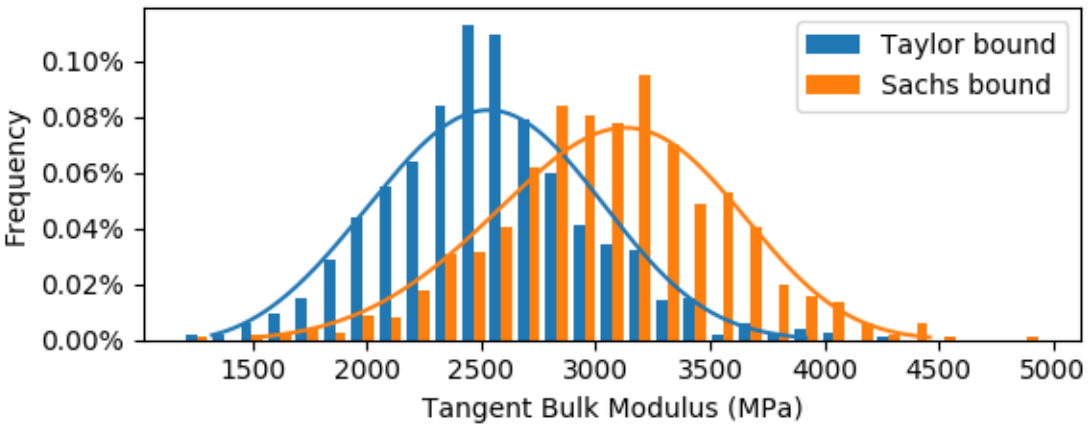

Figure 0.18: Tangent Bulk Modulus for $1x10^3$ Particle Ensemble at 20MPa

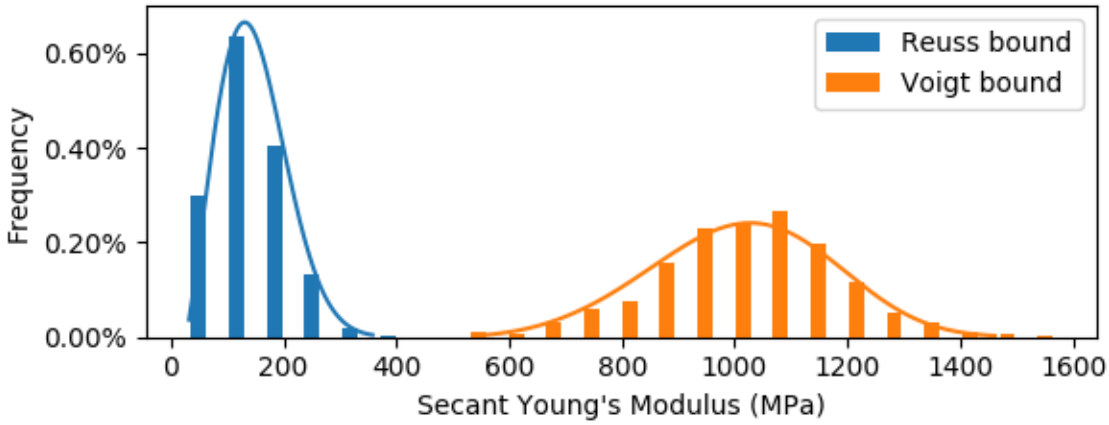

Figure 0.19: Secant Young's Modulus for $1x10^4$ Particle Ensemble at 1MPa

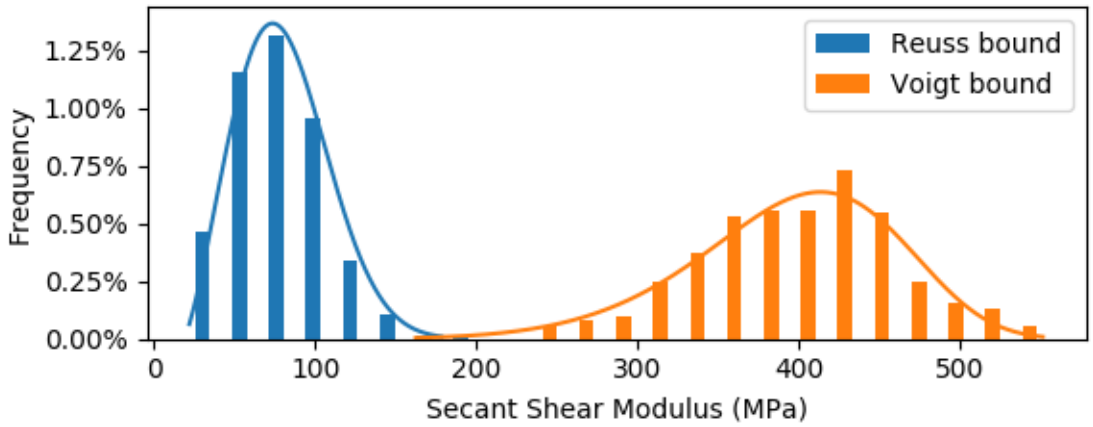

Figure 0.20: Secant Shear Modulus for $1x10^4$ Particle Ensemble at 1MPa

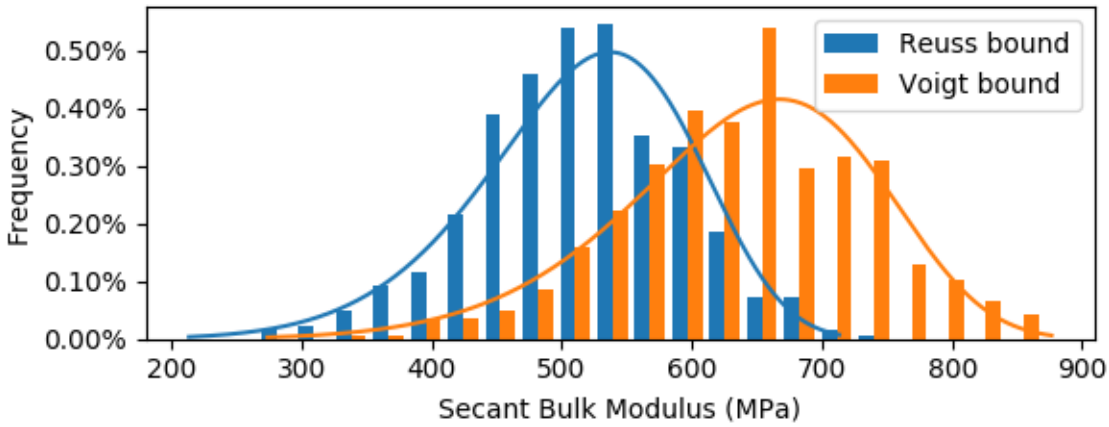

Figure 0.21: Secant Bulk Modulus for $1x10^4$ Particle Ensemble at 1MPa

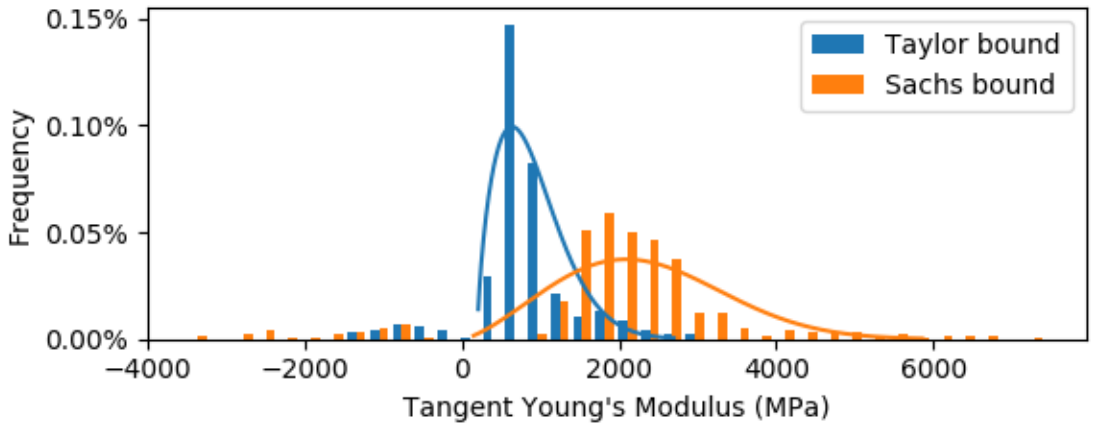

Figure 0.22: Tangent Young's Modulus for $1x10^4$ Particle Ensemble at 1MPa

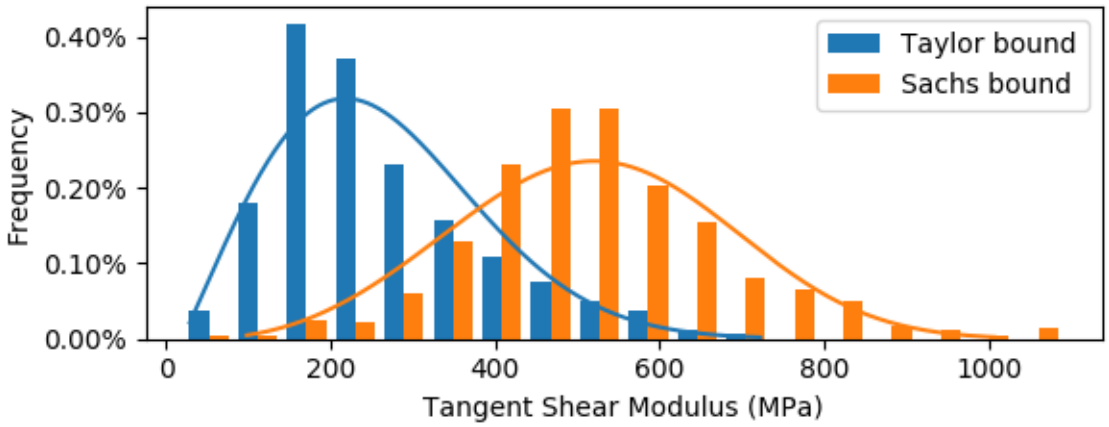

Figure 0.23: Tangent Shear Modulus for $1x10^4$ Particle Ensemble at 1MPa

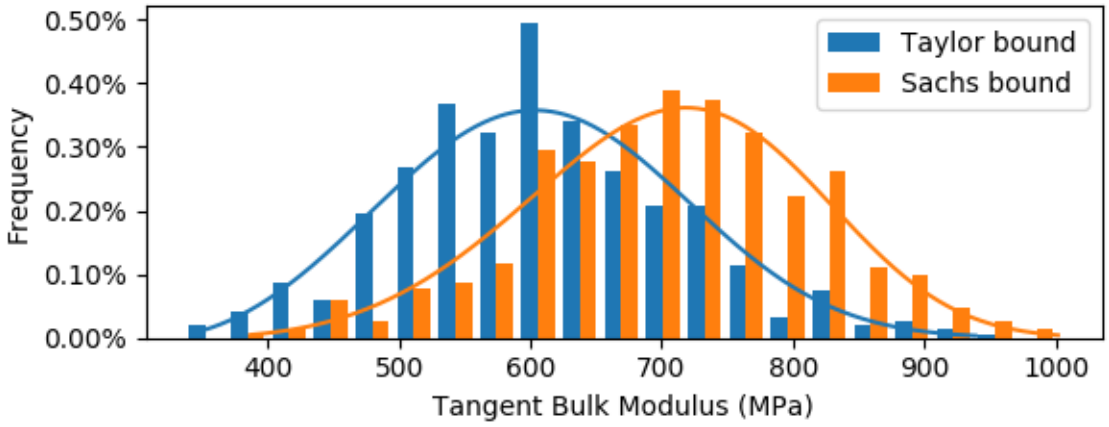

Figure 0.24: Tangent Bulk Modulus for $1x10^4$ Particle Ensemble at 1MPa

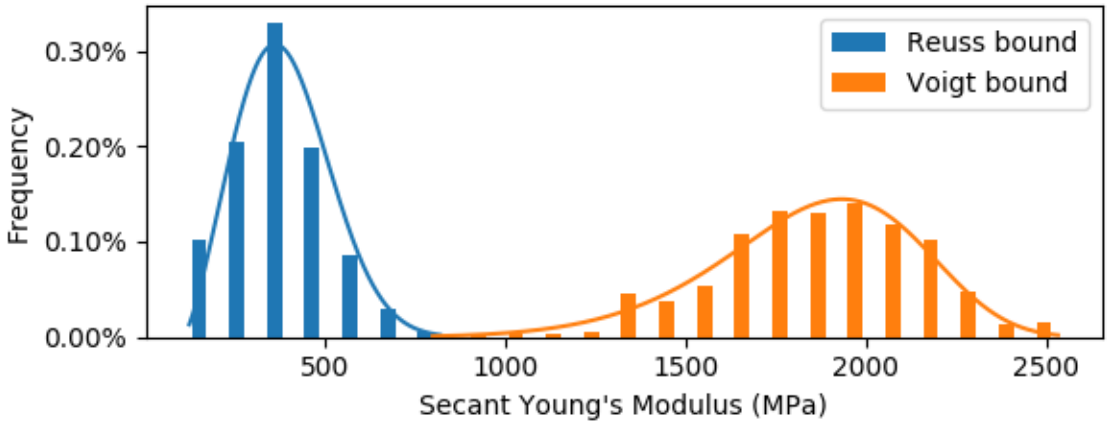

Figure 0.25: Secant Young's Modulus for $1x10^4$ Particle Ensemble at 5MPa

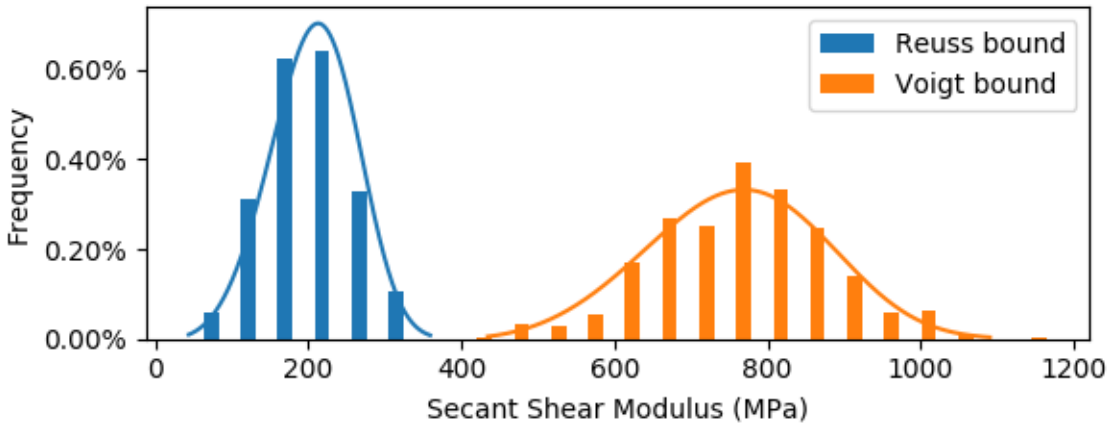

Figure 0.26: Secant Shear Modulus for $1x10^4$ Particle Ensemble at 5MPa

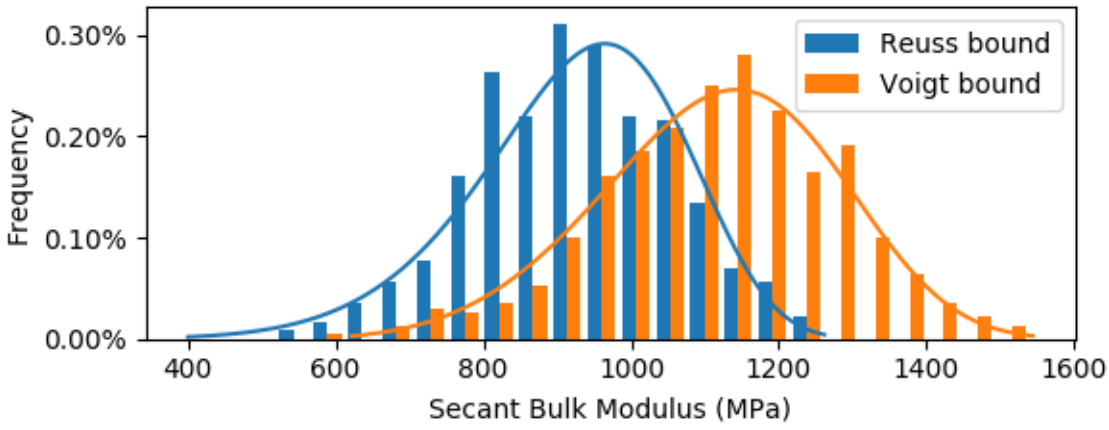

Figure 0.27: Secant Bulk Modulus for $1x10^4$ Particle Ensemble at 5MPa

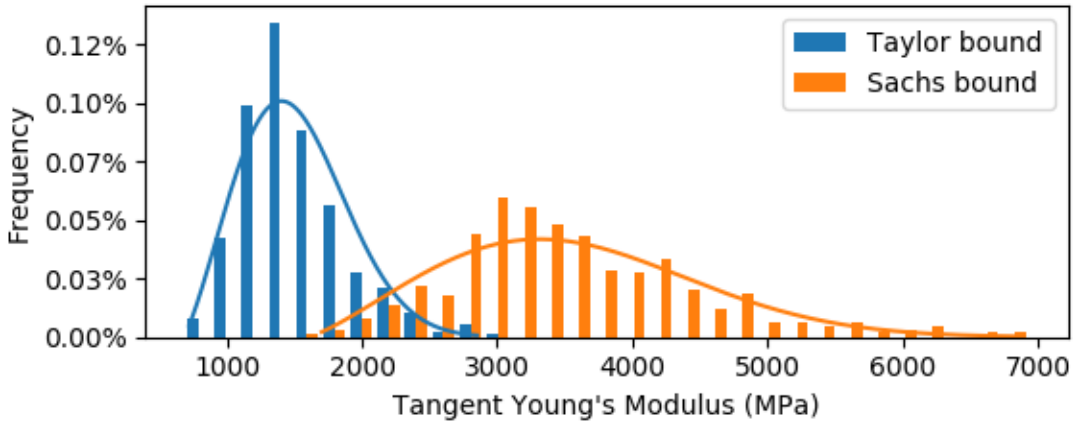

Figure 0.28: Tangent Young's Modulus for $1x10^4$ Particle Ensemble at 5MPa

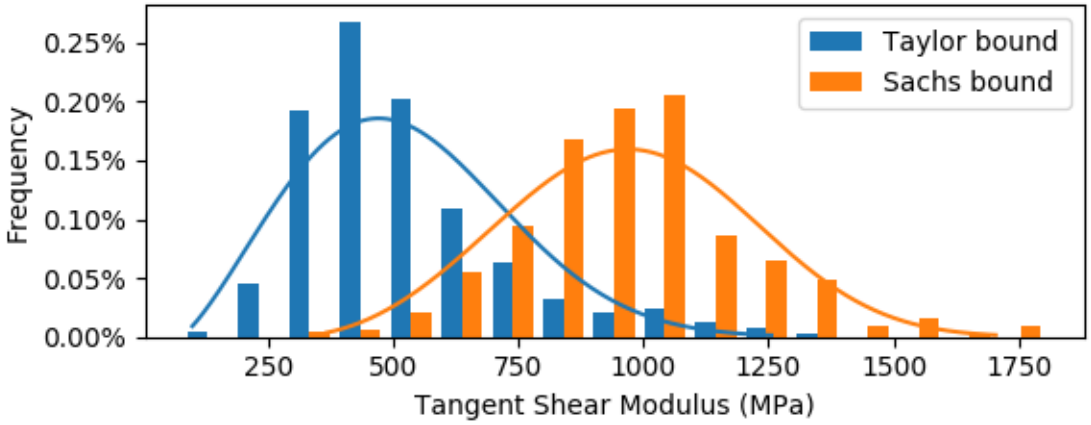

Figure 0.29: Tangent Shear Modulus for $1x10^4$ Particle Ensemble at 5MPa

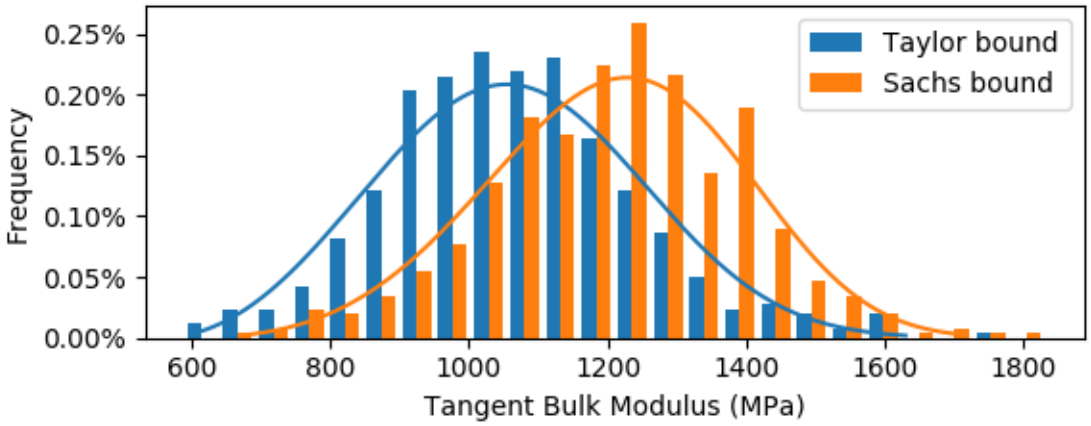

Figure 0.30: Tangent Bulk Modulus for $1x10^4$ Particle Ensemble at 5MPa

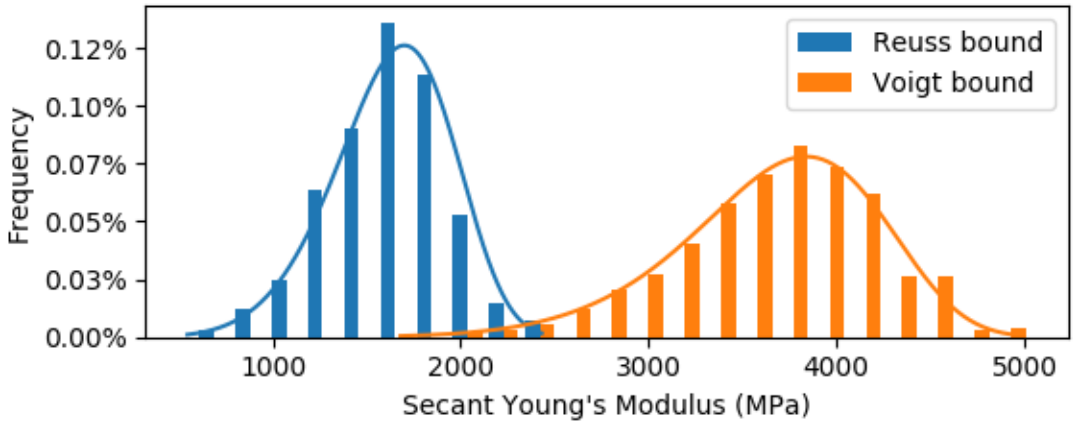

Figure 0.31: Secant Young's Modulus for $1x10^4$ Particle Ensemble at 20MPa

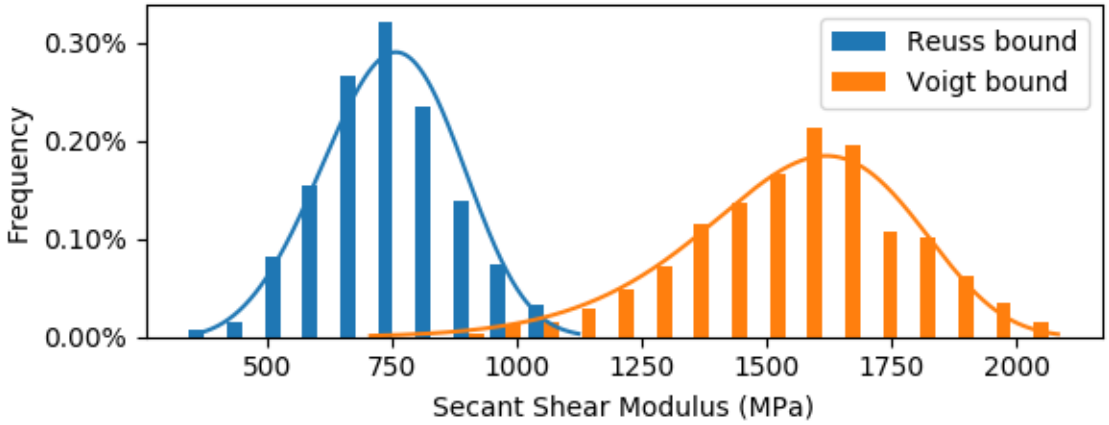

Figure 0.32: Secant Shear Modulus for $1x10^4$ Particle Ensemble at 20MPa

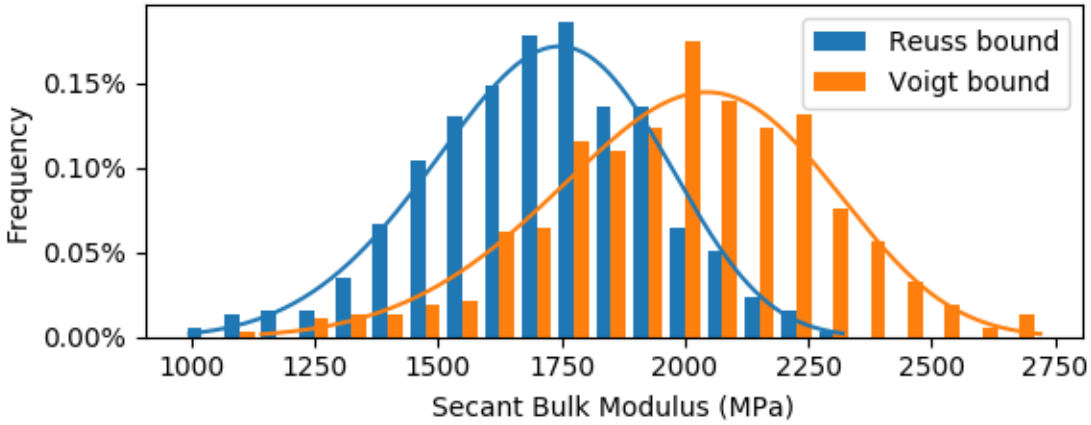

Figure 0.33: Secant Bulk Modulus for $1x10^4$ Particle Ensemble at 20MPa

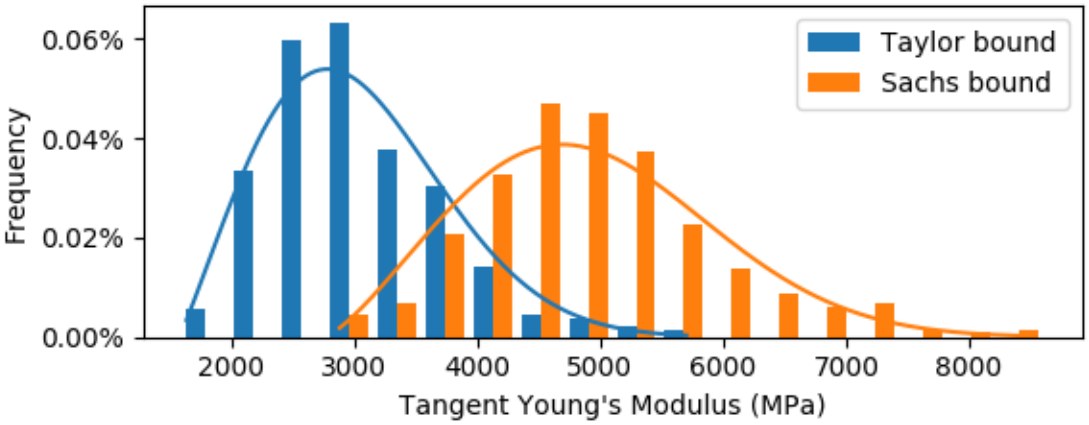

Figure 0.34: Tangent Young's Modulus for $1x10^4$ Particle Ensemble at 20MPa

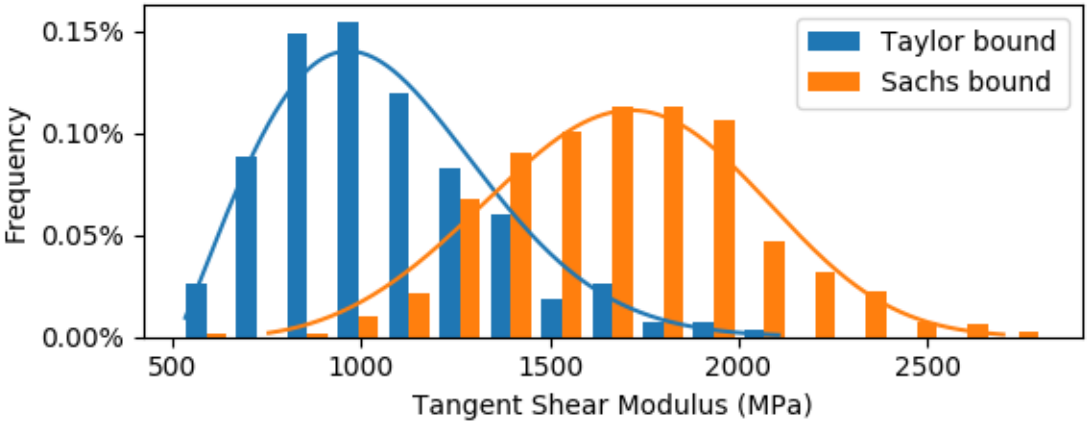

Figure 0.35: Tangent Shear Modulus for $1x10^4$ Particle Ensemble at 20MPa

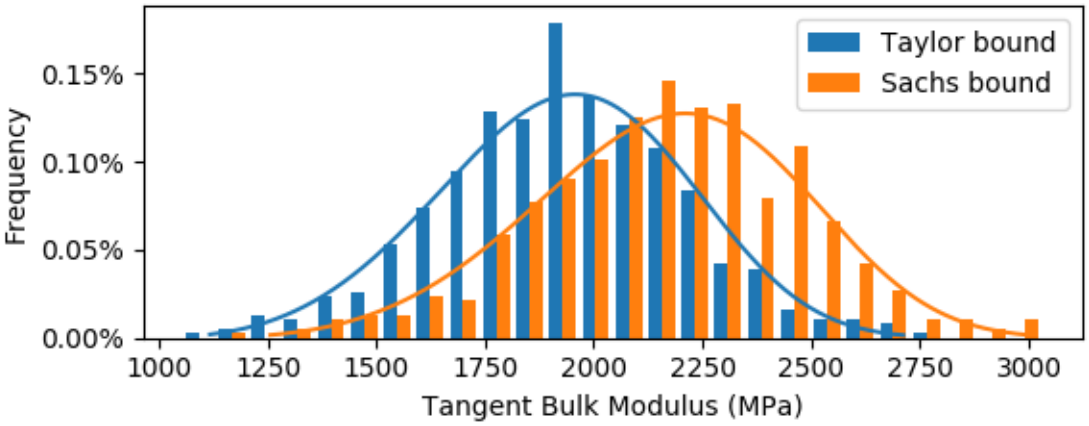

Figure 0.36: Tangent Bulk Modulus for $1x10^4$ Particle Ensemble at 20MPa

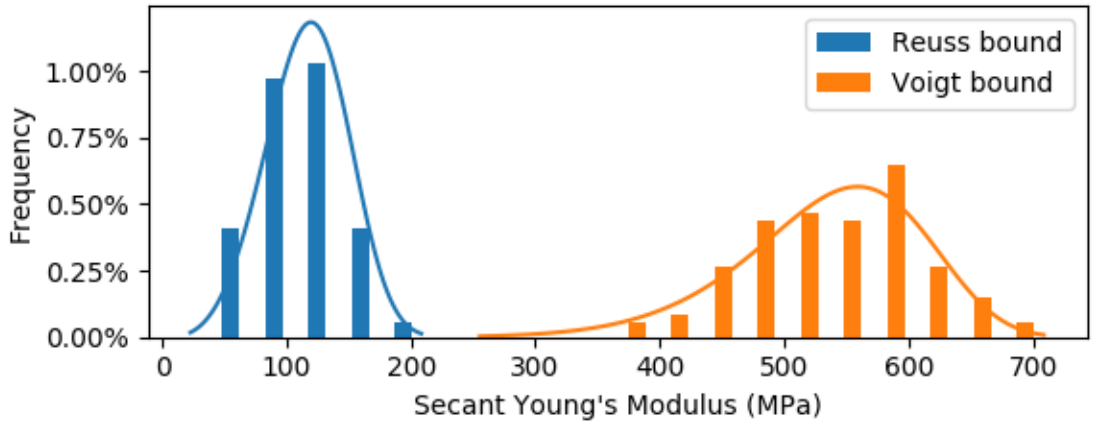

Figure 0.37: Secant Young's Modulus for $1x10^5$ Particle Ensemble at 1MPa

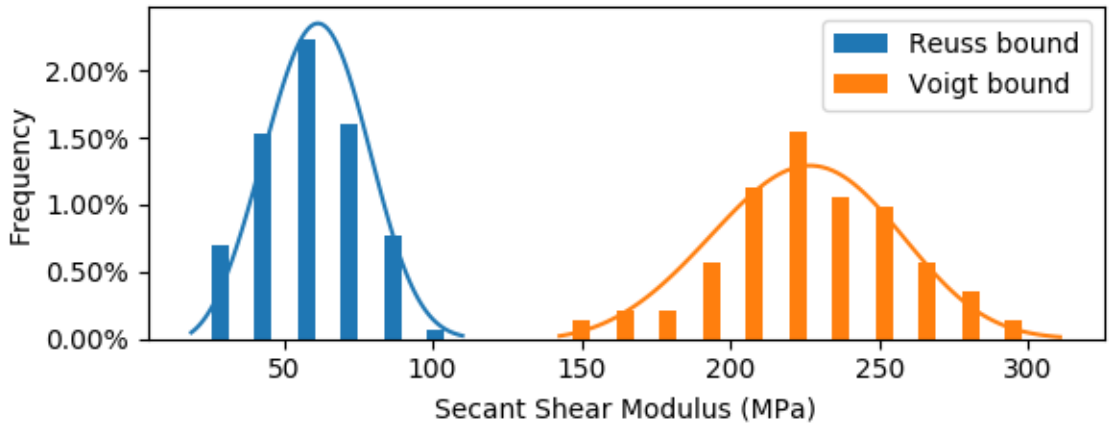

Figure 0.38: Secant Shear Modulus for $1x10^5$ Particle Ensemble at 1MPa

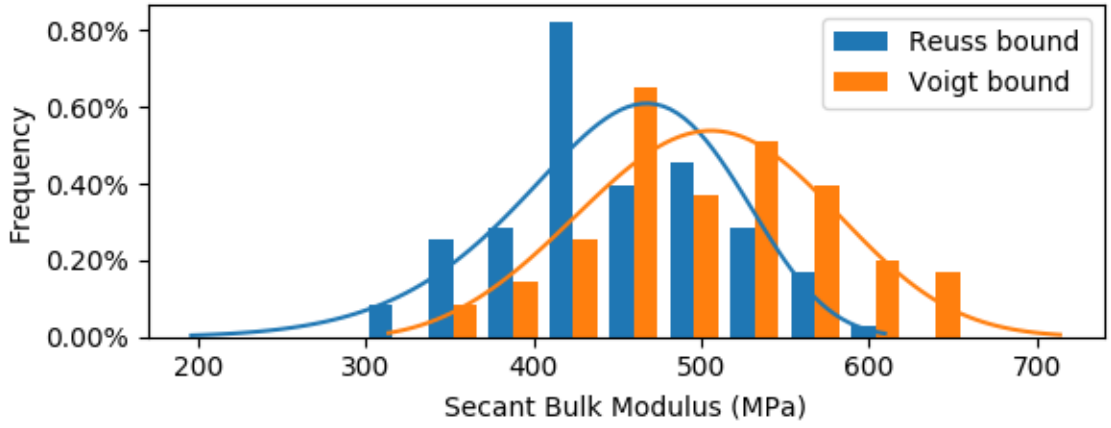

Figure 0.39: Secant Bulk Modulus for $1x10^5$ Particle Ensemble at 1MPa

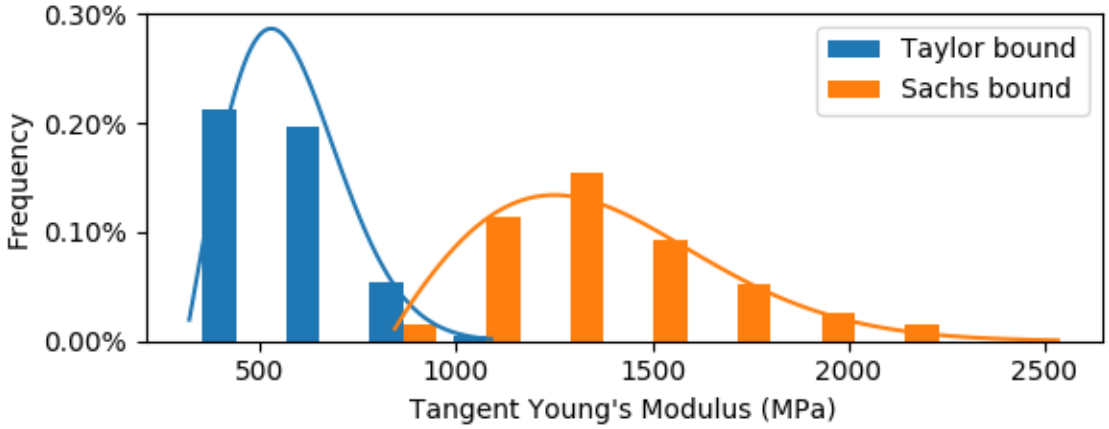

Figure 0.40: Tangent Young's Modulus for $1x10^5$ Particle Ensemble at 1MPa

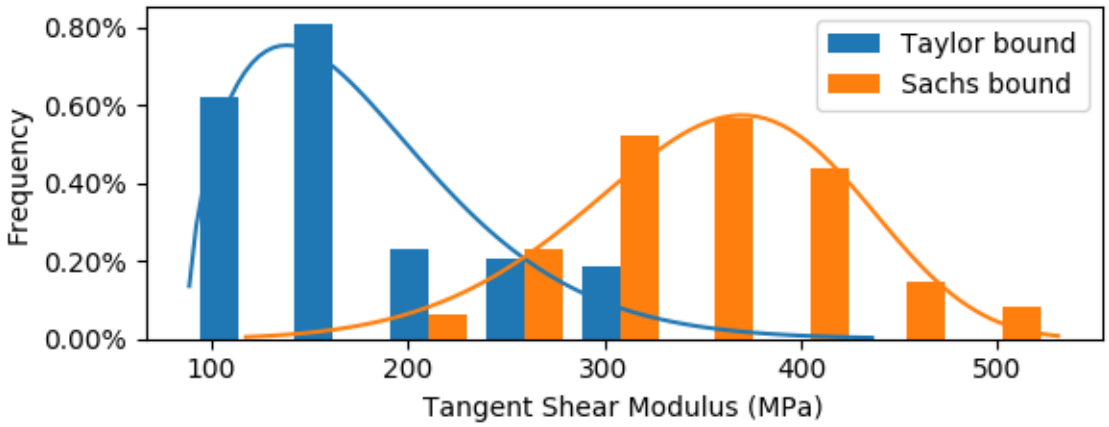

Figure 0.41: Tangent Shear Modulus for $1x10^5$ Particle Ensemble at 1MPa

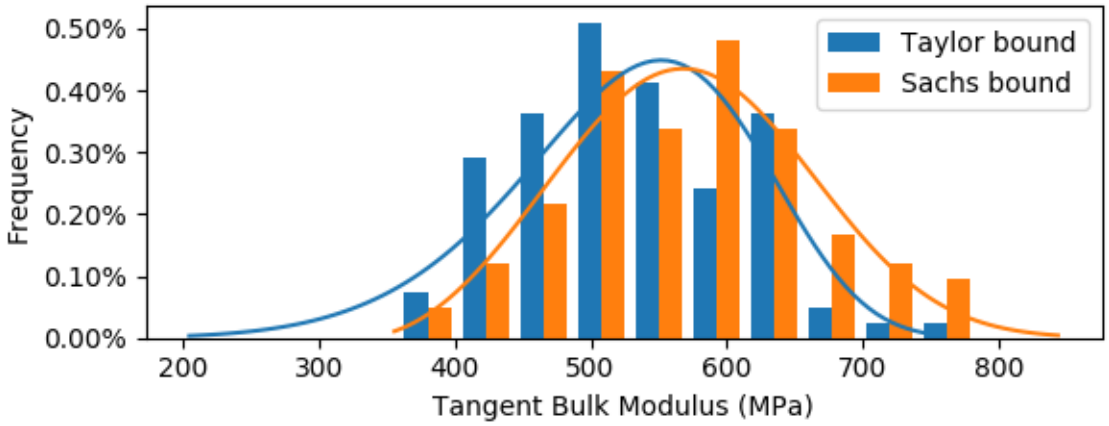

Figure 0.42: Tangent Bulk Modulus for $1x10^5$ Particle Ensemble at 1MPa

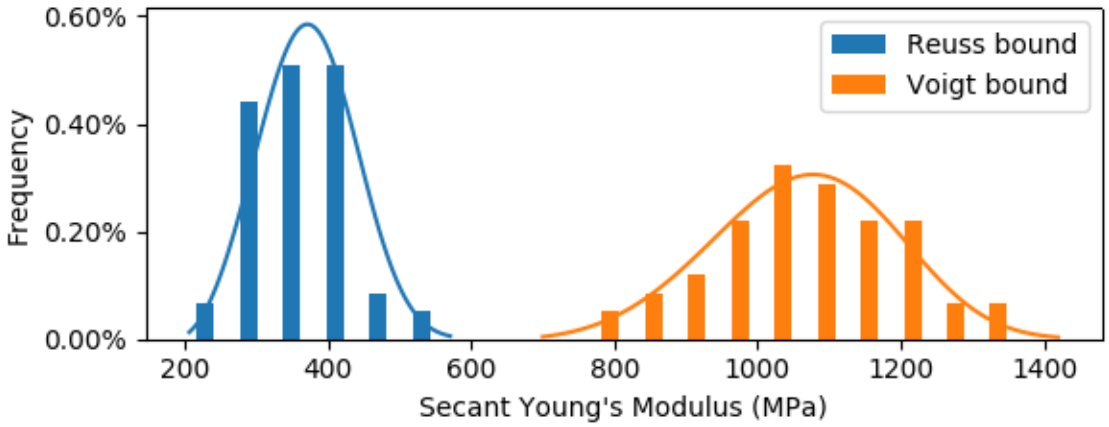

Figure 0.43: Secant Young's Modulus for $1x10^5$ Particle Ensemble at 5MPa

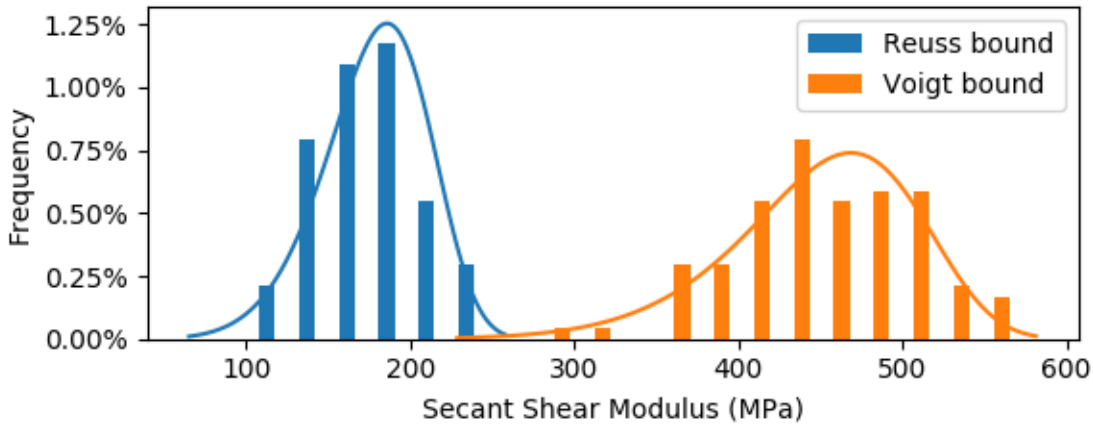

Figure 0.44: Secant Shear Modulus for $1x10^5$ Particle Ensemble at 5MPa

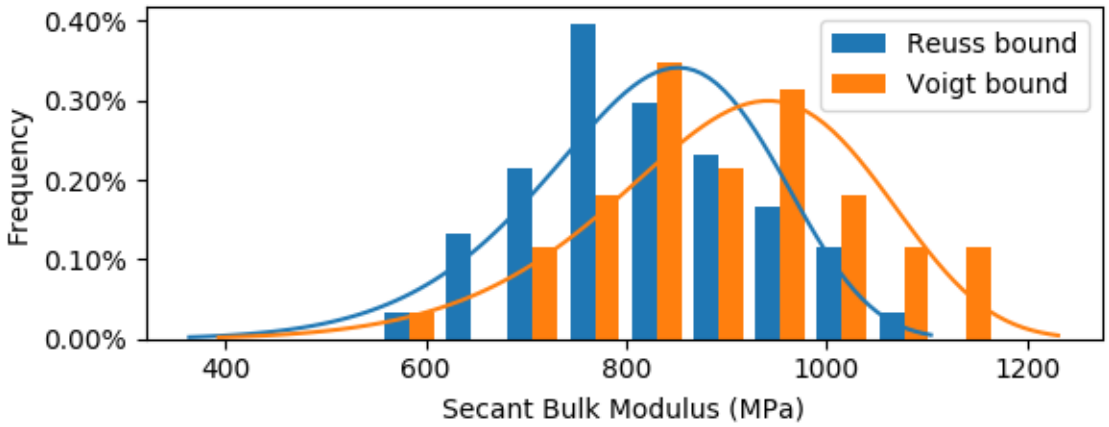

Figure 0.45: Secant Bulk Modulus for $1x10^5$ Particle Ensemble at 5MPa

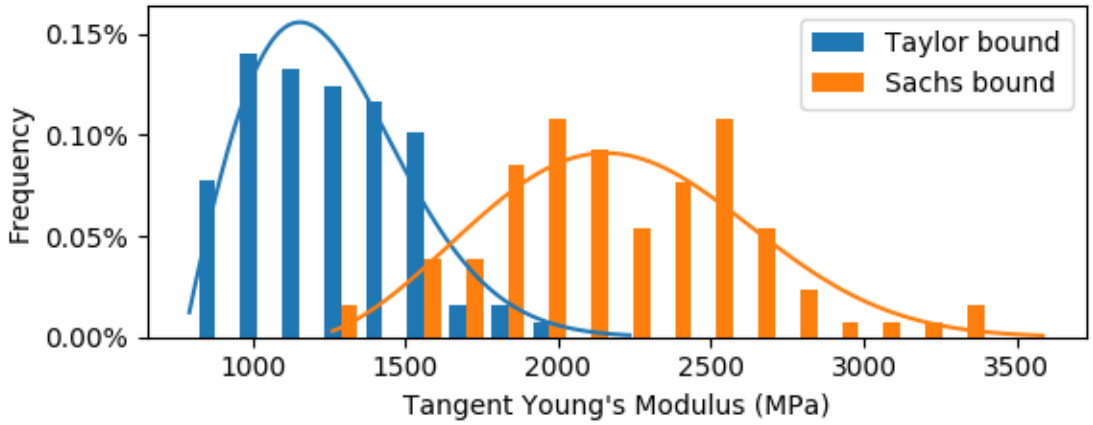

Figure 0.46: Tangent Young's Modulus for $1x10^5$ Particle Ensemble at 5MPa

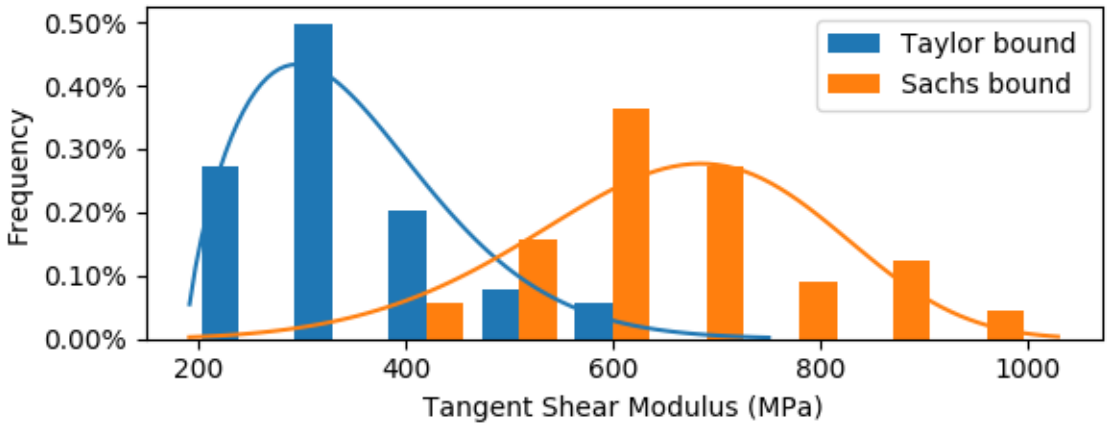

Figure 0.47: Tangent Shear Modulus for $1x10^5$ Particle Ensemble at 5MPa

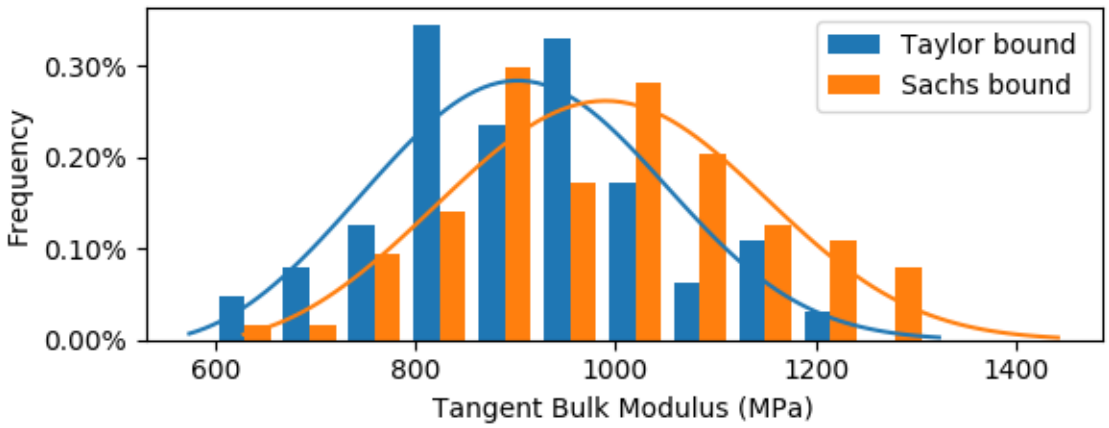

Figure 0.48: Tangent Bulk Modulus for $1x10^5$ Particle Ensemble at 5MPa

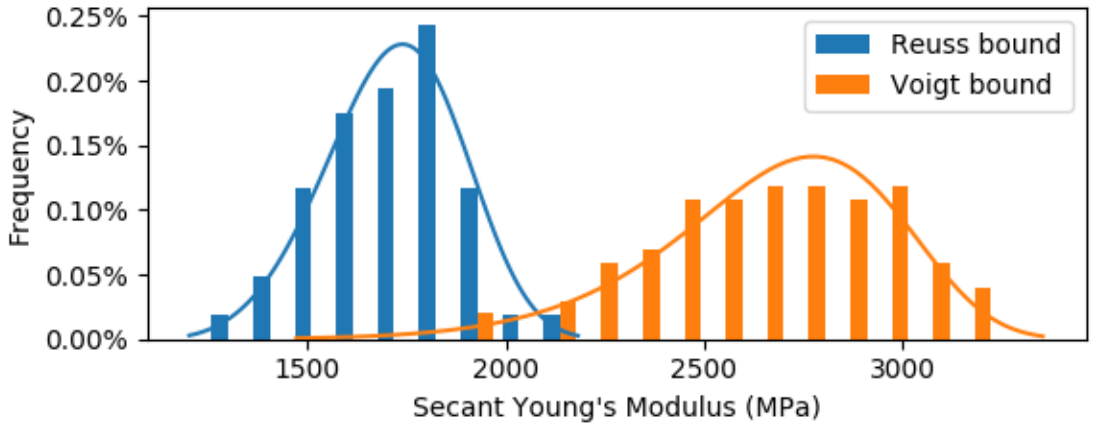

Figure 0.49: Secant Young's Modulus for $1x10^5$ Particle Ensemble at 20MPa

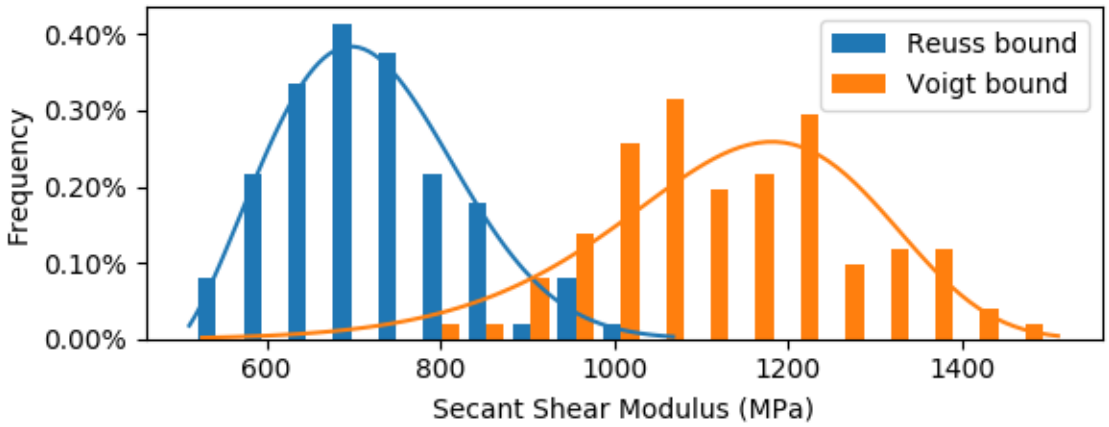

Figure 0.50: Secant Shear Modulus for $1x10^5$ Particle Ensemble at 20MPa

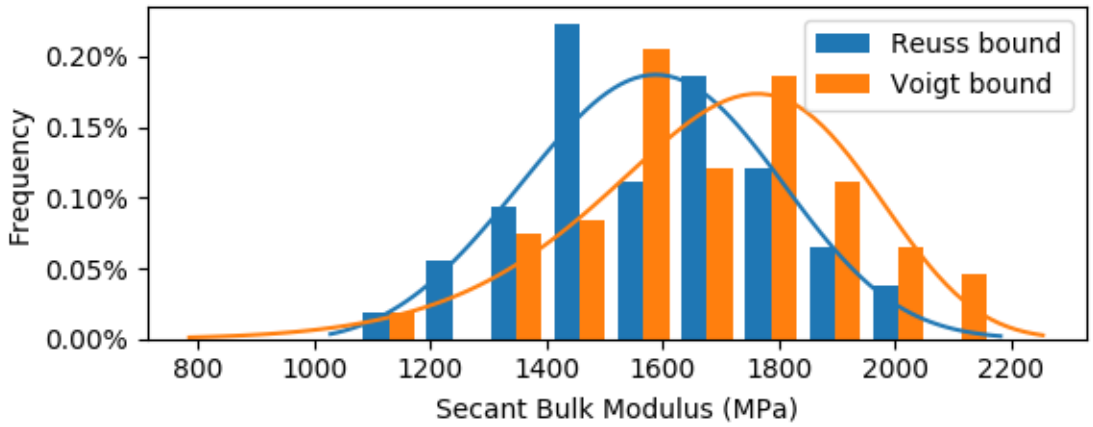

Figure 0.51: Secant Bulk Modulus for $1x10^5$ Particle Ensemble at 20MPa

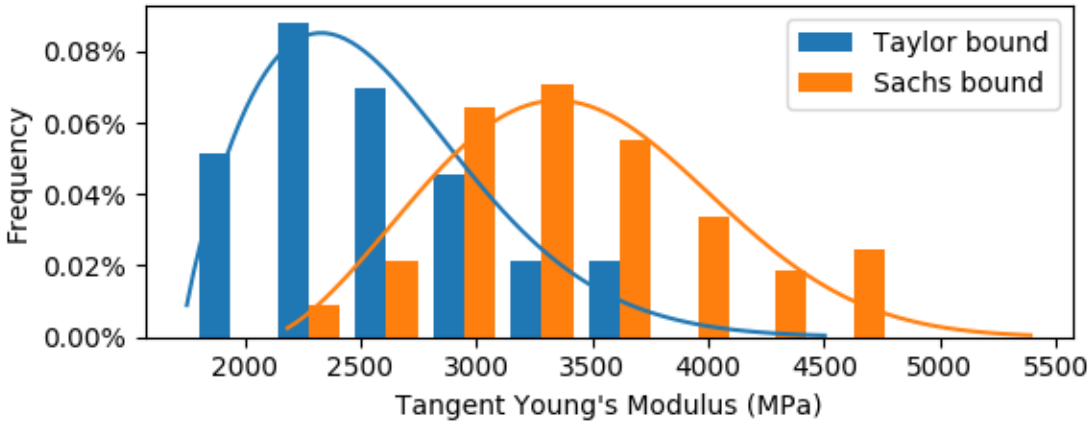

Figure 0.52: Tangent Young's Modulus for $1x10^5$ Particle Ensemble at 20MPa

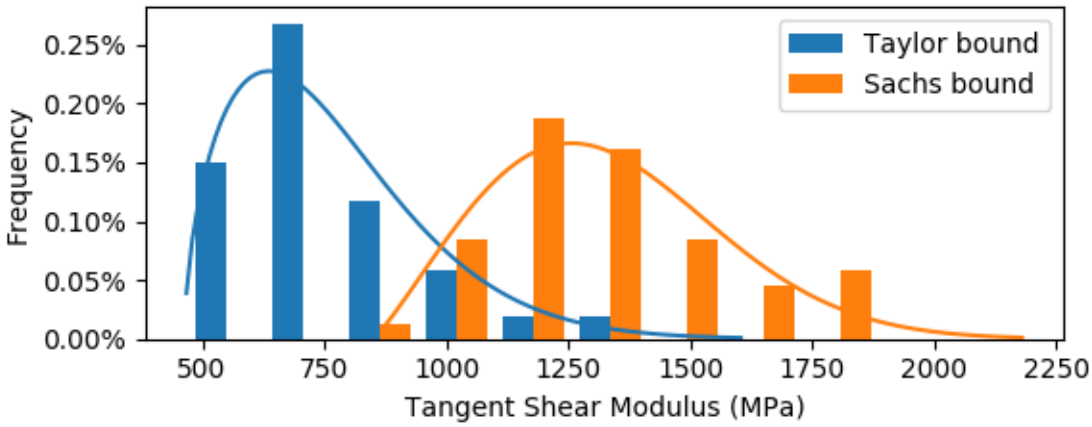

Figure 0.53: Tangent Shear Modulus for $1x10^5$ Particle Ensemble at 20MPa

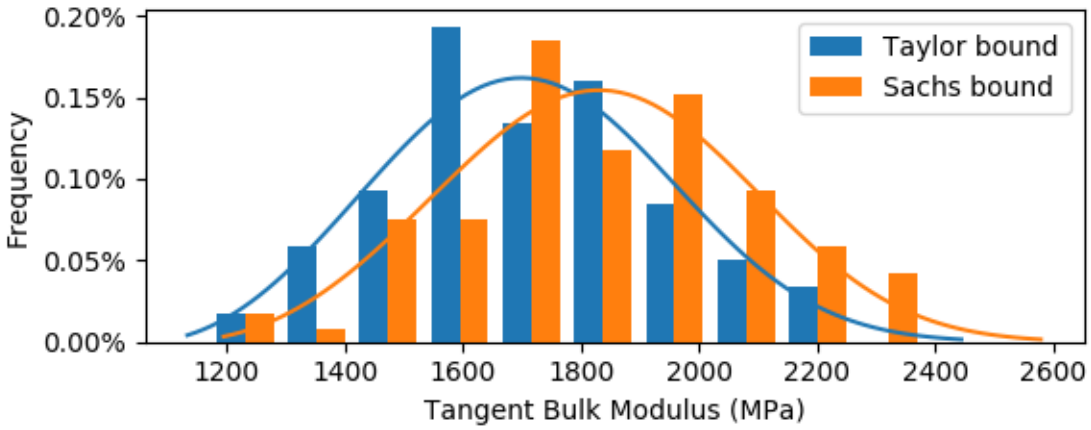

Figure 0.54: Tangent Bulk Modulus for $1x10^5$ Particle Ensemble at 20MPa

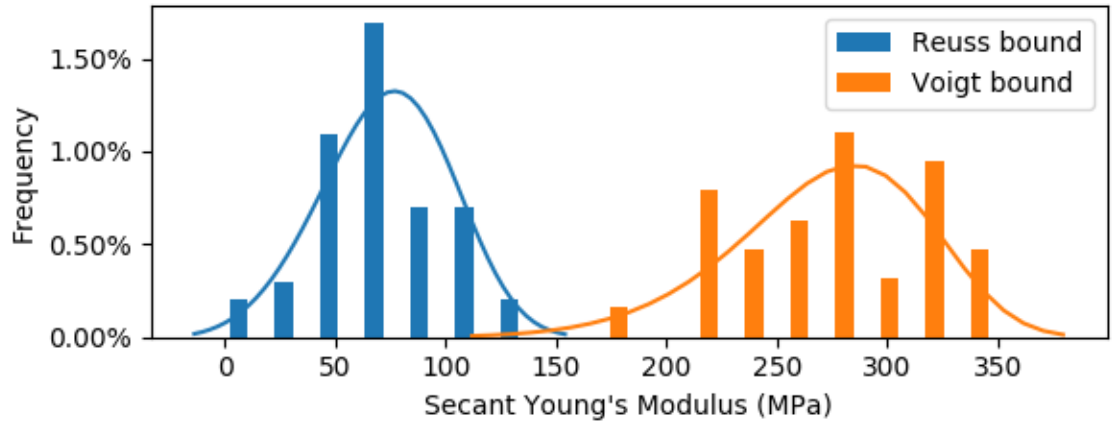

Figure 0.55: Secant Young's Modulus for $1x10^6$ Particle Ensemble at 1MPa

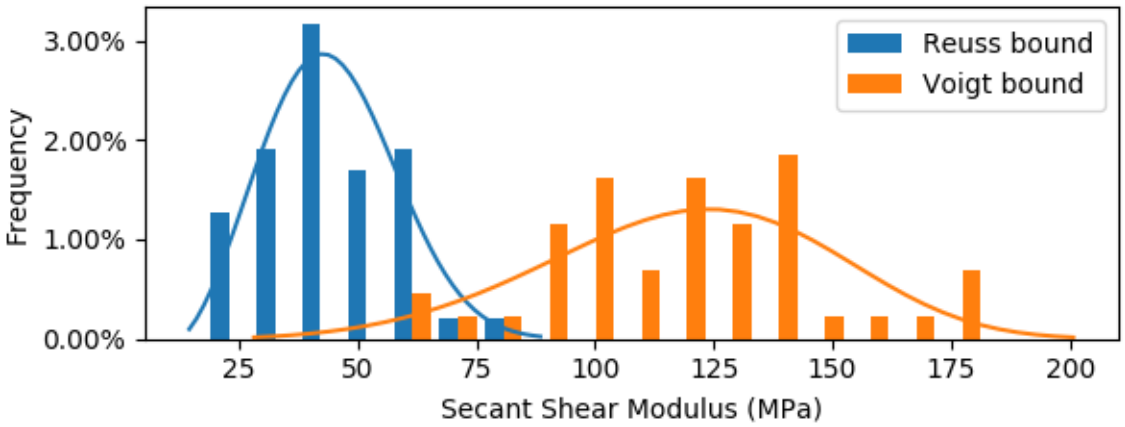

Figure 0.56: Secant Shear Modulus for $1x10^6$ Particle Ensemble at 1MPa

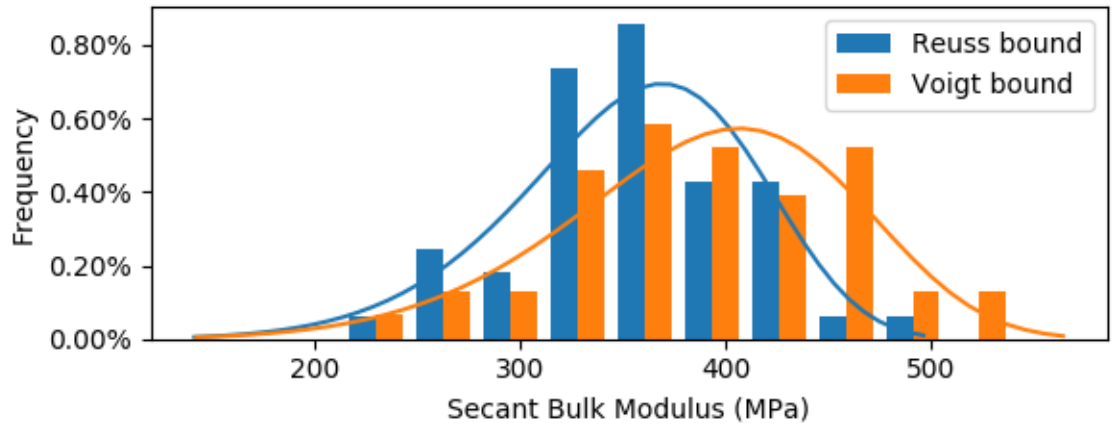

Figure 0.57: Secant Bulk Modulus for $1x10^6$ Particle Ensemble at 1MPa

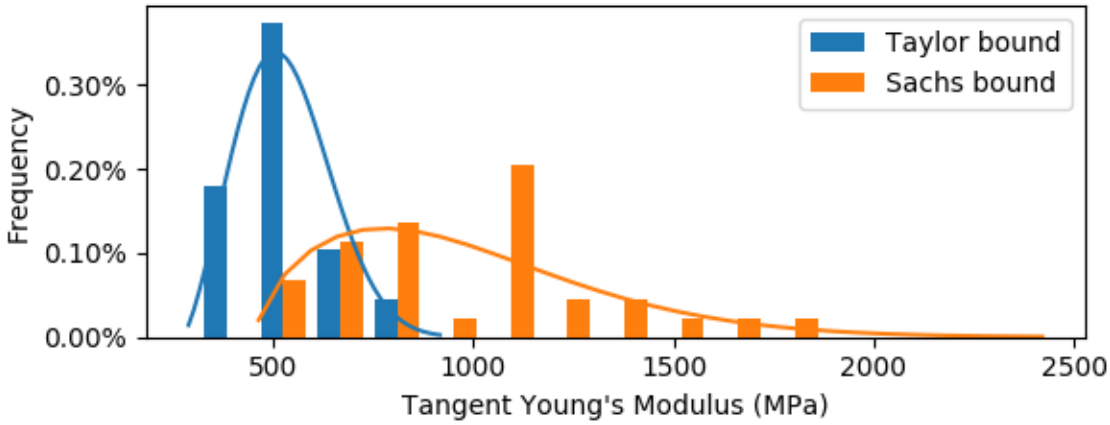

Figure 0.58: Tangent Young's Modulus for $1x10^3$ Particle Ensemble at 1MPa

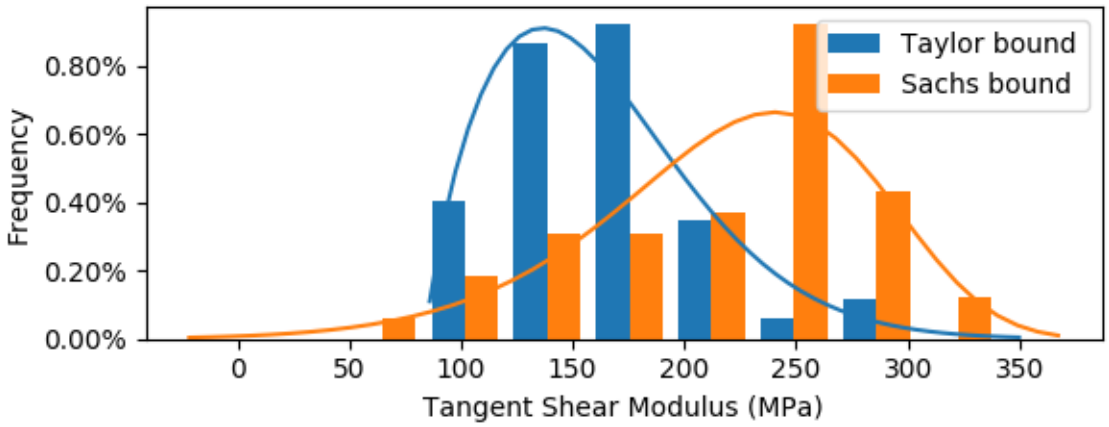

Figure 0.59: Tangent Shear Modulus for $1x10^6$ Particle Ensemble at 1MPa

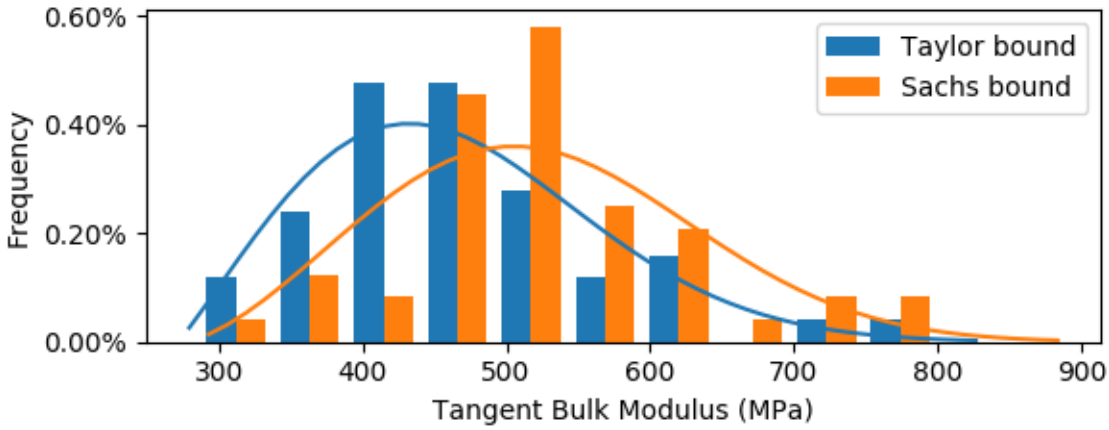

Figure 0.60: Tangent Bulk Modulus for $1x10^6$ Particle Ensemble at 1MPa

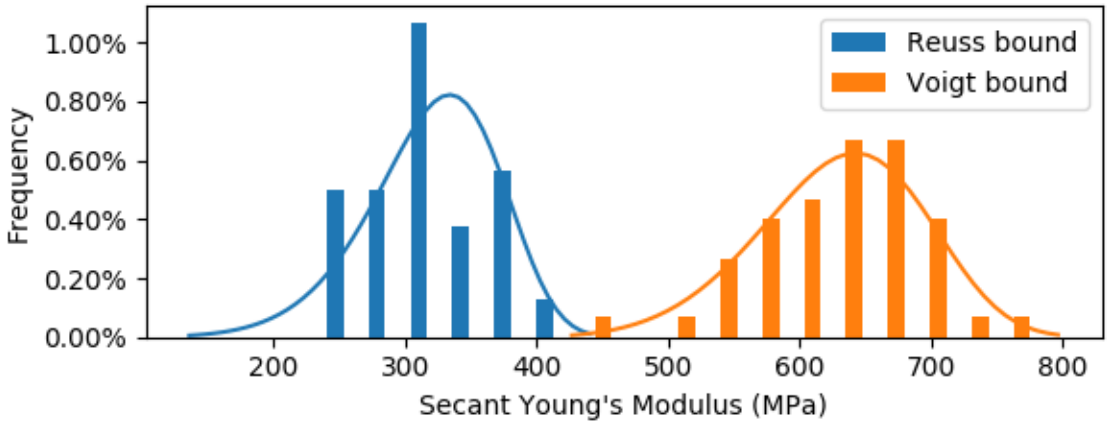

Figure 0.61: Secant Young's Modulus for $1x10^6$ Particle Ensemble at 5MPa

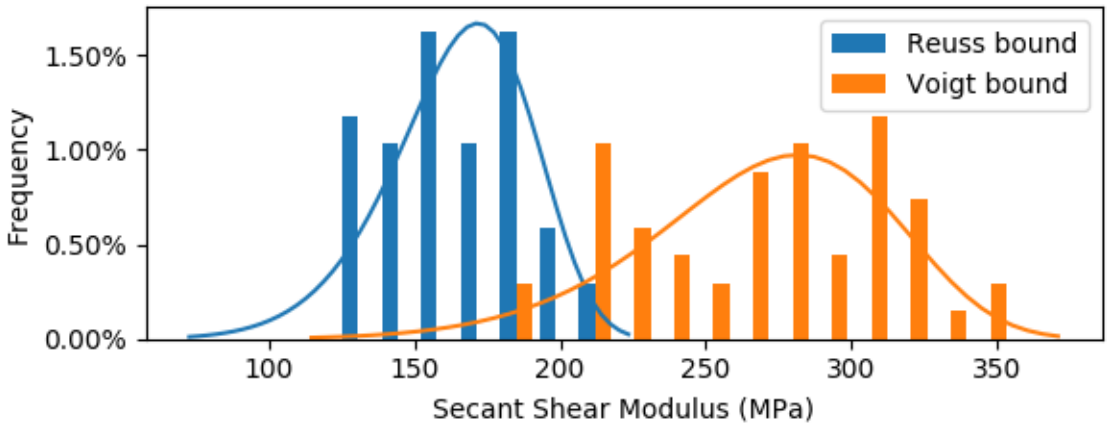

Figure 0.62: Secant Shear Modulus for $1x10^6$ Particle Ensemble at 5MPa

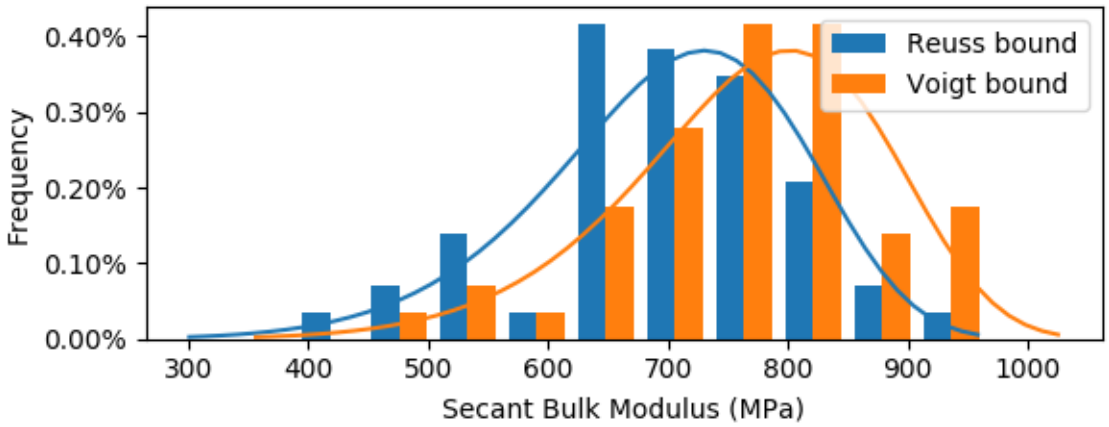

Figure 0.63: Secant Bulk Modulus for $1x10^6$ Particle Ensemble at 5MPa

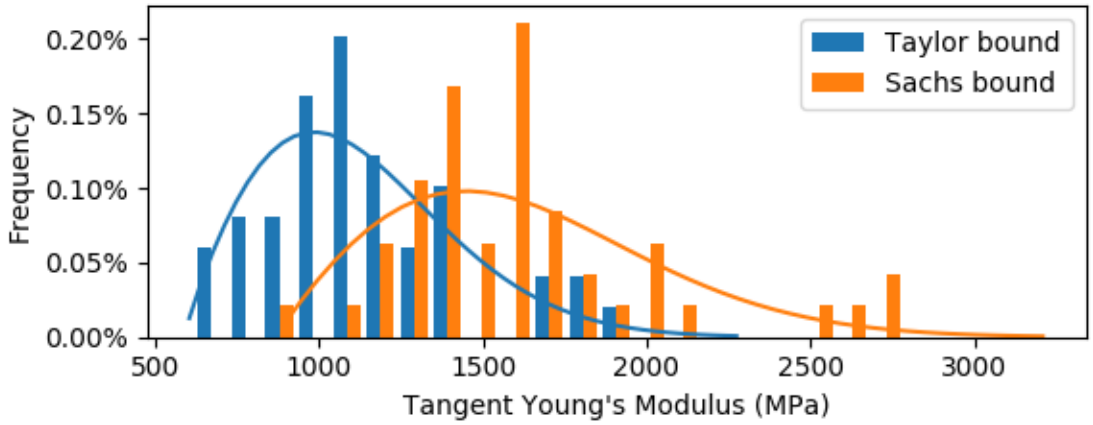

Figure 0.64: Tangent Young's Modulus for $1x10^6$ Particle Ensemble at 5MPa

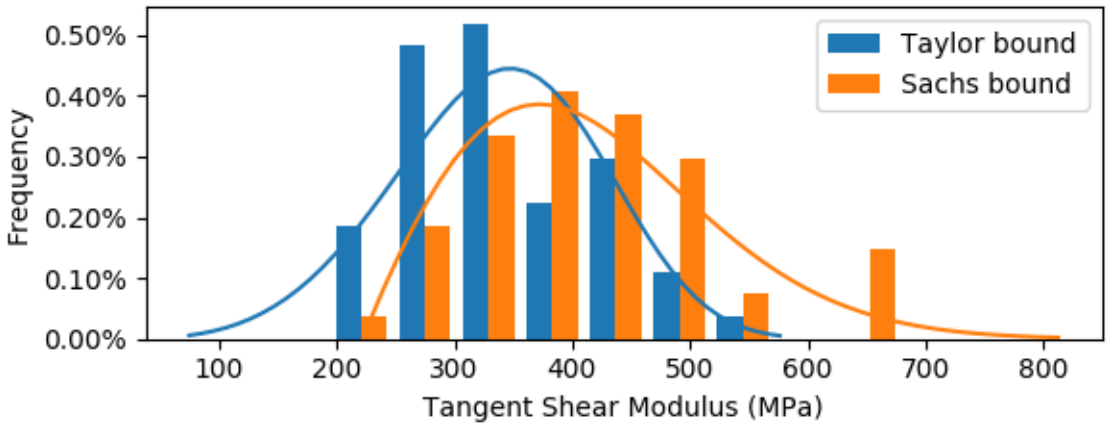

Figure 0.65: Tangent Shear Modulus for $1x10^6$ Particle Ensemble at 5MPa

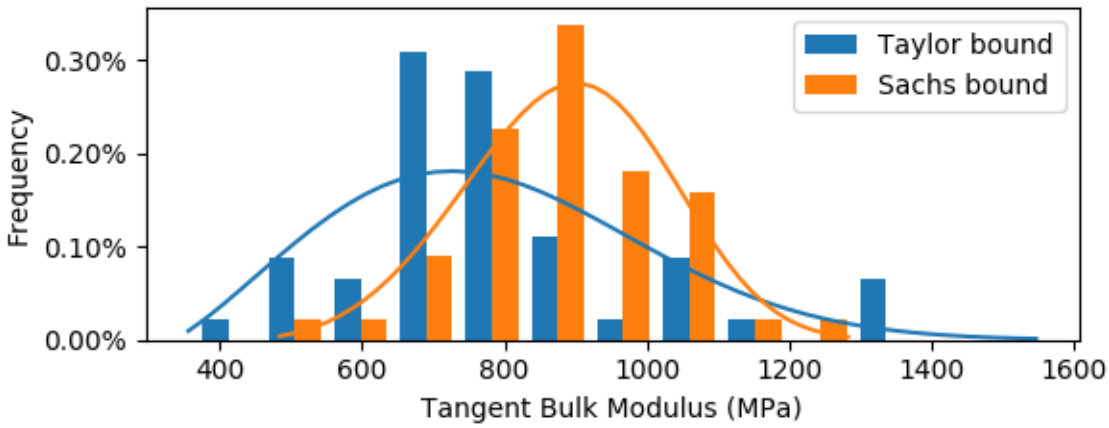

Figure 0.66: Tangent Bulk Modulus for $1x10^6$ Particle Ensemble at 5MPa

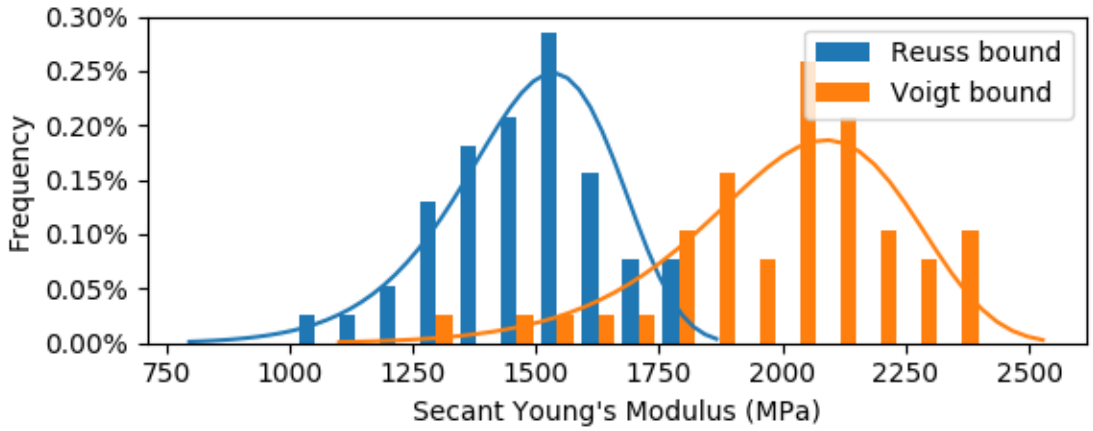

Figure 0.67: Secant Young's Modulus for $1x10^6$ Particle Ensemble at 20MPa

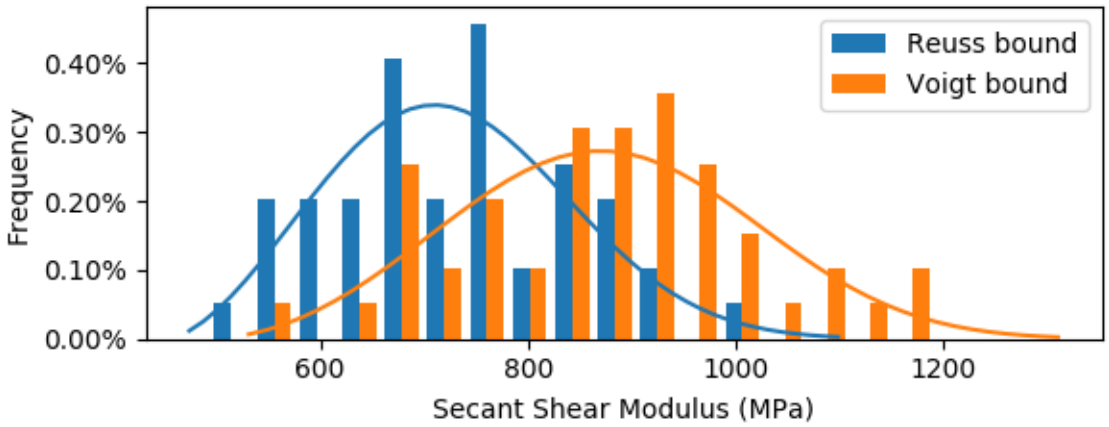

Figure 0.68: Secant Shear Modulus for $1x10^6$ Particle Ensemble at 20MPa

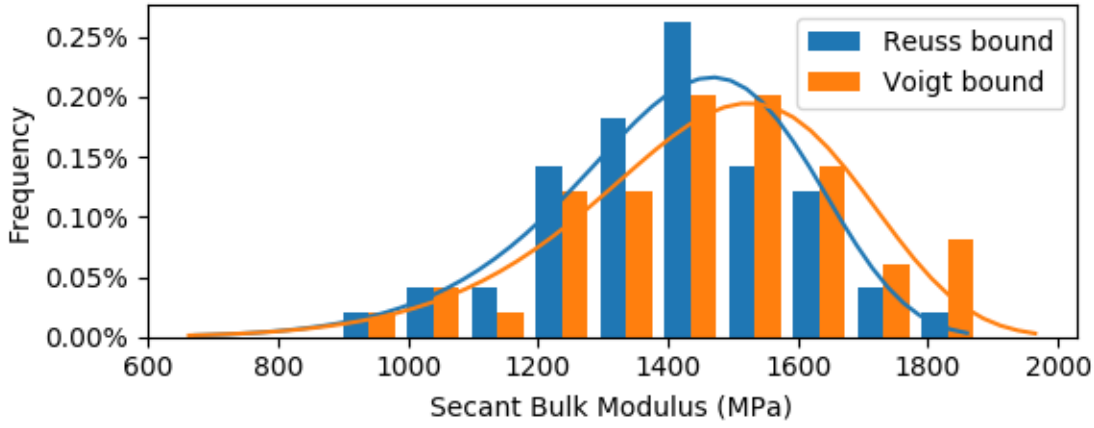

Figure 0.69: Secant Bulk Modulus for $1x10^6$ Particle Ensemble at 20MPa

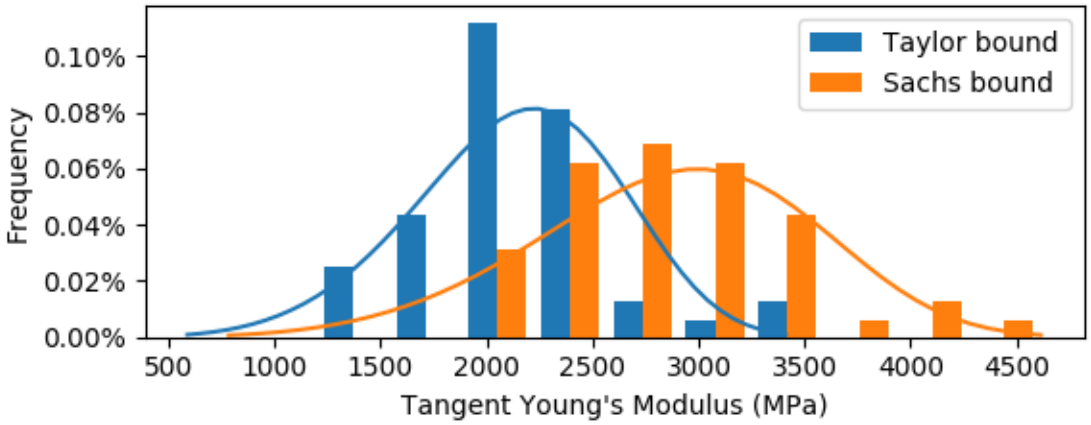

Figure 0.70: Tangent Young's Modulus for $1x10^6$ Particle Ensemble at 20MPa

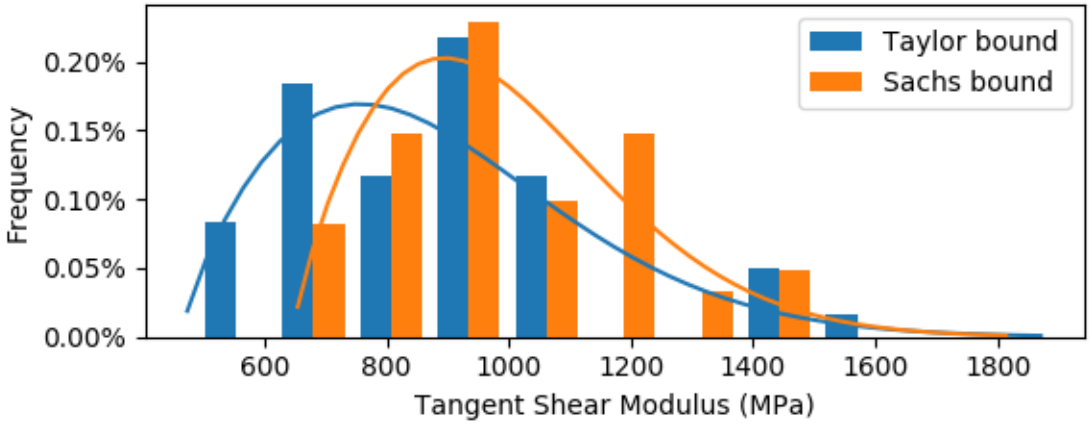

Figure 0.71: Tangent Shear Modulus for $1x10^6$ Particle Ensemble at 20MPa

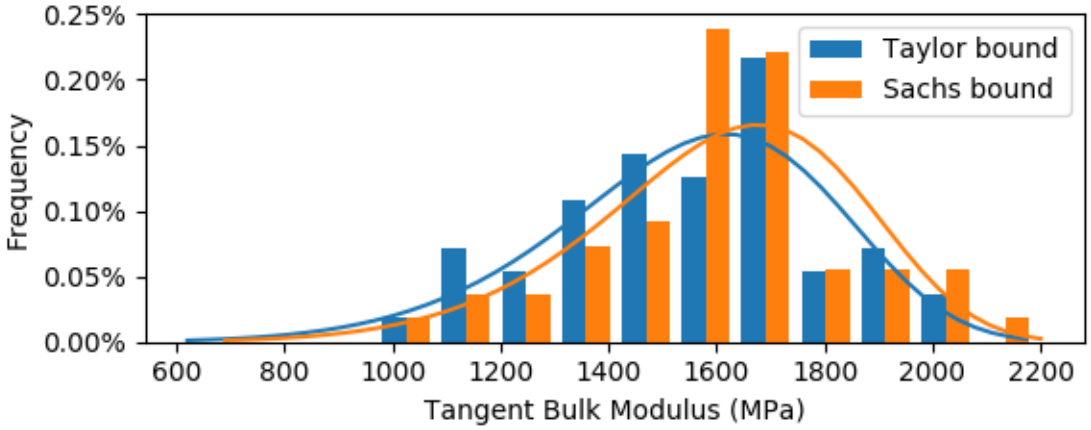

Figure 0.72: Tangent Bulk Modulus for $1x10^6$ Particle Ensemble at 20MPa

APPENDIX B

HISTOGRAMS OF MESOSCALE ELASTIC MODULI OF EGLIN SAND AFTER COMMINUTION

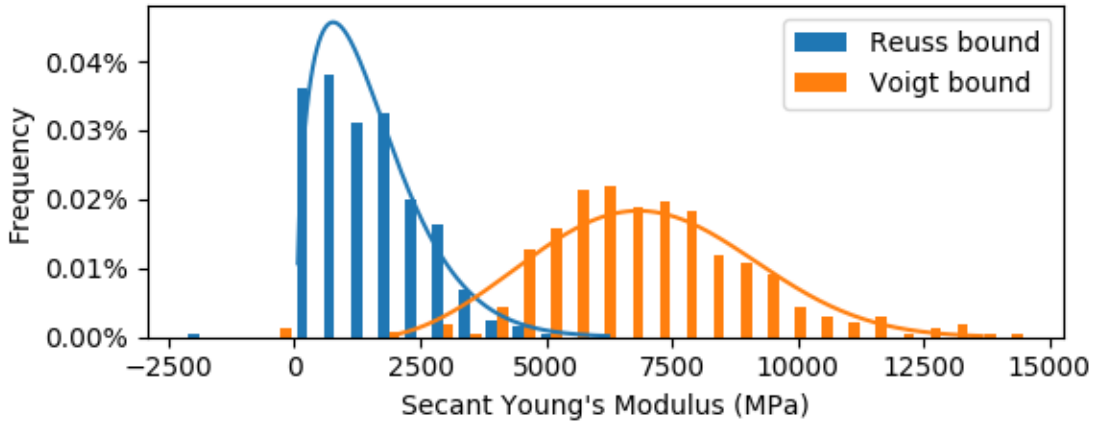

Figure A.1: Secant Young's Mod. for $1x10^3$ Comminuted Particle Ensemble at 20 MPa

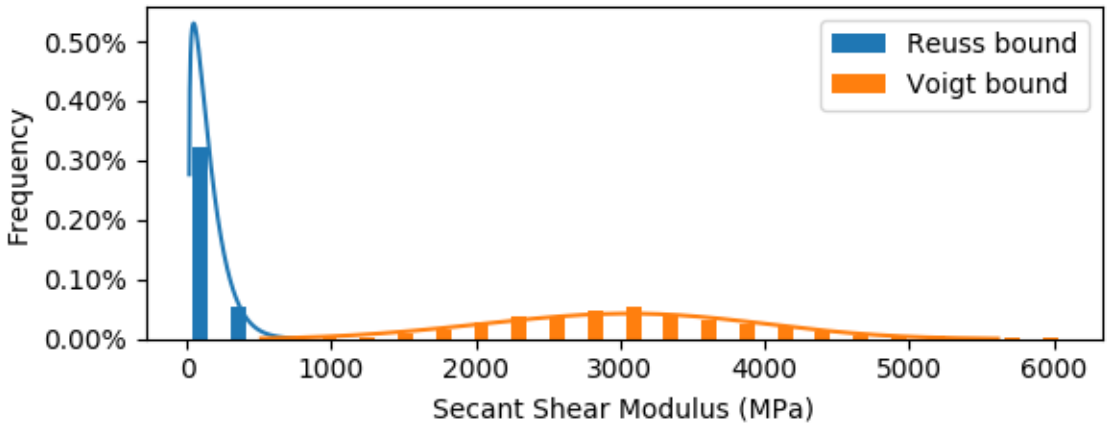

Figure A.2: Secant Shear Modulus for $1x10^3$ Comminuted Particle Ensemble at 20 MPa

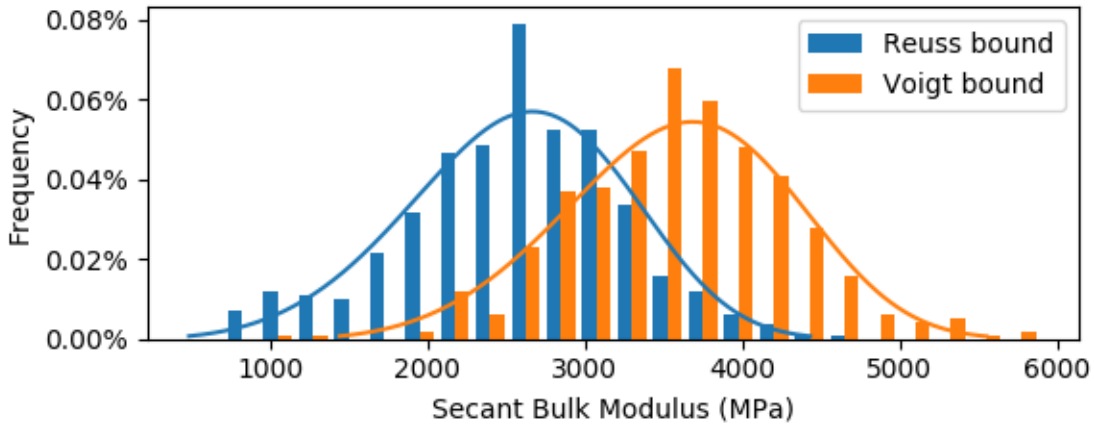

Figure A.3: Secant Bulk Modulus for $1x10^3$ Comminuted Particle Ensemble at 20 MPa

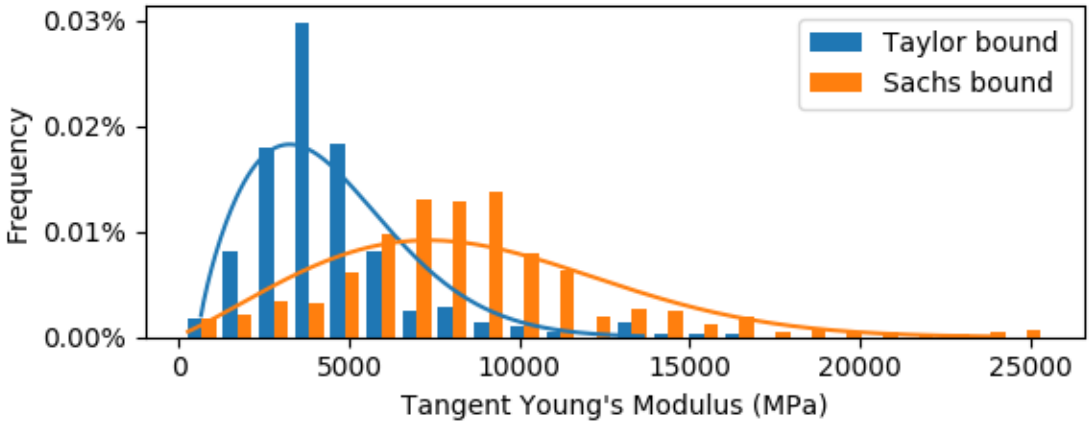

Figure A.4: Tangent Young's Mod. for $1x10^3$ Comminuted Particle Ensemble at 20 MPa

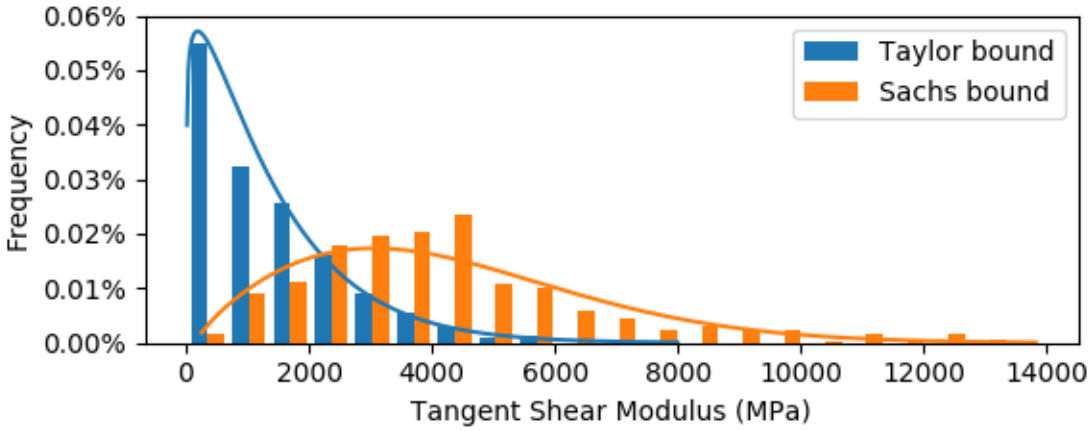

Figure A.5: Tangent Shear Mod. for $1x10^3$ Comminuted Particle Ensemble at 20 MPa

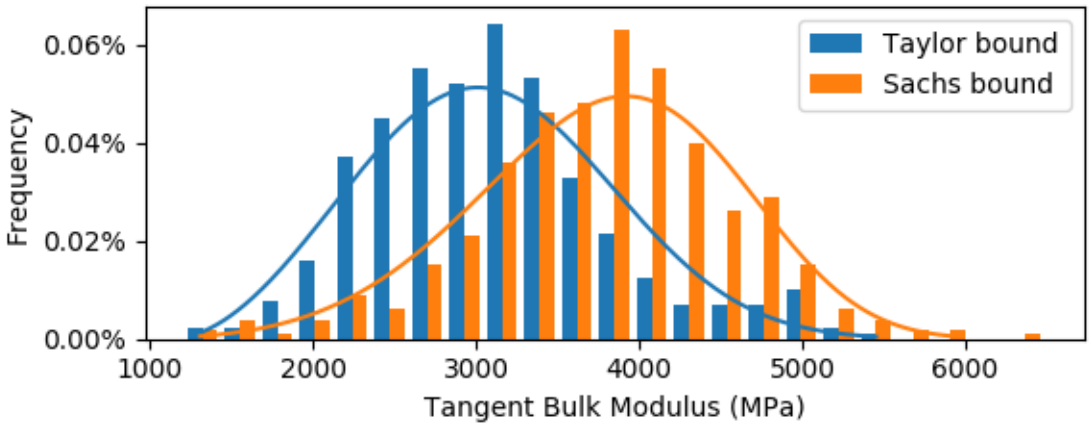

Figure A.6: Tangent Bulk Mod. for $1x10^3$ Comminuted Particle Ensemble at 20 MPa

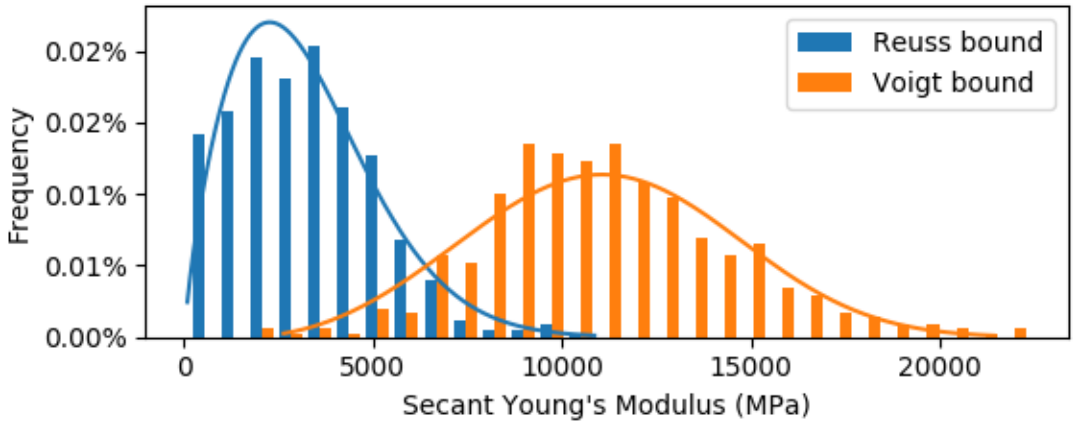

Figure A.7: Secant Young's Mod. for 1x10^3 Comminuted Particle Ensemble at 50 MPa

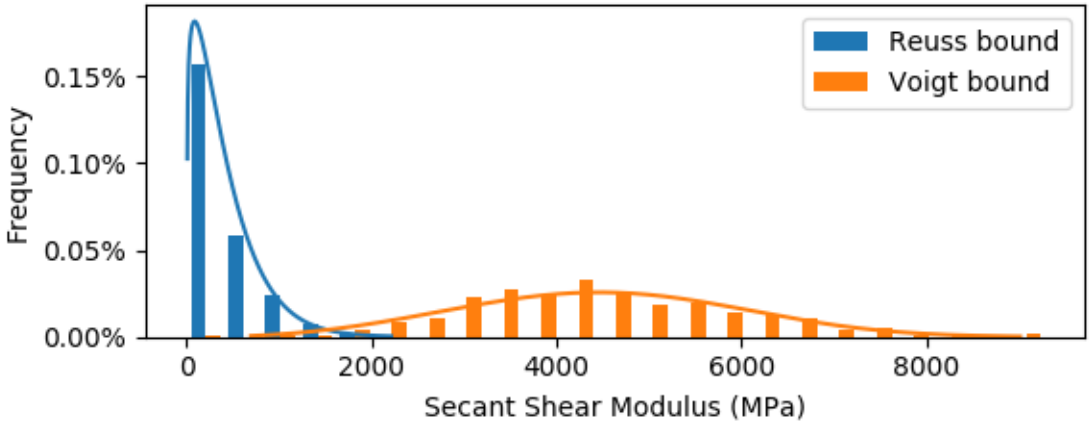

Figure A.8: Secant Shear Modulus for 1x10^3 Comminuted Particle Ensemble at 50 MPa

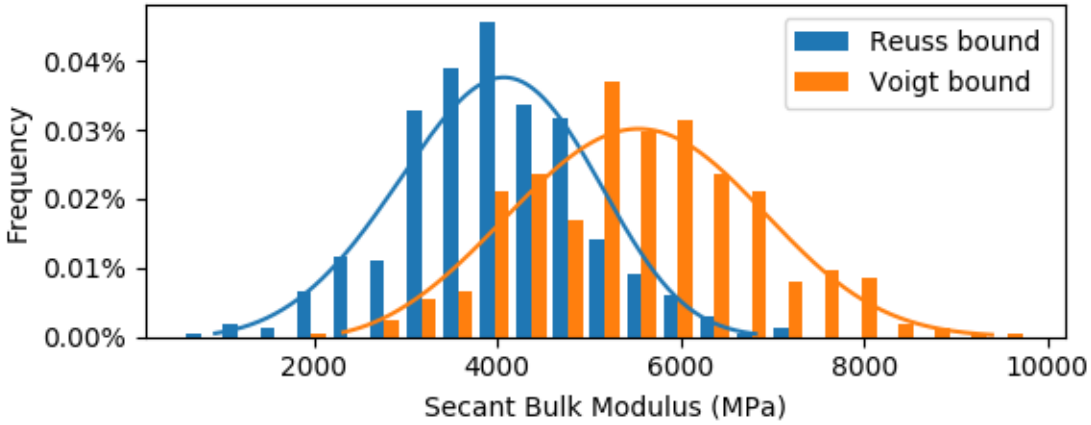

Figure A.9: Secant Bulk Modulus for 1x10^3 Comminuted Particle Ensemble at 50 MPa

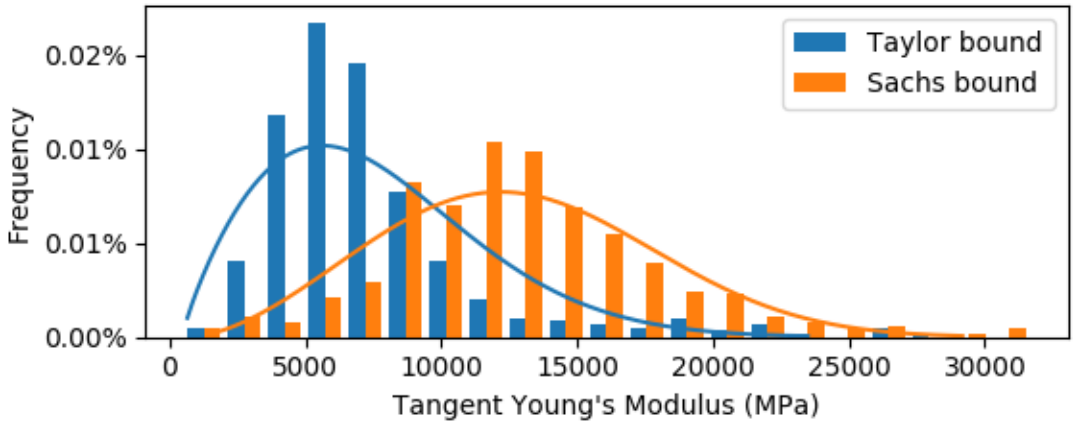

Figure A.10: Tangent Young's Mod. for $1x10^3$ Comminuted Particle Ensemble at 50 MPa

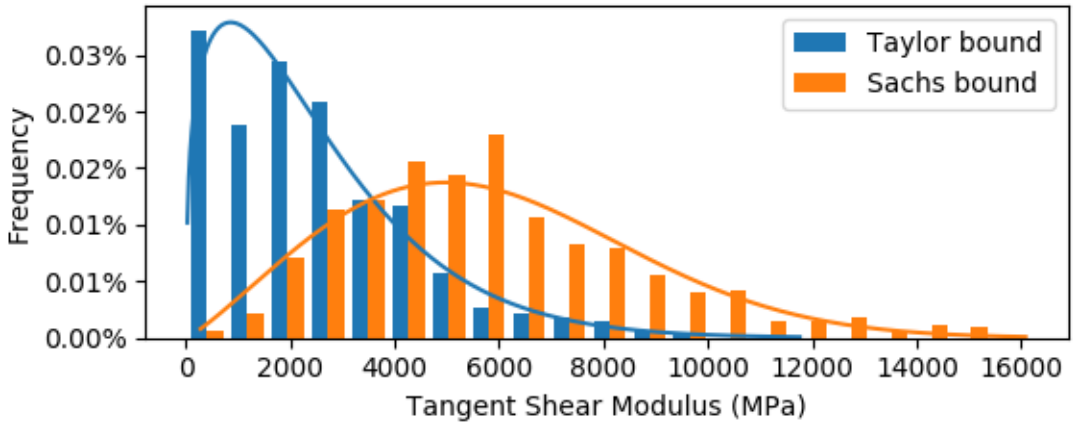

Figure A.11: Tangent Shear Mod. for $1x10^3$ Comminuted Particle Ensemble at 50 MPa

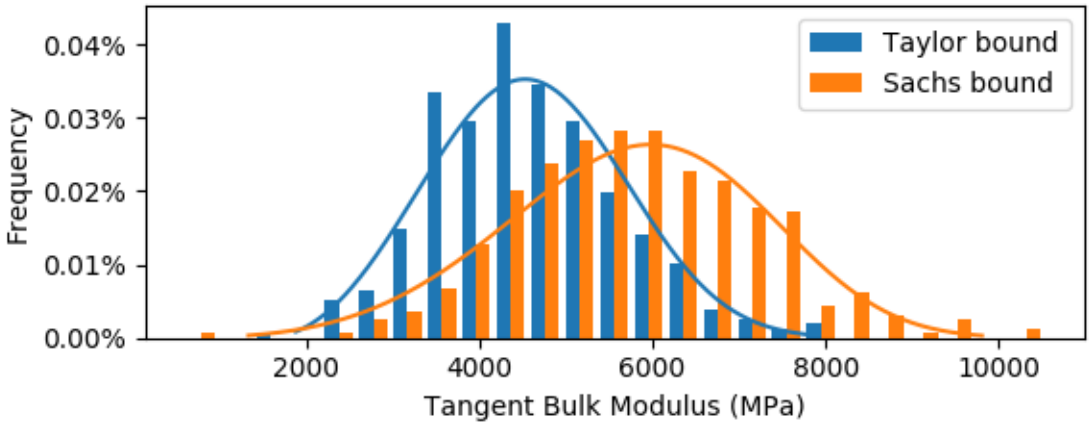

Figure A.12: Tangent Bulk Mod. for $1x10^3$ Comminuted Particle Ensemble at 50 MPa

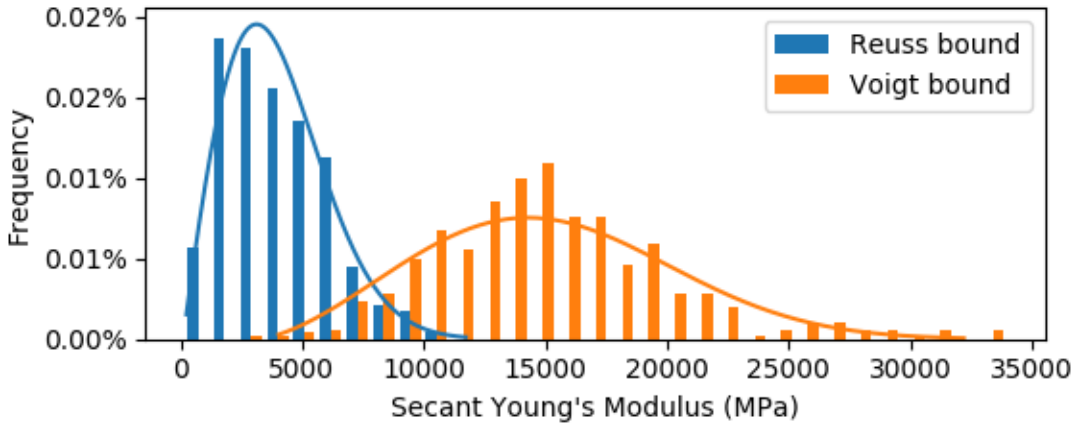

Figure A.13: Secant Young's Mod. for $1x10^3$ Comminuted Particle Ensemble at 100 MPa

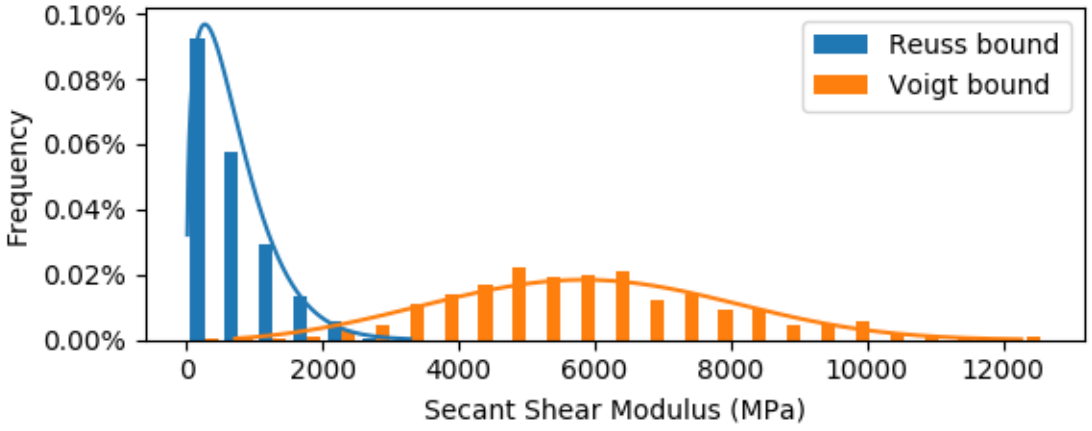

Figure A.14: Secant Shear Mod. for $1x10^3$ Comminuted Particle Ensemble at 100 MPa

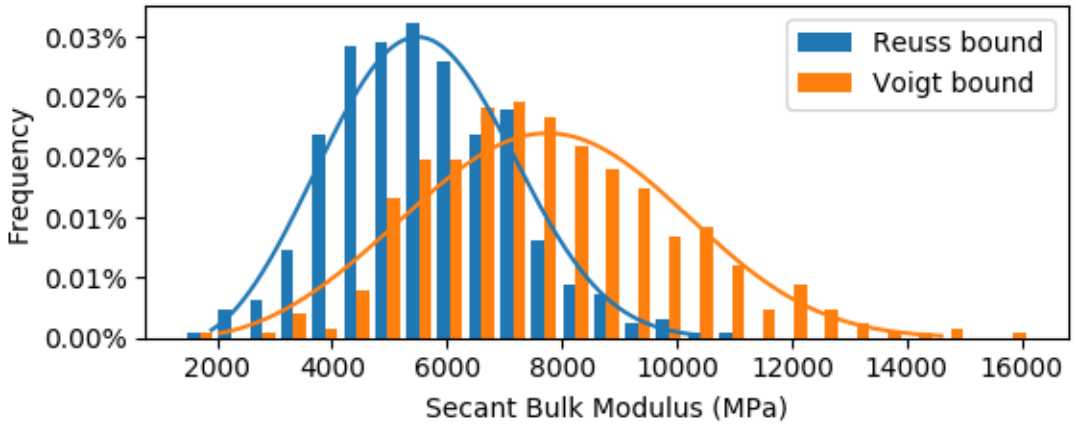

Figure A.15: Secant Bulk Mod. for $1x10^3$ Comminuted Particle Ensemble at 100 MPa

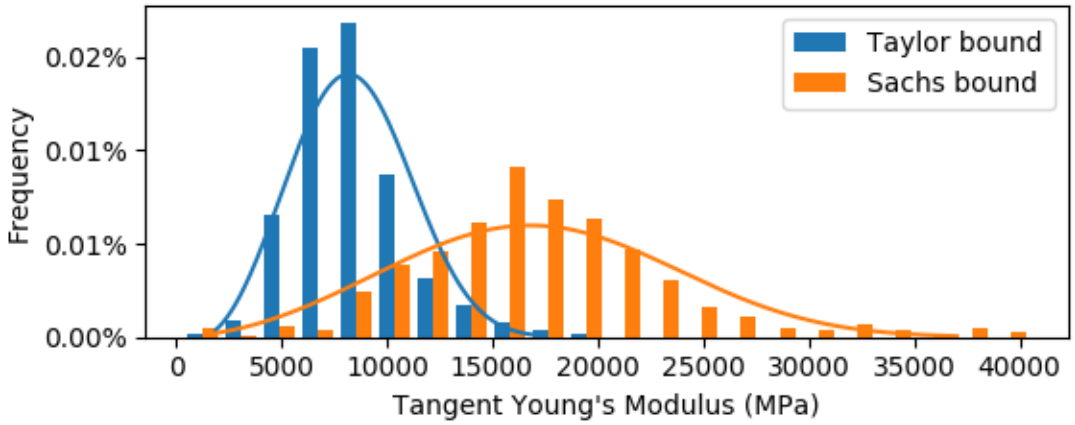

Figure A.16: Tangent Young's Mod. for $1x10^3$ Comminuted Particle Ensemble at 100 MPa

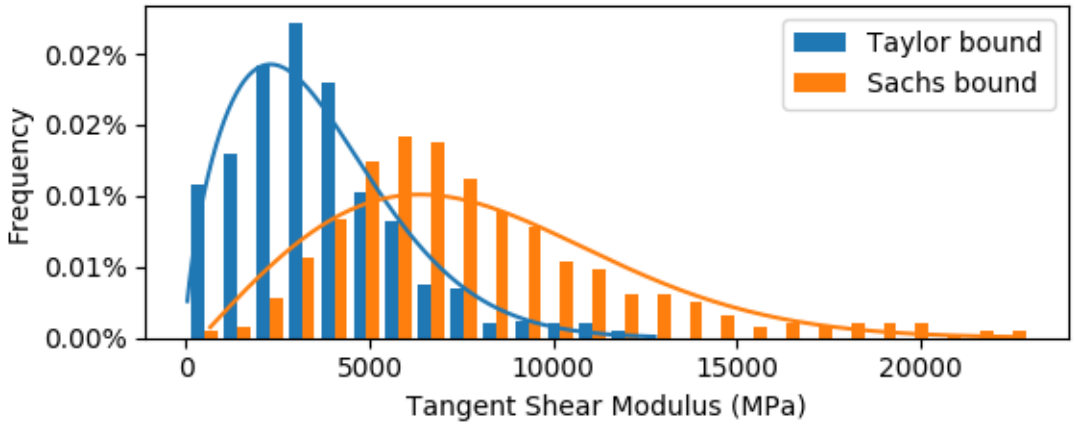

Figure A.17: Tangent Shear Mod. for $1x10^3$ Comminuted Particle Ensemble at 100 MPa

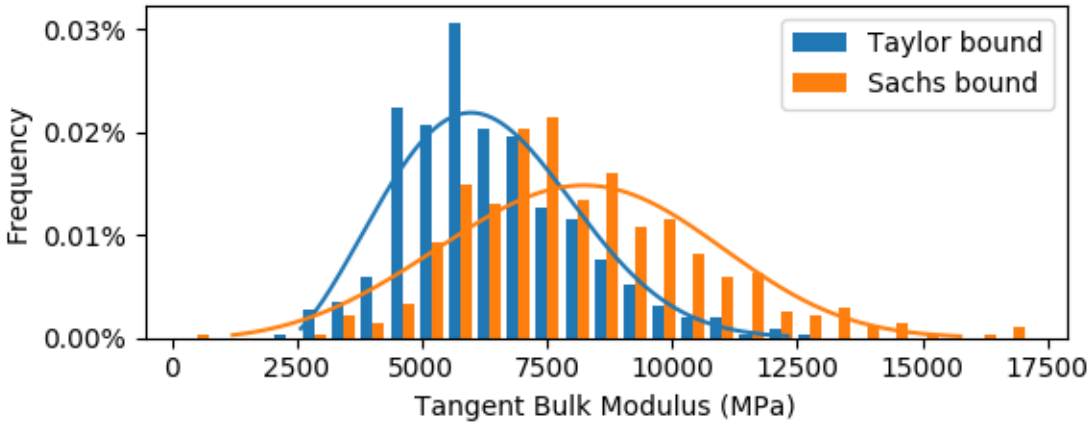

Figure A.18: Tangent Bulk Mod. for $1x10^3$ Comminuted Particle Ensemble at 100 MPa

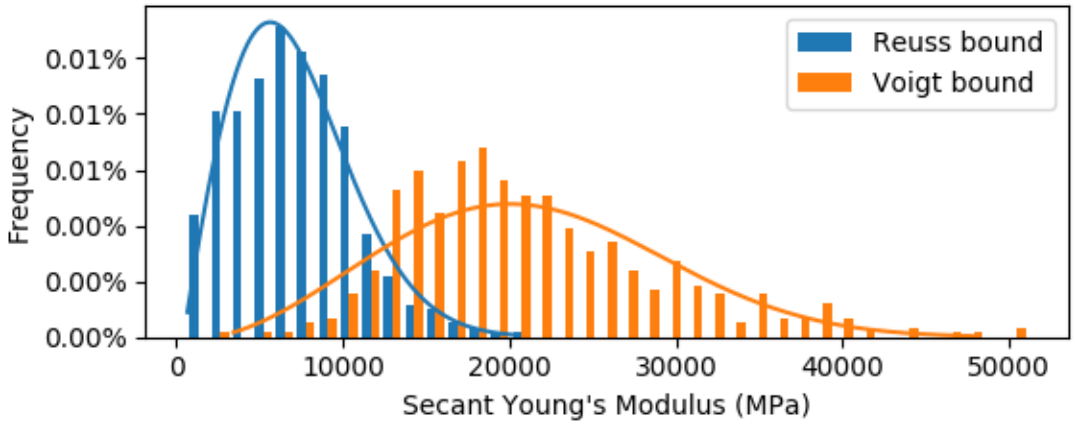

Figure A.19: Secant Young's Mod. for $1x10^3$ Comminuted Particle Ensemble at 200 MPa

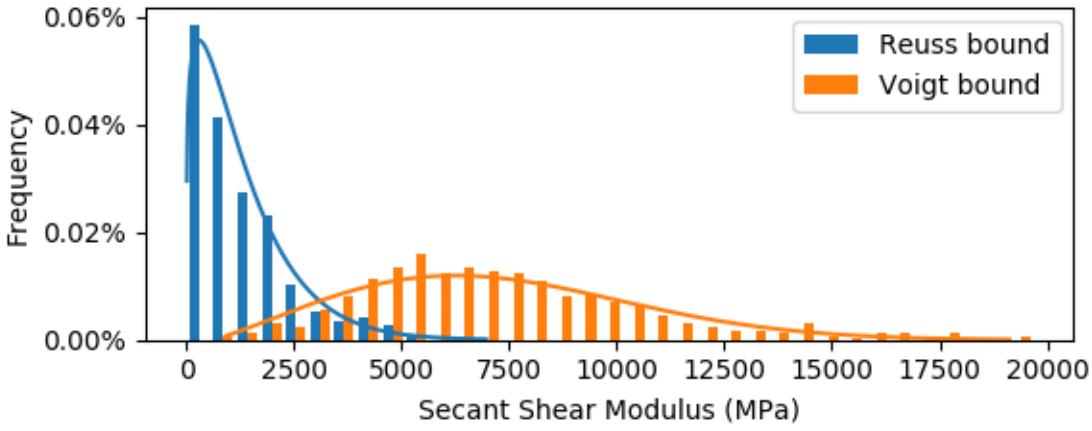

Figure A.20: Secant Shear Mod. for $1x10^3$ Comminuted Particle Ensemble at 200 MPa

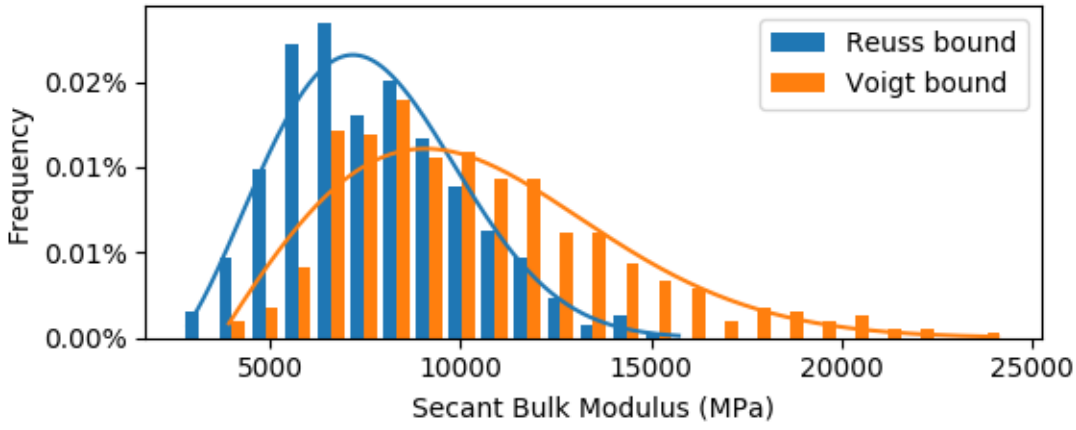

Figure A.21: Secant Bulk Mod. for $1x10^3$ Comminuted Particle Ensemble at 200 MPa

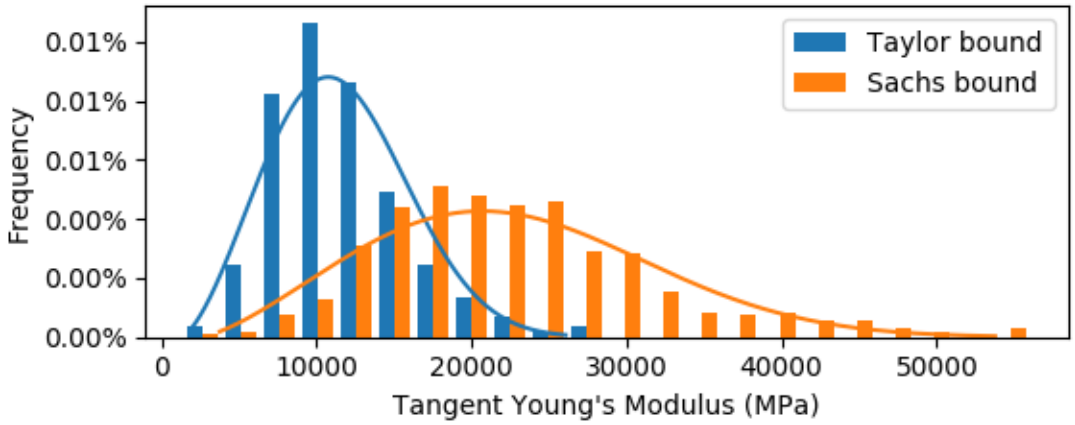

Figure A.22: Tangent Young's Mod. for $1x10^3$ Comminuted Particle Ensemble at 200 MPa

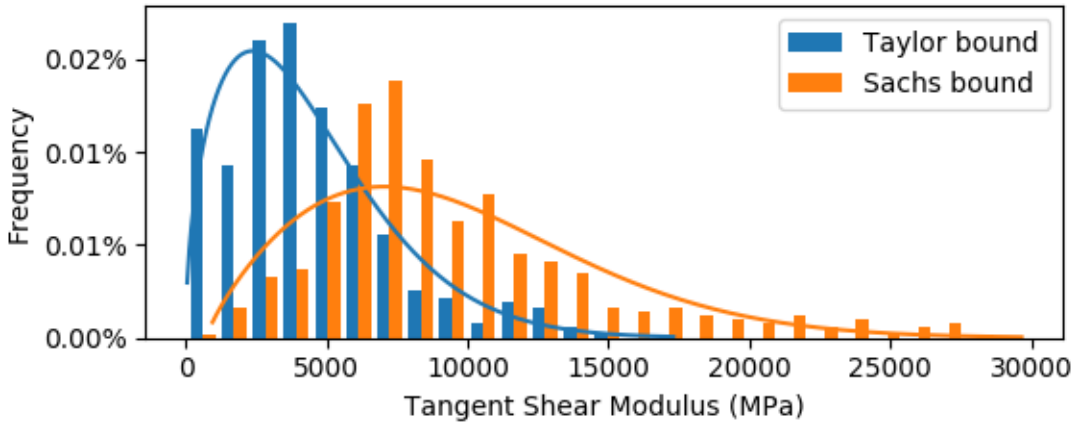

Figure A.23: Tangent Shear Mod. for $1x10^3$ Comminuted Particle Ensemble at 200 MPa

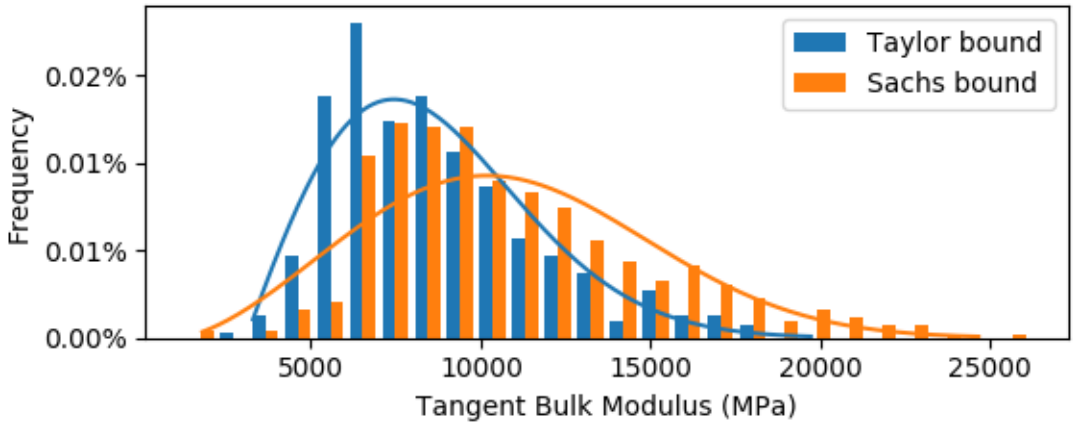

Figure A.24: Tangent Bulk Mod. for $1x10^3$ Comminuted Particle Ensemble at 200 MPa

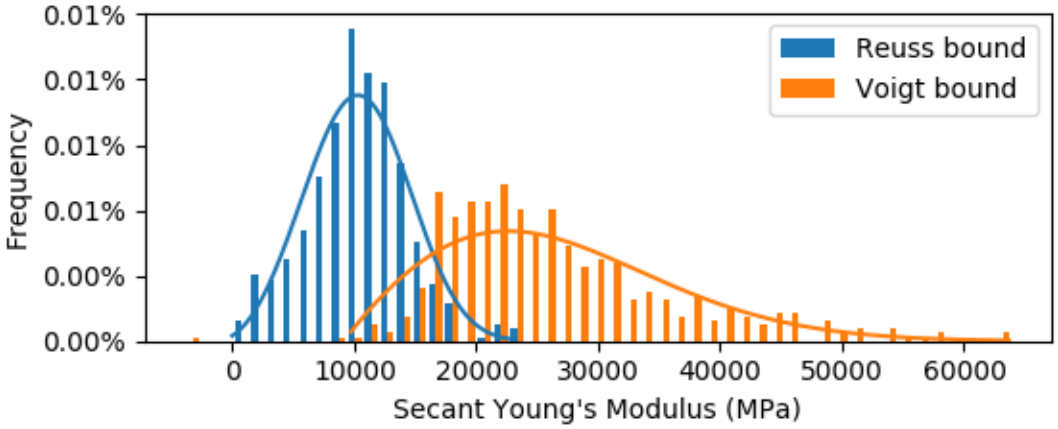

Figure A.25: Secant Young's Mod. for $1x10^3$ Comminuted Particle Ensemble at 400 MPa

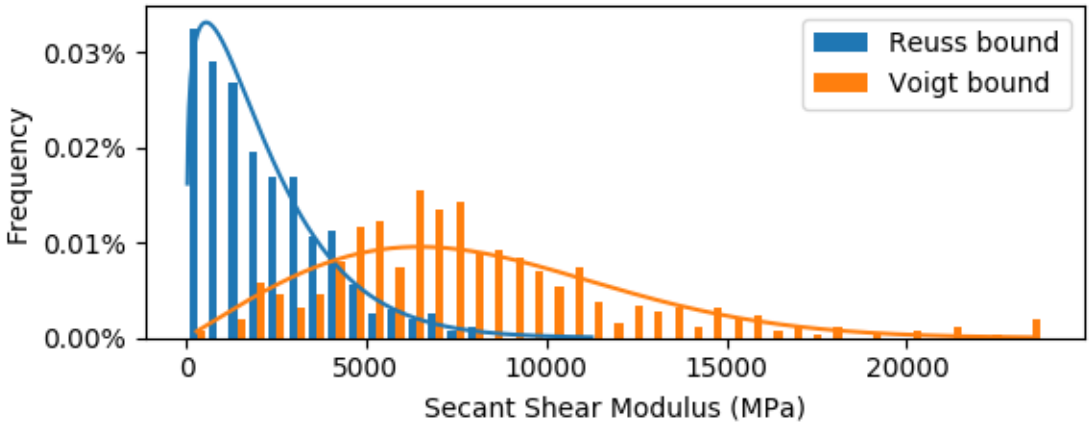

Figure A.26: Secant Shear Mod. for $1x10^3$ Comminuted Particle Ensemble at 400 MPa

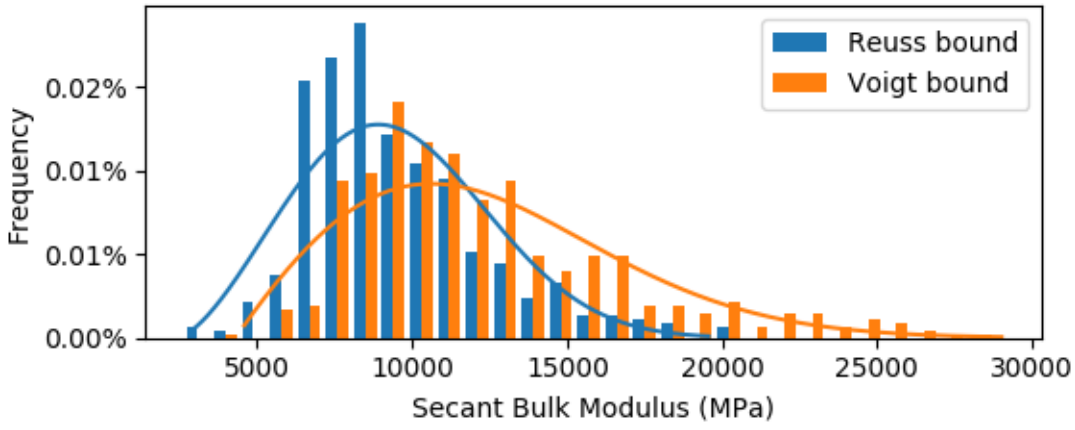

Figure A.27: Secant Bulk Mod. for $1x10^3$ Comminuted Particle Ensemble at 400 MPa

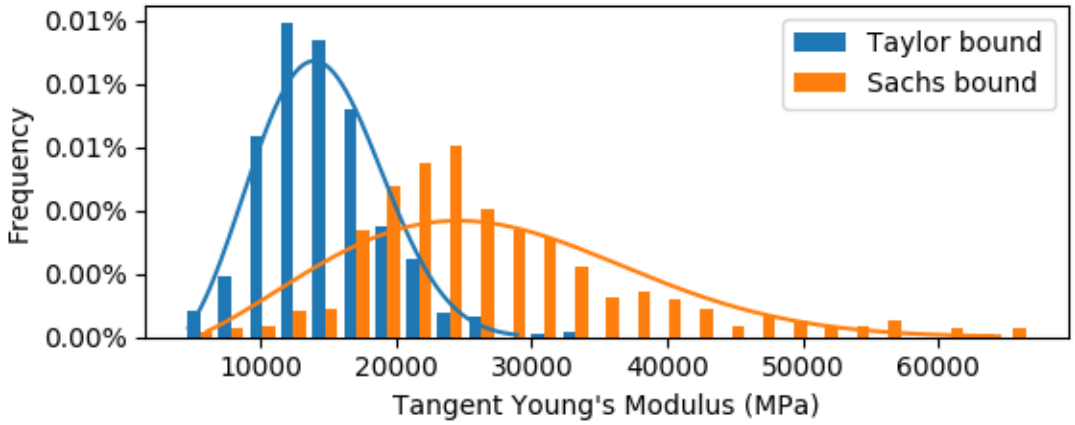

Figure A.28: Tangent Young's Mod. for $1x10^3$ Comminuted Particle Ensemble at 400 MPa

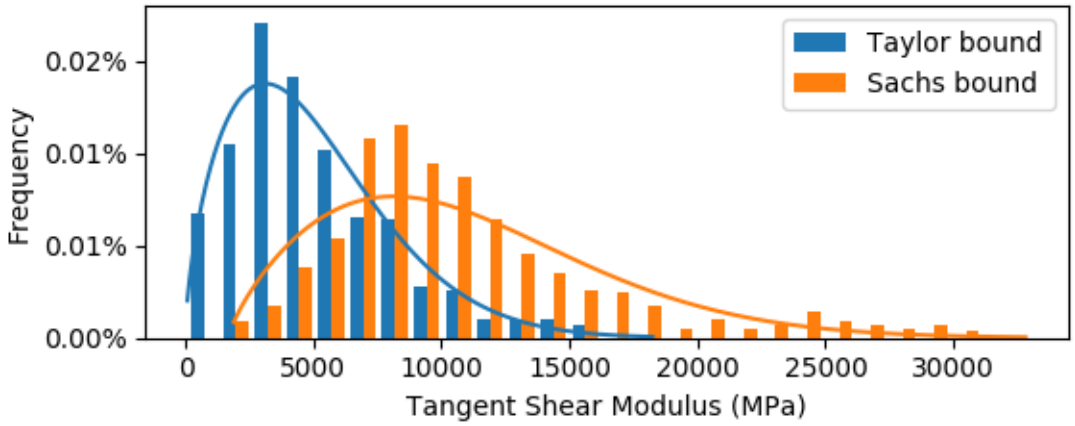

Figure A.29: Tangent Shear Mod. for $1x10^3$ Comminuted Particle Ensemble at 400 MPa

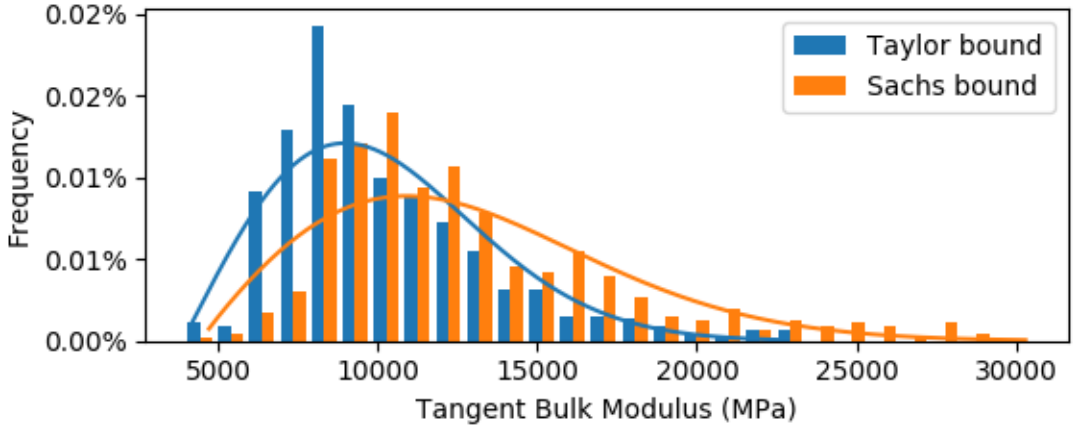

Figure A.30: Tangent Bulk Mod. for $1x10^3$ Comminuted Particle Ensemble at 400 MPa

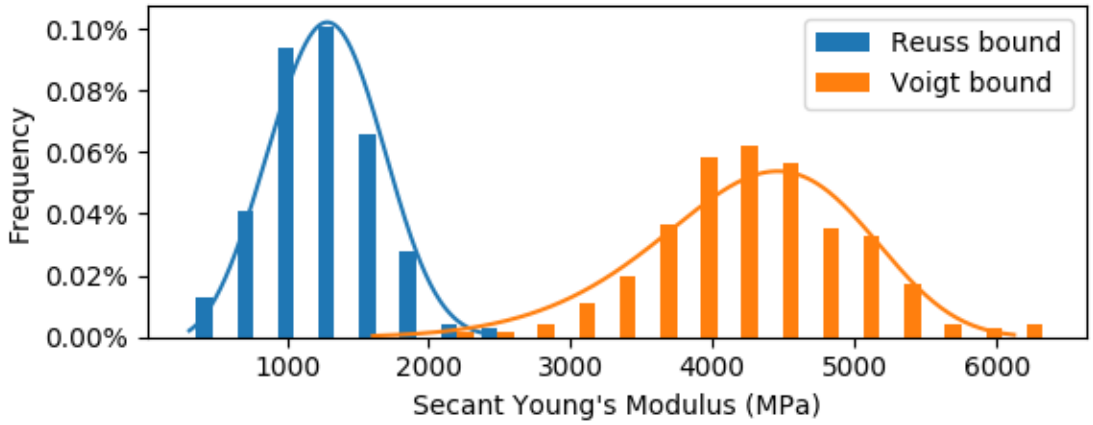

Figure A.31: Secant Young's Mod. for 1x10^4 Comminuted Particle Ensemble at 20 MPa

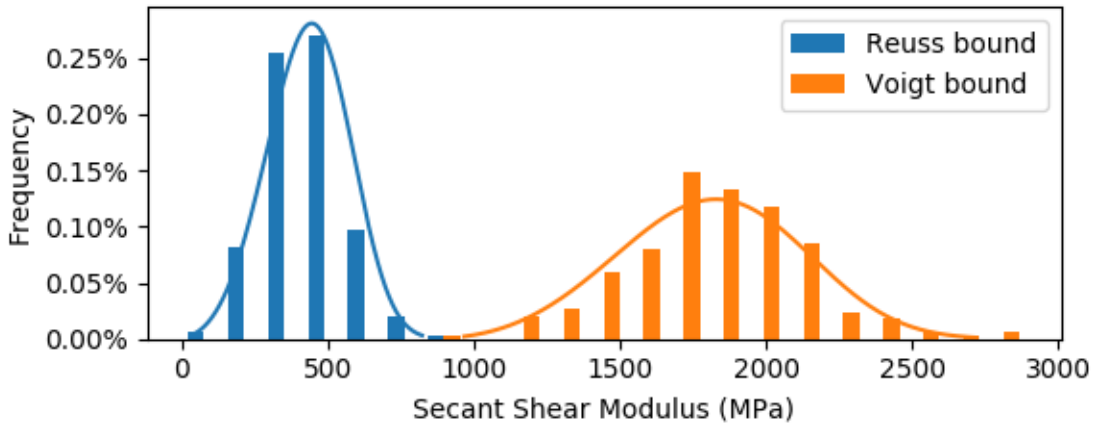

Figure A.32: Secant Shear Modulus for 1x10^4 Comminuted Particle Ensemble at 20 MPa

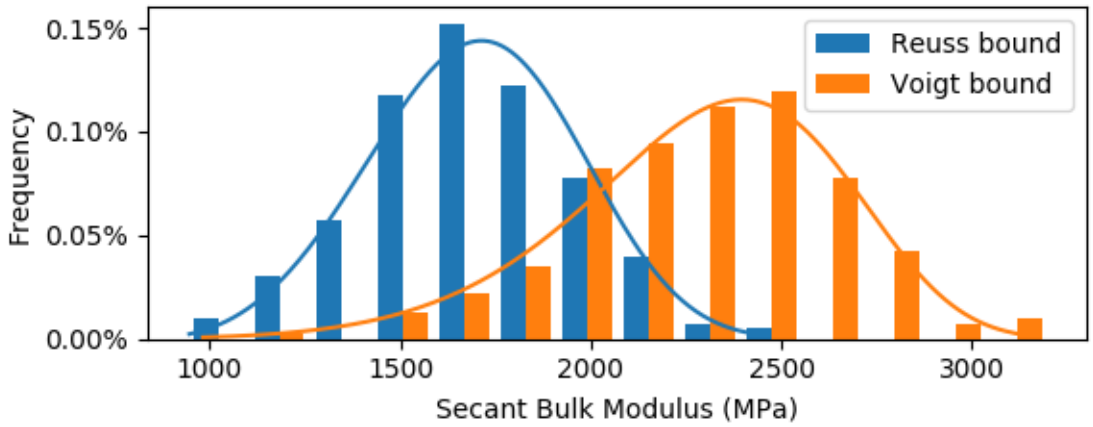

Figure A.33: Secant Bulk Modulus for 1x10^4 Comminuted Particle Ensemble at 20 MPa

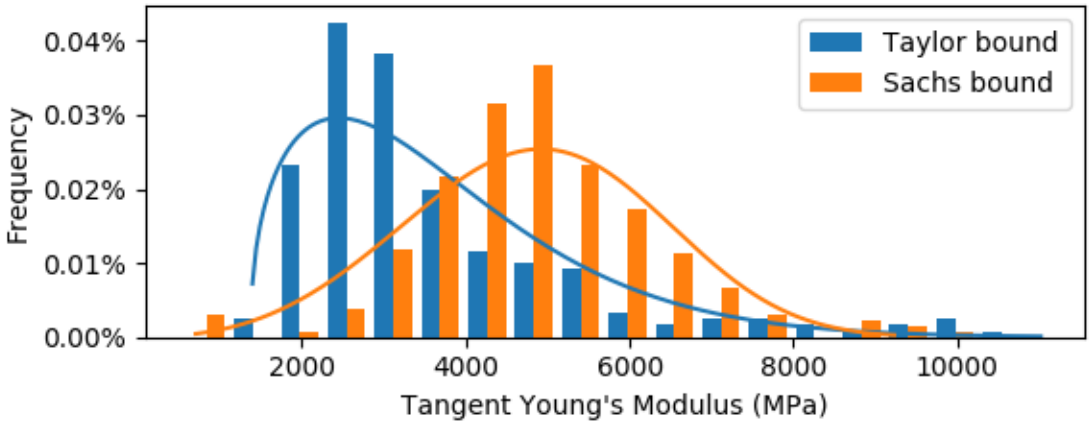

Figure A.34: Tangent Young's Mod. for $1x10^4$ Comminuted Particle Ensemble at 20 MPa

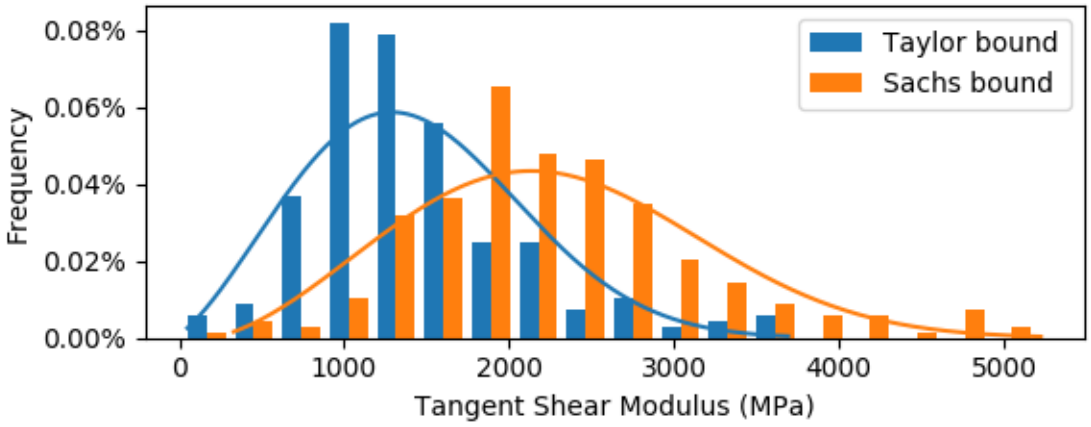

Figure A.35: Tangent Shear Mod. for $1x10^4$ Comminuted Particle Ensemble at 20 MPa

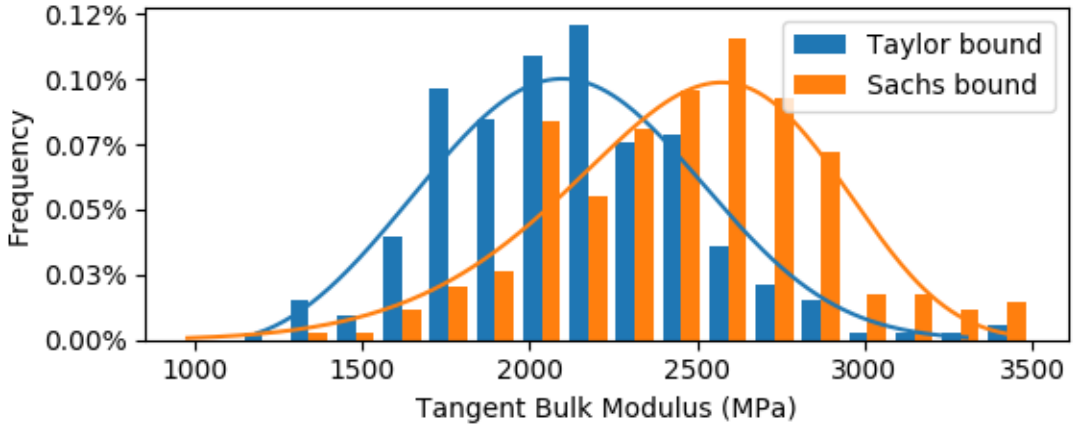

Figure A.36: Tangent Bulk Mod. for $1x10^4$ Comminuted Particle Ensemble at 20 MPa

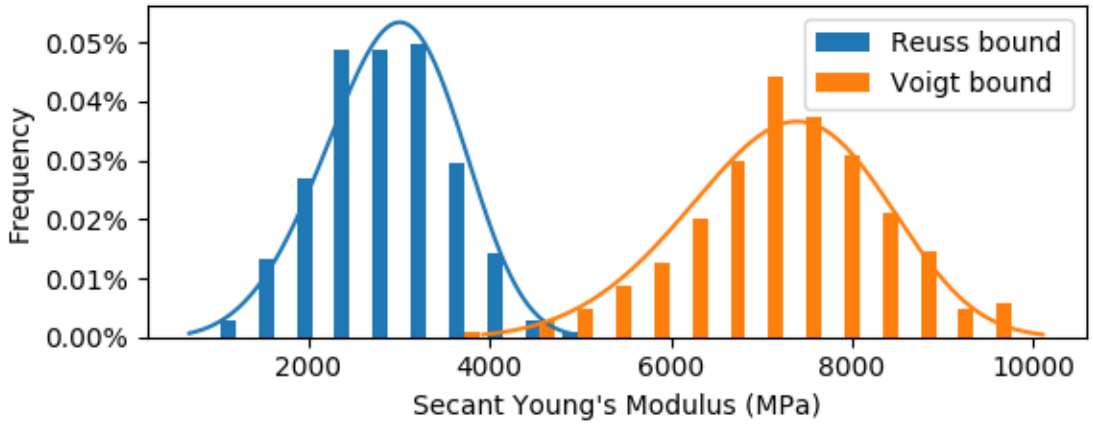

Figure A.37: Secant Young's Mod. for $1x10^4$ Comminuted Particle Ensemble at 50 MPa

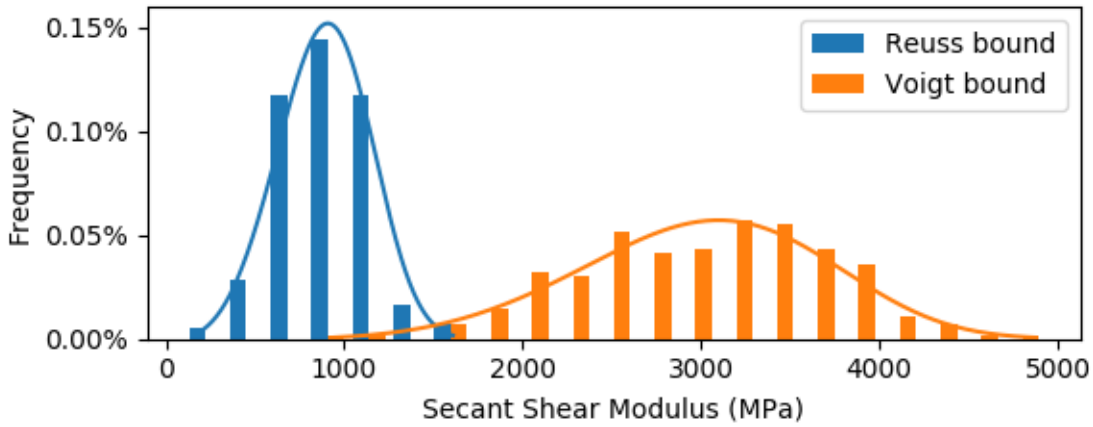

Figure A.38: Secant Shear Mod. for $1x10^4$ Comminuted Particle Ensemble at 50 MPa

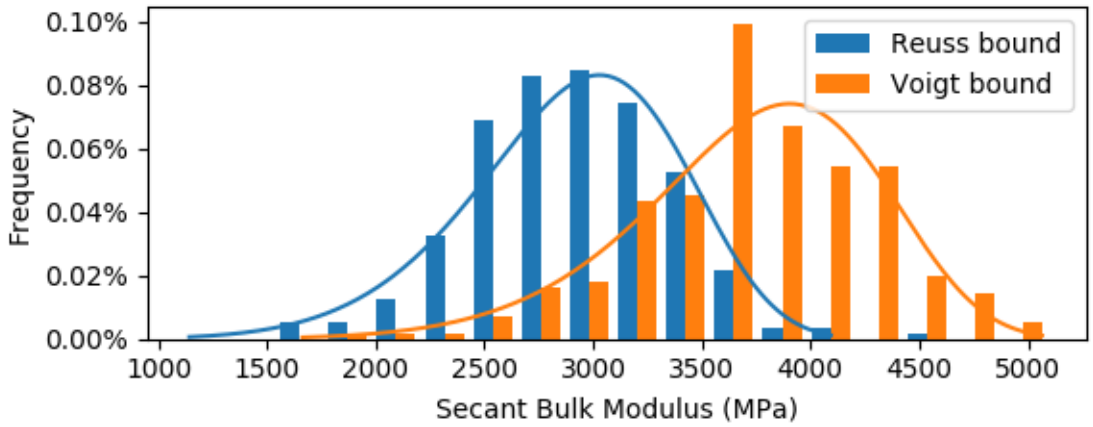

Figure A.39: Secant Bulk Modulus for $1x10^4$ Comminuted Particle Ensemble at 50 MPa

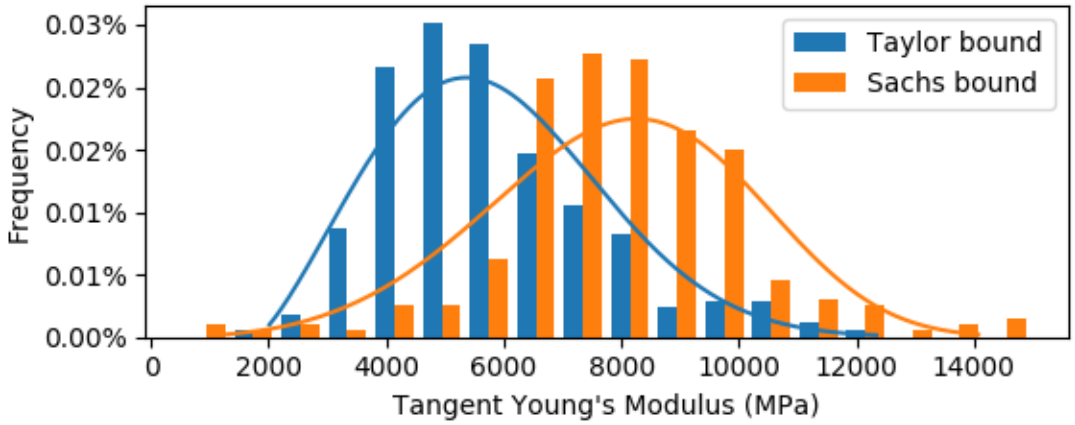

Figure A.40: Tangent Young's Mod. for $1x10^4$ Comminuted Particle Ensemble at 50 MPa

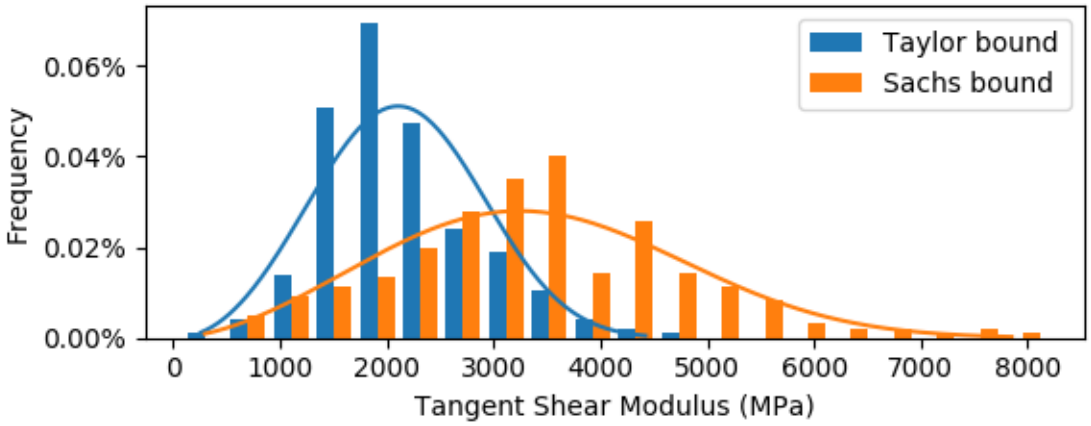

Figure A.41: Tangent Shear Mod. for $1x10^4$ Comminuted Particle Ensemble at 50 MPa

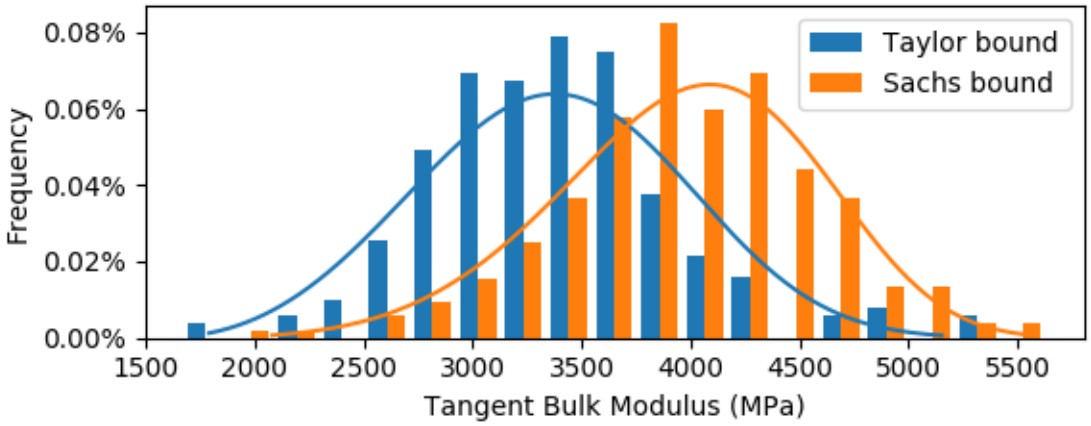

Figure A.42: Tangent Bulk Mod. for $1x10^4$ Comminuted Particle Ensemble at 50 MPa

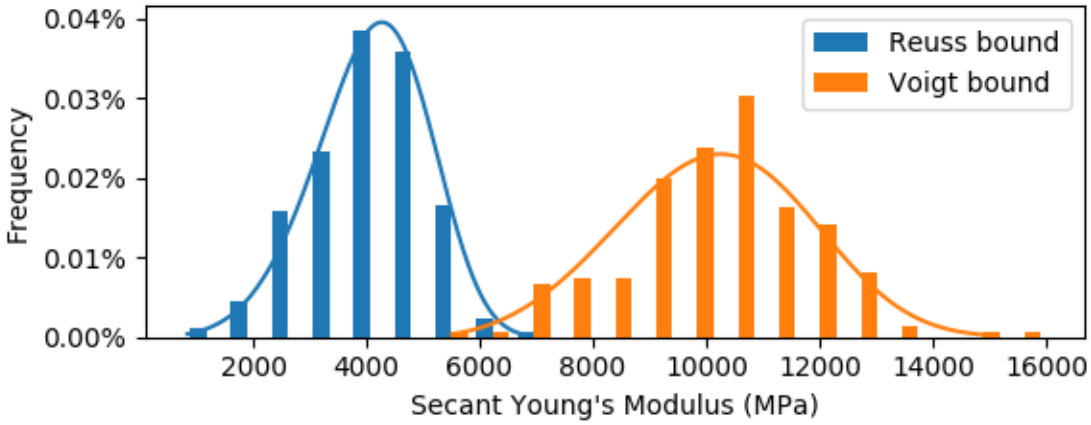

Figure A.43: Secant Young's Mod. for 1x10^4 Comminuted Particle Ensemble at 100 MPa

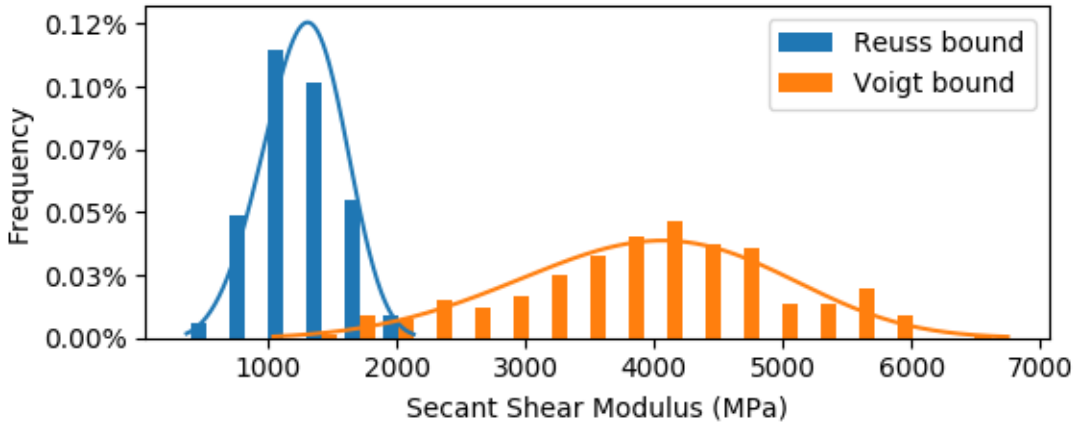

Figure A.44: Secant Shear Mod. for 1x10^4 Comminuted Particle Ensemble at 100 MPa

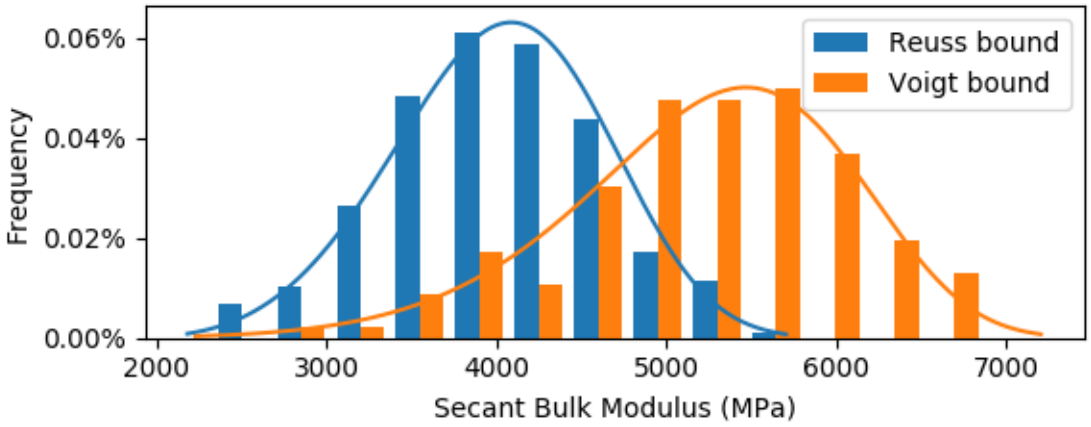

Figure A.45: Secant Bulk Mod. for 1x10^4 Comminuted Particle Ensemble at 100 MPa

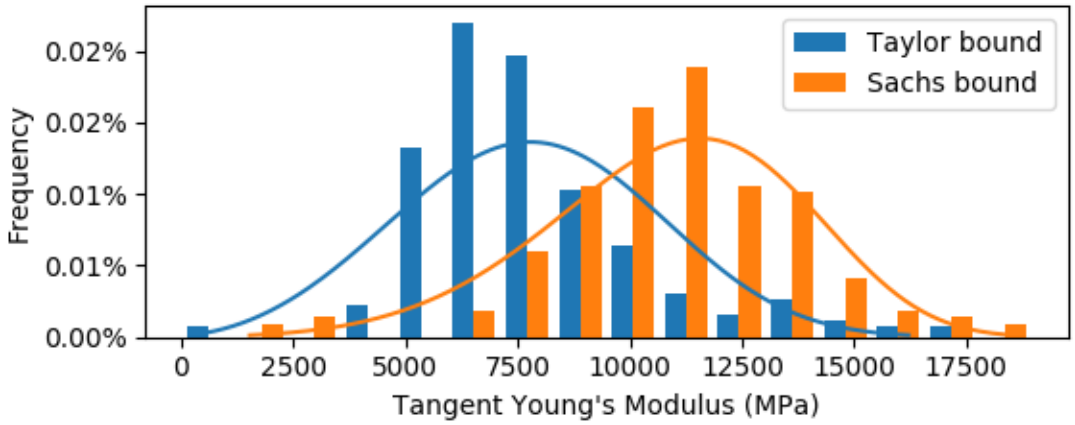

Figure A.46: Tangent Young's Mod. for 1x10^4 Comminuted Particle Ensemble at 100 MPa

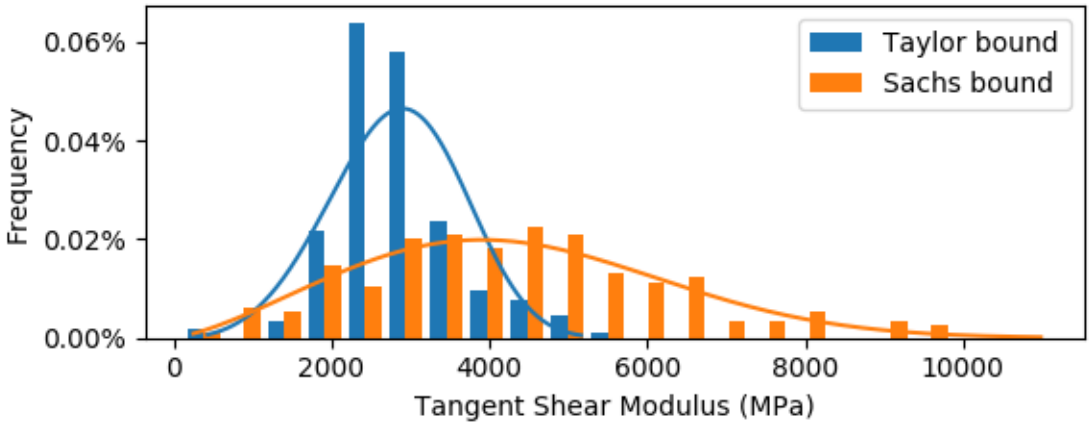

Figure A.47: Tangent Shear Mod. for 1x10^4 Comminuted Particle Ensemble at 100 MPa

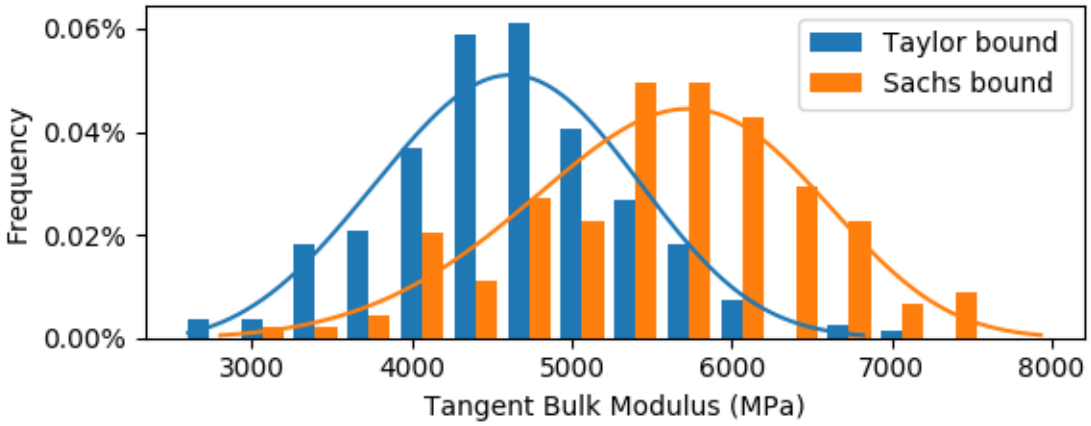

Figure A.48: Tangent Bulk Mod. for 1x10^4 Comminuted Particle Ensemble at 100 MPa

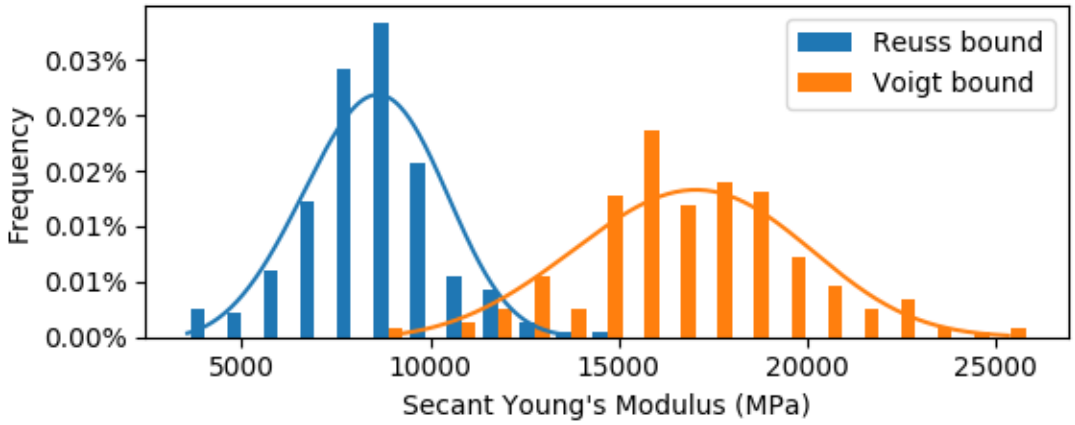

Figure A.49: Secant Young's Mod. for $1x10^4$ Comminuted Particle Ensemble at 200 MPa

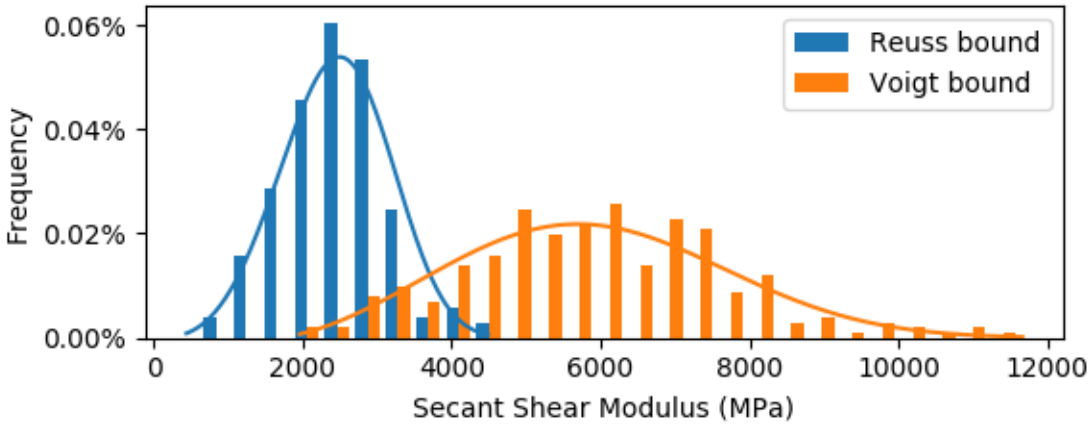

Figure A.50: Secant Shear Mod. for $1x10^4$ Comminuted Particle Ensemble at 200 MPa

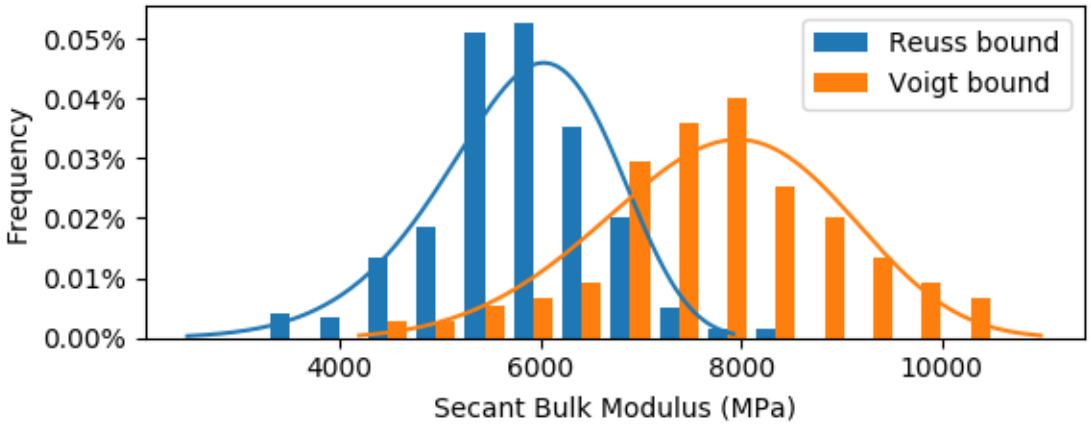

Figure A.51: Secant Bulk Mod. for $1x10^4$ Comminuted Particle Ensemble at 200 MPa

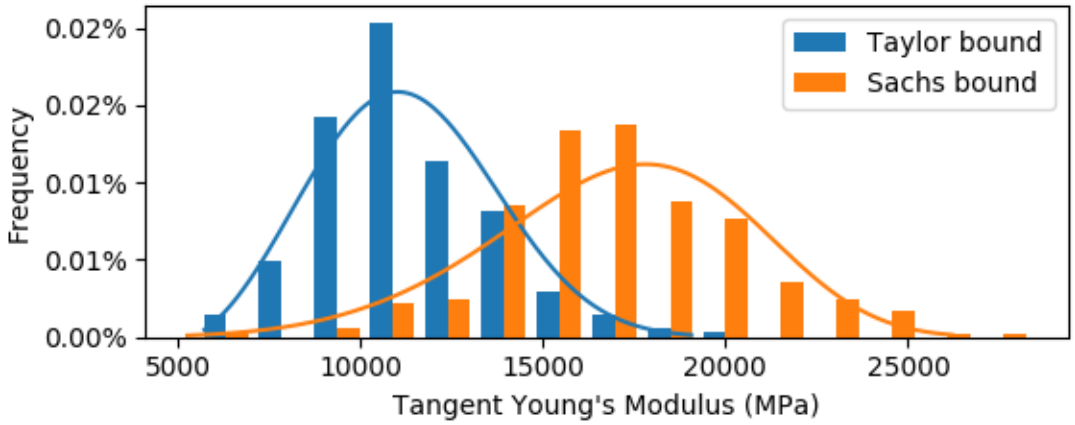

Figure A.52: Tangent Young's Mod. for $1x10^4$ Comminuted Particle Ensemble at 200 MPa

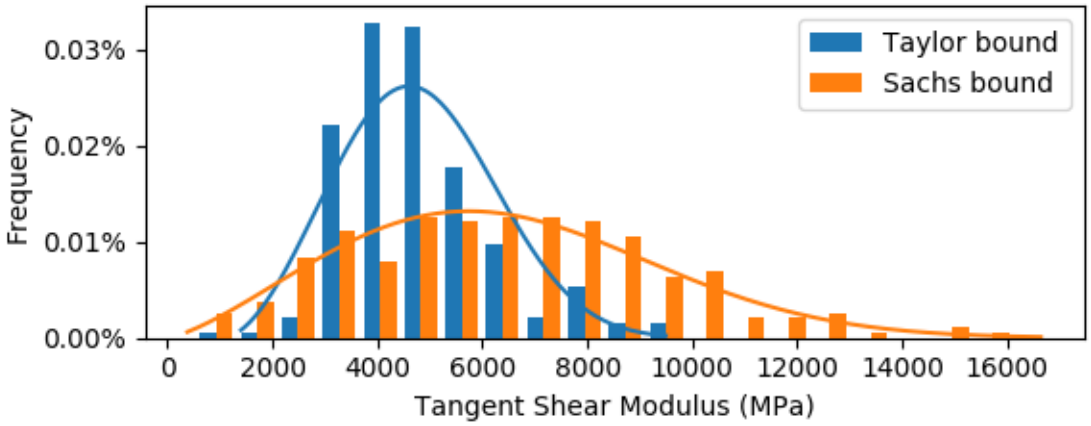

Figure A.53: Tangent Shear Mod. for $1x10^4$ Comminuted Particle Ensemble at 200 MPa

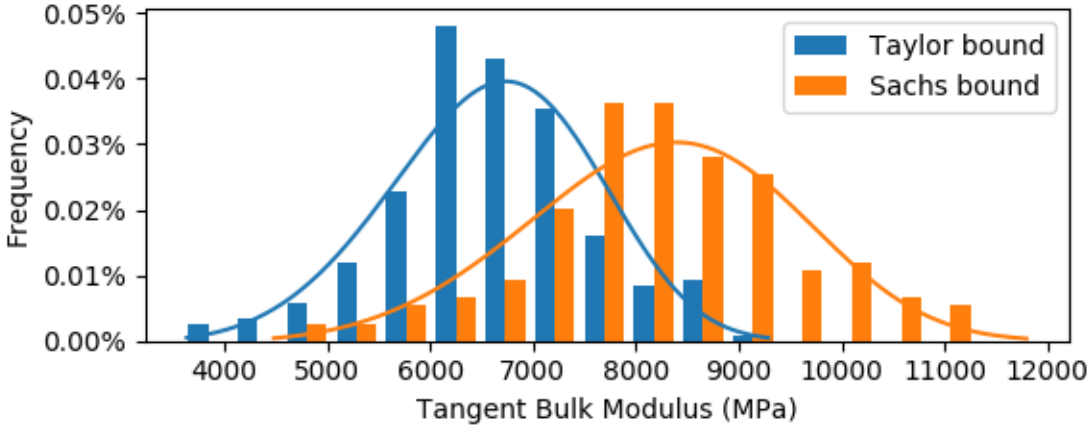

Figure A.54: Tangent Bulk Mod. for $1x10^4$ Comminuted Particle Ensemble at 200 MPa

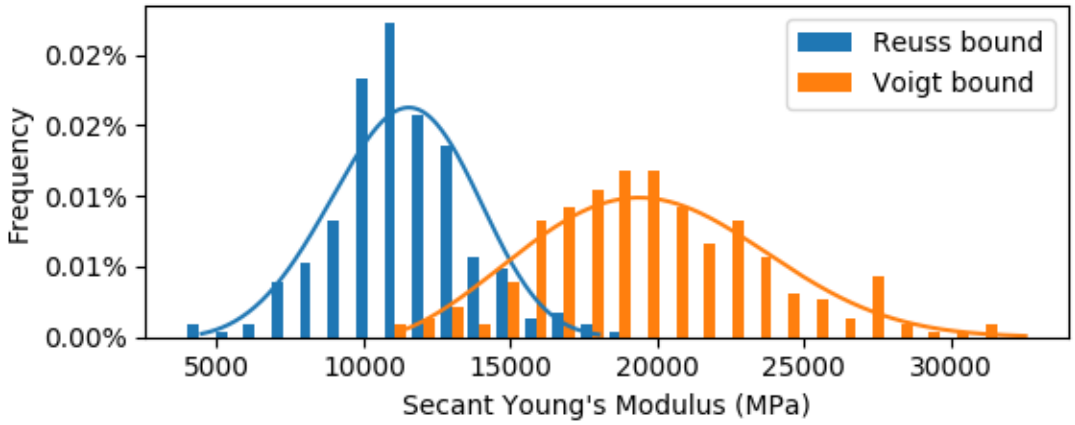

Figure A.55: Secant Young's Mod. for 1x10^4 Comminuted Particle Ensemble at 400 MPa

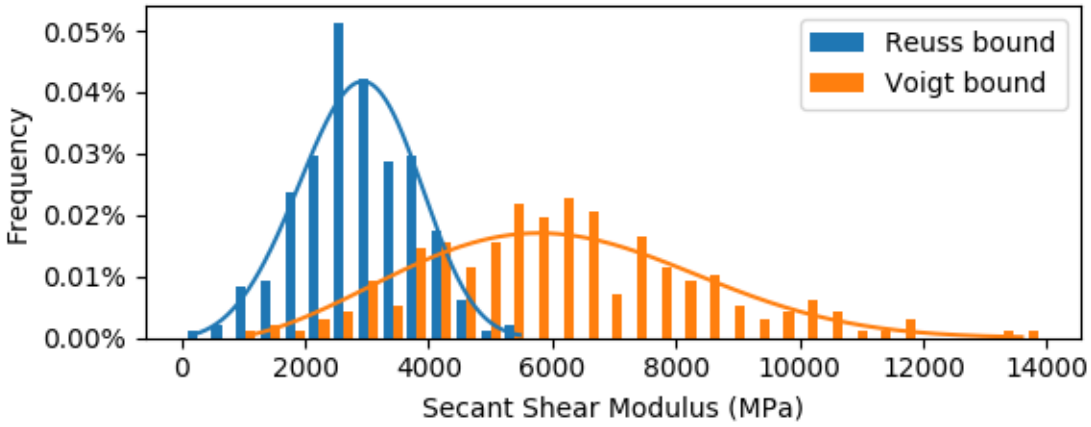

Figure A.56: Secant Shear Mod. for 1x10^4 Comminuted Particle Ensemble at 400 MPa

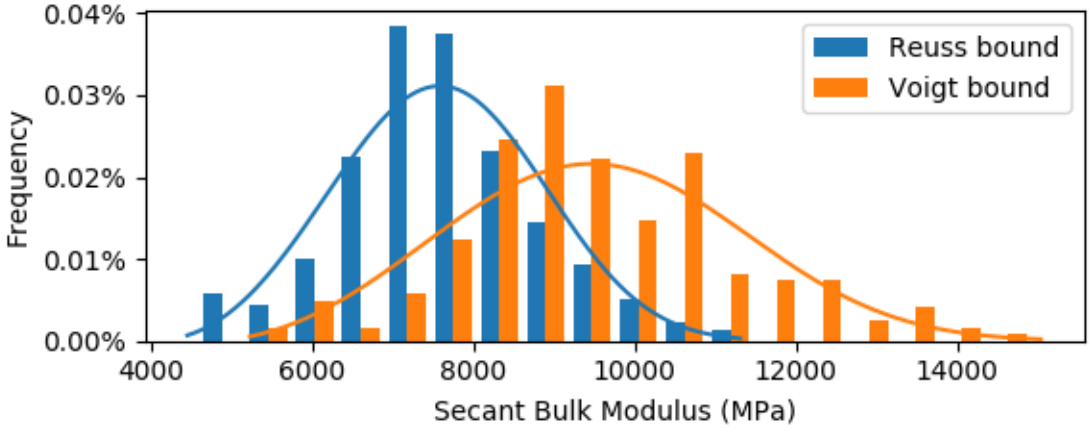

Figure A.57: Secant Bulk Mod. for 1x10^4 Comminuted Particle Ensemble at 400 MPa

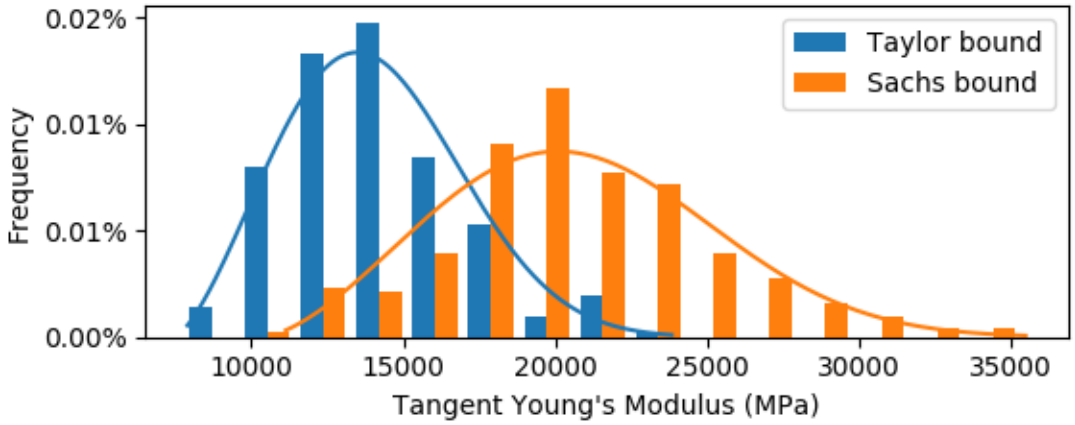

Figure A.58: Tangent Young's Mod. for 1x10^4 Comminuted Particle Ensemble at 400 MPa

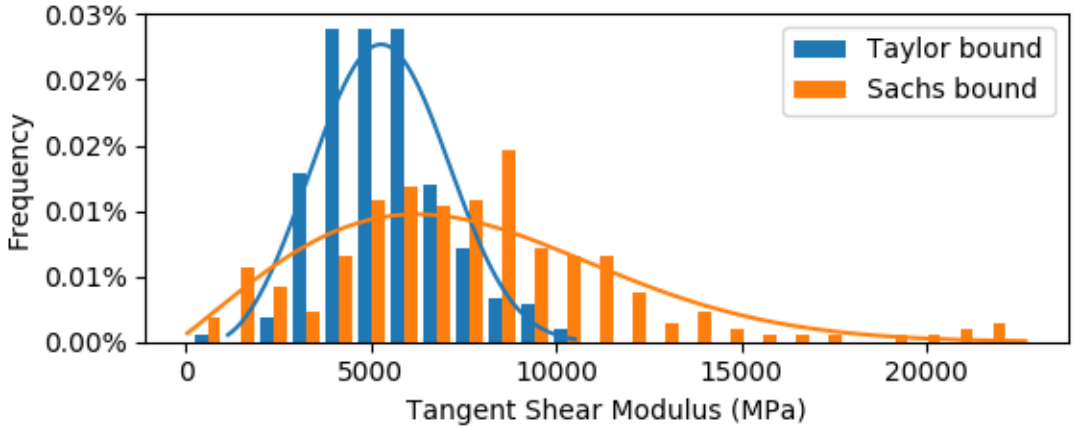

Figure A.59: Tangent Shear Mod. for 1x10^4 Comminuted Particle Ensemble at 400 MPa

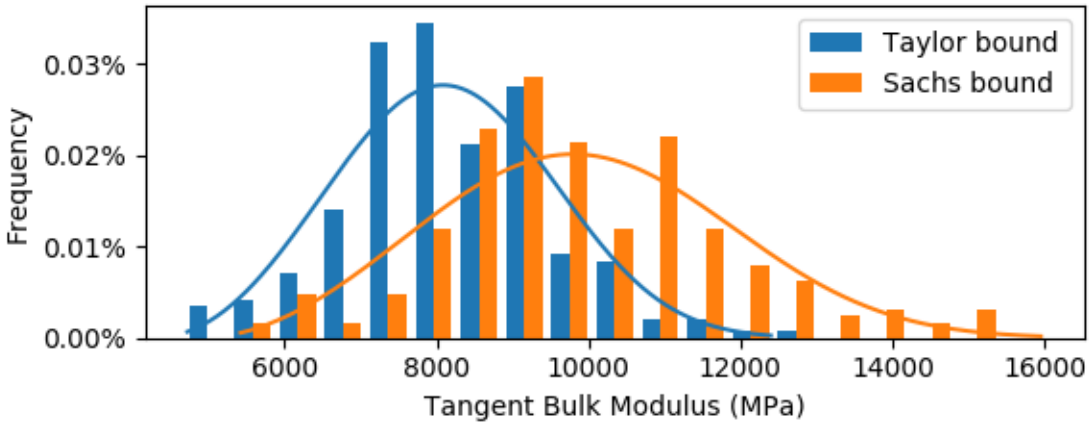

Figure A.60: Tangent Bulk Mod. for 1x10^4 Comminuted Particle Ensemble at 400 MPa

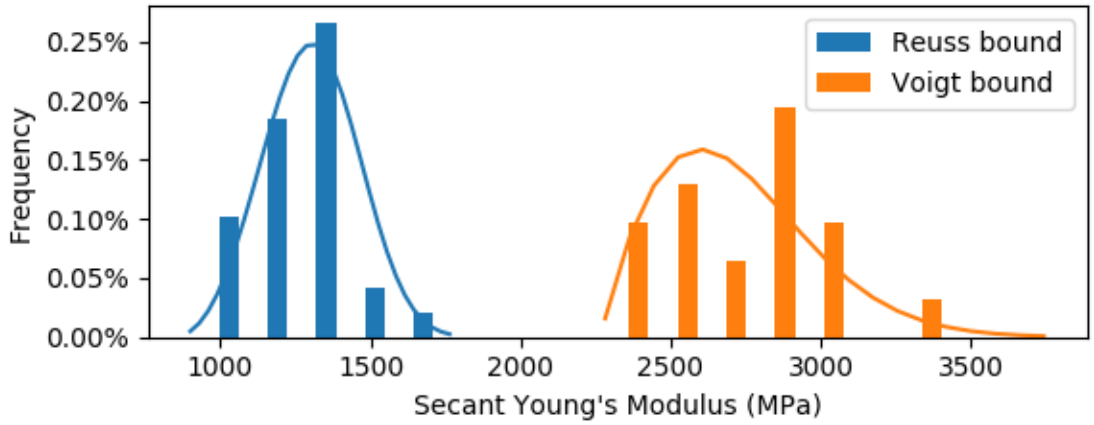

Figure A.61: Secant Young's Mod. for $1x10^5$ Comminuted Particle Ensemble at 20 MPa

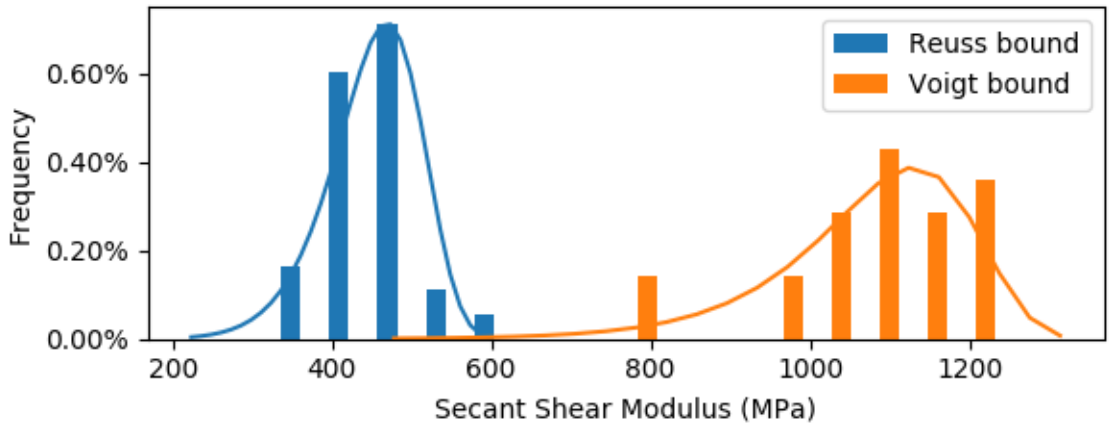

Figure A.62: Secant Shear Modulus for $1x10^5$ Comminuted Particle Ensemble at 20 MPa

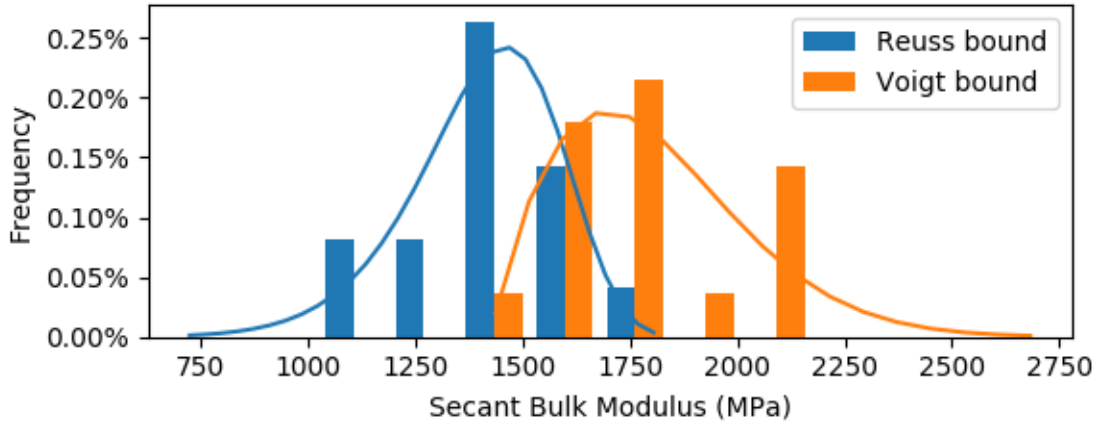

Figure A.63: Secant Bulk Modulus for $1x10^5$ Comminuted Particle Ensemble at 20 MPa

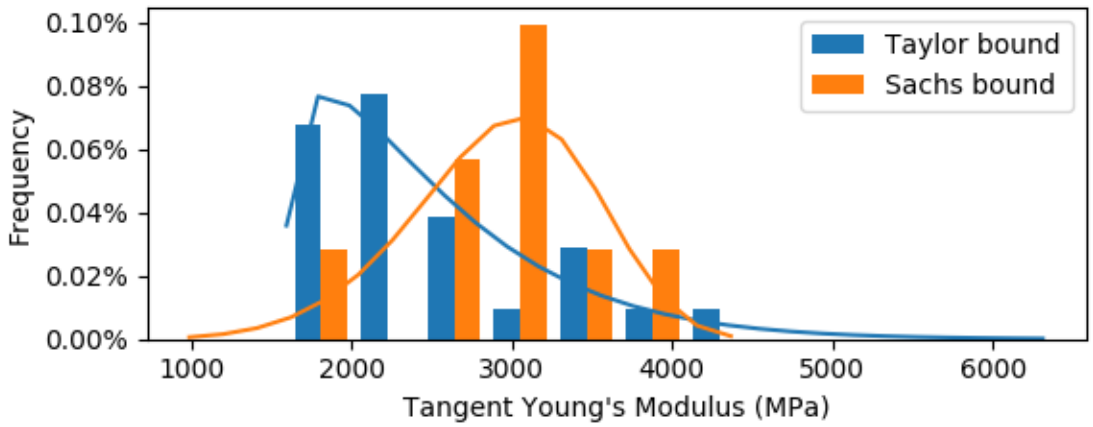

Figure A.64: Tangent Young's Mod. for $1x10^5$ Comminuted Particle Ensemble at 20 MPa

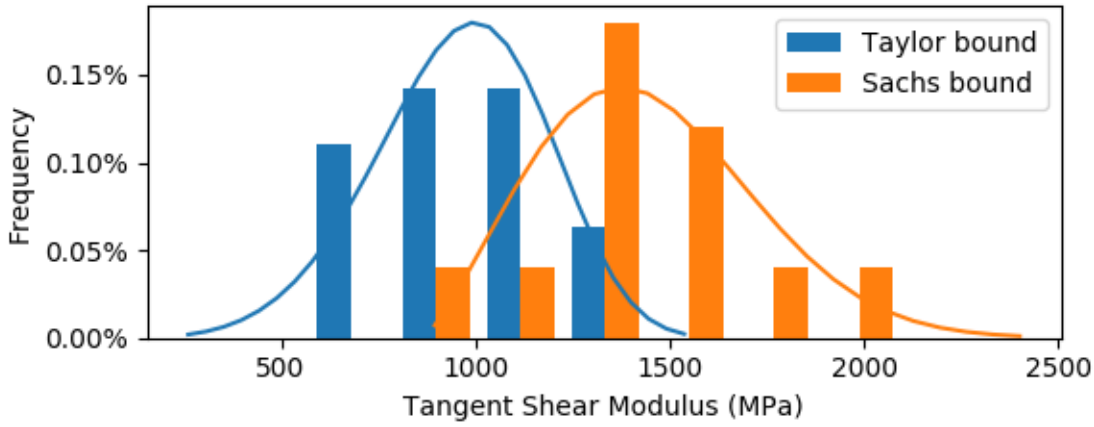

Figure A.65: Tangent Shear Mod. for $1x10^5$ Comminuted Particle Ensemble at 20 MPa

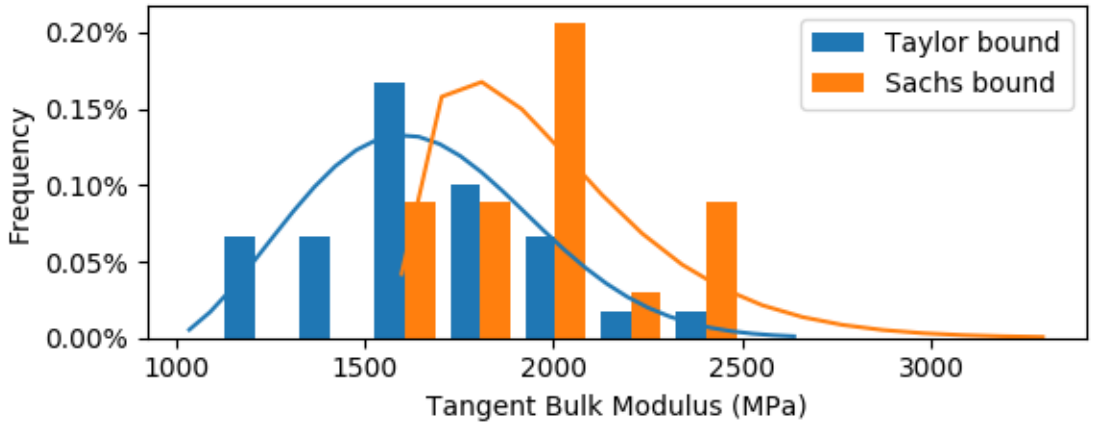

Figure A.66: Tangent Bulk Mod. for $1x10^5$ Comminuted Particle Ensemble at 20 MPa

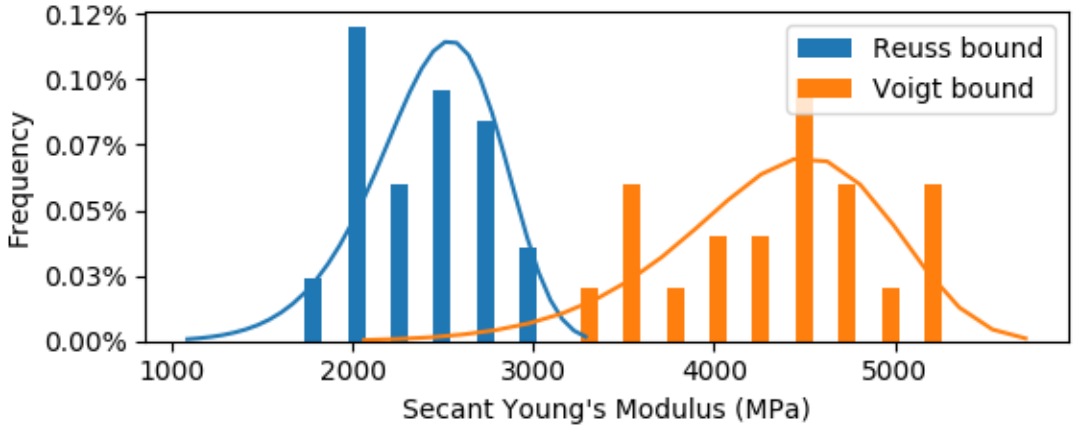

Figure A.67: Secant Young's Mod. for $1x10^5$ Comminuted Particle Ensemble at 50 MPa

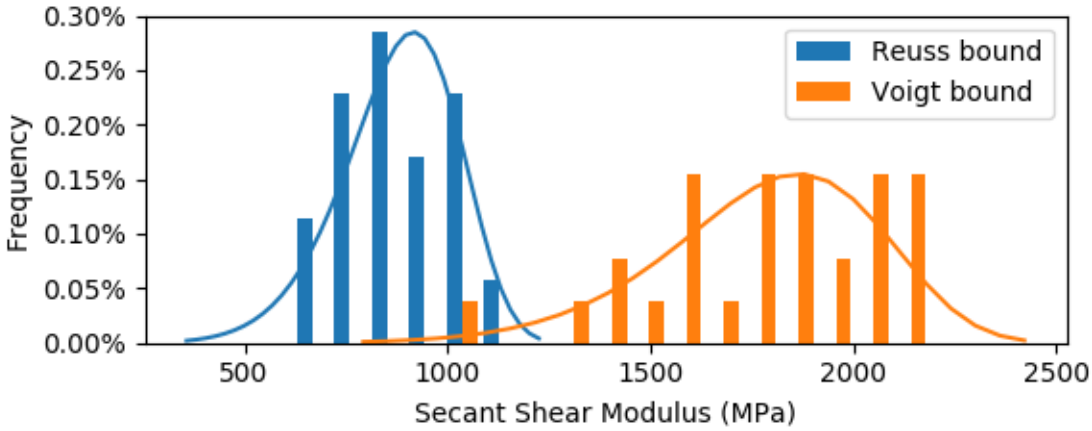

Figure A.68: Secant Shear Mod. for $1x10^5$ Comminuted Particle Ensemble at 50 MPa

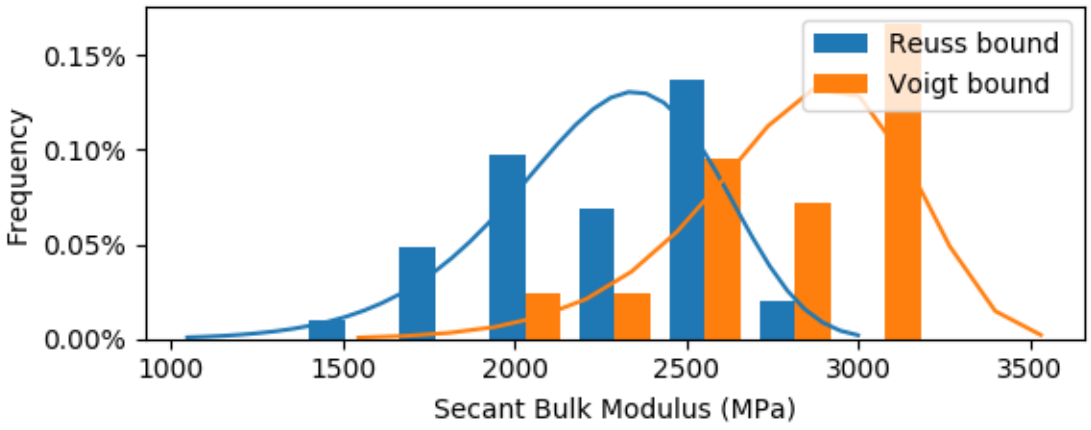

Figure A.69: Secant Bulk Modulus for $1x10^5$ Comminuted Particle Ensemble at 50 MPa

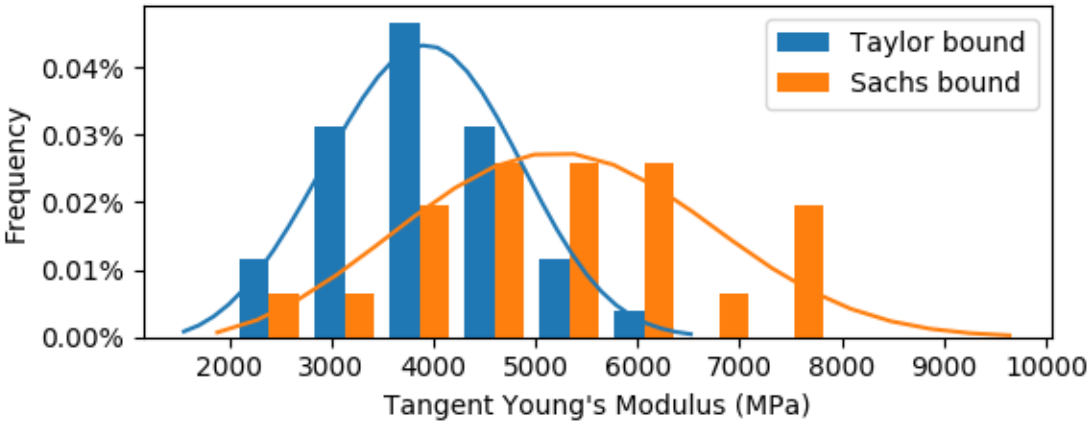

Figure A.70: Tangent Young's Mod. for $1x10^5$ Comminuted Particle Ensemble at 50 MPa

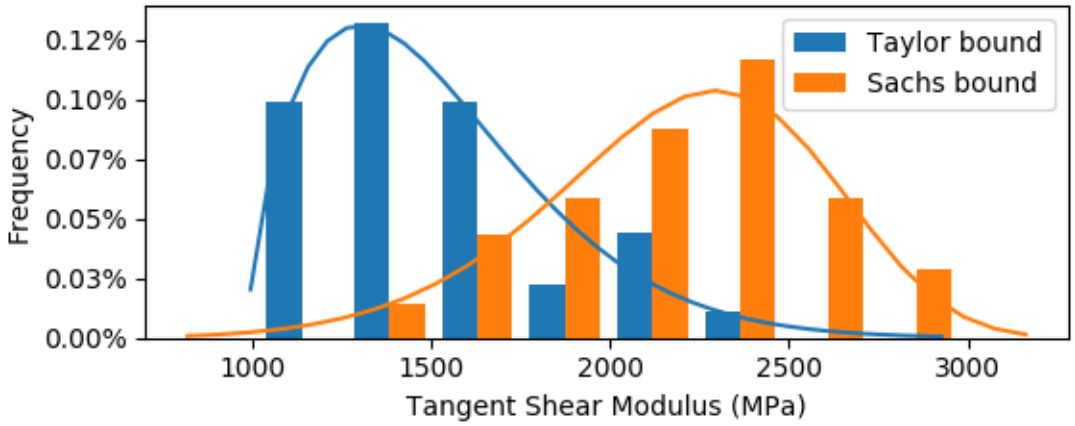

Figure A.71: Tangent Shear Mod. for $1x10^5$ Comminuted Particle Ensemble at 50 MPa

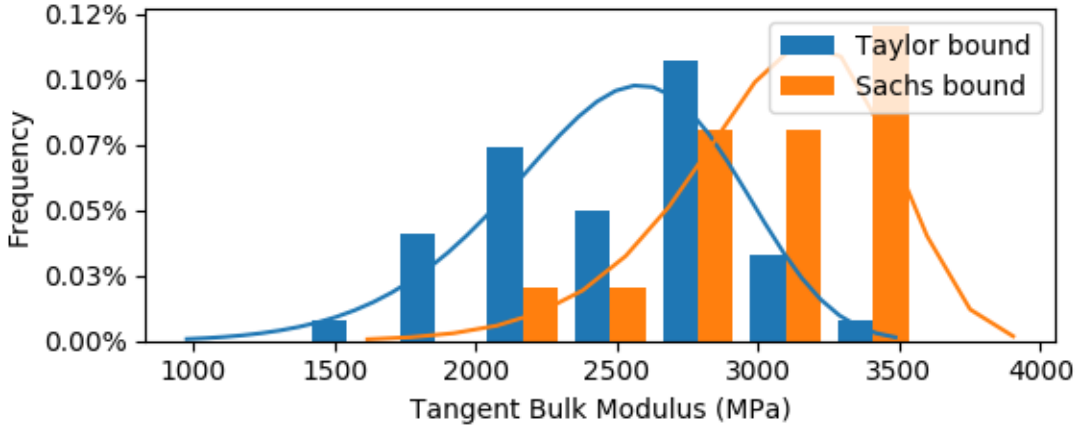

Figure A.72: Tangent Bulk Mod. for $1x10^5$ Comminuted Particle Ensemble at 50 MPa

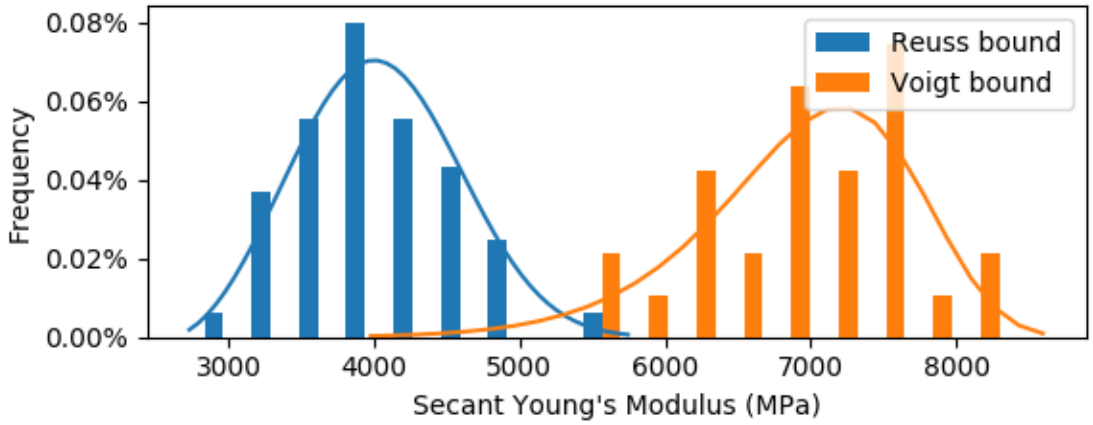

Figure A.73: Secant Young's Mod. for $1x10^5$ Comminuted Particle Ensemble at 100 MPa

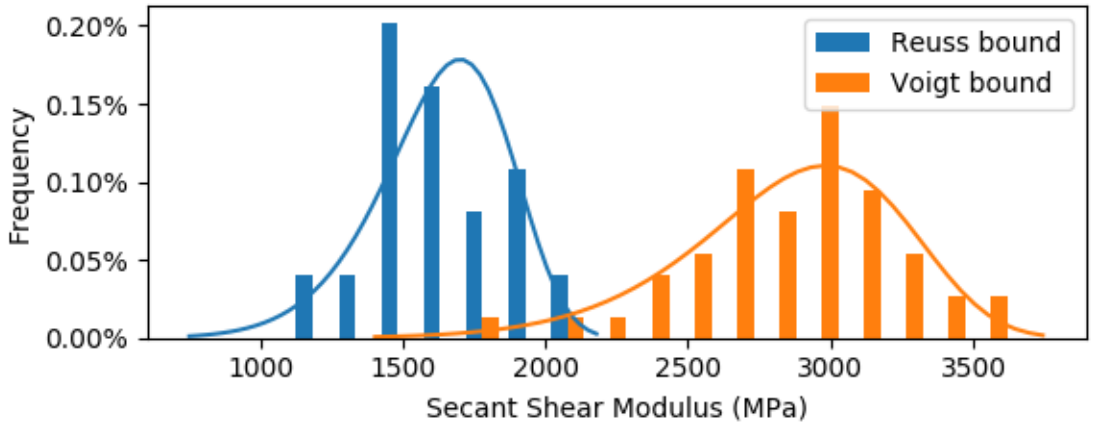

Figure A.74: Secant Shear Mod. for $1x10^5$ Comminuted Particle Ensemble at 100 MPa

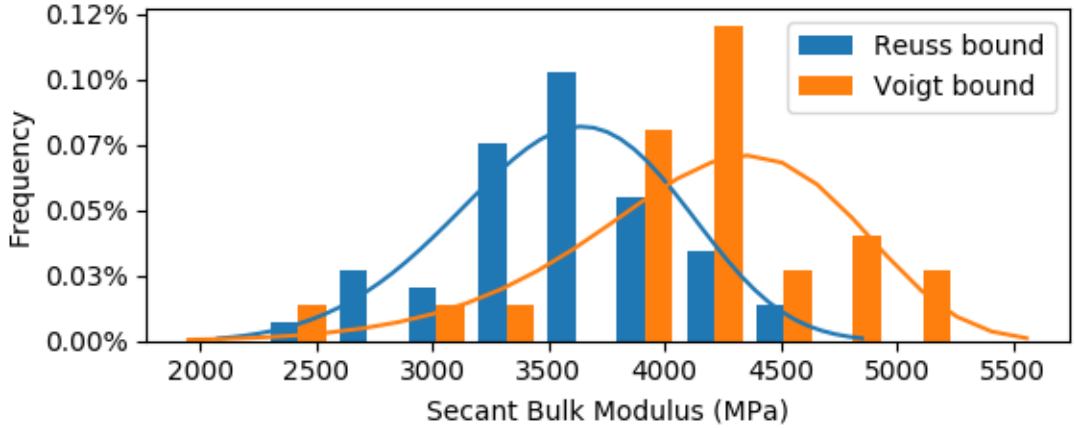

Figure A.75: Secant Bulk Mod. for $1x10^5$ Comminuted Particle Ensemble at 100 MPa

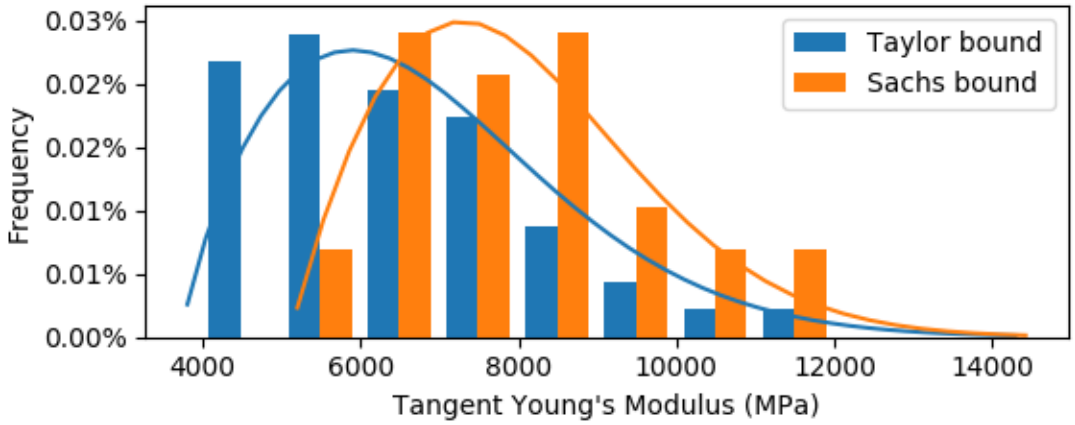

Figure A.76: Tangent Young's Mod. for $1x10^5$ Comminuted Particle Ensemble at 100 MPa

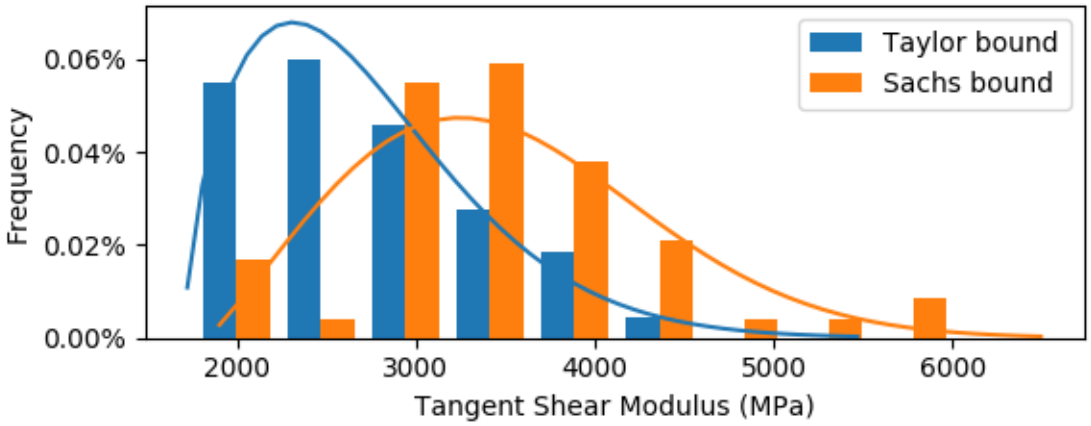

Figure A.77: Tangent Shear Mod. for $1x10^5$ Comminuted Particle Ensemble at 100 MPa

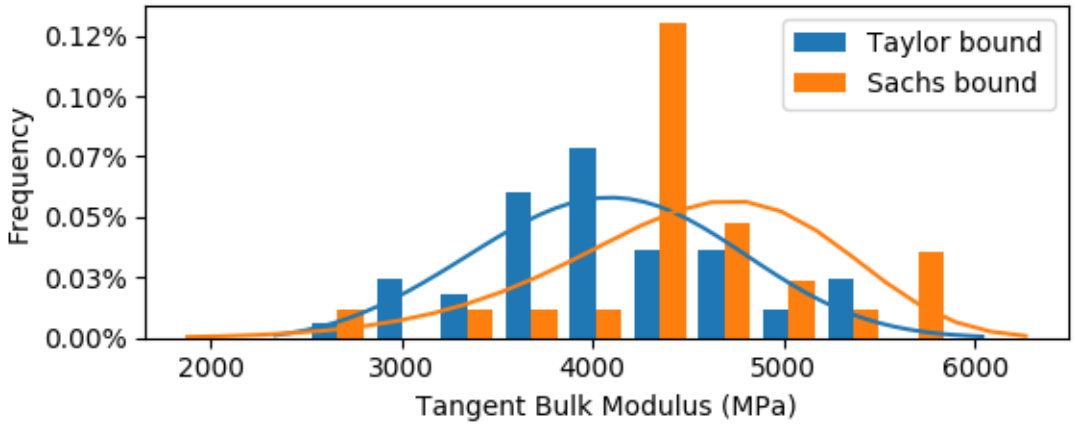

Figure A.78: Tangent Bulk Mod. for $1x10^5$ Comminuted Particle Ensemble at 100 MPa

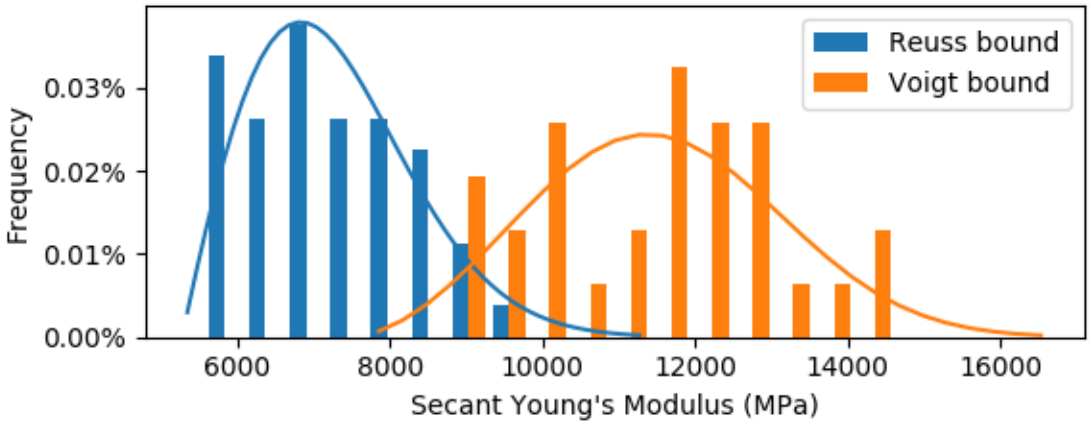

Figure A.79: Secant Young's Mod. for $1x10^5$ Comminuted Particle Ensemble at 200 MPa

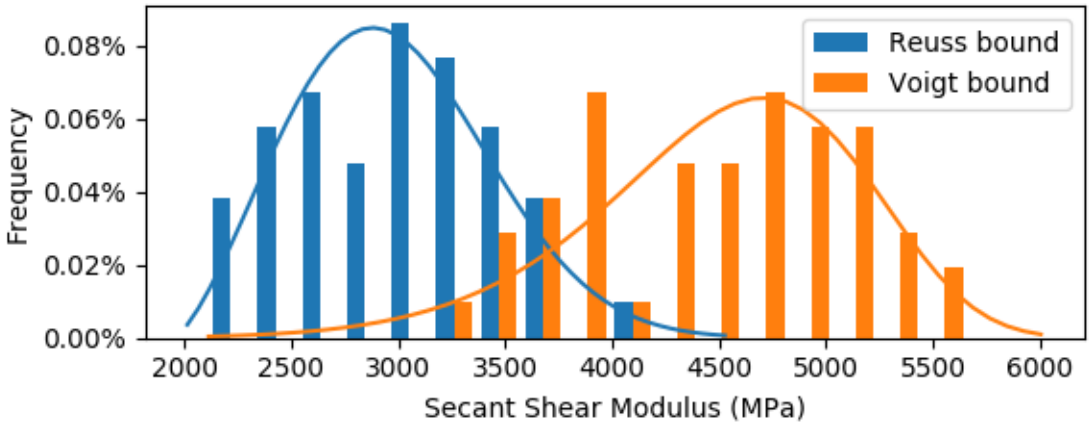

Figure A.80: Secant Shear Mod. for $1x10^5$ Comminuted Particle Ensemble at 200 MPa

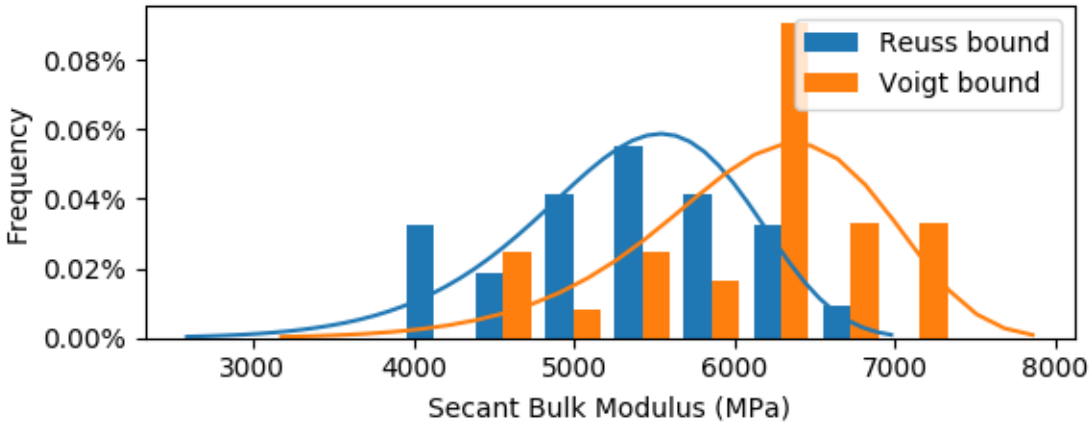

Figure A.81: Secant Bulk Mod. for $1x10^5$ Comminuted Particle Ensemble at 200 MPa

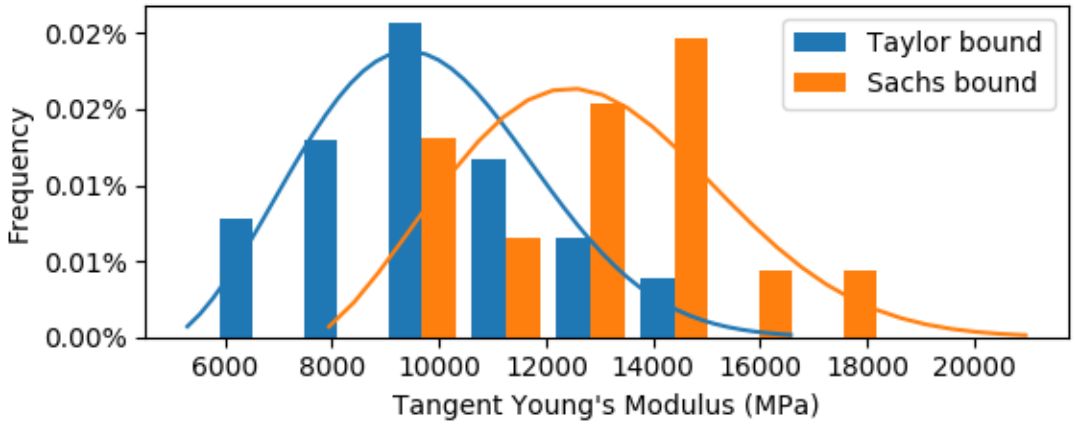

Figure A.82: Tangent Young's Mod. for $1x10^5$ Comminuted Particle Ensemble at 200 MPa

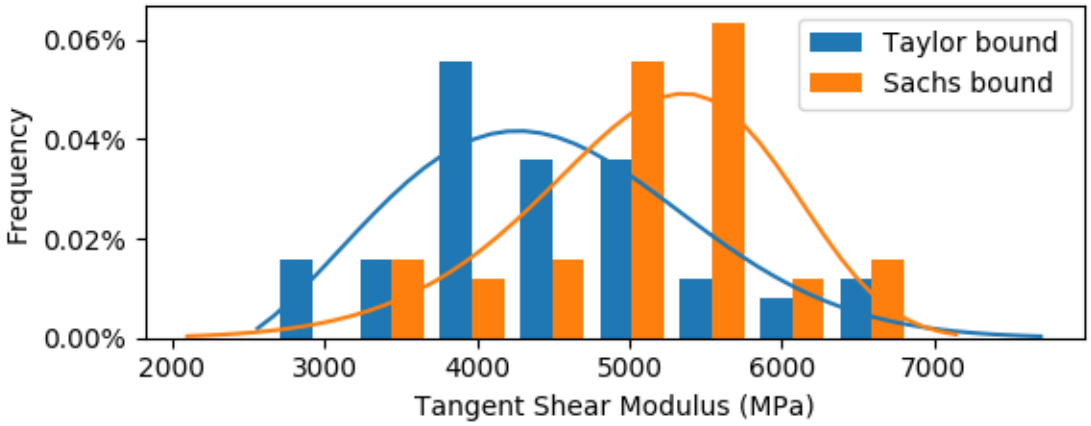

Figure A.83: Tangent Shear Mod. for $1x10^5$ Comminuted Particle Ensemble at 200 MPa

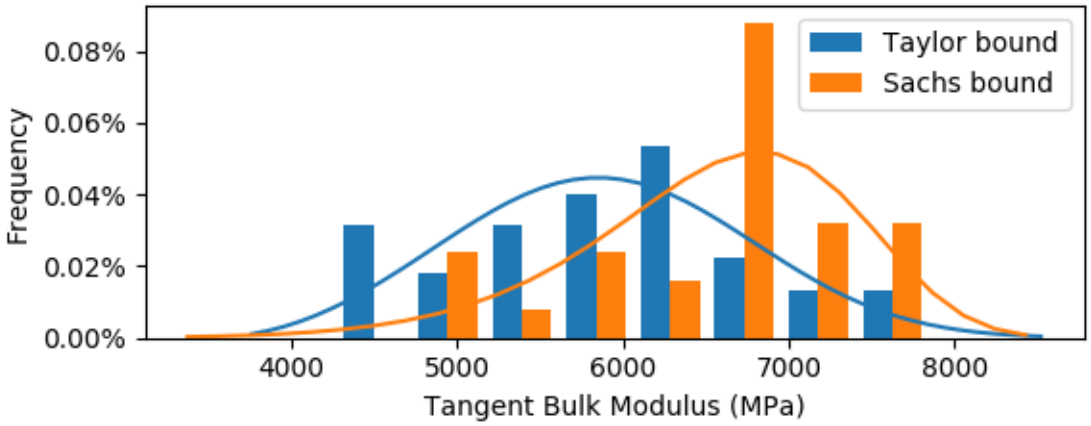

Figure A.84: Tangent Bulk Mod. for $1x10^5$ Comminuted Particle Ensemble at 200 MPa

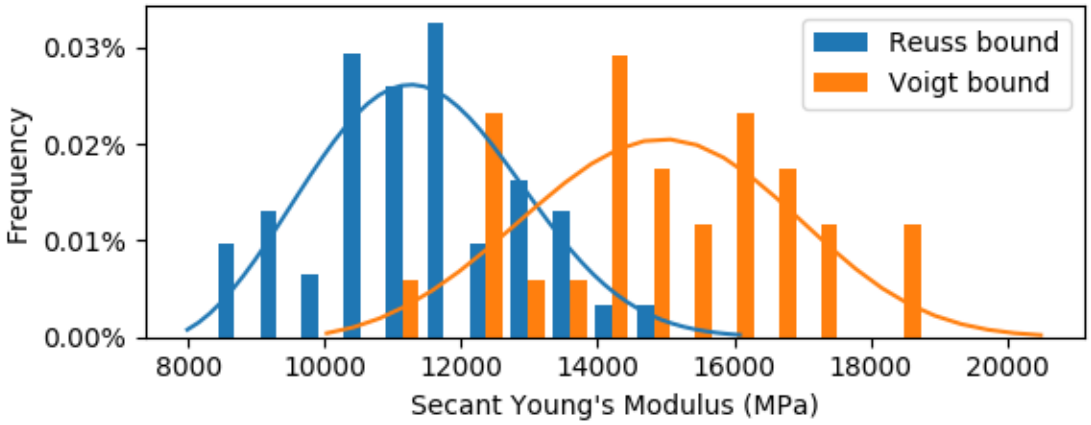

Figure A.85: Secant Young's Mod. for $1x10^5$ Comminuted Particle Ensemble at 400 MPa

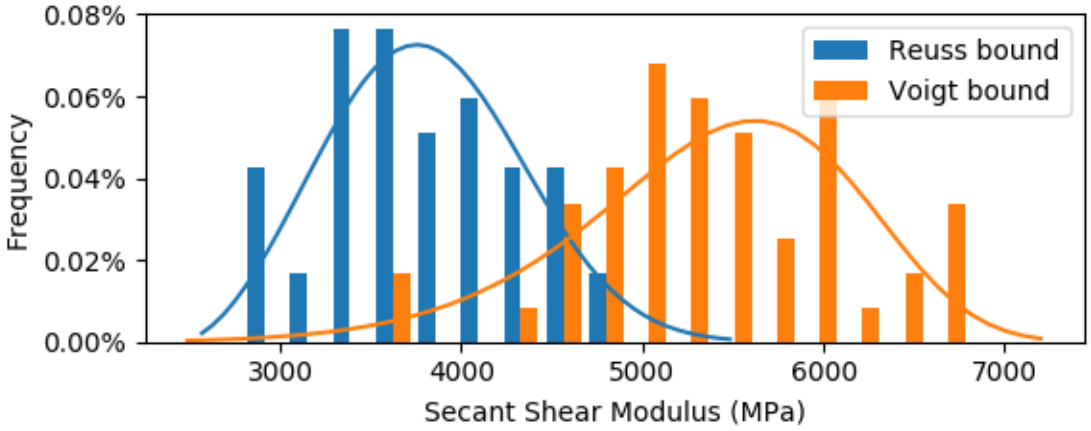

Figure A.86: Secant Shear Mod. for $1x10^5$ Comminuted Particle Ensemble at 400 MPa

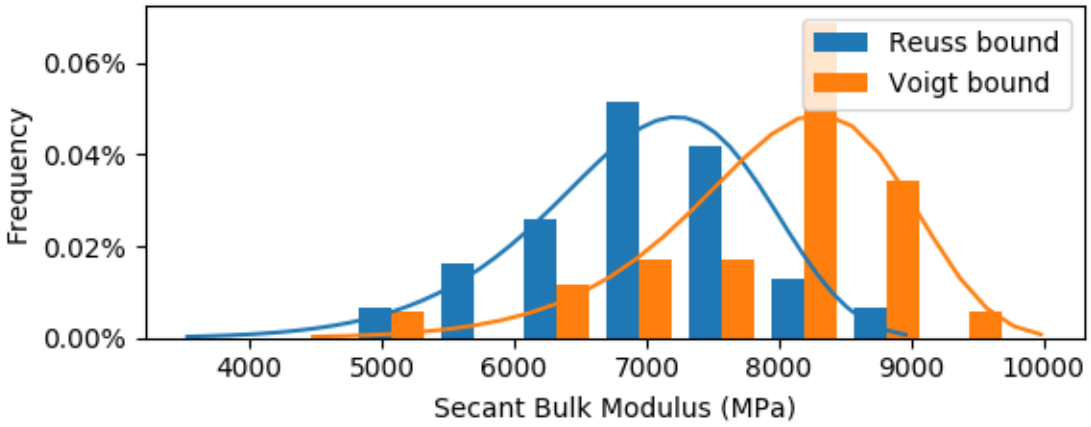

Figure A.87: Secant Bulk Mod. for $1x10^5$ Comminuted Particle Ensemble at 400 MPa

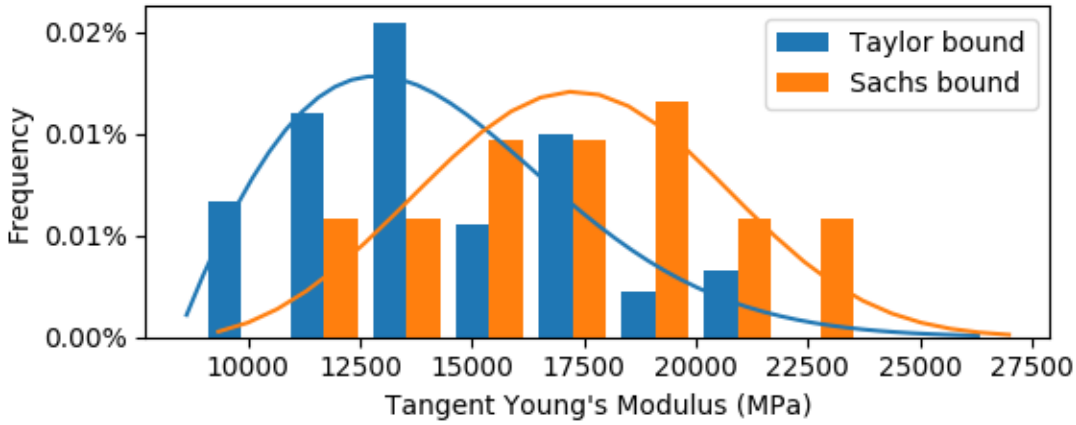

Figure A.88: Tangent Young's Mod. for $1x10^5$ Comminuted Particle Ensemble at 400 MPa

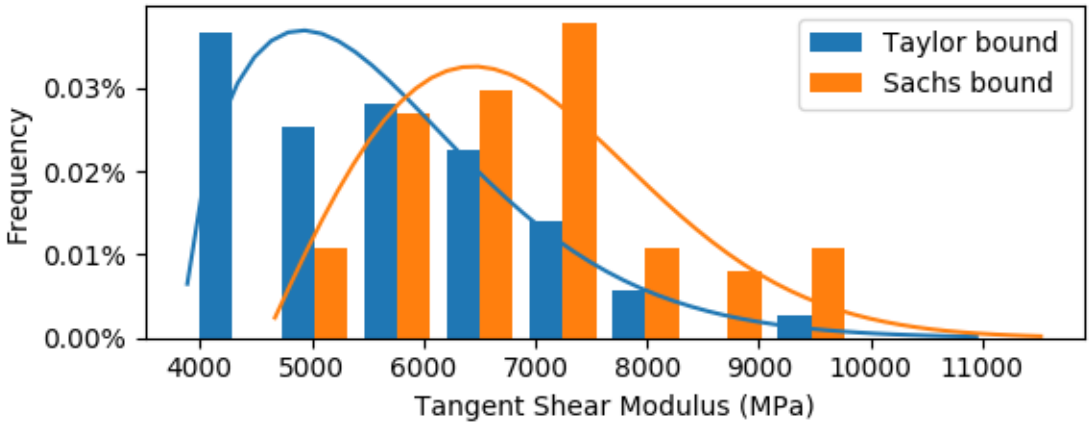

Figure A.89: Tangent Shear Mod. for $1x10^5$ Comminuted Particle Ensemble at 400 MPa

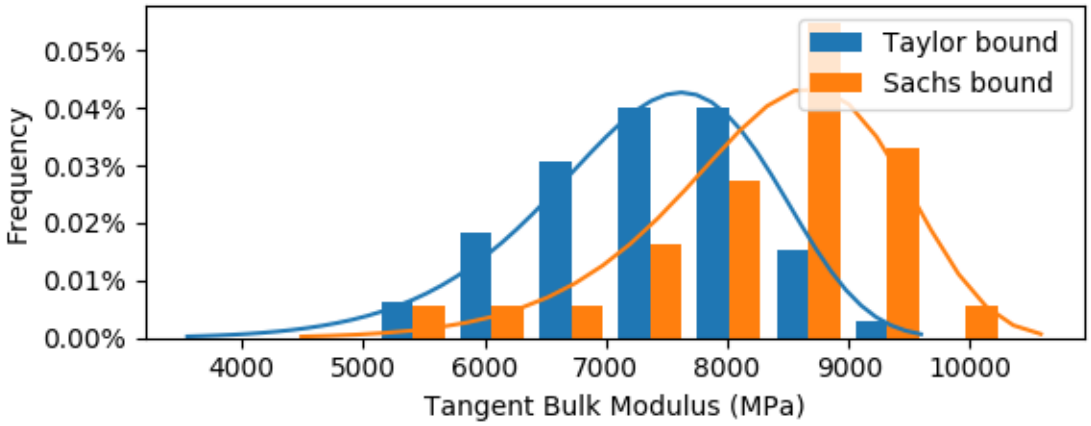

Figure A.90: Tangent Bulk Mod. for $1x10^5$ Comminuted Particle Ensemble at 400 MPa